Vortex Filament Equation for some Regular Polygonal Curves

Sandeep Kumar

Department of Mathematics and Statistics and Operations Research

Supervised by

Luis Vega González and *Francisco de la Hoz Méndez*

This dissertation is submitted for the degree of

Doctor of Philosophy

May 2020

Vortex Filament Equation for some Regular Polygonal Curves

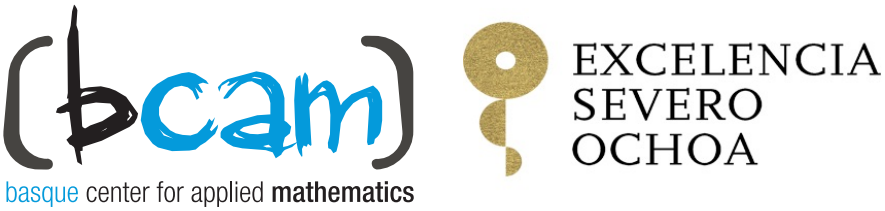

Sandeep Kumar

Research Area: Analysis of Partial Differential Equations

Supervised by

Luis Vega González and *Francisco de la Hoz Méndez*

This dissertation is submitted for the degree of

Doctor of Philosophy

May 2020

Purnamadah Purnamidam Purnat Purnamudachyate
Purnasya Purnamadaya Purnamevavashisyate

– Brihadaranyaka Upanishad 5.1.1

I would like to dedicate this thesis to my loving parents.

This research was carried out at the Basque Center for Applied Mathematics (BCAM) within the Analysis of Partial Differential Equations (APDE) - the Linear and Non-Linear Waves research group and was supported by the Basque Government through the BERC 2018-2021 programs, by the Spanish Ministry of Economics and Competitiveness MINECO through the BCAM Severo Ochoa excellence accreditation SEV-2013-0323, Predoc Severo Ochoa 2014 (Ref. SVP-C-2014-0002) and by the Spanish State Research Agency through BCAM Severo Ochoa excellence accreditation SEV-2017-0718 and ERCEA Advanced Grant 2014 669689-HADE. The support of Severo Ochoa and BERC Grants is acknowledged for the three months visit at the University of California, Santa Barbara, USA.

Declaration

I hereby declare that except where specific reference is made to the work of others, the contents of this dissertation are original and have not been submitted in whole or in part for consideration for any other degree or qualification in this, or any other University.

Sandeep Kumar
May 2020

Acknowledgements

Pursuing the Ph.D. has been a truly life-changing experience for me and this would not have been possible without the support and guidance I received from different people.

First of all, I would like to express my sincere gratitude to my advisors Prof. Luis Vega and Prof. Francisco de la Hoz for the continuous support of my Ph.D. studies and related research, for their patience, motivation, and immense knowledge. Their guidance helped me in all the time of research and writing of this thesis. I am truly pleased to have been their student. *¡Muchas gracias!*

Special thanks to people at UCSB for their hospitality and having me there for three months. Most importantly to Prof. Carlos Garcia-Cervera for giving me this opportunity, insightful mathematical interactions, encouragement, and guidance.

I would like to express my sincere thanks to all the teachers I have had so far, in particular, from SSSIHL, India, for making me eligible enough to pursue doctoral studies.

A big thanks to all the people at BCAM for creating and maintaining a lively and workable environment. I thank the staff members for making all the bureaucracy so smoothly and flawlessly. Many thanks to my officemates Josu, Mathi, Daniel, Gabriela in the first year, and Dani for the rest (thanks for helping me learn the Spanish language, culture, and keeping a disciplined and friendly atmosphere in the office, *Eskerrik asko*). I thank Nicole, Mauricio, Isabella, Diana, Luz, Javi, Antsa for the lunch breaks, and chats. Thanks to Ananyo for sharing coffee from all over the world, for motivation and encouragement. A heartfelt thanks to Marco for being a nice friend and helping me out right from the beginning of my stay in Bilbao until now, *Muchas gracias*. I thank Arthur for the unforgettable conversations about life and mathematics, *Merci beaucoup*. Thanks to Daniel, Enrique, Jorge in Bilbao and Kyle, Jay, Steve in Santa Barbara for their friendly company. Special thanks to doctors in *Osakidetza*, especially for the last year of this period. I would like to thank my Indian friends and their families in Bilbao for not letting me miss my home country; to Ankan, Surajit, Upanshu, Sugeet for always being there over the phone calls. I thank Baldur, Oleksii, Hanna, Aitor for the hiking, and excursions around Bilbao. It will be hard to forget the numerous

virtual lunch sessions with Fernando, Christina, Tamara, Simone, Abolfazl, Pratyusha, Kaoutar during the COVID-19 lockdown which helped me a lot in keeping up the work spirit in the last months, Thank you.

In the end, I would like to thank my parents for allowing me to stay away right from my undergraduate studies and to pursue whatever I wished. Their presence has always been a driving force. Thanks to my family members Nisha, Neetu, Vijay, and Ira for their continuous support, love, and affection. And finally to Havva for everything! It's impossible to count but in short, this journey was full of ups and downs but her company, support, patience and encouragement, made me trust in myself and reach till the end, *Çok teşekkür ederim.*

Contents

List of Figures

List of Tables

Summary

One of the most interesting phenomena in fluid literature is the occurrence and evolution of vortex filaments. Some of their examples in the real world are smoke rings, whirlpools, and tornadoes. For an ideal fluid, there have been several models and governing equations to describe this evolution; however, due to its simplicity and geometric properties, the vortex filament equation (VFE) has recently gained substantial attention. As an approximation of the dynamics of a vortex filament, the equation first appeared in the work of Da Rios in the beginning of twentieth century [53]. This model is usually known as the localized induction approximation (LIA).

In this work, we examine the evolution of VFE for regular polygonal curves both from a numerical and theoretical point of view in the Euclidean as well as hyperbolic geometry. This has been achieved through four chapters where the first chapter briefly describes the model, previous work and motivation; the second chapter deals with the regular polygons with nonzero torsion in the Euclidean setting and in the third and fourth chapters, we consider the case of regular planar polygons in the hyperbolic setting. In the following lines, we summarize each of these chapters briefly.

Summary of Chapter 1

The chapter begins with a brief introduction to VFE,

$$\mathbf{X}_t = \mathbf{X}_s \wedge_{\pm} \mathbf{X}_{ss}, \tag{1}$$

where $\mathbf{X}$ is an arc-length parameterized curve representing vortex filament, s the arc-length parameter, t time and $\wedge_{\pm}$ is the cross product given by

$$\mathbf{a} \wedge_{\pm} \mathbf{b} = (\pm(a_2b_3 - a_3b_2), a_3b_1 - a_1b_3, a_1b_2 - a_2b_1),$$

where the positive sign corresponds to the Euclidean case and the negative sign to the hyperbolic case. The tangent vector $\mathbf{T} = \mathbf{X}_s$, satisfies the so-called Schrödinger map

equation onto the sphere

$$\mathbf{T}_t = \mathbf{T} \wedge_{\pm} \mathbf{T}_{ss}, \tag{2}$$

which has a very important property that during its evolution $\mathbf{T}$ preserves its size. Through a transformation given by H. Hasimoto in 1970, (1)–(2) are related to the cubic nonlinear Schrödinger equation [38].

In this work, we are mainly interested in filaments with corners. The evolution of curves with one corner otherwise smooth has been understood thoroughly both from a theoretical and numerical point of view, and the corresponding problem we refer to as *one-corner problem* [21, 36]. However, the case of curves with multiple corners was unaddressed until very recently. In this direction, the evolution of a regular planar M-sided polygon in the Euclidean case revealed several interesting properties of VFE. In this work, the corresponding problem will be referred to as *planar M-polygon problem* [22]. This chapter briefly describes and highlights the key points of the two problems. Furthermore, we discuss some exact solutions of VFE in the hyperbolic space which also helps us in understanding the nature of polygonal curves in that setting. Finally, we state some recent theoretical results on the evolution of VFE for polygonal lines that play a very important role in obtaining certain preserved quantities [8, 9].

Summary of Chapter 2

The key ingredients of this chapter are M-polygons with nonzero torsion (helical M-polygons) in the Euclidean space $\mathbb{R}^3$, and using them we show that the helices and straight lines have the same instability as the one already established for circles [22, 25]. In this direction, we consider the initial curve as a helical M-polygon which is characterized by two parameters M and b. The parameter b corresponds to the third component of the tangent vector $\mathbf{T}$, a 2π-periodic function that takes M values on the unit sphere $\mathbb{S}^2$; moreover, these parameters also determine the curvature angle ρ_0 and torsion angle θ_0. At the level of the NLS equation, the nonzero-torsion problem can be seen as a Galilean transformation of the planar M-polygon problem. Consequently, using some algebraic computations, the evolution can be described for times that are rational multiple of $2\pi/M^2$, i.e., when $t = t_{pq} = (2\pi/M^2)(p/q)$, with $\gcd(p, q) = 1$, $p \in \mathbb{Z}, q \in \mathbb{N}$. It is found that the helical M-polygon curve at time t_{pq} is a polygon with Mq sides (if q odd) or $Mq/2$ sides (if q even). The presence of torsion causes a lack of space and time periodicity which gives rise to what we call as *Galilean shift* and *phase shift*. Then, a principle of conservation of energy proved in [8] allows us to compute the angle ρ_q between any two adjacent sides of the resulting polygon, so,

using the generalized quadratic Gauß sums, we can construct the polygonal curve, up to a rigid movement. Later on, using algebraic techniques as in [23], an expression for the speed of the center of mass c_M is given. With all these ingredients, the algebraic solution can be computed up to a rotation that remains undetermined.

For the numerical evolution, we use a pseudo-spectral discretization in space and a fourth-order Runge–Kutta method in time. The symmetries of the tangent vectors allow us to reduce the computation cost quite effectively. Numerical simulations show that apart from the formation of new sides, the helical M-polygon moves in the vertical direction at a constant speed and a rotation about the z-axis. Furthermore, we have computed the angle between the new sides and speed numerically and have compared the values with their algebraic counterparts.

We also study the trajectory of a point which is multifractal, but no more planar as in the case of a regular planar M-polygon. Then, by taking b, such that $\theta_0 = \pi c/d$, with $\gcd(c,d) = 1$, $c, d \in \mathbb{N}$, the periodicity in space can be recovered for large times i.e., multiples of $2\pi/M^2$. For such time period, after removing the vertical height, the third component of $\mathbf{X}(0,t)$ is periodic, and its structure can be compared with the imaginary part of

$$\phi_{c,d}(t) = \sum_{k \in A_{c,d}} \frac{e^{2\pi i k t}}{k}, \quad t \in \begin{cases} [0,1/2], & \text{if } c \cdot d \text{ odd}, \\ [0,1], & \text{if } c \cdot d \text{ even}, \end{cases}$$

where the set $A_{c,d}$ is defined in (2.47). After applying an appropriate scaling, and expressing it in terms of its Fourier expansion, we get

$$\lim_{M \to \infty} |n\, b_{n,M}| = \begin{cases} 1/4, & \text{if } n \in A_{c,d} \text{ and } c \cdot d \text{ odd}, \\ 1/2, & \text{if } n \in A_{c,d} \text{ and } c \cdot d \text{ even}, \\ 0, & \text{otherwise}, \end{cases}$$

where $b_{n,M}$ are the Fourier coefficients. In the case of the straight lines, the trajectory $\mathbf{X}(0,t)$ in the XY-plane tends to a 2π-periodic closed curve, which can be compared to

$$\phi_M(t) = \sum_{k \in A_M} \frac{e^{2\pi i k^2 t}}{k^2}, \quad t \in [0,1],$$

where the set A_M is defined in (2.50). Thus, after removing the vertical height of $\mathbf{X}(0,t)$ and then performing a stereographic projection of the resulting curve, with a proper orientation and scaling, we approximate its Fourier coefficients c_n, to show that,

for a given M,

$$\lim_{b\to 1^-} |n\, c_n| = \begin{cases} 1, & \text{if } n \in A_M, \\ 0, & \text{otherwise.} \end{cases}$$

We also examine the behavior of $\mathbf{T}$ for rational times t_{pq}, with $q \gg 1$, and compare it with the zero-torsion case. Finally, we briefly describe the numerical relationship between the helical M-polygon and one-corner problems.

Thus, we see that these new solutions of VFE can be used to illustrate numerically that smooth solutions such as helices and straight lines share the same instability as the one already established for circles. This has been accomplished by showing the existence of variants of the so-called Riemann's non-differentiable function that are as close to smooth curves as desired when measured in the right topology. This topology is motivated by some recent results on the well-posedness of VFE, which proves that the self-similar solutions of VFE have finite renormalized energy.

Summary of Chapter 3

In this chapter, we concentrate on the regular polygonal curve in the hyperbolic space where the unit tangent vector $\mathbf{T} \in \mathbb{H}^2$ (hyperbolic 2-space[1]) and the corresponding curve $\mathbf{X} \in \mathbb{R}^{1,2}$ (Minkowski 3-space[3]). The regular polygonal curve with zero torsion is characterized by a parameter $l > 0$ which denotes the hyperbolic angle between any of its two sides, we will call this curve a planar l-polygon. Let us mention that curves with one corner and otherwise smooth in the Minkowski 3-space have already been addressed; however, nothing has been done in the direction of curves with multiple corners [21, 24]. The main motivation to consider them comes from the Euclidean case where the evolution of M-polygons reveals many interesting features of VFE as discussed previously.

One of our primary goals is to compute the evolution of a planar l-polygon both theoretically and numerically. In this direction, for the algebraic computation, the relationship of (1)–(2) with the NLS equation of defocussing type turns out to be very useful where with the help of Galilean invariance, we obtain the evolution at the rational times. The conservation law mentioned in Chapter 2 holds true in the hyperbolic case as well, as a result, the mutual angle between any of the two sides of the new polygon can be determined. With this and the quadratic Gauß sums, $\mathbf{T}$ and $\mathbf{X}$ are recovered up to a rigid movement. On the other hand, for the numerical solution,

[1]See Appendix A

we work with the coupled system of (1)–(2). Unlike in the Euclidean case, where a pseudo-spectral discretization in space appears to be very efficient, in the hyperbolic case, we solve the system using different numerical schemes. Moreover, since the planar l-polygon has infinite length, to solve it numerically we truncate it and thus, the choice of boundary conditions becomes very crucial. We have used the following numerical methods with different boundary treatment:

1. A fourth-order finite difference discretization in space and a fourth-order Runge–Kutta method in time with
   (a) Dirichlet boundary conditions on $\mathbf{T}$,
   (b) Dirichlet boundary conditions on $\mathbf{X}$;
2. Chebyshev spectral discretization in space (Dirichlet boundary condition on $\mathbf{T}$) with
   (a) a fourth-order Runge–Kutta method in time,
   (b) a second-order semi-implicit backward differentiation formula (SBDF) in time as in [24],
   (c) a second-order SBDF method for the stereographic projection of (2).

Among these schemes, we found that the finite difference scheme with fixed boundary conditions on $\mathbf{T}$ gives the best results both in terms of accuracy and computational cost. In this way, we verify the numerical evolution by comparing it with the algebraic one. Remark that at a numerical level, the case of hyperbolic polygons is very different from its Euclidean counterpart which makes it challenging in the following aspects. First, the planar l-polygon is open and closed at infinity, therefore, only a part of the polygon is considered for the numerical evolution. Moreover, due to the exponential growth of the tangent vectors, working with a large value of l is not possible. In the Euclidean case, due to the symmetries of the tangent vector $\mathbf{T}$, the numerical computation could be performed using only one side of the M-polygon, however, in the hyperbolic case, because of the fixed boundary conditions, all sides of the planar l-polygon need to be considered which in turn makes it more computationally expensive.

Numerical experiments show that during its evolution the center of mass of the planar l-polygon propagates in the z-axis direction with a constant speed c_l, and follows a periodic trajectory along the y-axis whereas, it remains stationary along the x-axis. We compute c_l numerically and compare it with an exact expression which is later obtained in Chapter 4. Moreover, $\mathbf{X}(0,t)$, i.e., the time evolution of a single point

on the planar l-polygon lies in the YZ-plane and has a multifractal structure which reminds us of the Riemann's non-differentiable function as observed in the Euclidean case. As a consequence, we can say that Riemann's function and its variants appear as universal objects in the dynamics of singular solutions of (1). Moreover, these universal objects are, in the right topology, as close as desired to smooth curves as mentioned previously.

Summary of Chapter 4

In this chapter, we follow the steps of the Euclidean case and try to answer up to what extent the l-polygon problem in the hyperbolic case is related to the one-corner problem. In this regard, we give numerical evidence of this relationship between the two problems and claim that for infinitesimal times the multiple-corner problem can be seen as a superposition of several one-corner problems. As a consequence, through the one-corner problem, an exact expression for the speed of the center of mass of the planar l-polygon is obtained and later, a numerical proof of the same has been provided. Using the asymptotics of the tangent vector in the one-corner problem, exact expressions for its second and third components at time zero have been obtained. On the other hand, with the Laplace transform, using a completely different approach, the expression for the first component has been recovered as well. Finally, we also compute the linear momentum for the planar l-polygon numerically and show that its evolution has an intermittent behavior.

Resumen

Uno de los fenómenos más interesantes en la literatura sobre fluidos es la aparición y evolución de filamentos de vórtice. Algunos de sus ejemplos en el mundo real son los anillos de humo, los remolinos y los tornados. Para un fluido ideal, existen varios modelos y ecuaciones que describen su evolución. Sin embargo, debido a su simplicidad y propiedades geométricas, la VFE (Vortex Filament Equation) ha llamado recientemente la atención. Como una aproximación de la dinámica de un filamento de vórtice, la ecuación apareció por primera vez en el trabajo de Da Rios a principios del siglo XX [53]. Este modelo generalmente se conoce como LIA (localized induction approximation).

En este trabajo, examinamos la evolución de VFE para curvas poligonales regulares tanto desde un punto de vista numérico y teórico en la geometría euclidiana como hiperbólica. Esto lo hemos elaborado a lo largo de cuatro capítulos donde el primer capítulo describimos brevemente el modelo, el trabajo previo y la motivación; El segundo capítulo trata de los polígonos regulares con torsión distinta de cero en la configuración euclidiana y en los capítulos tercero y cuarto, consideramos el caso de los polígonos planos regulares en la configuración hiperbólica. En las siguientes líneas, resumimos brevemente cada uno de estos capítulos.

Resumen del capítulo 1

El capítulo comienza con una breve introducción a la VFE que fue obtenida por primera vez por L.S. Da Rios en 1905 [53] como

$$\mathbf{X}_t = \mathbf{X}_s \wedge_{\pm} \mathbf{X}_{ss}, \tag{3}$$

donde $\mathbf{X}$ es una curva parametrizada de longitud de arco que representa el filamento de vórtice, s el parámetro por longitud de arco, t el tiempo y $\wedge_{\pm}$ es el producto vectorial

dado por

$$\mathbf{a} \wedge_{\pm} \mathbf{b} = (\pm(a_2b_3 - a_3b_2), a_3b_1 - a_1b_3, a_1b_2 - a_2b_1),$$

donde el signo positivo corresponde al caso euclidiano y el signo negativo al caso hiperbólico. El vector tangente $\mathbf{T} = \mathbf{X}_s$ satisface la llamada *Schrödinger map equation* en la esfera

$$\mathbf{T}_t = \mathbf{T} \wedge_{\pm} \mathbf{T}_{ss}, \tag{4}$$

que tiene una propiedad importante de esta ecuación es que T conserva su tamaño durante la evolución. Mediante una transformación dada por H. Hasimoto en 1970, (3)-(4) se relacionan con la ecuación cúbica no lineal de Schrödinger [38].

En este trabajo, estamos interesados principalmente en filamentos con esquinas. El *one-corner problem*, es decir, la evolución de curvas suaves excepto en una esquina, ha sido estudiada a fondo tanto desde un punto de vista teórico como numérico [21, 36]. Sin embargo, el caso de las curvas con múltiples esquinas no ha sido abordado hasta hace muy poco. En esta dirección, la evolución de un polígono plano de M lados en el caso euclidiano reveló varias propiedades interesantes de la VFE. En este trabajo, llamaremos a este problema *planar M-polygon problem* [22]. En este capítulo se describen brevemente los dos problemas y se destacan sus puntos clave. Además, estudiamos algunas soluciones exactas de la VFE en el espacio hiperbólico que también nos ayuda a comprender la naturaleza de las curvas poligonales en ese entorno. Finalmente, exponemos algunos resultados teóricos recientes sobre la evolución del flujo binormal para líneas poligonales que juegan un papel muy importante en la obtención de ciertas cantidades preservadas [8, 9].

Resumen del capítulo 2

Los ingredientes claves de este capítulo son los M-polígonos con torsión no nula (M-polígonos helicoidales) en el espacio euclidiano $\mathbb{R}^3$, y al usarlos mostramos que las hélices y las líneas rectas también tienen la misma inestabilidad como la que ya se estableció para los círculos [22, 25]. En esta dirección, consideramos la curva inicial como un M-polígono helicoidal que se caracteriza por dos parámetros M y b. El parámetro b corresponde a la tercera componente del vector tangente $\mathbf{T}$, una función 2π-periódica que toma M valores en $\mathbb{S}^2$. Además, estos parámetros también determinan el ángulo de curvatura ρ_0 y el ángulo de torsión θ_0. A nivel de la ecuación NLS, el problema de la torsión no nula puede verse como una transformación galileana del problema del M-polígono plano. En consecuencia, utilizando algunos cálculos algebraicos, la

evolución se puede describir en los tiempos $t = t_{pq} = (2\pi/M^2)(p/q)$, con $\mathrm{mcd}(p,q) = 1$, $p \in \mathbb{Z}, q \in \mathbb{N}$, es decir, en momentos que son múltiplos racionales de $2\pi/M^2$. En concreto, la curva helicoidal M-polígono en el tiempo t_{pq} es un polígono con Mq lados (si q es impar) o $Mq/2$ lados (si q es par). La presencia de torsión provoca la falta de periodicidad en espacio y tiempo, lo que da lugar a lo que llamamos *Galilean shift* y *phase shift*. Entonces, un principio de conservación de energía demostrado en [8] nos permite calcular el ángulo ρ_q entre dos lados adyacentes del polígono resultante, y por lo tanto, utilizando las sumas de Gauß cuadráticas generalizadas, podemos construir la curva poligonal excepto por un movimiento rígido. Más adelante, usando técnicas algebraicas como en [23], se da una expresión para la velocidad del centro de masa c_M. Con todos estos ingredientes, la solución algebraica se puede calcular excepto por una rotación indeterminada.

Para la evolución numérica, utilizamos una discretización pseudo-espectral en espacio y un método Runge–Kutta de cuarto orden en tiempo. Las simetrías de los vectores tangentes nos permiten reducir el costo de cálculo de manera bastante efectiva. Las simulaciones numéricas muestran que, aparte de la formación de nuevos lados, el M-polígono helicoidal se mueve en dirección vertical a una velocidad constante y rotando alrededor del eje z. Hemos calculado el ángulo entre los nuevos lados y la velocidad numéricamente y hemos comparado los valores con sus contrapartes algebraicas.

También estudiamos la trayectoria de un punto, que es multifractal pero no plana como en el caso de un M-polígono plano y regular. Además, al tomar b, de modo que $\theta_0 = \pi c/d$, con $\gcd(c,d) = 1$, $c, d \in \mathbb{N}$, la periodicidad en espacio puede recuperarse para grandes tiempos, es decir, múltiplos de $2\pi/M^2$. Además, para dicho período de tiempo, después de eliminar la altura vertical, la tercera componente de $\mathbf{X}(0,t)$ es periódica, y su estructura se puede comparar con la parte imaginaria de

$$\phi_{c,d}(t) = \sum_{k \in A_{c,d}} \frac{e^{2\pi i k t}}{k}, \quad t \in \begin{cases} [0, 1/2], & \text{si } c \cdot d \text{ impar}, \\ [0,1], & \text{si } c \cdot d \text{ par}, \end{cases}$$

donde el conjunto $A_{c,d}$ se define en (2.47). Después de aplicar una escala adecuada y expresarla en términos de su expansión de Fourier, obtenemos

$$\lim_{M \to \infty} |n\, b_{n,M}| = \begin{cases} 1/4, & \text{si } n \in A_{c,d} \text{ y } c \cdot d \text{ impar}, \\ 1/2, & \text{si } n \in A_{c,d} \text{ y } c \cdot d \text{ par}, \\ 0, & \text{en cualquier otro caso}, \end{cases}$$

donde $b_{n,M}$ son los coeficientes de Fourier. En el caso de las líneas rectas, la trayectoria $\mathbf{X}(0,t)$ en el plano XY tiende a una curva cerrada periódica de 2π, que se puede comparar con

$$\phi_M(t) = \sum_{k \in A_M} \frac{e^{2\pi i k^2 t}}{k^2}, \quad t \in [0,1],$$

donde el conjunto A_M se define en (2.50). Por lo tanto, después de eliminar la altura vertical de $\mathbf{X}(0,t)$ y de realizar una proyección estereográfica de la curva resultante, con una orientación y escala adecuadas, aproximamos sus coeficientes de Fourier c_n para mostrar que, para un determinado M,

$$\lim_{b \to 1^-} |n\, c_n| = \begin{cases} 1, & \text{si } n \in A_M, \\ 0, & \text{en cualquier otro caso.} \end{cases}$$

También examinamos el comportamiento de $\mathbf{T}$ para tiempos racionales t_{pq} con $q \gg 1$ y lo comparamos con el caso de torsión nula. Finalmente, describimos brevemente la relación numérica entre los problemas de M esquinas con torsión no nula y una esquina.

Por lo tanto, vemos que estas nuevas soluciones de la VFE se pueden usar para ilustrar numéricamente que las soluciones suaves como las hélices y las líneas rectas comparten la misma inestabilidad que la ya establecida para los círculos. Esto se ha logrado mostrando la existencia de variantes de la función no diferenciable de Riemann que están tan cerca de las curvas suaves como se desee cuando se mide en la topología correcta. Esta topología está motivada por algunos resultados recientes que muestran que la VFE está bien definida y que las soluciones autosemejantes de la VFE tienen energía renormalizada finita.

Resumen del capítulo 3

En este capítulo, nos concentramos en la curva poligonal regular en el espacio hiperbólico tal que $\mathbf{T}$ in $\mathbb{H}^2$ y $\mathbf{X}$ in $\mathbb{R}^{1,2}$, donde $\mathbf{T}$ es el vector tangente unitario y $\mathbf{X}$ la curva. La curva poligonal regular con torsión nula se caracteriza por un parámetro $l > 0$ que denota el ángulo hiperbólico entre cualquiera de sus dos lados. Llamaremos a esta curva un l-polígono planar.

Mencionemos que las curvas suaves excepto en una esquina en el espacio de Minkowski $\mathbf{X} \in \mathbb{R}^{1,2}$ ya se han abordado; sin embargo, no se ha trabajado en la dirección de curvas con múltiples esquinas [21, 24]. La principal motivación para

considerarlas proviene del caso euclidiano donde la evolución de los M-polígonos revela muchas características interesantes de la VFE como se ha comentado anteriormente.

Uno de nuestros objetivos principales es calcular la evolución de un l-polígono plano tanto teórica como numéricamente. En esta dirección, para el cálculo algebraico, la relación de (3)-(4) con la ecuación NLS *defocussing* resulta ser muy útil cuando con la ayuda de la invariancia galileana obtenemos la evolución en los tiempos racionales. La ley de conservación mencionada en el Capítulo 2 también es válida en el caso hiperbólico, y por lo tanto, se puede determinar el ángulo mutuo entre dos lados cualesquiera. Con esto y las sumas cuadráticas de Gauß, M y $\mathbf{X}$ se recuperan excepto por un movimiento rígido. Por otro lado, para la solución numérica, trabajamos con el sistema acoplado de (3)-(4).

A diferencia del caso euclidiano, donde una discretización pseudo-espectral en el espacio parece ser muy eficiente, en el caso hiperbólico resolvemos el sistema usando diferentes planteamientos numéricos. Además, dado que el l-polígono planar tiene una longitud infinita, para resolverlo numéricamente lo truncamos y, por lo tanto, la elección de las condiciones de contorno se vuelve crucial. Hemos utilizado los siguientes métodos numéricos con un tratamiento de contorno diferente:

1. Una discretización por diferencias finitas de cuarto orden en espacio y un método Runge–Kutta de cuarto orden tiempo con:
   (a) Condición de contorno de Dirichlet en $\mathbf{X}$,
   (b) Condición de contorno de Dirichlet en $\mathbf{T}$,
2. Discretización espectral de Chebyshev en el espacio (condición de contorno de Dirichlet en $\mathbf{T}$) con:
   (a) un método de Runge-Kutta de cuarto orden en tiempo,
   (b) una fórmula de diferenciación hacia atrás (SBDF) semi-implícita de segundo orden en tiempo como en [24],
   (c) un método SBDF de segundo orden para la proyección estereográfica de (4).

Entre estos planteamientos, vemos que el de diferencias finitas con condiciones de contorno fijas en $\mathbf{T}$ brinda los mejores resultados tanto en términos de precisión como de eficiencia. De esta forma, verificamos la evolución numérica comparándola con la algebraica. Observamos que que, a nivel numérico, el caso de los polígonos hiperbólicos es muy diferente de su contraparte euclidiana, lo que lo convierte en un desafío en los siguientes aspectos. Primero, el l-polígono planar es abierto abierto y cerrado en

el infinito, por lo tanto, solo una parte del polígono se considera para la evolución numérica. Además, debido al crecimiento exponencial de los vectores tangentes, no es posible trabajar con un valor grande de l. En el caso euclidiano, debido a las simetrías del vector tangente $\mathbf{T}$, el cálculo numérico podría realizarse utilizando solo un lado del M-polígono, pero en el caso hiperbólico, debido a las condiciones de contorno predefinidas, es necesario tener en cuenta todos los lados del l-polígono plano, lo que a su vez lo hace más costoso desde el punto de vista computacional.

Los experimentos numéricos muestran que durante su evolución el centro de masa del l-polígono se propaga en la dirección del eje z con una velocidad constante c_l y que sigue una trayectoria periódica a lo largo del eje y, mientras que permanece estacionario a lo largo el eje x. Calculamos c_l numéricamente y lo comparamos con una expresión exacta que luego se obtiene en el Capítulo 4. Además, al calcular $\mathbf{X}(0,t)$, es decir, la evolución temporal de un solo punto en el l-polígono, notamos que se encuentra en el plano YZ y tiene una estructura multifractal que nos recuerda la función no diferenciable de Riemann como se observa en el caso euclidiano. Como consecuencia, podemos decir que la función de Riemann y sus variantes aparecen como objetos universales en la dinámica de soluciones singulares de (3). Además, estos objetos universales están, en la topología correcta, tan cerca como se desee de curvas suaves como se mencionó anteriormente.

Resumen del Capítulo 4

Siguiendo los pasos del caso euclidiano, en este capítulo tratamos de responder hasta qué punto el problema del l-polígono en el caso hiperbólico está relacionado con el problema de una esquina. En este sentido, damos evidencia numérica de esta relación entre los dos problemas y afirmamos que, en tiempos infinitesimales, el problema de las esquinas múltiples puede verse como una superposición de varios problemas de una esquina. Como consecuencia, a través del problema de una esquina se obtiene una expresión precisa para la velocidad del centro de masa del l-polígono plano y luego se proporciona una prueba numérica del mismo.

Usando las asintóticas del vector tangente en el problema de una esquina, se han obtenido expresiones exactas para sus componentes segunda y tercera en tiempo cero. Por otro lado, con la transformación de Laplace, la expresión para el primer componente también se ha recuperado. Finalmente, también calculamos el momento lineal para el l-polígono planar numéricamente y mostramos que su evolución tiene un comportamiento intermitente.

Chapter 1

Introduction

The primary goal of this chapter is to provide the key ingredients which help us in introducing the main theme of the memoir. This has been achieved by introducing the vortex filament equation, its properties, self-similar solutions, and recent work on the corner shaped solutions. Some explicit solutions in the Minkowski space are considered as well which will be one of the main objects of interest for us. Finally, we state some recent theoretical results on polygonal lines whose application will play an important role in this work.

1.1 Vortex filament equation

In this section, we discuss about the physical meaning behind the origin of the vortex filament equation, its equivalent forms and their properties.

Given a three-dimensional ideal (non-viscous, incompressible) fluid with velocity $\mathbf{u}$ and vorticity ω (curl of $\mathbf{u}$), a *vortex tube* is a tubular region of the fluid where the vorticity is very high compared to its surroundings, and a *vortex filament* is a vortex tube with an infinitesimal cross-section. In other words, a vortex filament is an imaginary spatial curve that induces a rotary flow in the space through which it passes. The ability of the filament to induce circulation around it depends on its strength which we denote as Γ.

We represent the vortex filament by an arc-length parameterized curve $\mathbf{X}(s,t)$ in $\mathbb{R}^3$, where s is the arc-length parameter and t time. Assuming the curvature κ to be nonzero and torsion τ, to every point of the curve, we can associate the tangent $\mathbf{T}$, normal $\mathbf{n}$ and binormal vector $\mathbf{b}$ which form an orthonormal basis and satisfy the

Frenet–Serret system

$$\begin{pmatrix} \mathbf{T} \\ \mathbf{n} \\ \mathbf{b} \end{pmatrix}_s = \begin{pmatrix} 0 & \kappa & 0 \\ -\kappa & 0 & \tau \\ 0 & -\tau & 0 \end{pmatrix} \begin{pmatrix} \mathbf{T} \\ \mathbf{n} \\ \mathbf{b} \end{pmatrix}. \tag{1.1}$$

We consider the geometric flow

$$\mathbf{X}_t = \mathbf{X}_s \wedge_+ \mathbf{X}_{ss}, \tag{1.2}$$

where $\wedge_+$ is the cross product in the Euclidean space. The flow was first obtained by L.S. Da Rios in 1906 as a model to describe the flow of a vortex filament that evolves according to Euler equations [53]. This model is known as the vortex filament equation (VFE). Moreover, by using the definition of tangent vector $\mathbf{T} = \mathbf{X}_s$ and (1.1), we can express the flow as

$$\mathbf{X}_t = \kappa\, \mathbf{b}, \tag{1.3}$$

which implies that the filament curve moves in time in the direction of the binormal vector with speed κ. Equation (1.3) is also known as the binormal equation. In order to describe the model, since a vortex filament can be closed or extend to infinity in both directions, for simplicity we take $s \in \mathbb{R}$. Suppose that the vorticity of the given fluid is supported along the filament; in other words, ω is a singular vectorial measure

$$\omega = \Gamma \mathbf{T} ds,$$

where the circulation Γ is constant along the filament. Thus, using the Biot–Savart integral, at any point $\mathbf{P}$ located outside of the filament, velocity $\mathbf{u}$ can be given by

$$\mathbf{u}(\mathbf{P}) = \frac{\Gamma}{4\pi} \int_{-\infty}^{\infty} \frac{\mathbf{X}(s,\cdot) - \mathbf{P}}{\|\mathbf{X}(s,\cdot) - \mathbf{P}\|^3} \wedge_+ \mathbf{T}(s,\cdot)\, ds, \tag{1.4}$$

where $\|\cdot\|$ denotes the Euclidean distance.

Observe that the Biot–Savart integral is well-defined as long as the point $\mathbf{P}$ is not on the filament, thus to find a law for the evolution of the filament, one identifies the velocity of a point $\mathbf{Q}$ on the filament with that of the fluid at that point. However, the main idea is to calculate the velocity of the filament as a limit of $\mathbf{u}(\mathbf{P})$ when $\mathbf{P}$ approaches the filament. In this regard, in [53] a truncated Taylor expansion of $\mathbf{X}(s,\cdot)$ at the point $\mathbf{Q}$ was considered. Note that since this approximation takes in account only the parts of filament close to the given point $\mathbf{Q}$, the binormal flow is also known as the localized induction approximation (LIA) in the context of vortex dynamics.

The strong assumptions in the derivation of the binormal flow makes this model less useful from a physical point of view; however, like the Euler equations, the binormal flow preserves the following quantities [55]:

(i) kinetic energy: $\int \kappa^2$,

(ii) linear momentum or fluid impulse: $\frac{1}{2}\int \mathbf{X} \wedge_+ \omega$,

(iii) angular momentum: $\frac{1}{3}\int \mathbf{X} \wedge_+ (\mathbf{X} \wedge_+ \omega)$,

(iv) helicity: $\int \kappa^2\tau$,

(v) total torsion: $\int \tau$.

On the other hand, the binormal flow captures some of the well-known examples of vortex filaments. For instance, some of its explicit solutions are the circle, helix, and a straight line. The last case corresponds to the line vortex, which does not move [11, p. 93], and is related to tornadoes or bathtub vortices. As for the circle, it moves normal to its plane with a constant velocity given by the inverse of the radius. The direction of propagation is determined by the orientation given to the circle; this example represents the smoke rings that are generated in real fluids [11, p. 522]. Finally, during its evolution, the helix does not change its shape either and depending on the orientation, its movement involves a translation and a rotation about its axis. Vortices with a helical shape are easy to generate; for example, they can be seen behind the tips of the blades of a propeller. In fact, there are explicit solutions of Euler equations that have a helical shape [37, 52].

Differentiating (1.2) with respect to s, yields the following equation for $\mathbf{T}$:

$$\mathbf{T}_t = \mathbf{T} \wedge_+ \mathbf{T}_{ss}, \tag{1.5}$$

which is known as the Schrödinger map flow onto the sphere. Equation (1.5) is a special case of the Landau–Lifshitz equation for ferromagnetism and one of its important properties is that during its evolution the norm of $\mathbf{T}$ remains preserved, i.e.,

$$\frac{1}{2}\frac{d}{dt}(\mathbf{T} \circ_+ \mathbf{T}) = \mathbf{T} \circ_+ \mathbf{T}_t = \mathbf{T} \circ_+ (\mathbf{T} \wedge_+ \mathbf{T}_{ss}) = 0,$$

where $\circ_+$ is the Euclidean inner product, hence, the arc-length parameterization is preserved. In fact, this is considered as one of the drawbacks as an approximation of (1.4). However, after a scaling, one can write $\mathbf{T}$ as a unit length vector. By writing it

in a more geometric way, i.e.,

$$\mathbf{T}_t = \mathbf{J}\mathbf{D}_s\mathbf{T}_s, \tag{1.6}$$

where $\mathbf{D}$ is the covariant derivative, $\mathbf{J}$ is the complex structure of the sphere, (1.5) can be generalized to more general domains and images [41]. In the following lines, we will discuss some of them.

1.1.1 The binormal flow in the Minkowski space

Consider the Minkowski 3-space[1] $\mathbb{R}^{1,2} = \{(x_1, x_2, x_3) : ds^2 = -dx_1^2 + dx_2^2 + dx_3^2\}$ and the cross product $\wedge_-$ defined as

$$\mathbf{a} \wedge_- \mathbf{b} = (-(a_2b_3 - a_3b_2), a_3b_1 - a_1b_3, a_1b_2 - a_2b_1), \ \mathbf{a}, \mathbf{b} \in \mathbb{R}^{1,2}. \tag{1.7}$$

Then, the equation of $\mathbf{T}$ is

$$\mathbf{T}_t = \mathbf{T} \wedge_- \mathbf{T}_{ss}, \tag{1.8}$$

and, equivalently, $\mathbf{X} \in \mathbb{R}^{1,2}$ solves

$$\mathbf{X}_t = \mathbf{X}_s \wedge_- \mathbf{X}_{ss}. \tag{1.9}$$

As seen before, during its evolution $\mathbf{T}$ preserves its magnitude and we have

$$\|\mathbf{T}\|_0^2 = (\mathbf{T} \circ_- \mathbf{T}) = \pm 1, \tag{1.10}$$

where the Minkowski pseudo-inner product

$$\mathbf{a} \circ_- \mathbf{b} = -a_1b_1 + a_2b_2 + a_3b_3,$$

defines the Minkowski norm[2] $\|\cdot\|_0$. Thus, in (1.10)

1. the negative sign implies that $\mathbf{T}$ belongs to $\mathbb{H}^2 = \{(x_1, x_2, x_3) : -x_1^2 + x_2^2 + x_3^2 = -1, \ x_1 > 0\}$, i.e., the hyperbolic unit sphere and the corresponding curve $\mathbf{X}$ is time-like. In this case, the Schrödinger flow of maps (1.8) is called the *Minkowski Heisenberg ferromagnet model*;

2. the positive sign implies that $\mathbf{T}$ belongs to $\mathbb{S}^{1,1} = \{(x_1, x_2, x_3) : -x_1^2 + x_2^2 + x_3^2 = 1\}$, also known as the *de Sitter 2-space* in general relativity. The corresponding curve

[1] See Appendix A

[2] Note that, $\|\cdot\|_0$ is a pseudo-norm, however, with some abuse of notation, in this work, we call it Minkowski norm.

X is space-like and the Schrödinger flow of maps (1.8) is called the *heat Heisenberg model* [27–29].

Note that for $\mathbf{T} \in \mathbb{H}^2$, i.e., for an arc-length parameterized time-like curve $\mathbf{X}$ with generalized curvature κ and torsion τ, the Frenet–Serret frame is given by

$$\begin{pmatrix} \mathbf{T} \\ \mathbf{n} \\ \mathbf{b} \end{pmatrix}_s = \begin{pmatrix} 0 & \kappa & 0 \\ \kappa & 0 & \tau \\ 0 & -\tau & 0 \end{pmatrix} \begin{pmatrix} \mathbf{T} \\ \mathbf{n} \\ \mathbf{b} \end{pmatrix}, \tag{1.11}$$

where $\mathbf{T} \circ_- \mathbf{T} = -1$, $\mathbf{n} \circ_- \mathbf{n} = 1$, $\mathbf{b} \circ_- \mathbf{b} = 1$, $\mathbf{T} \circ_- \mathbf{n} = \mathbf{T} \circ_- \mathbf{b} = \mathbf{n} \circ_- \mathbf{b} = 0$, $\mathbf{T} \wedge_- \mathbf{n} = \mathbf{b}$, $\mathbf{n} \wedge_- \mathbf{b} = -\mathbf{T}$, $\mathbf{T} \wedge_- \mathbf{b} = -\mathbf{n}$, and the normal $\mathbf{n}$ and binormal $\mathbf{b}$ vectors are space-like [45].

In this work, we concentrate only on the cases when $\mathbf{T}$ lies in $\mathbb{S}^2$ and $\mathbb{H}^2$. Thus, for the ease of notation, we combine and write the equation for $\mathbf{X}$ as

$$\mathbf{X}_t = \mathbf{X}_s \wedge_\pm \mathbf{X}_{ss}, \tag{1.12}$$

and that for $\mathbf{T}$ as

$$\mathbf{T}_t = \mathbf{T} \wedge_\pm \mathbf{T}_{ss}, \tag{1.13}$$

where the positive sign corresponds to (1.2), (1.5), and the negative sign to (1.8), (1.9).

1.1.2 The Hasimoto transformation

There is a natural connection between (1.12)–(1.13) and the nonlinear Schrödinger equation (NLS). In [38], Hasimoto established this relationship by defining the filament function

$$\psi(s,t) = \kappa(s,t) e^{i \int_0^s \tau(s',t) ds'}, \tag{1.14}$$

and proving that such a ψ solves the NLS equation:

$$i\psi_t + \psi_{ss} \pm \left(\frac{1}{2} (|\psi|^2 + A(t)) \right) \psi = 0, \tag{1.15}$$

with $A(t)$ a time dependent real valued function which depends on the values of $\kappa(s,t)$, $\tau(s,t)$ at $s = 0$. Thus, the Euclidean case (positive sign) corresponds to a focusing type and the hyperbolic case (negative sign) to the defocussing type NLS equation. Note that by using

$$\Psi(s,t) = \psi(s,t) e^{\frac{i}{2} \int^t A(t') dt'},$$

one can get rid of $A(t)$ in (1.15) and obtain

$$i\Psi_t + \Psi_{ss} \pm \frac{1}{2}|\Psi|^2\Psi = 0, \tag{1.16}$$

a completely integrable system which exhibits a soliton behavior. Later in [44] it was shown that the Heisenberg ferromagnet model (HF model) is equivalent to the NLS equation obtained above through the Hasimoto transformation.

Let us mention that in this thesis, we will be mainly working with polygonal curves, as a result, in order to avoid issues related to vanishing curvature, it's more convenient to work with a generalized version of the Frenet–Serret frame[3], formed by the orthonormal vectors $\mathbf{T}$, $\mathbf{e}_1$ and $\mathbf{e}_2$

$$\begin{pmatrix} \mathbf{T} \\ \mathbf{e}_1 \\ \mathbf{e}_2 \end{pmatrix}_s = \begin{pmatrix} 0 & \alpha & \beta \\ \mp\alpha & 0 & 0 \\ \mp\beta & 0 & 0 \end{pmatrix} \cdot \begin{pmatrix} \mathbf{T} \\ \mathbf{e}_1 \\ \mathbf{e}_2 \end{pmatrix}, \tag{1.17}$$

where $\mathbf{T} \wedge_\pm \mathbf{e}_1 = \mathbf{e}_2$, $\mathbf{e}_1 \wedge_\pm \mathbf{e}_2 = \pm\mathbf{T}$ and $\mathbf{T} \wedge_\pm \mathbf{e}_2 = -\mathbf{e}_1, \mathbf{T} \circ_\pm \mathbf{T} = \pm 1, \mathbf{e}_1 \circ_\pm \mathbf{e}_1 = 1 = \mathbf{e}_2 \circ_\pm \mathbf{e}_2$. Moreover, under this setting, the filament function can be expressed as [22]

$$\psi \equiv \alpha + i\beta, \tag{1.18}$$

where

$$\begin{aligned} \alpha(s,t) &= \kappa(s,t)\cos\Big(\int_0^s \tau(\xi,t)d\xi\Big), \\ \beta(s,t) &= \kappa(s,t)\sin\Big(\int_0^s \tau(\xi,t)d\xi\Big). \end{aligned} \tag{1.19}$$

It's easy to check that the new definition of ψ also satisfies (1.15) [3].

Thanks to the relationship between (1.12)–(1.13) and (1.15), for a given time t, from $\psi(s,t)$, we can obtain $\mathbf{T}(s,t)$ and $\mathbf{X}(s,t)$ up to a rigid movement, as a result, the main idea is to work with (1.15). Note that, if we define

$$\tilde{\psi} \equiv e^{i\lambda}\psi = e^{i\lambda}(\alpha + i\beta),\ \lambda \in \mathbb{R},$$

and integrate (1.17) for $\tilde{\psi}$, the corresponding solution is $\{\tilde{\mathbf{T}}, \tilde{\mathbf{e}_1}, \tilde{\mathbf{e}_2}\}$, where $\tilde{\mathbf{T}} \equiv \mathbf{T}$, and $\tilde{\mathbf{e}_1} + i\tilde{\mathbf{e}_2} \equiv e^{i\lambda}(\mathbf{e}_1 + i\mathbf{e}_2)$, thus, $\mathbf{T}$ remains the same.

The Schrödinger map equation can also be transformed to a nonlinear Schrödinger equation by using a stereographic projection of $\mathbf{T} \equiv (T_1, T_2, T_3)^T$[4] onto the complex

[3] See Appendix A

[4] Note that, along this work, we have taken all the vectors in the column form.

plane $\mathbb{C}$ [10]. In this regard, we define

$$z = x + iy \equiv (x, y) \equiv \left(\frac{T_2}{1 + T_1}, \frac{T_3}{1 + T_1} \right), \tag{1.20}$$

where $\mathbf{T}$ is projected from $(-1, 0, 0)^T$ into $\mathbb{R}^2$, identifying $\mathbb{R}^2$ with $\mathbb{C}$. In the Euclidean case, since $\mathbf{T} \in \mathbb{S}^2$, there is a point on the sphere, $(-1, 0, 0)^T$, corresponding to which there is no point in $\mathbb{C}$, as a result, there is a bijection between $\mathbb{S}^2 - \{(-1, 0, 0)^T\}$ and $\mathbb{R}^2$. On the other hand, in the hyperbolic case, $\mathbf{T} \in \mathbb{H}^2$, there is a bijection between $\mathbb{D}$ and $\mathbb{H}^2$, where

$$\mathbb{D} = \{(x, y) \in \mathbb{R}^2 \mid x^2 + y^2 < 1\},$$

is also known as Poincaré disc. Consequently, the tangent vector can be recovered by

$$\mathbf{T} = (T_1, T_2, T_3)^T \equiv \left(\frac{1 \mp x^2 \mp y^2}{1 \pm x^2 \pm y^2}, \frac{2x}{1 \pm x^2 \pm y^2}, \frac{2y}{1 \pm x^2 \pm y^2} \right)^T.$$

Next, by differentiating (1.20) and using (1.13), one can arrive at the following nonlinear Schrödinger equation

$$z_t - i z_{ss} \pm \frac{2i\bar{z} z_s^2}{1 \pm |z|^2} = 0.$$

We will see later in Chapter 3 that this form can also be used for the numerical evolution of (1.8).

1.2 One-corner problem

As mentioned previously, our main object of interests in this work are curves with multiple corners. In that direction, it becomes natural to address first the case of curves with one corner, which appear in the evolution of self-similar solutions of (1.12)–(1.13).

Apart from the explicit solutions of (1.12)–(1.13), another important class is the one of self-similar solutions which are characterized by one parameter and for any time $t > 0$, $s \in \mathbb{R}$, are given by

$$\mathbf{X}(s, t) = \sqrt{t} \mathbf{X} \left(\frac{s}{\sqrt{t}}, 1 \right),$$

that corresponds to the one-parameter family curve with curvature and torsion as

$$\kappa(s, t) = c_0 / \sqrt{t}, \ \tau(s, t) = s/2t, \tag{1.21}$$

respectively. One of the interesting properties of these solutions is that they develop a corner-shaped singularity in finite time [21, 36]. Here, depending on the underlying framework, $\mathbf{X}$ can be a curve in $\mathbb{R}^3$ or $\mathbb{R}^{1,2}$ [5]. Note that the parameter c_0 is the curvature at time $t = 1$. Thus, for any time $t > 0$, using Frenet–Serret frame (1.1) or (1.11) with (1.21) and the following initial conditions

$$\begin{cases} \mathbf{X}(0,t) = 2c_0\sqrt{t}(0,0,1)^T, \\ \mathbf{T}(0,t) = (1,0,0)^T, \\ \mathbf{n}(0,t) = (0,1,0)^T, \\ \mathbf{b}(0,t) = (0,0,1)^T, \end{cases} \tag{1.22}$$

the basis vectors $\mathbf{T}$, $\mathbf{n}$, $\mathbf{b}$ and hence, the curve $\mathbf{X}$ can be obtained up to a rigid movement. And for $c_0 = 0$, we define $\mathbf{X}_0(s,t) = s(1,0,0)^T$.

As t tends to zero, the formation of singularity happens at $s = 0$ and the corresponding curve $\mathbf{X}$ approaches to two non-parallel straight lines forming an (Euclidean or time-like) angle ρ_0 at the corner. Thus, at $t = 0$,

$$\mathbf{X}(s,0) = \begin{cases} \mathbf{A}^1 s, \ s \leq 0, \\ \mathbf{A}^2 s, \ s \geq 0 \end{cases}, \ \mathbf{T}(s,0) = \begin{cases} \mathbf{A}^1, \ s < 0, \\ \mathbf{A}^2, \ s > 0, \end{cases} \tag{1.23}$$

where $\mathbf{A}^j$ satisfy $\mathbf{A}^j \circ_\pm \mathbf{A}^j = \pm 1$, $j = 1, 2$ and are given as

$$\mathbf{A}^1 = (A_1^1, -A_2^1, -A_3^1)^T, \ \mathbf{A}^2 = (A_1^2, A_2^2, A_3^2)^T. \tag{1.24}$$

Let us also recall the very useful relationship between the parameter c_0 and the first component of $\mathbf{A}^j$, i.e.,

$$A_1^1 = A_1^2 = e^{\pm c_0^2 \pi/2}. \tag{1.25}$$

which was obtained in [36] for the Euclidean case and in [21] for the hyperbolic case and it was also shown that for $t > 0$, the solution curve $\mathbf{X}$ is $\mathcal{C}^\infty$. Furthermore, (1.25) also allows us to express the parameter c_0 in terms of the angle ρ_0:

$$c_0 = \begin{cases} \left[(2/\pi)\ln\left(\cosh\left(\rho_0/2\right)\right)\right]^{1/2}, & \text{if } \mathbf{A}^j \circ_- \mathbf{A}^j = -1, \ j = 1,2, \\ \\ \left[-(2/\pi)\ln\left(\cos\left(\rho_0/2\right)\right)\right]^{1/2}, & \text{if } \mathbf{A}^j \circ_+ \mathbf{A}^j = 1, \ j = 1,2. \end{cases} \tag{1.26}$$

[5] In this work, unlike in [21], instead of $\mathbb{R}^{2,1}$, we work with $\mathbb{R}^{1,2}$ and accordingly change the rest of expressions. See Appendix A for the difference in their definitions.

One can note that at the level of NLS equation, from (1.14) and (1.21),

$$\psi(s,t) = \frac{c_0}{\sqrt{t}} e^{is^2/4t}, \tag{1.27}$$

is the solution of (1.15) with $A(t) = -c_0^2/t$ and $\psi(s,0) = \sqrt{i}c_0\delta$, where δ is the Dirac distribution. Moreover, in this setting, the L^2 norm can be understood as the kinetic energy. As $|\psi(s,t)|^2 = c_0^2/t$, ψ is not in $L^2(\mathbb{R})$, i.e., have infinite energy. However, by using a pseudo conformal transformation it was shown that the solutions have finite energy. This fact allows authors to prove some stability results and find adequate function spaces so that the corresponding problem is well-posed. This work has been carried out in a series of papers by Banica and Vega [3–6]. In other words, the existence and uniqueness of the initial value problem, i.e., (1.2) with $\mathbf{X}(s,0)$ as in (1.23) is proved which also shows that there is a unique way in which the solution can be extended in a continuous way for $t \leq 0$ within the set of self-similar solutions [6, see Theorem 1.2, 1.3]. More concretely, the velocity at the point where the corner is located is determined by the self-similar solution that at time zero has a corner with the same angle. In fact, in [8] it was proved that there exists just one self-similar solution with this property.

On the other hand, the numerical treatment of the problem was first addressed in [15], and later a careful study for both Euclidean and Hyperbolic cases was done in [24], where using appropriate boundary conditions, the formation of corner-shaped singularity was captured numerically. Moreover, for the forward problem, i.e., starting with a corner-shaped initial datum, the self-similar solutions were also recovered numerically. It was found that due to the exponential growth of the first component A_1, the hyperbolic case becomes difficult to deal at the numerical level for all values of c_0; however, for smaller values, there was almost no difference between the two. In the rest of this work, we will refer to this problem as *one-corner problem*.

1.3 Planar M-polygon problem

Although the one-corner problem has been well-addressed, a multiple-corner curve as an initial datum has received attention very recently. The numerical evolution of the (1.2), (1.5) for a polygonal initial curve was first considered in [40] where it was observed that a unit square propagates in the vertical direction in such a way that at later times also it is a polygon with different number of sides. In particular, at a certain time, it reappears but with the axes turned by $\pi/4$-angle with respect to the

initial configuration. For the numerical simulations, the method proposed in [15] was used where (1.5) is discretized using Crank–Nicolson type scheme, and the curve is recovered by integration with respect to the arc-length parameter.

Later, in [22], a planar M-polygon, i.e., a regular planar polygonal curve with M sides was taken as an initial datum and it was shown that at rational times of the form $t_{pq} = (2\pi/M^2)(p/q)$, $\gcd(p,q) = 1$, $p \in \mathbb{Z}$, $q \in \mathbb{N}$, depending on q, a regular polygonal curve with multiple sides appears again. To be precise, if q is odd, the new polygon has Mq sides, and for q even, it has $Mq/2$ sides, and during its evolution, the planar M-polygon also moves in the vertical direction with a constant speed c_M. For the numerical simulations, a pseudo-spectral discretization in space with a fourth-order Runge–Kutta method in time was employed. The results thus obtained not only verify the observations made in [40], but also reveal several interesting properties of the binormal flow. Some of these we will discuss in the following lines.

In the absence of torsion, at the level of NLS equation, the initial condition is given by

$$\psi(s,0) = \frac{2\pi}{M} \sum_{k=-\infty}^{\infty} \delta\left(s - \frac{2\pi k}{M}\right), \tag{1.28}$$

where the coefficients $2\pi/M$ are obtained using the fact that the planar M-polygon is closed.

Observe that, (1.28) satisfies $e^{iMks}\psi(s,0) = \psi(s,0)$, for all $k \in \mathbb{Z}$, as a result, using the Galilean symmetry of (1.15) which says that if ψ is a solution, then so is $\tilde{\psi}_n(s,t) = e^{ins - in^2 t}\psi(s - 2nt, t)$, for all $n, t \in \mathbb{R}$. If we choose the initial datum such that $\tilde{\psi}_n(s,0) = \psi(s,0)$, i.e., $\psi(s,0) = e^{ins}\psi(s,0)$, for all $n \in \mathbb{R}$, and if the solution is unique, then $\psi(s,t) = e^{ins - in^2 t}\psi(s - 2nt, t)$, for all $n, t \in \mathbb{R}$. Hence, $\psi(s,t) = e^{iMks - i(Mk)^2 t}\psi(s - 2Mkt, t)$, for all $k \in \mathbb{Z}$. One of the important consequences of this invariance is that

$$\hat{\psi}(k,t) = e^{-i(Mk)^2 t}\hat{\psi}(0,t), \ \forall k \in \mathbb{Z},$$

which implies that

$$\psi(s,t) = \hat{\psi}(0,t) \sum_{k=-\infty}^{\infty} e^{-(Mk)^2 t + iMks}, \tag{1.29}$$

and

$$|\hat{\psi}(k,t)|^2 = |\hat{\psi}(0,t)|^2.$$

Moreover, if $\psi(s,t) \in L^2([0,2\pi))$, then from Parseval's theorem, $\sum_{k=-\infty}^{\infty} |\hat{\psi}(k,t)|^2 < \infty$, which would imply $\hat{\psi}(0,t)$ and thus, $\psi(s,t)$ is equal to zero. At this point recall that, in

the one-corner problem ψ was not in L^2, but in L^2_{loc}; however, in the current scenario, none of them is the case. However, by assuming uniqueness and considering only the rational times t_{pq}, through some algebraic techniques, one obtains

$$\psi(s,t_{pq}) = \frac{2\pi}{Mq}\hat{\psi}(0,t_{pq}) \sum_{k=-\infty}^{\infty}\sum_{m=0}^{q-1} G(-p,m,q)\ \delta\left(s - \frac{2\pi k}{M} - \frac{2\pi m}{Mq}\right), \tag{1.30}$$

where

$$G(a,b,c) = \sum_{l=0}^{c-1} e^{2\pi i(al^2+bl)/c},$$

is the generalized quadratic Gauß sum, and $\hat{\psi}(0,t_{pq})$ that can be assumed to be real, is the mean of $\psi(s,t_{pq})$ over a period

$$\hat{\psi}(0,t_{pq}) = \frac{M}{2\pi}\int_0^{2\pi/M} \psi(s,t_{pq})\ ds.$$

By using the properties of the Gauß sum (see [22, Appendix]), we can write

$$G(-p,m,q) = \begin{cases} \sqrt{q}e^{i\theta_m}, & \text{if } q \text{ odd }, \\ \sqrt{2q}e^{i\theta_m}, & \text{if } q \text{ even} \wedge q/2 \equiv m \bmod 2, \\ 0, & \text{if } q \text{ even} \wedge q/2 \not\equiv m \bmod 2, \end{cases} \tag{1.31}$$

for a certain angle θ_m that depends on m (and also p, q). Furthermore, by defining

$$\rho_m = \begin{cases} \frac{2\pi}{M\sqrt{q}}\hat{\psi}(0,t_{pq}), & \text{if } q \text{ odd }, \\ \frac{2\pi}{M\sqrt{q/2}}\hat{\psi}(0,t_{pq}), & \text{if } q \text{ even} \wedge q/2 \equiv m \bmod 2, \\ 0, & \text{if } q \text{ even} \wedge q/2 \not\equiv m \bmod 2, \end{cases} \tag{1.32}$$

(1.30) can be expressed as

$$\psi(s,t_{pq}) = \sum_{k=-\infty}^{\infty}\sum_{m=0}^{q-1} \rho_m e^{i\theta_m}\delta\left(s - \frac{2\pi k}{M} - \frac{2\pi m}{Mq}\right). \tag{1.33}$$

The above expression shows that at any rational time t_{pq}, there are Mq new, equally spaced Dirac deltas, which corresponds to Mq sides of the newly formed regular polygonal curve. However, except for initial, half and final time period, i.e., at $t = 0$, $t_{1,2}$, $t_{1,1}$, the coefficients multiplying Dirac deltas are not real, as a result, $\psi(s,t_{pq})$ does

not correspond to a planar polygonal at those times. Finally, when q is even, half of the ρ_m are zero, as a result, there are only $Mq/2$ sides.

Integrating the Frenet–Serret frame using $\psi(s, t_{pq})$, yields a rotation with an angle ρ_m about an axis determined by θ_m, which in turn gives $\mathbf{T}$ and hence, the curve $\mathbf{X}$ up to a rigid movement. By using the fact that the corresponding polygon is closed, the angle $\rho_m \equiv \rho$ can be obtained as

$$\rho = \begin{cases} 2\arccos(\cos^{1/q}(\pi/M)), & \text{if } q \text{ odd}, \\ 2\arccos(\cos^{2/q}(\pi/M)), & \text{if } q \text{ even}. \end{cases} \tag{1.34}$$

In the case of a planar M-polygon (from now on, referred to as *planar M-polygon problem*), $\psi(s, t_{pq})$ and $\mathbf{T}$ are periodic in time with a period $2\pi/M^2$.

Note that taking $\hat{\psi}(0, t) = 1$, in (1.29) gives

$$\psi(s,t) = \sum_{k=-\infty}^{\infty} e^{-(Mk)^2 t + iMks} = \theta\left(\frac{M}{2\pi}, \frac{M^2}{\pi}\right), \tag{1.35}$$

where $\theta(s, t)$ is the Jacobi theta function, and it is precisely the solution of the free Schrödinger equation, i.e., $\psi_t = i\psi_{ss}$ for initial data given by (1.28). On the other hand, $\hat{\psi}(0, t_{pq}) = 1$ in (1.30) gives the mathematical expression for the well-known optical phenomenon called Talbot effect [58]. Furthermore, in [12, 13], the authors used free Schrödinger equation to model the Talbot effect and showed that at rational times the solution can be obtained as a finite overlapping of translates of the initial datum, while at irrational times the images have a fractal profile. The latter was also observed in the case of planar M-polygon problem where the numerical simulation showed that the tangent vector $\mathbf{T}$ has a fractal-like structure for the irrational times (see [22, Figure 8]). Let us mention that the fractal structures were also observed in [50] where using (1.2), (1.5), an aortic valve model was proposed that described the apparent fractal character of the valve's fiber architecture. The fractal dimension of those curves was calculated numerically in [57]. Furthermore, the axis-switching phenomenon observed in the real fluids appears at the level of the curve $\mathbf{X}$ in the planar M-polygon case as well. For instance, in Figure 1.1, we have taken $M = 3$, and on the right hand side, we have plotted the curve $\mathbf{X}(s, t)$ at $t = 0$, $t_{1,2}$, $t_{1,1}$. The phenomenon is clearly visible at $t = t_{1,2}$ (in red) which has also been well observed in the evolution of a vortex filament created in a lab experiment Figure 1.1 [42](see also [34, Figure 6], [35, Figure 10]).

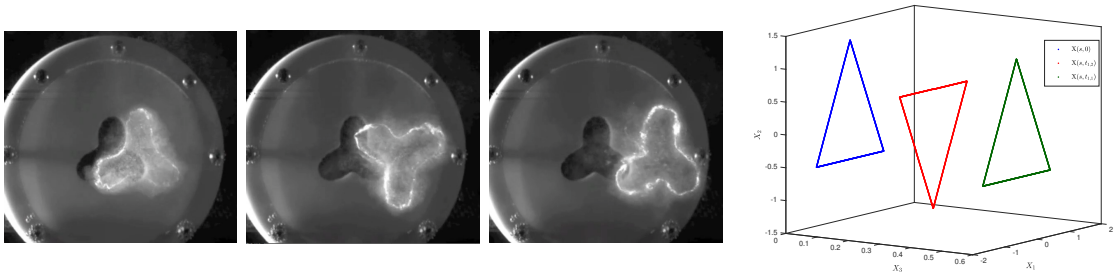

Figure 1.1 Vortex filaments in a lab experiment [42] and an equilateral triangle at time initial, half and final time. The axis-switching phenomenon is clearly visible in both the cases.

Hence, we see that the evolution of M-sided polygon reveals many fascinating properties of VFE. Another such is the trajectory of a single point, i.e, $\mathbf{X}(0,t)$ which we discuss in the following lines.

Trajectory of $\mathbf{X}(0,t)$

Taking into account the symmetries of the planar M-polygon, it is easy to see that, for a given M, the trajectory of a single point $\mathbf{X}(0,t)$ lies in a plane. Hence, by projecting it onto $\mathbb{C}$, we define

$$\tilde{z}(t) = \|(X_1(0,t), X_2(0,t))\| + iX_3(0,t), \quad t \in [0, 2\pi/M^2],$$

where $\|\cdot\|$ is the Euclidean norm. Moreover, if we remove the constant vertical movement,

$$\tilde{z}_M(t) = z(t) - ic_M t, \quad t \in [0, 2\pi/M^2],$$

then the resulting curve is closed, $2\pi/M^2$-periodic and can be seen as a nonlinear version of

$$\phi(t) = \sum_{k=1}^{\infty} \frac{e^{\pi i k^2 t}}{i\pi k^2}, \quad t \in [0, 2]. \tag{1.36}$$

Figure 1.2 shows $\tilde{z}(t)$ (left) and $\tilde{z}_M(t)$ (right) for $M = 3$, and the latter can be compared to Figure 3.15 (in red). The function $\phi(t)$ was used in [30] where its real part, i.e.,

$$f(t) = \sum_{k=1}^{\infty} \frac{\sin(\pi k^2 t)}{\pi k^2}, \quad t \in [0, 2],$$

also known as Riemann's non-differentiable function was studied. This function is nowhere differentiable except at rational points $t = p/q$ with p, q both odd. The proof

of the multifractality of Riemann's function is given in [39], and in [18], some other relevant trigonometric sums are considered. However, in [22], using an appropriate scaling that depends on M, a strong numerical evidence is given to show that, as M tends to infinity, $\tilde{z}_M$ converges to ϕ. Furthermore, we redefine

$$\phi(t) = \sum_{k=1}^{\infty} \frac{e^{2\pi i k^2 t}}{k^2}, \ t \in [0,1], \tag{1.37}$$

and compute the Fourier coefficients $\tilde{a}_{n,M}$ of the scaled version of $\tilde{z}_M$, where the scaling is obtained by comparing it with the new definition of ϕ. Hence, it can be concluded that

$$\lim_{M\to\infty} |n\,\tilde{a}_{n,M}| = \begin{cases} 1, & \text{if } n = k^2, k \in \mathbb{N}, \\ 0, & \text{otherwise;} \end{cases}$$

where $\mathbb{N} = \{1, 2, \ldots\}$. In this work, we will call the plot of $n\tilde{a}_{n,M}$ as a function of n as a *fingerprint*.

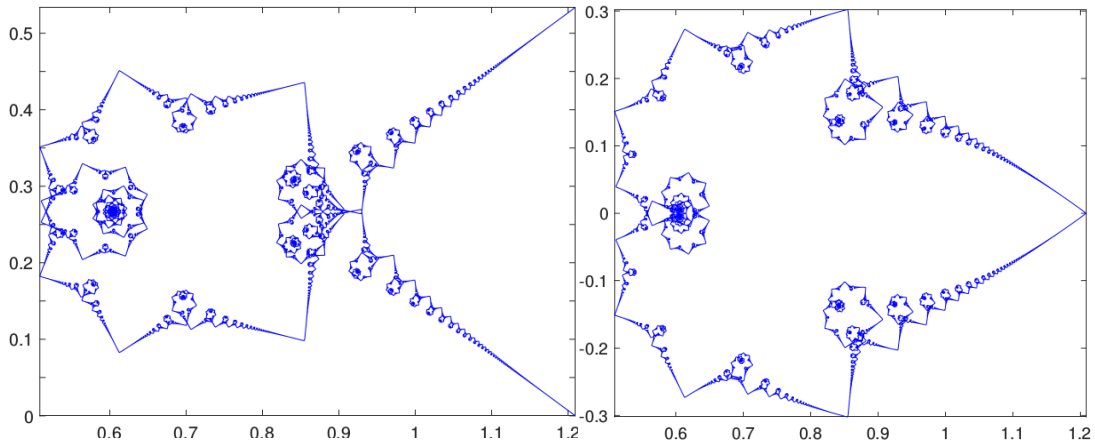

Figure 1.2 Left: $\tilde{z}(t)$ and right: $\tilde{z}_M(t)$ for $t \in [0, 2\pi/M^2]$, $M = 3$.

Having learned about the one-corner and planar M-polygon problems, one natural question to ask is up to what extent the two are related. This was addressed in [23] where it was shown that at infinitesimal times, the planar M-polygon problem can be explained as a superposition of M one-corner problems. Besides that, this relationship turns out to have deeper implications, for instance, it allows computing the speed of the center of mass of the planar M-polygon theoretically using the one-corner problem.

Let us conclude this section by commenting on the linear momentum of curve $\mathbf{X}$ which is also called impulse in the fluid literature. As $\mathbf{X}$ is a closed curve, during the evolution its linear momentum is preserved [52]. However, in the case of self-similar solutions of the one-corner problem, it was found that this quantity is not preserved

[7]. Later in [23], for the planar M-polygon problem, it was shown numerically that these observations hold true and the second component of the linear momentum shows an intermittent behavior whose shape can be compared to the Riemann's function.

1.4 Some exact solutions in the Minkowski space

This section talks about some of the smooth solutions of (1.8)–(1.9) in the Minkowski space which help us in understanding the corresponding polygonal curves.

In Section 1.1, we saw that the curve $\mathbf{X} \in \mathbb{R}^{1,2}$ can be time-like or space-like; however, in the following lines, we will consider the binormal motion of only time-like curves.

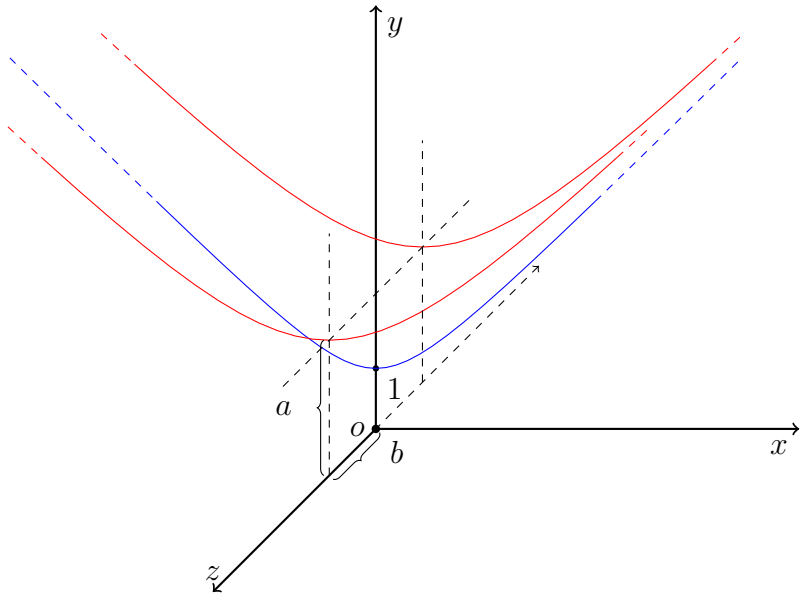

Figure 1.3 The hyperbolic 2-space $\mathbb{H}^2$ and parameters a and b such that $a^2 - b^2 = 1$. The red (blue) curves are the unit hyperbolas formed by the intersection of plane $z = \pm b$ ($z = 0$) with $\mathbb{H}^2$.

A helix with a constant curvature and torsion converges to a circle as the torsion tends to zero and to a straight line when the curvature goes to zero. In the Euclidean case, the initial curve $\mathbf{X}$ can be chosen such that its shape (curvature, torsion) is determined by the value of T_3, i.e., the third component of the tangent vector $\mathbf{T} \in \mathbb{S}^2$. For example, see Figure 2.1, where T_3 denoted as $b \in [-1, 1]$, corresponds to the torsion of the smooth curve $\mathbf{X}$ such that $a^2 + b^2 = 1$, with a as its curvature. Note that, choosing the third component is arbitrary and since the cross product $\wedge_+$ is invariant under the

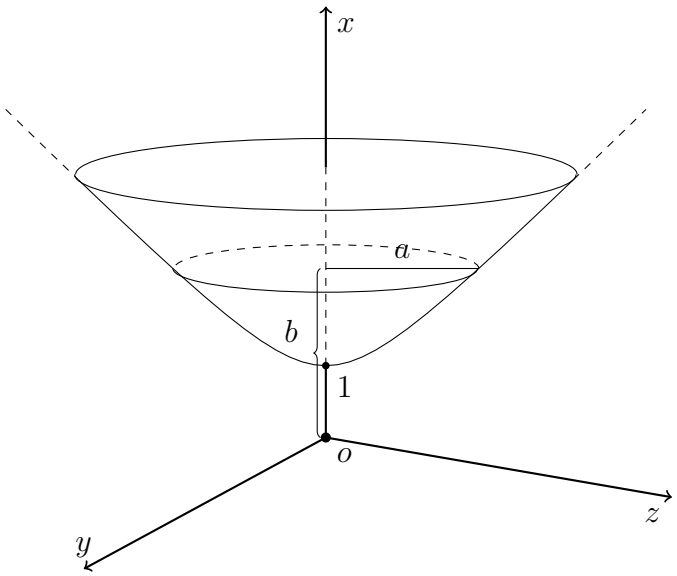

Figure 1.4 The hyperbolic 2-space $\mathbb{H}^2$ and parameters a and $b > 1$ such that $b^2 - a^2 = 1$.

Euclidean isometries, the torsion can be associated with the first or second component as well.

Proceeding with a similar reasoning, when $\mathbf{T} \in \mathbb{H}^2$, we note that due to the isometries in the Minkowski space, the torsion can be introduced in two different ways. Thus, characterized by the parameter b which corresponds to the initial value of the third component of the time-like vector $\mathbf{T}$, we write the most general form of a helix with a fixed axis as

$$\mathbf{X}(s,t) = a\sinh(s)\mathbf{x}(t) + a\cosh(s)\mathbf{y}(t) + bs\mathbf{z}_0 + \beta(t)\mathbf{z}_0,\ a^2 - b^2 = 1, \tag{1.38}$$

where s is the arc-length parameter and both a and b are positive. Here, $\mathbf{x}(t)$, $\mathbf{y}(t)$ are unit vectors which depend on time and make an orthonormal basis with the constant unit vector $\mathbf{z}_0$ being the fixed axis of the helix, and $\beta(t)$ is yet to be determined. By substituting $\mathbf{X}(s,t)$ in (1.9), we obtain

$$\frac{d\mathbf{x}}{dt} = b\mathbf{y}, \quad \frac{d\mathbf{y}}{dt} = b\mathbf{x}, \quad \frac{d\beta}{dt} = a^2,$$

which after solving gives

$$\begin{cases} \mathbf{x}(t) = \cosh(bt)\mathbf{x}_0 + \sinh(bt)\mathbf{y}_0, \\ \mathbf{y}(t) = \sinh(bt)\mathbf{x}_0 + \cosh(bt)\mathbf{y}_0, \\ \beta(t) = a^2 t, \end{cases} \tag{1.39}$$

with $\mathbf{x}(0) = \mathbf{x}_0$, $\mathbf{y}(0) = \mathbf{y}_0$. As a result, we get

$$\mathbf{X}(s,t) = a\sinh(s+bt)\mathbf{x}_0 + a\cosh(s+bt)\mathbf{y}_0 + (bs + a^2t)\mathbf{z}_0, \tag{1.40}$$

and the tangent vector

$$\mathbf{T}(s,t) = a\cosh(s+bt)\mathbf{x}_0 + a\sinh(s+bt)\mathbf{y}_0 + b\mathbf{z}_0,\ a^2 - b^2 = 1. \tag{1.41}$$

Figure 1.3 shows $\mathbf{T}$ at $t = 0$ for $b = 0$ (blue) and $b \neq 0$, $a > 0$ (red). It is important to mention that (1.39) and thus, (1.40) imply that the evolution of $\mathbf{X}$ is composed of two different movements: a vertical translation along its axis with a speed $1 + b^2$, and a rotation of angle b about its space-like axis. Furthermore, the evolution of $\mathbf{T}$ consists of the same angular movement as in the case of $\mathbf{X}$ while its third component remains fixed. Note that the limiting case $b = 0$ leads to the planar curve $\mathbf{X}$, a hyperbola, which moves in a vertical direction along its axis with unit speed. On the other hand, as b goes to infinity, both angular velocity and vertical speed will tend to infinity as well. As in [60], we call the curve $\mathbf{X}$ in (1.40) at $t = 0$, a *hyperbolic helix* .

On the other hand, when the parameter b corresponds to the initial value of the first component of the time-like vector $\mathbf{T}$, the most general form of a helix with a fixed axis can be written as

$$\mathbf{X}(s,t) = bs\mathbf{x}_0 + \beta(t)\mathbf{x}_0 + a\sin(s)\mathbf{y}(t) - a\cos(s)\mathbf{z}(t),\ b^2 - a^2 = 1, \tag{1.42}$$

where both a and b are positive, $\mathbf{y}(t)$, $\mathbf{z}(t)$ are time dependent unit vectors that make an orthonormal basis with a constant unit vector $\mathbf{x}_0$, i.e., the fixed axis of helix, and $\beta(t)$ is yet to be determined. As before, substitution of $\mathbf{X}(s,t)$ in (1.9) yields

$$\frac{d\mathbf{y}}{dt} = -b\mathbf{z}, \quad \frac{d\mathbf{z}}{dt} = b\mathbf{y}, \quad \frac{d\beta}{dt} = -a^2,$$

which after solving with $\mathbf{y}(0) = \mathbf{y}_0$, $\mathbf{z}(0) = \mathbf{z}_0$, gives

$$\mathbf{X}(s,t) = (bs - a^2t)\mathbf{x}_0 + a\sin(s-bt)\mathbf{y}_0 - a\cos(s-bt)\mathbf{z}_0. \tag{1.43}$$

The corresponding tangent vector

$$\mathbf{T}(s,t) = b\mathbf{x}_0 + a\cos(s-bt)\mathbf{y}_0 + a\sin(s-bt)\mathbf{z}_0, \tag{1.44}$$

where $b^2 - a^2 = 1$, $b > 1$; Figure 1.4 shows $\mathbf{T}$ at $t = 0$. Observe that (1.43) imply that the evolution of $\mathbf{X}$ is composed of two different movements: a translation in the downward direction along the axis with a speed $b^2 - 1$, and a negative rotation of angle b about its time-like axis. Furthermore, the evolution of $\mathbf{T}$ consists of the same angular movement as in the case of $\mathbf{X}$ while its first component remains fixed. Note that the limiting case $b = 1$ leads to the stationary solution straight line and the corresponding tangent vector will lie on the south pole of the hyperpoloid. On the other hand, as b goes to infinity, both angular velocity and vertical speed will tend to infinity as well. In this work, we denote the curve $\mathbf{X}$ in (1.43) at $t = 0$, by a *circular helix* [60].

1.5 Some existence and uniqueness results

In this section, we discuss some recent results on the well-posedness of VFE for certain kind of initial data. Let us first mention that the existence results for curves with curvature and torsion in Sobolev spaces of higher order were given in [38, 43, 47]; later, in the framework of a weak formulation of the binormal flow, some existence results for currents were obtained in [40]. Furthermore, the well-posedness of the one-corner problem, i.e., when the initial data has just one corner and is otherwise smooth, has already been discussed in Section 1.2.

In this work, we are interested in filament curves with corners which implies delta functions as the initial data for (1.15) or piecewise continuous functions as the initial data for (1.5). Therefore, we work with data in critical spaces and the problem turns out to be much more involved. Recently, it has been proved that, for polygonal lines that, at any given time, are asymptotically close at infinity to two straight lines, the initial value problem is well-posed in an appropriate topology [8]. In other words, a class of smooth solutions of the binormal flow that generates several corners in finite time has been proposed. In the following lines, we summarize the results obtained there.

The main idea is to consider a polygonal line with corners located at integers and curvature angles θ_k's. Then, by choosing the coefficients such that some moments of the sequence $\{\alpha_k\}$ are squared integrable, a strong smooth solution of VFE for $t \neq 0$ which is a weak solution for all t, has been constructed. In particular, consider an initial datum as a sum of Dirac masses

$$u(0) = \sum_{k \in \mathbb{Z}} \alpha_k \delta_k,$$

with coefficients in weighted summation spaces, i.e., $\|\alpha_k\|_{l^{p,s}} < \infty$, where

$$\|\alpha_k\|_{l^{p,s}} := \sum_{k\in\mathbb{Z}} (1+|k|)^{ps}|\alpha_k|^p,$$

and

$$\widehat{u(0)}(\xi) = \sum_{k\in\mathbb{Z}} \alpha_k e^{-ik\xi},$$

is 2π-periodic. Moreover, $\{\alpha_k\} \in l^{2,s}$ implies that $\widehat{u(0)} \in H^s(0,2\pi)$, and we define

$$\begin{aligned} H^s_{pF} &:= \{u \in \mathcal{S}'(\mathbb{R}), \hat{u}(\xi+2\pi) = \hat{u}(\xi), \hat{u} \in H^s(0,2\pi)\} \\ &\subset \{u \in \mathcal{S}'(\mathbb{R}), \{\|\hat{u}\|_{H^s(2\pi j, 2\pi(j+1))}\}_j \in l^\infty\}, \end{aligned}$$

and

$$\|u\|_{H^s_{pF}} = \|\hat{u}\|_{H^s(0,2\pi)}.$$

Thus, the following results are obtained in [8].

Theorem 1 (Evolution of polygonal lines through the binormal flow)**.** *Let* $\mathbf{X}(s,0)$ *be an arc-length parameterized polygonal line with corners located at* $s \in \mathbb{Z}$*, with the sequence of angles* $\theta_n \in (0,\pi)$ *such that the sequence defined by*

$$\sqrt{-\frac{2}{\pi}\ln\left(\sin\left(\frac{\theta_n}{2}\right)\right)}, \tag{1.45}$$

belongs to $l^{2,3}$*. Then there exists* $\mathbf{X}(s,t)$*, smooth solution of the binormal flow* (1.3) *on* $t \neq 0$ *and solution of* (1.3) *in the weak sense on* $\mathbb{R}$*, with*

$$|\mathbf{X}(s,t) - \mathbf{X}(s,0)| \leq C\sqrt{t},\ \forall s \in \mathbb{R}, |t| \leq 1.$$

Theorem 2 (Solutions of 1-D cublic NLS with several Dirac masses as initial data)**.** *Consider the following initial value problem for the 1-D cubic NLS equation*

$$\begin{cases} i\partial_t u + \partial_{ss} u \pm \frac{1}{2}\left(|u|^2 - \frac{Q}{2\pi t}\right) u = 0, \\ u(0) = \sum_{k\in\mathbb{Z}} \alpha_k \delta_k, \end{cases} \tag{1.46}$$

with $Q = \sum_{k\in\mathbb{Z}} |\alpha_k|^2$, *and let* $s > 1/2$, $0 < \gamma < 1$ *and* $\{\alpha\} \in l^{2,s}$. *Then, there exists* $T > 0$ *and a unique solution on* $(0, T)$ *of the form*

$$u(s,t) = \sum_{k\in\mathbb{Z}} A_k(t) e^{it\partial_{ss}} \delta_k(s), \tag{1.47}$$

where $A_k(t) = e^{\mp i \frac{|\alpha_k|^2}{4\pi} \ln\sqrt{t}} (\alpha_k + R_k(t))$, *such that* $\lim_{t\to 0} A_k(t) = \alpha_k$, *and*

$$\sup_{0<t<T} t^{-\gamma} \|\{R_k(t)\}\|_{l^{2,s}} + t\|\{\partial_t R_k(t)\}\|_{l^{2,s}} < C. \tag{1.48}$$

Furthermore, if an initial datum as a finite sum of N *Dirac masses is considered in* (1.46) *such that*

$$|\alpha_k| = \alpha,$$

and the NLS equation is renormalized with $Q = (N - 1/2)\alpha^2$, *then there exists a unique solution*

$$u(t) = e^{it\partial_{ss}} u(0) \pm \frac{i}{2} e^{i\partial_{ss}} \left(\left(|u(\tau)|^2 - \frac{Q}{2\pi\tau} \right) u(\tau) \right) d\tau,$$

such that $\widehat{e^{-it\partial_{ss}} u}(t) \in \mathcal{C}^1((-T,T), H^s(0,2\pi))$ *with*

$$\|e^{-it\partial_{ss}} u(t) - u(0)\|_{H^s_{pF}} \leq Ct^\gamma, \ \forall t \in (-T,T).$$

Moreover, if $s \geq 1$, *then the solution is global in time.*

Thus, from the unique solution of (1.46), one can construct the curve $\mathbf{X}$ through tangent vector $\mathbf{T}$ and the generalized Frenet–Serret frame as explained before. One of the important properties of the solution obtained above is that it satisfies the conservation law

$$Q = \sum_{k\in\mathbb{Z}} |\alpha_k|^2 = \sum_{k\in\mathbb{Z}} |A_k(t)|^2. \tag{1.49}$$

At this point, one natural question to ask is if there are conserved quantities such as (1.49) associated to (1.2), (1.5). In this direction, the authors consider a new topology where the Fourier transform of the initial solution is measured in the L^∞ norm. Note that for the smooth solution of (1.5) the energy density is given by

$$|\mathbf{T}_s|^2 \, ds = \kappa^2 \, ds,$$

where κ is the curvature. Consequently, the solutions of (1.5) that are obtained from that of NLS equation with finite L^2 norm, will have energy which is also finite. However,

it is shown that this is not true for the solutions constructed above, and the result is as follows [9].

Theorem 3. *Let* $\mathbf{X}$ *be the solution curve with initial data as mentioned above, and* $\mathbf{T}$ *its tangent vector. Define*

$$\mathcal{E}(\mathbf{T}(t)) := \lim_{k\to\infty} \int_k^{k+1} |\hat{\mathbf{T}}_s(t,\xi)|^2 d\xi. \tag{1.50}$$

Then, for all $t > 0$ *the following conservation law holds true:*

$$\mathcal{E}(\mathbf{T}(t)) = 4\pi \sum_{k\in\mathbb{Z}} |\alpha_k|^2, \tag{1.51}$$

and at $t = 0$*, when the singularities are created*

$$\int_k^{k+1} |\hat{\mathbf{T}}_s(0,\xi)|^2 d\xi = 4 \sum_{j\in\mathbb{Z}} (1 - e^{-\pi|\alpha_j|^2}), \ \forall k \in \mathbb{Z}. \tag{1.52}$$

Hence, there is a jump discontinuity of $\mathcal{E}(\mathbf{T}(t))$ at time $t = 0$, showing an instantaneous growth for positive times at large frequencies

$$\mathcal{E}(\mathbf{T}(0)) < \mathcal{E}(\mathbf{T}(t)).$$

The knowledge of these results will be extremely useful in this work as it will allow us to compute some of the preserved quantities of the polygonal curves both in the Euclidean and hyperbolic geometries.

1.6 Outline of the thesis

The objective of this Ph.D. thesis lies in the direction of describing the evolution of the binormal flow for polygonal curves. As mentioned in Section 1.1, the equation plays an important role in both Euclidean and hyperbolic cases, therefore, we consider polygons in both settings. In the following lines, we state the organization of this thesis.

- In Chapter 1, we have discussed the background, motivation and relevant literature. In particular, the notion of one-corner and planar M-polygon problems has been explained which lay an important foundation in following the rest of the text.

- Chapter 2 concentrates on the evolution of the helical M-polygon in the Euclidean case. This can be seen as an extension of the planar M-polygon case explained in Section 1.3. Apart from obtaining the numerical and algebraic solutions up to a rotation, one of the most interesting outcomes of this work is to find new variants of Riemann's non-differentiable function in the trajectory of one point. The results of this chapter are contained in the research article [25].

- From Chapter 3 onwards we delve into the hyperbolic setting and examine the evolution of (1.8)–(1.9) for a regular planar l-polygon where the parameter l stands for the hyperbolic angle between any two sides. Unlike its Euclidean counterpart, the planar l-polygon is open and both of its endpoints grow exponentially, as a result, solving the problem numerically becomes quite challenging. However, with appropriate boundary conditions, we solve the system numerically and compare it with the algebraic solution. We also draw a comparison between the Euclidean and hyperbolic versions of the multifractal curve $\mathbf{X}(0,t)$. The results of this and the next chapter are contained in the research article [26]

- Chapter 4 describes the relationship between the l-polygon and one-corner problems in the Minkowski space. We show this relationship numerically and as its consequence, through analytic techniques, we compute the speed of the center of mass of the planar l-polygon with which it moves in the vertical direction. We also give closed-form expressions of the components of the tangent vector $\mathbf{T}(s,0)$ in the one-corner problem.

- In Chapter 5, we summarize the main conclusions of the thesis and present its possible extensions in a form of the future work.

- The thesis contains an appendix as well that covers the main elements of the Minkowski space we need, such as definitions, notations, and isometries. A brief introduction to the pseudo-spectral methods and their application to the numerical method employed in Chapter 2 are also added in this appendix.

.

Chapter 2

Regular M-polygons with nonzero torsion in the Euclidean space

The path isn't a straight line; it's a spiral. You continually come back to things you thought you understood and see deeper truths.

Barry H. Gillespie

Contents

2.1 Introduction

We consider the geometric flow in the Euclidean space and write

$$\mathbf{X}_t = \mathbf{X}_s \wedge_+ \mathbf{X}_{ss}, \tag{2.1}$$

where s is the arc-length parameter, t time and $\wedge_+$ the usual cross product. The curve $\mathbf{X}(s,\cdot) : \mathbb{R} \to \mathbb{R}^3$ is arc-length parameterized and the tangent vector $\mathbf{T} \in \mathbb{S}^2$ solves

$$\mathbf{T}_t = \mathbf{T} \wedge_+ \mathbf{T}_{ss}, \tag{2.2}$$

With a curvature κ and a torsion τ, through the filament function

$$\psi(s,t) = \kappa(s,t) e^{i\int_0^s \tau(s',t)ds'} = \tilde{\alpha}(s,t) + i\tilde{\beta}(s,t), \tag{2.3}$$

and the parallel-frame

$$\begin{pmatrix} \mathbf{T} \\ \mathbf{e}_1 \\ \mathbf{e}_2 \end{pmatrix}_s = \begin{pmatrix} 0 & \tilde{\alpha} & \tilde{\beta} \\ -\tilde{\alpha} & 0 & 0 \\ -\tilde{\beta} & 0 & 0 \end{pmatrix} \cdot \begin{pmatrix} \mathbf{T} \\ \mathbf{e}_1 \\ \mathbf{e}_2 \end{pmatrix}, \tag{2.4}$$

where $\mathbf{T}$, $\mathbf{e}_1$, $\mathbf{e}_2$ form a unit orthonormal system, (2.1)–(2.2) are related to the focusing type nonlinear Schrödinger equation (NLS)

$$\psi_t = i\psi_{ss} + \frac{i}{2}\psi\left(|\psi|^2 + A(t)\right), \tag{2.5}$$

for some $A(t)$, a real function of t. Thus, for a given $t > 0$, from ψ, through an integration operation, $\mathbf{T}$ and $\mathbf{X}$ can be recovered up to a rigid movement. Let us also mention that if we define

$$\tilde{\psi} \equiv e^{i\lambda}\psi = e^{i\lambda}(\tilde{\alpha} + i\tilde{\beta}),\ \lambda \in \mathbb{R},$$

and integrate (2.4) for $\tilde{\psi}$, the corresponding solution is $\{\tilde{\mathbf{T}}, \tilde{\mathbf{e}_1}, \tilde{\mathbf{e}_2}\}$, where $\tilde{\mathbf{T}} \equiv \mathbf{T}$, and $\tilde{\mathbf{e}_1} + i\tilde{\mathbf{e}_2} \equiv e^{i\lambda}(\mathbf{e}_1 + i\mathbf{e}_2)$, therefore, $\mathbf{T}$ remains the same.

In this chapter, we look at the evolution of (2.1)-(2.2) for an initial datum as an M-sided polygon with nonzero torsion (helical M-polygons). The torsion in the initial curve is determined by the parameter b, which without loss of generality can be taken as the third component of tangent vector $\mathbf{T}$. Hence, in Section 2.2, we formulate the problem and obtain the evolution for rational times by algebraic means. Having done

that, in Section 2.3, the problem has been solved numerically and thus, we compare certain properties of the evolved curve with their algebraic counterparts. We note that unlike in the zero-torsion case, the evolution is not time periodic; moreover, the multifractal trajectory of the point $\mathbf{X}(0,t)$ is not planar and appears to be a helix. In order to understand it further, we perform a Fourier analysis at a numerical level and show the existence of variants of the so-called Riemann's non-differentiable function whose structure depends on the torsion introduced in the initial data [25]. This has been documented in Section 2.4 which constitutes one of the main differences between the planar and helical M-polygons. In Section 2.5, we compute the evolution of rational times with a large denominator and thus, compare it with the zero-torsion case. Finally, the numerical relationship between the helical M-polygon and one-corner problems has been described in Section 2.6.

2.2 A solution of VFE for a regular helical M-polygon

Our main goal is to construct the solutions of (2.1) and describe their corresponding dynamics, for initial data given by regular helical M-polygons. Let us mention that the initial data is characterized by two parameters, i.e., the number of tangent vectors M and the torsion b as in Figure 2.1; we will soon see that parameter b determines the curvature angle ρ_0 and torsion angle θ_0. As it will be explained in this section, the behavior of regular polygons with nonzero torsion is a consequence of the Galilean symmetry present in the set of solutions of (2.5). Therefore, this work can be regarded as an extension of the zero-torsion case considered in [22], and as a result, [22, Theorem 1] holds true here as well. By denoting the filament function (2.3) by ψ_θ for $\theta_0 \neq 0$, and the corresponding curve as helical M-polygon, and ψ, when $\theta_0 = 0$, and the curve $\mathbf{X}$ as planar M-polygon, we have the following:

Theorem 4. *Assume that there exists a unique solution of the initial value problem*

$$\mathbf{X}_t = \mathbf{X}_s \wedge_+ \mathbf{X}_{ss}, \tag{2.6}$$

with $\mathbf{X}(s,0)$ as a helical M-polygon. Then, at a time t_{pq}, a rational multiple of $2\pi/M^2$, i.e., $t_{pq} \equiv (2\pi/M^2)(p/q)$, $p \in \mathbb{Z}$, $q \in \mathbb{N}$, $\gcd(p,q) = 1$, the solution is a helical polygonal curve with Mq sides (if q odd) or $Mq/2$ sides (if q even). All the new sides have the same length, and the angle ρ_q between two adjacent sides is constant. Moreover, the

polygon at a time t_{pq} is the solution of the generalized Frenet–Serret system

$$\begin{pmatrix} \mathbf{T}(s,t_{pq}) \\ \mathbf{e}_1(s,t_{pq}) \\ \mathbf{e}_2(s,t_{pq}) \end{pmatrix}_s = \begin{pmatrix} 0 & \alpha(s,t_{pq}) & \beta(s,t_{pq}) \\ -\alpha(s,t_{pq}) & 0 & 0 \\ -\beta(s,t_{pq}) & 0 & 0 \end{pmatrix} \cdot \begin{pmatrix} \mathbf{T} \\ \mathbf{e}_1 \\ \mathbf{e}_2 \end{pmatrix}, \tag{2.7}$$

where $\alpha(s,t_{pq}) + i\beta(s,t_{pq}) = \Psi_\theta(s,t_{pq})$, for $s \in [0,2\pi)$, and

$$\Psi_\theta(s,t_{pq}) = \begin{cases} \frac{\rho_q}{\sqrt{q}} \sum\limits_{k=-\infty}^{\infty} \sum\limits_{m=0}^{q-1} G(-p,m,q) \\ \quad e^{i(k\theta_0+m\theta_0/q)} \delta\left(s - \frac{2\theta_0 p}{Mq} - \frac{2\pi k}{M} - \frac{2\pi m}{Mq}\right), \quad \textit{if } q \textit{ odd}, \\ \frac{\rho_q}{\sqrt{2q}} \sum\limits_{k=-\infty}^{\infty} \sum\limits_{m=0}^{q-1} G(-p,m,q) \\ \quad e^{i(k\theta_0+m\theta_0/q)} \delta\left(s - \frac{2\theta_0 p}{Mq} - \frac{2\pi k}{M} - \frac{2\pi m}{Mq}\right), \quad \textit{if } q \textit{ even}, \end{cases} \tag{2.8}$$

with $G(a,b,c)$ being a generalized quadratic Gauß sum.

It is important to mention that due to the critical regularity of the initial data, the uniqueness is a very challenging problem. The well-posedness of the problem with initial datum as a smooth curve with just one corner has been established in a series of papers by Banica and Vega [3–6]. Moreover, as mentioned in Chapter 1, the existence and uniqueness for a polygonal line as an initial datum have been proved in [8]. These results are also useful in addressing the case of periodic setting and as we will see later, using the conservation law obtained there, we can compute the angle

$$\rho_q = \begin{cases} 2\arccos(\cos^{1/q}(\rho_0/2)), & \text{if } q \text{ odd}, \\ 2\arccos(\cos^{2/q}(\rho_0/2)), & \text{if } q \text{ even}. \end{cases} \tag{2.9}$$

2.2.1 Problem definition and formulation

Let us consider an arc-length parameterized regular M-polygon with a torsion depending on a parameter b. Due to the fact that (2.1)-(2.2) are rotation invariant, we can assume that the 2π-periodic tangent vector $\mathbf{T}(s,0)$ lies on a circle of radius a, with $a^2+b^2=1$ (see Figure 2.1):

$$\mathbf{T}(s,0) = \left(a\cos\left(\frac{2\pi k}{M}\right), a\sin\left(\frac{2\pi k}{M}\right), b\right)^T \equiv (a\, e^{2\pi i k/M}, b), \quad s \in (s_k, s_{k+1}), \tag{2.10}$$

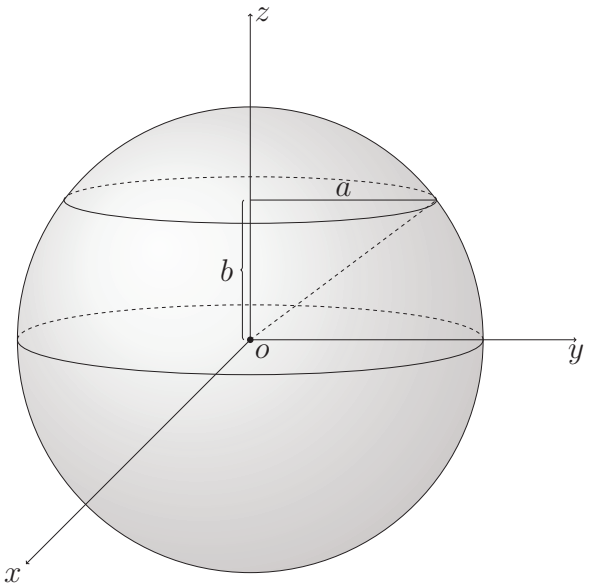

Figure 2.1 The unit sphere $\mathbb{S}^2$, and parameters a and b, where $a^2 + b^2 = 1$.

where $k = 0, 1, \ldots, M-1$. The corresponding curve $\mathbf{X}(s, 0)$ is a helical polygon with corners located at

$$\mathbf{X}(s_k, 0) = \left(\frac{a\pi \sin(\pi(2k-1)/M)}{M \sin(\pi/M)}, -\frac{a\pi \cos(\pi(2k-1)/M)}{M \sin(\pi/M)}, b\, s_k \right)^T, \tag{2.11}$$

so that for any $s \in (s_k, s_{k+1})$, the corresponding point $\mathbf{X}(s, 0)$ lies on the line segment joining $\mathbf{X}(s_k, 0)$ and $\mathbf{X}(s_{k+1}, 0)$. Since $\mathbf{T} \in \mathbb{S}^2$, it follows that $b \in [-1, 1]$; in this work, we deal with $b > 0$, because the case with $b < 0$ can be recovered by the symmetries. Note that $b = 0$ reduces back to the planar M-polygon case, $b = 1$ to the straight line, and, for an intermediate value of b, the corresponding polygonal curve has a helical shape. Let us denote $\mathbf{T}_k = \mathbf{T}(s, 0)$, for $s \in (s_k, s_{k+1})$. The curvature angle ρ_0 between any two sides of the polygon is constant and is computed as

$$\begin{aligned}
\cos(\rho_0) &= \mathbf{T}_k \circ_+ \mathbf{T}_{k+1} \\
&= a^2 \cos\left(\frac{2\pi k}{M}\right) \cos\left(\frac{2\pi(k-1)}{M}\right) + a^2 \sin\left(\frac{2\pi k}{M}\right) \sin\left(\frac{2\pi(k-1)}{M}\right) + b^2 \\
&= a^2 \cos\left(\frac{2\pi}{M}\right) + b^2 = 1 - a^2(1 - \cos\left(\frac{2\pi}{M}\right)) \\
&= 1 - 2a^2 \sin^2\left(\frac{\pi}{M}\right),
\end{aligned}$$

simplifies to

$$\rho_0 = 2\arcsin\left(a\sin\left(\frac{\pi}{M}\right)\right), \tag{2.12}$$

which does not depend on k. On the other hand, the torsion angle θ_0 is defined as the angle between $(\mathbf{T}_{k-1} \wedge_+ \mathbf{T}_k)$ and $(\mathbf{T}_k \wedge_+ \mathbf{T}_{k+1})$, for all k. Thus, denoting the Euclidean norm by $\|\cdot\|$, we have

$$\cos(\theta_0) = \frac{(\mathbf{T}_{k-1} \wedge_+ \mathbf{T}_k) \circ_+ (\mathbf{T}_k \wedge_+ \mathbf{T}_{k+1})}{\|\mathbf{T}_{k-1} \wedge_+ \mathbf{T}_k\| \, \|\mathbf{T}_k \wedge_+ \mathbf{T}_{k+1}\|}, \tag{2.13}$$

where $\mathbf{T}_k \wedge_+ \mathbf{T}_{k+1}$

$$= \left(ab\left(\sin\left(\tfrac{2\pi k}{M}\right) - \sin\left(\tfrac{2\pi(k+1)}{M}\right)\right), -ab\left(\cos\left(\tfrac{2\pi k}{M}\right) - \cos\left(\tfrac{2\pi(k+1)}{M}\right)\right), a^2\sin\left(\tfrac{2\pi}{M}\right)\right)^T$$

$$= \left(-2ab\sin\left(\tfrac{\pi}{M}\right)\cos\left(\tfrac{\pi(2k+1)}{M}\right), -2ab\sin\left(\tfrac{\pi}{M}\right)\sin\left(\tfrac{\pi(2k+1)}{M}\right), a^2\sin\left(\tfrac{2\pi}{M}\right)\right)^T,$$

and

$$\|\mathbf{T}_k \wedge_+ \mathbf{T}_{k+1}\| = a\sin\left(\frac{2\pi}{M}\right)\sqrt{1 + b^2\tan^2\left(\frac{\pi}{M}\right)}. \tag{2.14}$$

Therefore, $(\mathbf{T}_{k-1} \wedge_+ \mathbf{T}_k) \circ_+ (\mathbf{T}_k \wedge_+ \mathbf{T}_{k+1})$

$$\begin{aligned}
&= 4a^2b^2\sin^2\left(\tfrac{\pi}{M}\right)\left(\cos\left(\tfrac{\pi(2k-1)}{M}\right)\cos\left(\tfrac{\pi(2k+1)}{M}\right) + \sin\left(\tfrac{\pi(2k-1)}{M}\right)\sin\left(\tfrac{\pi(2k+1)}{M}\right)\right) \\
&+ a^4\sin^2\left(\tfrac{2\pi}{M}\right) \\
&= 4a^2b^2\sin^2\left(\tfrac{\pi}{M}\right)\cos\left(\tfrac{2\pi}{M}\right) + a^4\sin^2\left(\tfrac{2\pi}{M}\right).
\end{aligned}$$

Substituting above expressions in (2.13) gives

$$\begin{aligned}
\cos(\theta_0) &= \frac{4a^2b^2\sin^2(\pi/M)\cos(2\pi/M) + a^4\sin^2(2\pi/M)}{a^2\sin^2(2\pi/M)\,(1 + b^2\tan^2(\pi/M))} = \frac{a^2 + b^2\frac{1-2\sin^2(\pi/M)}{\cos^2(\pi/M)}}{1 + b^2\tan^2(\pi/M)} \\
&= \frac{\cos^2(\pi/M) - b^2\cos^2(\pi/M) + b^2 - 2b^2\sin^2(\pi/M)}{\cos^2(\pi/M)(1 + b^2\tan^2(\pi/M))} = \frac{1 - b^2\tan^2(\pi/M)}{1 + b^2\tan^2(\pi/M)},
\end{aligned}$$

which simplifies to

$$\theta_0 = 2\tan^{-1}\left(b\tan\left(\frac{\pi}{M}\right)\right). \tag{2.15}$$

Moreover,

$$\left\|\frac{\mathbf{T}_k \wedge_+ \mathbf{T}_{k+1}}{\|\mathbf{T}_k \wedge_+ \mathbf{T}_{k+1}\|}\right\| = 1,$$

implies that $\left\|\left(\frac{-b\cos(\theta_0/2)\cos((2k+1)\pi/M)}{\cos(\pi/M)}, \frac{-b\cos(\theta_0/2)\sin((2k+1)\pi/M)}{\cos(\pi/M)}, a\cos(\theta_0/2)\right)\right\|$

$$= \left(\frac{b^2}{\cos^2(\pi/M)} + a^2\right)\cos^2(\theta_0/2) = \frac{b^2 + a^2\cos^2(\pi/M)}{\cos^2(\pi/M)}\cos^2(\theta_0/2)$$
$$= \frac{1 - a^2\sin^2(\pi/M)}{\cos^2(\pi/M)}\cos^2(\theta_0/2) = 1,$$

and thus,

$$\cos(\theta_0/2) = \frac{\cos(\pi/M)}{\sqrt{1 - a^2\sin^2(\pi/M)}} \Longleftrightarrow \cos\left(\frac{\theta_0}{2}\right)\cos\left(\frac{\rho_0}{2}\right) = \cos\left(\frac{\pi}{M}\right). \tag{2.16}$$

The above relation gives a relationship between the curvature angle ρ_0 and torsion angle θ_0 and M. Moreover, the following identities also hold true:

(i) $\tan\left(\frac{\theta_0}{2}\right) = b\tan\left(\frac{\pi}{M}\right)$,

(ii) $\sin\left(\frac{\rho_0}{2}\right) = a\sin\left(\frac{\pi}{M}\right)$,

(iii) $b\tan\left(\frac{\rho_0}{2}\right) = a\sin\left(\frac{\theta_0}{2}\right)$,

(iv) $\sin\left(\frac{\theta_0}{2}\right)\cos\left(\frac{\rho_0}{2}\right) = b\sin\left(\frac{\pi}{M}\right)$.

Spatial symmetries

Note that, (2.1)-(2.2) are rotation invariant, so, for an Euclidean rotation $\mathbf{R}$, if $\mathbf{X}$ and $\mathbf{T}$ are the respective solutions then, $\mathbf{R}\cdot\mathbf{X}$ and $\mathbf{R}\cdot\mathbf{T}$ also satisfy the equations. The symmetries of the initial data for the zero-torsion case (see [22, (29)]) are also valid here, as a result, $\mathbf{X}(s,t)$ and $\mathbf{T}(s,t)$ are invariant under a rotation of angle $2\pi k/M$ around the z-axis, with the only exception that the third component X_3 has now a translation symmetry, i.e.,

$$\begin{aligned}
T_1(s+\frac{2\pi k}{M},t) + iT_2(s+\frac{2\pi k}{M},t) &= e^{i\frac{2\pi k}{M}}(T_1(s,t) + iT_2(s,t)),\\
T_3(s+\frac{2\pi k}{M},t) &= T_3(s,t),\\
X_1(s+\frac{2\pi k}{M},t) + iX_2(s+\frac{2\pi k}{M},t) &= e^{i\frac{2\pi k}{M}}(X_1(s,t) + iX_2(s,t)),\\
X_3(s+\frac{2\pi k}{M},t) &= X_3(s,t) + \frac{2\pi kb}{M}.
\end{aligned} \tag{2.17}$$

Furthermore, due to the mirror invariance $\mathbf{T}(s,t)$ and $\mathbf{T}(-s,t)$ are symmetric about the XZ-plane; consequently, $\mathbf{X}(s,t)$ and $\mathbf{X}(-s,t)$ are symmetric about the y-axis, for all t.

Thus, if $\mathbf{T}(s,0) = \tilde{\mathbf{T}}(s,0)$ is the initial solution then at any time during the evolution the symmetry remains preserved and $\mathbf{T}(s,t) = \tilde{\mathbf{T}}(s,t)$ and same holds true for $\mathbf{X}$. An important corollary of the aforementioned symmetries is that $\mathbf{X}(s+2\pi k,t) - \mathbf{X}(s,t) = 2\pi b\, k(0,0,1)^T$, for all $k \in \mathbb{Z}$ which will be useful later.

Galilean invariance of the NLS equation

One of the important properties of the NLS equation is its invariance under the Galilean transformations, i.e., if ψ is a solution of (2.5), so is $\tilde{\psi}_n(s,t) = e^{ins - in^2 t}\psi(s-2nt,t)$, for all $n,t \in \mathbb{R}$. Thus, if we choose the initial datum such that $\tilde{\psi}_n(s,0) = e^{ins}\psi(s,0)$, i.e., $\psi(s,0) = e^{ins}\psi(s,0)$, for all $n \in \mathbb{R}$ and if the solution is unique then $\psi(s,t) = e^{ins-in^2t}\psi(s-2nt,t)$, for all $n,t \in \mathbb{R}$.

Let us write the initial data of the NLS equation corresponding to the planar M-polygon problem as

$$\psi(s,0) = c_0 \sum_{k=-\infty}^{\infty} \delta(s - 2\pi k/M), \quad s \in [0,2\pi], \tag{2.18}$$

and when $\theta_0 \neq 0$, as

$$\psi_\theta(s,0) = c_{\theta,0}\, e^{i\gamma s} \sum_{k=-\infty}^{\infty} \delta(s - 2\pi k/M), \quad s \in [0,2\pi],$$

where $\gamma = M\theta_0/2\pi$ satisfies $\lim_{M\to\infty}\gamma = b$; and c_0 and $c_{\theta,0} > 0$ are constants depending on the initial configuration of the respective curve. In particular, with

$$c_{\theta,0} = \sqrt{-\frac{2}{\pi}\ln\left(\cos\left(\frac{\rho_0}{2}\right)\right)},\ c_0 = \sqrt{-\frac{2}{\pi}\ln\left(\cos\left(\frac{\pi}{M}\right)\right)}, \tag{2.19}$$

we have

$$\psi_\theta(s,0) = \frac{c_{\theta,0}}{c_0}\, e^{i\gamma s}\psi(s,0). \tag{2.20}$$

Thus, by using the Galilean invariance of (2.5), we obtain

$$\psi_\theta(s,t) = \frac{c_{\theta,0}}{c_0}\, e^{i\gamma s - i\gamma^2 t}\psi(s-2\gamma\, t,t). \tag{2.21}$$

On the other hand, as observed in [22], (2.18) satisfies $\psi(s,0) = e^{iMks}\psi(s,0)$, so using Galilean invariance again, $\psi(s,t) = e^{iMks - i(Mk)^2 t}\psi(s-2Mkt,t)$, for all $k \in \mathbb{Z}$, and for

all $t \in \mathbb{R}$. Moreover, the j^{th} coefficient of $\psi(s,t)$ is given by

$$\hat{\psi}(j,t) = e^{-(Mk)^2 t - iM(j-k)(2Mkt)} \hat{\psi}(j-k,t),$$

for all $j,k \in \mathbb{Z}$. In particular, with $j=k$, $\hat{\psi}(k,t) = e^{-(Mk)^2 t}\hat{\psi}(0,t)$, and thus, we can write

$$\psi(s,t) = \hat{\psi}(0,t) \sum_{k=-\infty}^{\infty} e^{-(Mk)^2 t + iMks}. \tag{2.22}$$

which through (2.18) gives $\hat{\psi}(0,0) = Mc_0/2\pi$. Therefore, combining (2.21) and (2.22), we get

$$\psi_\theta(s,t) = \frac{c_{\theta,0}}{c_0}\hat{\psi}(0,t) e^{i\gamma s - i\gamma^2 t} \sum_{k=-\infty}^{\infty} e^{-i(Mk)^2 t + iMk(s-2\gamma t)}, \tag{2.23}$$

where $\hat{\psi}(0,t)$ is a constant depending on time, which, as mentioned in [22], can be assumed to be real, for all t. Note that, in (2.21), ψ is $2\pi/M$-space-periodic and $2\pi/M^2$-time periodic; but when $\gamma \in (0,1)$, $\psi_\theta(s,t)$ is not periodic. However, by taking γ rational, space periodicity can be recovered; and if $\gamma = 1$, $\psi_\theta(s,t)$ is both space and time periodic. During the evolution of a helical M-polygon, this will give rise to a phase shift and a Galilean shift, as explained later.

2.2.2 The evolution at rational multiples of time $t = 2\pi/M^2$

When $t = t_{pq} = (2\pi/M^2)(p/q)$, with $p \in \mathbb{Z}$, $q \in \mathbb{N}$, and $\gcd(p,q) = 1$, by substituting t_{pq}, γ in (2.23), we compute

$$\begin{aligned}
\psi_\theta(s,t_{pq}) &= \frac{c_{\theta,0}}{c_0}\hat{\psi}(0,t_{pq}) e^{i\left(\frac{M\theta_0}{2\pi}s - \frac{\theta_0^2}{2\pi}\frac{p}{q}\right)} \sum_{k=-\infty}^{\infty} e^{-2\pi i k^2 \frac{p}{q} + i(Mks - 2k\theta_0 \frac{p}{q})} \\
&= \frac{c_{\theta,0}}{c_0}\hat{\psi}(0,t_{pq}) e^{i(\frac{M\theta_0}{2\pi}s - \frac{\theta_0^2}{2\pi}\frac{p}{q})} \sum_{k=-\infty}^{\infty}\sum_{w=0}^{q-1} e^{-2\pi i(kq+w)^2 \frac{p}{q} + i(M(kq+w)s - 2(kq+w)\theta_0 \frac{p}{q})} \\
&= \frac{c_{\theta,0}}{c_0}\hat{\psi}(0,t_{pq}) e^{i\left(\frac{M\theta_0}{2\pi}s - \frac{\theta_0^2}{2\pi}\frac{p}{q}\right)} \sum_{w=0}^{q-1} e^{-2\pi i w^2 \frac{p}{q} + iMw(s - \frac{2\theta_0 p}{Mq})} \sum_{k=-\infty}^{\infty} e^{iMkq(s - \frac{2\theta_0 p}{Mq})}.
\end{aligned}$$

Next, by using

$$\sum_{k=-\infty}^{\infty} e^{iMkq(s - \frac{2\theta_0 p}{Mq})} = \frac{2\pi}{Mq}\sum_{k=-\infty}^{\infty} \delta\left(s - \frac{2\theta_0 p}{Mq} - \frac{2\pi k}{Mq}\right),$$

and evaluating the resulting expression at $s = \frac{2\theta_0 p}{Mq} + \frac{2\pi k}{Mq}$, yields

$$
\begin{aligned}
\psi_\theta(s,t_{pq}) &= \frac{2\pi}{Mq}\frac{c_{\theta,0}}{c_0}\hat{\psi}(0,t_{pq})\sum_{k=-\infty}^{\infty}\sum_{w=0}^{q-1} \\
&\qquad e^{-2\pi i w^2\frac{p}{q}+iMw(\frac{2\pi k}{Mq})+i\frac{M\theta_0}{2\pi}(\frac{2\theta_0 p}{Mq}+\frac{2\pi k}{Mq})}\delta\left(s-\frac{2\theta_0 p}{Mq}-\frac{2\pi k}{Mq}\right), \\
&= \frac{2\pi}{Mq}\frac{c_{\theta,0}}{c_0}\hat{\psi}(0,t_{pq})e^{i\frac{\theta_0^2}{2\pi}\frac{p}{q}}\sum_{w=0}^{q-1}e^{-2\pi i w^2\frac{p}{q}}\sum_{k=-\infty}^{\infty}\sum_{m=0}^{q-1} \\
&\qquad e^{2\pi i(kq+m)\frac{w}{q}+i(kq+m)\frac{\theta_0}{q}}\delta\left(s-\frac{2\theta_0 p}{Mq}-\frac{2\pi k}{M}-\frac{2\pi m}{Mq}\right) \\
&= \frac{2\pi}{Mq}\frac{c_{\theta,0}}{c_0}\hat{\psi}(0,t_{pq})e^{i\frac{\theta_0^2}{2\pi}\frac{p}{q}}\sum_{k=-\infty}^{\infty}\sum_{m=0}^{q-1}\sum_{w=0}^{q-1} \\
&\qquad e^{2\pi i\frac{(-pw^2+mw)}{q}}e^{i(k\theta_0+m\frac{\theta_0}{q})}\delta\left(s-\frac{2\theta_0 p}{Mq}-\frac{2\pi k}{M}-\frac{2\pi m}{Mq}\right) \\
&= \frac{2\pi}{Mq}\frac{c_{\theta,0}}{c_0}\hat{\psi}(0,t_{pq})e^{i(\theta_0^2/(2\pi))(p/q)}\sum_{k=-\infty}^{\infty}\sum_{m=0}^{q-1} \\
&\qquad G(-p,m,q)e^{i(k\theta_0+m\theta_0/q)}\delta\left(s-\frac{2\theta_0 p}{Mq}-\frac{2\pi k}{M}-\frac{2\pi m}{Mq}\right),
\end{aligned}
$$

where $G(-p,m,q)=\sum_{w=0}^{q-1}e^{(-2\pi i w^2 p+2\pi i w m)/q}$ is a generalized quadratic Gauß sum. Using the properties of these sums, i.e., (1.31), we get

$$
\psi_\theta(s,t_{pq}) = \begin{cases}
\frac{2\pi}{M\sqrt{q}}\frac{c_{\theta,0}}{c_0}\hat{\psi}(0,t_{pq})e^{i(\theta_0^2/(2\pi))(p/q)}\sum\limits_{k=-\infty}^{\infty}\sum\limits_{m=0}^{q-1} & \\
\quad e^{i(\xi_m+k\theta_0+m\theta_0/q)}\delta\left(s-\frac{2\theta_0 p}{Mq}-\frac{2\pi k}{M}-\frac{2\pi m}{Mq}\right), & \text{if } q \text{ odd}, \\
\frac{2\pi}{M\sqrt{q/2}}\frac{c_{\theta,0}}{c_0}\hat{\psi}(0,t_{pq})e^{i(\theta_0^2/(2\pi))(p/(q/2))}\sum\limits_{k=-\infty}^{\infty}\sum\limits_{m=0}^{q/2-1} & \\
\quad e^{i(\xi_{2m}+k\theta_0+2m\theta_0/q)}\delta\left(s-\frac{2\theta_0 p}{Mq}-\frac{2\pi k}{M}-\frac{4\pi m}{Mq}\right), & \text{if } \frac{q}{2} \text{ even}, \\
\frac{2\pi}{M\sqrt{q/2}}\frac{c_{\theta,0}}{c_0}\hat{\psi}(0,t_{pq})e^{i(\theta_0^2/(2\pi))(p/(q/2))}\sum\limits_{k=-\infty}^{\infty}\sum\limits_{m=0}^{q/2-1} & \\
\quad e^{i(\xi_{2m+1}+k\theta_0+(2m+1)\theta_0/q)}\delta\left(s-\frac{2\theta_0 p}{Mq}-\frac{2\pi k}{M}-\frac{2\pi(2m+1)}{Mq}\right), & \text{if } \frac{q}{2} \text{ odd},
\end{cases}
\tag{2.24}
$$

for a certain angle ξ_m depending on m, p and q. Hence, at any rational time t_{pq}, the initial M Dirac deltas in $s\in[0,2\pi)$ turn into Mq Dirac deltas (if q odd), or $Mq/2$ Dirac deltas (if q even). Moreover, at those times, the absolute value of their coefficients is constant, and since the Dirac deltas are equally spaced, the sides of the resulting polygon are equally lengthed. On the other hand, as a result of the

Galilean transformation, a corner initially located at $2\pi k/M$, $k \in \mathbb{Z}$, is translated by $s_{pq} = 2\theta_0 p/Mq$ at time t_{pq}; we call this extra movement the Galilean shift. Although, strictly speaking, ψ_θ (and $\mathbf{X}$, $\mathbf{T}$) are not time periodic now, their structure repeats whenever t is increased by $2\pi/M^2$; along this chapter, we denote this important quantity $T_f \equiv 2\pi/M^2$, and refer to it, with some abuse of language, as the time period.

Computation of $\hat{\psi}(0, t_{pq})$

In the Euclidean case, for the regular planar M-polygons, $\hat{\psi}(0, t_{pq})$ was obtained using the fact that the polygon is closed. This was later confirmed in [23, Section 7] where it was suggested that $\hat{\psi}(0, t_{pq})$ might be obtained from a conservation law. In [9, Section 4], it has been recently observed that this conservation law is a consequence of the one established from non-closed polygonal lines (see Theorem 2). The argument is as follows.

Let us consider the following initial value problem for the 1-D NLS equation

$$\begin{cases} i\partial\psi + \partial_{ss}\psi \pm \frac{1}{2}(|\psi|^2 - A(t))\psi = 0, \\ \psi(s,0) = \sum_{k=-\infty}^{\infty} \alpha_k(0)\delta(s-k), \end{cases} \tag{2.25}$$

where $\{\alpha_k(0)\} \in l^{2,s},\ s > 1/2$. Then, there exists a unique solution

$$\psi(s,t) = \sum_{k=-\infty}^{\infty} \alpha_k(t) e^{it\partial_s^2}\delta(s-k),$$

with $A(t) = Q/2\pi t$, and

$$\sum_{k=-\infty}^{\infty} |\alpha_k(t)|^2 = \sum_{k=-\infty}^{\infty} |\alpha_k(0)|^2 = Q,$$

where the coefficients $\alpha_k(t)$ satisfy

$$i\partial_t \alpha_k(t) = \mp\frac{1}{8\pi t} \sum_{k-j_1+j_2-j_3=0} e^{-i\frac{k^2-j_1^2+j_2^2-j_3^2}{4t}} \alpha_{j_1}(t)\overline{\alpha_{j_2}(t)}\alpha_{j_3}(t) \pm \frac{Q}{4\pi t}\alpha_k(t),$$

and can be obtained by doing a fixed point argument on $\tilde{\alpha}_k(t) = e^{-i\frac{|\alpha_k(0)|^2}{4\pi}\log\sqrt{t}}\alpha_k(t)$ for the equation

$$i\partial_t \tilde{\alpha}_k(t) = \mp f_k(t) \pm \frac{1}{8\pi t}(|\tilde{\alpha}_k(t)|^2 - |\alpha_k(0)|^2)\tilde{\alpha}_k(t),$$

with

$$f_k = \frac{1}{8\pi t} \sum_{(j_1,j_2,j_3)\in NR_k} e^{-i\frac{k^2-j_1^2+j_2^2-j_3^2}{4t}} e^{-i\frac{|\alpha_k(0)|^2-|\alpha_{j_1}(0)|^2-|\alpha_{j_2}(0)|^2-|\alpha_{j_3}(0)|^2}{4\pi}\log\sqrt{t}} \tilde{\alpha}_{j_1}(t)\overline{\tilde{\alpha}_{j_2}(t)}\tilde{\alpha}_{j_3}(t),$$

for $NR_k = \{(j_1, j_2, j_3) \in \mathbb{Z}^3, k - j_1 + j_2 - j_3 = 0, k^2 - j_1^2 + j_2^2 - j_3^2 \neq 0\}$, such that $\lim_{t\to 0} \tilde{\alpha}_k(t) = \alpha_k(0)$.

Observe that for $N \in \mathbb{N}$, $\{B_j(t)\}$ for $j \in \mathbb{N}$ with $B_j(t) = \tilde{\alpha}_{N+j}(t)$ also solve the last equation. Hence, if the initial data satisfies $\alpha_{k+N}(0) = e^{iNw}\alpha_k(0)$ for all k, $w \in \mathbb{R}$, $N \in \mathbb{N}$ and if the solution is unique, then it can be concluded that $\alpha_{k+N}(t) = e^{iNw}\alpha_k(t)$ for all k and t.

In the case of a helical M-polygon, we have chosen $c_{\theta,0}$ such that

$$\cos(\rho_0/2) = e^{-\pi c_{\theta,0}^2/2}, \tag{2.26}$$

where ρ_0 as in (2.12), is the angle between any two tangent vectors at $t = 0$. Thus, we have $\alpha_k(0) = c_{\theta,0}e^{ik\theta_0}$, and $\alpha_{k+M}(0) = e^{iM\theta_0}\alpha_k(0)$, so, if the solution is unique, then $\alpha_{k+M}(t) = e^{iM\theta_0}\alpha_k(t)$. Moreover,

$$\sum_{j=0}^{M-1} |\alpha_k(0)|^2 = \sum_{j=0}^{M-1} |\alpha_k(t)|^2 = Q.$$

Then,

$$|\alpha_k(0)| = c_{\theta,0} \Longrightarrow Q = \sum_{k=0}^{M-1} |c_{\theta,0}|^2 = Mc_{\theta,0}^2 = -\frac{2M}{\pi} \ln\cos\left(\frac{\rho_0}{2}\right).$$

Furthermore, at any rational time t_{pq} (taking q odd for now), there are from (2.24) Mq Dirac deltas with coefficients of equal modulus, which we call $c_{\theta,q}$. Therefore,

$$Mc_{\theta,0}^2 = Q = \sum_{k=0}^{Mq-1} |c_{\theta,q}|^2 = Mq \left|\frac{2\pi c_{\theta,0}}{M\sqrt{q}c_0}\hat{\psi}(0, t_{pq})\right|^2,$$

which yields $\hat{\psi}(0, t_{pq}) = Mc_0/2\pi = \hat{\psi}(0, 0)$ and $c_{\theta,q} = c_{\theta,0}/\sqrt{q}$. Note that (2.26) holds true whenever there is a singularity formation; e.g., in our case, at rational times t_{pq}. The expression for $c_{\theta,q}$ shows that the angle ρ_q between any two tangent vectors remains equal and can be computed by writing

$$\sqrt{-\frac{2}{\pi}\ln\left(\cos\left(\frac{\rho_q}{2}\right)\right)} = \frac{1}{\sqrt{q}}\sqrt{-\frac{2}{\pi}\ln\left(\cos\left(\frac{\rho_0}{2}\right)\right)} \implies \cos\left(\frac{\rho_0}{2}\right) = \cos^q\left(\frac{\rho_q}{2}\right).$$

After proceeding in the same way for q even, we conclude that

$$\cos\left(\frac{\rho_q}{2}\right) = \begin{cases} \cos^{1/q}\left(\dfrac{\rho_0}{2}\right), & \text{if } q \text{ odd}, \\ \cos^{2/q}\left(\dfrac{\rho_0}{2}\right), & \text{if } q \text{ even}, \end{cases} \tag{2.27}$$

which is the same expression as in [22, (25)], with $\rho_0 = 2\pi/M$.

2.2.3 Algebraic solution

In this section, we compute the tangent vector $\mathbf{T}$ and the curve $\mathbf{X}$ algebraically, which we denote by $\mathbf{T}_{alg}$ and $\mathbf{X}_{alg}$, respectively. We follow the approach in [22], and construct the algebraic solution up to a rigid movement. In this regard, let us define, for any rational time t_{pq} with q odd (the case with q even is similar):

$$\Psi_\theta(s, t_{pq}) = \frac{\rho_q}{c_{\theta,q}} e^{-i(\theta_0^2/(2\pi))(p/q)} \psi_\theta(s, t_{pq}); \tag{2.28}$$

and, since $\lim_{q\to\infty} \rho_q e^{-i(\theta_0^2/(2\pi))(p/q)}/c_{\theta,q} < \infty$, Ψ_θ is well-defined, hence, from (2.24),

$$\Psi_\theta(s, t_{pq}) = \begin{cases} \rho_q \displaystyle\sum_{k=-\infty}^{\infty} \sum_{m=0}^{q-1} e^{i(\xi_m + k\theta_0 + m\theta_0/q)} \\ \qquad \delta\left(s - \frac{2\theta_0 p}{Mq} - \frac{2\pi k}{M} - \frac{2\pi m}{Mq}\right), & \text{if } q \text{ odd}, \\ \rho_q \displaystyle\sum_{k=-\infty}^{\infty} \sum_{m=0}^{q/2-1} e^{i(\xi_{2m} + k\theta_0 + 2m\theta_0/q)} \\ \qquad \delta\left(s - \frac{2\theta_0 p}{Mq} - \frac{2\pi k}{M} - \frac{4\pi m}{Mq}\right), & \text{if } \frac{q}{2} \text{ even}, \\ \rho_q \displaystyle\sum_{k=-\infty}^{\infty} \sum_{m=0}^{q/2-1} e^{i(\xi_{2m+1} + k\theta_0 + (2m+1)\theta_0/q)} \\ \qquad \delta\left(s - \frac{2\theta_0 p}{Mq} - \frac{2\pi k}{M} - \frac{2\pi(2m+1)}{Mq}\right), & \text{if } \frac{q}{2} \text{ odd}. \end{cases} \tag{2.29}$$

After writing $\Psi_\theta(s, t_{pq}) = (\alpha_{k,m} + i\beta_{k,m})(s, t_{pq}) = \rho_q e^{i\zeta_{k,m}}$, we integrate (2.7) and obtain the rotation matrix

$$\mathbf{R}_{k,m} = \begin{pmatrix} c_{\rho_q} & s_{\rho_q} c_{\zeta_{k,m}} & s_{\rho_q} s_{\zeta_{k,m}} \\ -s_{\rho_q} c_{\zeta_{k,m}} & c^2_{\zeta_{k,m}}[c_{\rho_q} - 1] + 1 & c_{\zeta_{k,m}} s_{\zeta_{k,m}}[c_{\rho_q} - 1] \\ -s_{\rho_q} s_{\zeta_{k,m}} & c_{\zeta_{k,m}} s_{\zeta_{k,m}}[c_{\rho_q} - 1] & s^2_{\zeta_{k,m}}[c_{\rho_q} - 1] + 1 \end{pmatrix}, \tag{2.30}$$

which performs a rotation of angle ρ_q about the rotation axis $(0, \sin(\zeta_{k,m}), -\cos(\zeta_{k,m}))^T$ [22]. In other words, it describes the transition across a corner at $s = (2\pi(k +$

$1)/Mq + s_{pq})^-$, $k = 0, 1, \ldots, Mq-1$. Thus, we choose the basis vectors $\tilde{\mathbf{T}}(s)$, $\tilde{\mathbf{e}}_1(s)$, $\tilde{\mathbf{e}}_2(s)$, such that they form the identity matrix at $s = s_{pq}^-$, and obtain their values at $s = (2\pi(k+1)/Mq + s_{pq})^-$, $k = 0, 1, \ldots, Mq-1$, by the action of Mq rotation matrices. It is also important to mention that

$$\mathbf{R}_{M-1,q-1} \ldots \mathbf{R}_{M-1,1} \cdot \mathbf{R}_{M-1,0} \ldots \mathbf{R}_{0,q-1} \ldots \mathbf{R}_{0,1} \cdot \mathbf{R}_{0,0} = \begin{pmatrix} 1 & 0 & 0 \\ 0 & \cos(M\theta_0) & -\sin(M\theta_0) \\ 0 & \sin(M\theta_0) & \cos(M\theta_0) \end{pmatrix},$$

which holds true for any q and M, and implies that the following quantity is preserved:

$$\int_0^{2\pi} \tau(s', t_{pq}) ds' = \int_0^{2\pi} \tau(s', 0) ds' = \frac{M}{2\pi}\theta_0 \int_0^{2\pi} ds' = M\theta_0. \tag{2.31}$$

On the other hand, the vertices of $\tilde{\mathbf{X}}$ (i.e., $\mathbf{X}$ up to a rigid movement) are now shifted by the Galilean shift s_{pq}, and can be obtained by

$$\begin{cases} \tilde{\mathbf{X}}(s_{pq}) = \tilde{\mathbf{X}}(0) + s_{pq}\tilde{\mathbf{T}}(s_{pq}^-), \\ \tilde{\mathbf{X}}(\frac{2\pi(k+1)}{Mq} + s_{pq}) = \tilde{\mathbf{X}}(\frac{2\pi k}{Mq} + s_{pq}) + \frac{2\pi}{Mq}\tilde{\mathbf{T}}([\frac{2\pi(k+1)}{Mq} + s_{pq}]^-), \quad k = 0, 1, \ldots, Mq-1, \end{cases}$$

with $\tilde{\mathbf{X}}(0) = (0, 0, 0)^T$. In this way, we get the positions of the vertices corresponding to the interval $s \in [s_{pq}, 2\pi + s_{pq}]$, and by calculating the non-vertex points by linear interpolation, and using the symmetries mentioned in Section 2.2.1, $\tilde{\mathbf{X}}(s)$ can be obtained for all $s \in [0, 2\pi]$.

Note that the computation of $\tilde{\mathbf{X}}(2\pi + s_{pq})$ serves to define the correct rotation matrix $\mathbf{L}_1$, which allows the helical M-polygon to be aligned in such a way that its axis is parallel to the z-axis. More precisely, $\mathbf{L}_1$ performs a rotation of angle equal to the one between $\mathbf{v} = \tilde{\mathbf{X}}(2\pi + s_{pq}) - \tilde{\mathbf{X}}(s_{pq})$ and $(0, 0, 1)^T$, about an axis orthogonal to a plane spanned by these two vectors. As a result, $\mathbf{T} = \mathbf{L}_1 \cdot \tilde{\mathbf{T}}$, $\mathbf{X} = \mathbf{L}_1 \cdot \tilde{\mathbf{X}}$; then, we add a constant to the first and second components of $\mathbf{X}$, in such a way that the means of these components over a spatial period are zero, and obtain $\mathbf{X}$ and $\mathbf{T}$, up to a vertical movement, which can be computed at any time t_{pq} from the speed of the center of mass c_M, and a rotation about the z-axis. In regard to the latter, this is the main difference with respect to the planar M-polygons, where there was no rotation about the z-axis. In fact, the rotation of a helical M-polygon about its axis turns out to be a multifractal and, hence, its determination appears to be very difficult. We will discuss this further in the next section.

2.3 Numerical method and experiments

We solve numerically VFE and the Schrödinger map with the same numerical method as in [22] (see Section 4 and the references therein), to approximate (2.1)-(2.2) for the initial data $\mathbf{X}(s,0)$ and $\mathbf{T}(s,0)$, as given in (2.10) and (2.11), respectively. In this regard, we use a pseudo-spectral discretization in space and a fourth-order Runge–Kutta method in time. Since the tangent vector $\mathbf{T}$ is periodic in space, we can solve the system in terms of $\mathbf{T}$. Moreover, the space derivatives can be approximated using the discrete Fourier transform which can be done very efficiently using the `fft` algorithm in MATLAB.

More precisely, the space interval $[0, 2\pi)$ is discretized into N equally spaced nodes, i.e., $s_k = 2\pi k/N$, $k = 0, 1, \ldots, N-1$, and the time period $[0, T_f]$, with $T_f = 2\pi/M^2$, into $N_t + 1$ equally spaced time instants, taking $\Delta t = T_f/N_t$. Again, using the symmetries of $\mathbf{T}$, we can reduce all the discrete Fourier transforms of N elements, to N/M elements, reducing the computation cost quite effectively[1]. With respect to the stability constraints on N and Δt, they are also the same as in [22]; hence, N/M and N_t, once fixed for one value of M, can be used for all M. On the other hand, since $\Delta t = \mathcal{O}(1/M^2)$, we can expect more accurate results for larger M. In our numerical simulations, we have taken $N/M = 480 \cdot 2^r$, $N_t = 136080 \cdot 4^r$, $r = 0, 1, \ldots$, and different values of b (or θ_0).

Recall that the initial curve is characterized by two parameters, M and b. When $b \in (0, 1)$, as M is increased, the resulting initial curve tends to a helix. On the other hand, for a fixed M, as b tends to 1, the curve approaches a straight line. In our numerical simulations, we have analyzed both limits and computed the relevant quantities in each case. Apart from the fact that, at any rational time t_{pq}, there are Mq or $Mq/2$ corners in $s \in [0, 2\pi)$ (depending on whether q is odd or even), we observe that the evolution is not periodic in time. As mentioned above, due to the Galilean shift, a corner initially located at $s = 0$ moves to $s = 2\theta_0/M$ at the end of one time period; and the new helical M-polygon is rotated counterclockwise with respect to the z-axis by a certain amount, which we refer to as the phase shift. Figure 2.2 shows both shifts, for $M = 3$ and $\theta = \pi/2$.

Accuracy

Denoting the numerical solution as $\mathbf{T}_{num}(s,t)$, $\mathbf{X}_{num}(s,t)$, we have $\mathbf{T}_{num}(s,t) = \mathbf{T}(s,t) + \mathcal{O}(\Delta t^4)$. It is important to note that since the initial data for the tangent

[1] See Appendix A

Δt	$\|\mathbf{T}(\cdot,\Delta t)-\mathbf{T}(\cdot,\Delta t/2)\|$	$\log_2\left(\frac{\|\mathbf{T}(\cdot,\Delta t)-\mathbf{T}(\cdot,\Delta t/2)\|}{\|\mathbf{T}(\cdot,\Delta t/2)-\mathbf{T}(\cdot,\Delta t/4)\|}\right)$
$5.916370345743490\cdot 10^{-4}$	$1.150990969313999\cdot 10^{-1}$	2.241180926447556
$2.958185172871745\cdot 10^{-4}$	$1.361514265145060\cdot 10^{-3}$	4.160339679272480
$1.479092586435873\cdot 10^{-4}$	$7.970671544546493\cdot 10^{-5}$	4.094367008751559
$7.395462932179363\cdot 10^{-5}$	$5.089972204727020\cdot 10^{-6}$	3.968971596014078
$3.697731466089681\cdot 10^{-5}$	$3.261202549999181\cdot 10^{-7}$	3.964181824752017

Table 2.1 The order of accuracy of the Runge–Kutta method in time for $M=3$, $b=0.4$.

vector $\mathbf{T}$ is piecewise constant, the spectral accuracy with respect to the space variable can not be expected, nevertheless, we check the accuracy with respect to the time variable. In this direction, we have taken the parameters $M=3, b=0.4$, and different values of time steps, i.e., $\Delta t = 1.183274069148698\cdot 10^{-3}\cdot 2^{-n}$, $n=1,\dots,7$, $N/M=2^5$, $\Delta s = 6.544984694978735\cdot 10^{-2}$, $T_f = 2\pi/M^2$. Table 2.1 shows the corresponding error values for the tangent vector $\mathbf{T}$, and the norm $\|\cdot\|$ is given by

$$\|\mathbf{T}\| = \sqrt{\frac{1}{N}\sum_{i=1}^{3}\sum_{j=0}^{N-1} T_{i,j}^2}, \tag{2.32}$$

where $T_{i,j} = T_i(s_j,\cdot)$.

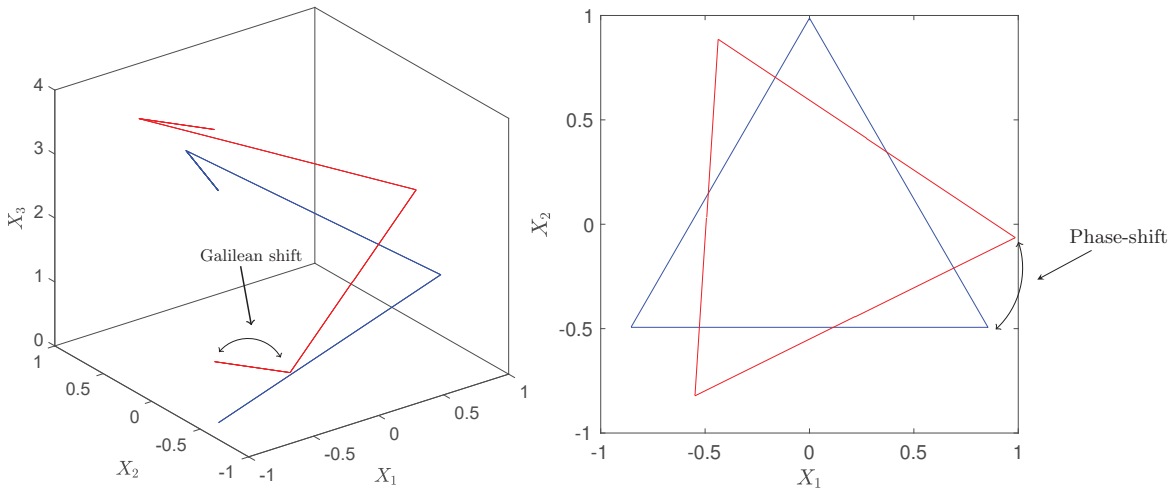

Figure 2.2 $\mathbf{X}(s,t)$, for $M=3$, $\theta_0=\pi/2$, $b=0.5774\ldots$, at $t=0$ (blue), and $t=T_f$ (red). The left-hand side shows the Galilean shift, and the right-hand side, the phase shift.

2.3.1 Numerical computation of ρ_q

It is also important to compare the numerical value of ρ_q with the one given by the algebraic expression in (2.27), so for a given q, we compute the following errors:

$$\begin{cases} \Delta\rho^{abs}_{q,N/M,M} = \max\limits_{\substack{p\in\{0,1,\ldots,q-1\}\\ \gcd(p,q)=1}} \max\limits_{j=0,1,\ldots,Mq-1} \left|\rho_q - \rho^{num,j}_{pq}\right|, \\ \Delta\rho^{rel}_{q,N/M,M} = \max\limits_{\substack{p\in\{0,1,\ldots,q-1\}\\ \gcd(p,q)=1}} \max\limits_{j=0,1,\ldots,Mq-1} \left|\dfrac{\rho_q - \rho^{num,j}_{pq}}{\rho_q}\right|, \end{cases} \tag{2.33}$$

where

$$\rho^{num,j}_{pq} = \arccos(\mathbf{T}_j \circ_+ \mathbf{T}_{j+1}), \tag{2.34}$$

$j = 0, 1, \ldots, Mq-1$. The value of the tangent vectors $\mathbf{T}_j$, which are piecewise constant at every time t_{pq}, has been calculated using the mean of the inner points; for example, for $\mathbf{T}(s)$, with $s \in [0, 2\pi/Mq)$, we take the mean of the values corresponding to $s \in [\pi/2Mq, 3\pi/2Mq)$, etc. Using (2.33), we compute the absolute and relative errors, for different values of b, q and M. The results for $b = 0.4$, $q = 5$, $M = 3, 4, \ldots, 20$, $N/M = 480, 960, \ldots, 7680$, are plotted in Figure 2.3. Note that each color corresponds to a different discretization in the numerical scheme, which clearly shows the convergence of the errors, and hence, the agreement between numerical and algebraic values.

Remark that in the case of closed planar M-polygons in [22], and later, in the case of closed irregular polygons in [23], it was observed that the product over a period $s \in [0, 2\pi)$ of the cosines of the halves of the angles between the adjacent sides is a conserved quantity. In other words,

$$\prod_m \cos\left(\frac{\rho_m(t_{p,q})}{2}\right) = \text{constant}, \quad m \in \{0, \ldots, \texttt{number\_of\_sides} - 1\}. \tag{2.35}$$

In the case of a helical M-polygon, we have used (2.34) to test how well (2.35) holds. In this regard, we compute

$$P(t_{pq}) = \prod_j \cos\left(\frac{\rho^{num,j}_{pq}}{2}\right), \tag{2.36}$$

where j runs through the sides of the helical M-polygon corresponding to $s \in [0, 2\pi)$; recall again that $\mathbf{X}$ is not periodic, but $\mathbf{T}$ is. In Table 2.2, we show the discrepancy between the known exact value $P(0) = 0.493039$, and $P(t_{pq})$, for $M = 6$, $N/M = 7680$, $b = 0.4$, taking different values of p and q, such that $\gcd(p, q) = 1$. Bearing in mind

that the values of $\mathbf{T}_j$ in (2.34) have been obtained from a numerical approximation of $\mathbf{T}(s)$ exhibiting the Gibbs phenomenon, we find the results remarkably accurate, in particular for small values of q.

p/q	$\lvert P(t_{pq}) - P(0)\rvert$	p/q	$\lvert P(t_{pq}) - P(0)\rvert$
1/12	$6.9145 \cdot 10^{-10}$	7/12	$6.0515 \cdot 10^{-7}$
1/10	$1.4740 \cdot 10^{-9}$	3/5	$1.7293 \cdot 10^{-7}$
1/6	$3.3064 \cdot 10^{-12}$	2/3	$1.0791 \cdot 10^{-11}$
1/5	$7.4831 \cdot 10^{-9}$	7/10	$4.6939 \cdot 10^{-8}$
1/4	$3.3640 \cdot 10^{-14}$	3/4	$1.4713 \cdot 10^{-12}$
3/10	$4.0038 \cdot 10^{-8}$	4/5	$1.8406 \cdot 10^{-7}$
1/3	$1.0676 \cdot 10^{-10}$	5/6	$1.2848 \cdot 10^{-9}$
2/5	$7.4827 \cdot 10^{-8}$	9/10	$3.0165 \cdot 10^{-7}$
5/12	$2.1332 \cdot 10^{-7}$	11/12	$5.4525 \cdot 10^{-7}$
1/2	$1.1335 \cdot 10^{-13}$	1	$2.4403 \cdot 10^{-13}$

Table 2.2 Discrepancy between (2.36) and $P(0) = 0.493039$, for $M = 6$, $N/M = 7680$, $b = 0.4$, taking different values of p and q, such that $\gcd(p, q) = 1$.

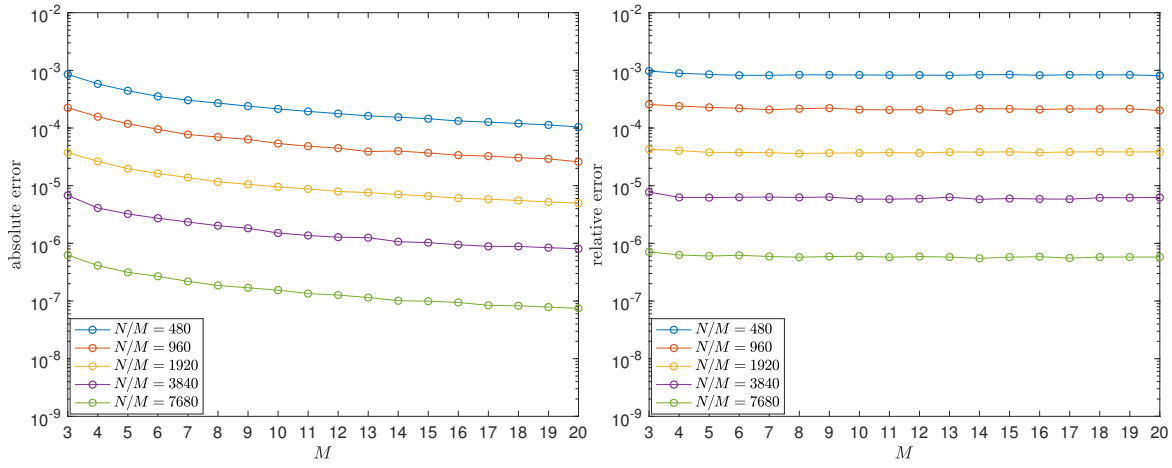

Figure 2.3 Absolute error (left) and relative error (right) as in (2.33), in semilogarithmic scale, for the angle ρ_q, taking $b = 0.4$, $q = 5$, $M = 3, 4, \ldots, 20$, and different values of N/M. The error clearly decreases, as N/M increases, showing the convergence between the numerical and theoretical values.

2.3.2 Center of mass

It is evident from the numerical simulations that apart from the formation of new corners, the evolution of a helical M-polygon involves a rotation about z-axis and a

vertical translation along it as well. In this following lines, we compute the speed of the center of mass of the polygonal curve and try to understand these movements.

Numerical computation of c_M

As done in the zero-torsion case, for any time $t \geq 0$, we compute the height of the center of mass of the given curve by taking the mean of all the values of each component of $\mathbf{X}(s_j, t)$:

$$h_{N,k}(t) = \frac{1}{N} \sum_{j=0}^{N-1} X_k(s_j, t), \quad k = 1, 2, 3.$$

The numerical computations show that $h_{N,k}(t)$ is equal to zero for $k = 1, 2$ and $h_{N,3}(t)$ increases linearly with time t. Thus, denoting $h_{N,3}(t)$ by $h_N(t)$, by making use of the symmetries as mentioned in (2.17), we have

$$\begin{aligned}\sum_{j=0}^{N-1} X_3(s_j, t) = \sum_{j=0}^{N/M-1} X_3(s_j, t) + \sum_{j=0}^{N/M-1} \left(X_3(s_j, t) + \tfrac{2\pi b}{M}\right) + \dots \\ \dots + \sum_{j=0}^{N/M-1} \left(X_3(s_j, t) + \tfrac{2\pi b}{M}(M-1)\right) \\ = M \sum_{j=0}^{N/M-1} X_3(s_j, t) + N\frac{2\pi b(M-1)M}{M^2}.\end{aligned}$$

With this,

$$\begin{aligned}h_N(t) = \frac{1}{N} \sum_{j=0}^{N-1} X_3(s_j, t) = \frac{M}{N} \sum_{j=0}^{N/M-1} X_3(s_j, t) + \frac{2\pi b(M-1)}{M} \\ = h_{N/M}(t) + \frac{\pi b}{M}(M-1).\end{aligned} \tag{2.37}$$

By removing the subscript and denoting the height as $h(t)$, the mean speed c_M^{num} can be computed numerically as

$$c_M^{num} = \frac{h(2\pi/M^2) - h(0)}{2\pi/M^2}.$$

Next, we compare c_M^{num} with the algebraic expression as in (2.45). Table 2.3 shows the value $|c_M - c_M^{num}|$, for $M = 3, 4, \dots, 20$, $b = 0.4$, $N/M = 480 \cdot 2^r$, $N_t = 136080 \cdot 4^r$, with $r = 0, 1, 2, 3, 4$. We note that, for a given value of M, when N/M is approximately doubled, the errors are divided by a factor slightly smaller than two, which implies

that the errors behave as $\mathcal{O}((N/M)^{-1})$, and shows the convergence of c_M^{num} to c_M. Moreover, as M increases, the errors reduce, which can be explained from the fact that $\Delta t = \mathcal{O}(1/M^2)$. Finally, let us mention that c_M converges to $1 - b^2 = 0.84$, as M tends to infinity.

M	$N/M = 480$	$N/M = 960$	$N/M = 1920$	$N/M = 3840$	$N/M = 7680$	c_M
3	$4.6546 \cdot 10^{-4}$	$2.8312 \cdot 10^{-4}$	$1.7068 \cdot 10^{-4}$	$1.0095 \cdot 10^{-4}$	$5.8967 \cdot 10^{-5}$	0.5482
4	$3.6695 \cdot 10^{-4}$	$2.1919 \cdot 10^{-4}$	$1.2842 \cdot 10^{-4}$	$7.4464 \cdot 10^{-5}$	$4.2869 \cdot 10^{-5}$	0.6936
5	$2.6525 \cdot 10^{-4}$	$1.5594 \cdot 10^{-4}$	$9.0443 \cdot 10^{-5}$	$5.2058 \cdot 10^{-5}$	$2.9801 \cdot 10^{-5}$	0.7509
6	$1.9506 \cdot 10^{-4}$	$1.1386 \cdot 10^{-4}$	$6.5718 \cdot 10^{-5}$	$3.7687 \cdot 10^{-5}$	$2.1512 \cdot 10^{-5}$	0.7798
7	$1.4803 \cdot 10^{-4}$	$8.6057 \cdot 10^{-5}$	$4.9532 \cdot 10^{-5}$	$2.8344 \cdot 10^{-5}$	$1.6151 \cdot 10^{-5}$	0.7964
8	$1.1573 \cdot 10^{-4}$	$6.7074 \cdot 10^{-5}$	$3.8535 \cdot 10^{-5}$	$2.2023 \cdot 10^{-5}$	$1.2534 \cdot 10^{-5}$	0.8070
9	$9.2671 \cdot 10^{-5}$	$5.3635 \cdot 10^{-5}$	$3.0776 \cdot 10^{-5}$	$1.7576 \cdot 10^{-5}$	$9.9931 \cdot 10^{-6}$	0.8141
10	$7.5791 \cdot 10^{-5}$	$4.3808 \cdot 10^{-5}$	$2.5118 \cdot 10^{-5}$	$1.4337 \cdot 10^{-5}$	$8.1465 \cdot 10^{-6}$	0.8191
11	$6.3086 \cdot 10^{-5}$	$3.6437 \cdot 10^{-5}$	$2.0874 \cdot 10^{-5}$	$1.1903 \cdot 10^{-5}$	$6.7637 \cdot 10^{-6}$	0.8228
12	$5.3297 \cdot 10^{-5}$	$3.0755 \cdot 10^{-5}$	$1.7614 \cdot 10^{-5}$	$1.0041 \cdot 10^{-5}$	$5.7034 \cdot 10^{-6}$	0.8256
13	$4.5601 \cdot 10^{-5}$	$2.6300 \cdot 10^{-5}$	$1.5057 \cdot 10^{-5}$	$8.5804 \cdot 10^{-6}$	$4.8729 \cdot 10^{-6}$	0.8278
14	$3.9449 \cdot 10^{-5}$	$2.2742 \cdot 10^{-5}$	$1.3017 \cdot 10^{-5}$	$7.4157 \cdot 10^{-6}$	$4.2106 \cdot 10^{-6}$	0.8295
15	$3.4456 \cdot 10^{-5}$	$1.9857 \cdot 10^{-5}$	$1.1362 \cdot 10^{-5}$	$6.4721 \cdot 10^{-6}$	$3.6742 \cdot 10^{-6}$	0.8308
16	$3.0349 \cdot 10^{-5}$	$1.7485 \cdot 10^{-5}$	$1.0003 \cdot 10^{-5}$	$5.6971 \cdot 10^{-6}$	$3.2339 \cdot 10^{-6}$	0.8319
17	$2.6931 \cdot 10^{-5}$	$1.5513 \cdot 10^{-5}$	$8.8735 \cdot 10^{-6}$	$5.053 \cdot 10^{-6}$	$2.8680 \cdot 10^{-6}$	0.8329
18	$2.4057 \cdot 10^{-5}$	$1.3855 \cdot 10^{-5}$	$7.9242 \cdot 10^{-6}$	$4.5119 \cdot 10^{-6}$	$2.5607 \cdot 10^{-6}$	0.8336
19	$2.1619 \cdot 10^{-5}$	$1.2448 \cdot 10^{-5}$	$7.1191 \cdot 10^{-6}$	$4.0531 \cdot 10^{-6}$	$2.3001 \cdot 10^{-6}$	0.8343
20	$1.9532 \cdot 10^{-5}$	$1.1245 \cdot 10^{-5}$	$6.4304 \cdot 10^{-6}$	$3.6607 \cdot 10^{-6}$	$2.0773 \cdot 10^{-6}$	0.8349

Table 2.3 $|c_M - c_M^{num}|$ computed for different M and N/M values and $b = 0.4$. The error decreases as N/M and M are increased and the reduction in the error is of the first order.

Algebraic computation of c_M

In this section, by using algebraic techniques, we compute the speed of the center of mass c_M. As observed in the zero-torsion case, we note that $h(t)$ behaves linearly, but when computed numerically, its derivative

$$\begin{aligned} h'(t) &= \frac{1}{N} \sum_{j=0}^{N-1} X_{3,t}(s_j, t) \\ &= \frac{1}{N} \sum_{j=0}^{N-1} \left(X_{1,s}(s_j, t) X_{2,ss}(s_j, t) - X_{1,ss}(s_j, t) X_{2,s}(s_j, t) \right), \end{aligned} \tag{2.38}$$

has a very singular shape, as shown in Figure 2.4 for $M = 3$, $b = 0.4$. In other words,

$$[\text{mean}(X_3)]'(t) \neq \text{mean}(X_{3,t})(t),$$

or,

$$c_M = h'(t) = \frac{d}{dt}\left(\frac{1}{2\pi}\int_0^{2\pi} X_3(s,t)ds\right) \neq \frac{1}{2\pi}\int_0^{2\pi} X_{3,t}(s,t)ds. \tag{2.39}$$

However, upon integrating $h'(t)$ in (2.38), the oscillations disappear completely and

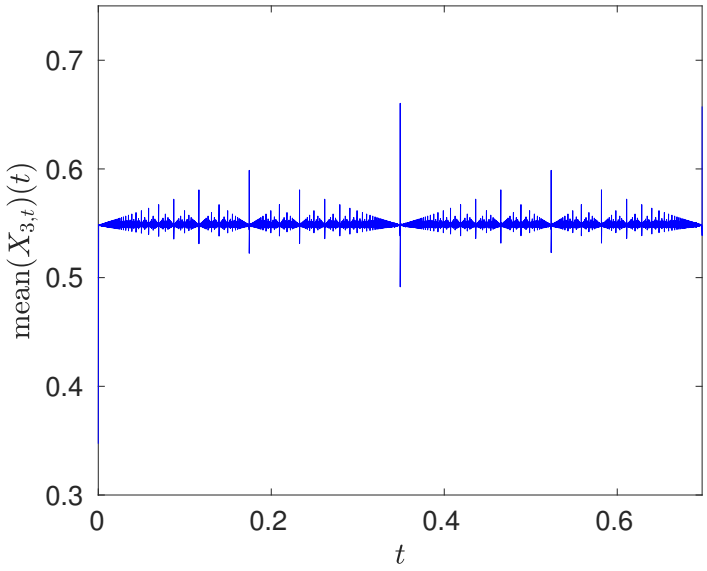

Figure 2.4 mean$(X_{3,t})(t)$, $t \in [0, 2\pi/M^2]$, for $M = 3$, $b = 0.4$, $N/M = 2^{11}$.

resulting $h(t)$ is linear whose slope can be compared with the one obtained by (2.37), when both computed numerically. With this observation, following the approach as described in [23], we compute the vertical height $h(t)$ as

$$h(t) - h(0) = \int_0^t \text{mean}(X_{3,t})(t')dt' = \int_0^t \left[\frac{1}{2\pi}\int_0^{2\pi} X_{3,t}(s,t')ds\right] dt'. \tag{2.40}$$

Thus, at the rational time $t = t_{pq}$, for the unit vector $\hat{k} = (0,0,1)^T$, we write

$$\int_0^{2\pi} X_{3,t}(s,t)ds = \int_0^{2\pi} (\mathbf{X}_t(s,t) \circ_+ \hat{k})ds = \left[\int_0^{2\pi} \mathbf{T}(s,t) \wedge_+ \mathbf{T}_s(s,t)ds\right] \circ_+ \hat{k}. \tag{2.41}$$

Next, in order to determine the cross product, we consider the fact that at any time t_{pq}, depending on q, there are Mq or $Mq/2$ tangent vectors which make a constant angle ρ_q mutually. Thus, without loss of generality, we can assume that at $s = 0$, the

tangent vector

$$\begin{cases} \mathbf{T}(0^-) = (1,0,0)^T, \\ \mathbf{T}(0^+) = (\cos(\rho_q), \sin(\rho_q), 0)^T, \end{cases} \tag{2.42}$$

form an angle ρ_q as in (2.27). Then,

$$\begin{aligned} \int_{-\infty}^{\infty} \mathbf{T}(s) \wedge_+ \mathbf{T}_s(s) ds &= \int_{0^-}^{0^+} \mathbf{T}(s) \wedge_+ \mathbf{T}_s(s) ds = \int_{0^-}^{0^+} \mathbf{T}(s) \wedge_+ (\alpha(s)\mathbf{e}_1 + \beta(s)\mathbf{e}_2) ds \\ &= \int_{0^-}^{0^+} \alpha(s)\mathbf{T}(s) \wedge_+ \mathbf{e}_1 ds + \int_{0^-}^{0^+} \beta(s)\mathbf{T}(s) \wedge_+ \mathbf{e}_2 ds \\ &= \int_{0^-}^{0^+} \rho_q \cos(k\theta_0)\delta(s)\mathbf{e}_2 ds - \int_{0^-}^{0^+} \rho_q \sin(k\theta_0)\delta(s)\mathbf{e}_1 ds \\ &= \rho_q \mathbf{e}_2(0^-) = \rho_q (0,0,1)^T, \end{aligned}$$

and since,

$$[\mathbf{T}(0^-) \wedge_+ \mathbf{T}(0^+)] = \hat{k} \sin(\rho_q) = (0,0,1)^T \sin(\rho_q),$$

we obtain

$$\int_{-\infty}^{\infty} \mathbf{T}(s) \wedge_+ \mathbf{T}_s(s) ds = \frac{\rho_q}{\sin(\rho_q)} [\mathbf{T}(0^-) \wedge_+ \mathbf{T}(0^+)].$$

Denoting $\mathbf{T}_k$, $k = 0, 1, \ldots, Mq-1$, or, $k = 0, 1, \ldots, Mq/2-1$ as the tangent vectors of corresponding helical polygon, at any time t_{pq}

$$\int_0^{2\pi} X_{3,t}(s,t) ds = \left[\frac{\rho_q}{\sin(\rho_q)} \sum_k \mathbf{T}_k \wedge_+ \mathbf{T}_{k+1} \right] \circ_+ \hat{k}. \tag{2.43}$$

In fact, since $\int_0^{2\pi} \mathbf{X}_t(s, t_{pq}) ds$ points in the $\hat{k}$ direction, we can write

$$\int_0^{2\pi} \mathbf{X}_t(s, t_{pq}) ds = \frac{\rho_q}{\sin(\rho_q)} \sum_k \mathbf{T}_k \wedge_+ \mathbf{T}_{k+1}.$$

However, the above equation can be rewritten as

$$\int_0^{2\pi} \mathbf{X}_t(s, t_{pq}) ds = \frac{\rho_q}{\sin(\rho_q)} \Delta s \sum_k \mathbf{T}_k \wedge_+ \frac{\mathbf{T}_{k+1} - \mathbf{T}_k}{\Delta s},$$

thus, formally,

$$\lim_{q \to \infty} \left[\frac{\rho_q}{\sin(\rho_q)} \Delta s \sum_k \mathbf{T}_k \wedge_+ \frac{\mathbf{T}_{k+1} - \mathbf{T}_k}{\Delta s} \right] = \int_0^{2\pi} \mathbf{T}(s) \wedge_+ \mathbf{T}_s(s) ds.$$

Note that in order to understand (2.43), we compute $\sum_k \mathbf{T}_k \wedge_+ \mathbf{T}_{k+1} \equiv \sum_k \mathbf{T}_{alg,k} \wedge_+ \mathbf{T}_{alg,k+1}$ using the symbolic computation in MATLAB. After computing this quantity for small values of q, we can conjecture that, for all p such that $\gcd(p,q)=1$,

$$\left[\sum_k \mathbf{T}_{alg,k} \wedge_+ \mathbf{T}_{alg,k+1}\right] \circ_+ \hat{k} = \begin{cases} \frac{(1-\cos(\rho_q))Mq}{\tan(\pi/M)}, & \text{if } q \equiv 1 \bmod 2, \\ \frac{(1-\cos(\rho_q))Mq/2}{\tan(\pi/M)}, & \text{if } q \equiv 0 \bmod 2. \end{cases}$$

With this, we can write the right hand side of (2.39) as

$$\frac{1}{2\pi}\int_0^{2\pi} X_{3,t}(s,t)ds = \begin{cases} \frac{1}{2\pi}\frac{\rho_q}{\sin(\rho_q)}\frac{(1-\cos(\rho_q))Mq}{\tan(\pi/M)}, & \text{if } q \equiv 1 \bmod 2, \\ \frac{1}{2\pi}\frac{\rho_q}{\sin(\rho_q)}\frac{(1-\cos(\rho_q))Mq/2}{\tan(\pi/M)}, & \text{if } q \equiv 0 \bmod 2. \end{cases} \tag{2.44}$$

Moreover, when $p \equiv 0 \bmod q$, we have

$$\frac{1}{2\pi}\int_0^{2\pi} X_{3,t}(s,t)ds = \frac{1}{2\pi}\frac{\rho_0}{\sin(\rho_0)}\frac{(1-\cos(\rho_0))M}{\tan(\pi/M)} = C(M,b) = C,$$

which is a constant depending on the initial structure of polygonal curve $\mathbf{X}$. Thus, with $\int_0^{2\pi} \mathbf{X}_{3,t}(s,t_{pq})ds$ we can now compute $h(t)$, and hence, c_M. Without loss of generality we can assume that q is an odd prime and in (2.40), we approximate the integral with respect to time using trapezoidal rule and compute it for the limit $q \to \infty$,

$$h(2\pi/M^2) - h(0) = \int_0^{2\pi/M^2} \left[\frac{1}{2\pi}\int_0^{2\pi} X_{3,t}(s,t')ds\right] dt'$$

$$= \lim_{q\to\infty}\left[\frac{2\pi}{M^2q}\frac{1}{2\pi}\left(\frac{1}{2}\int_0^{2\pi} X_{3,t}(s,t_{0q})ds + \sum_{p=1}^{q-1}\int_0^{2\pi} X_{3,t}(s,t_{pq})ds + \frac{1}{2}\int_0^{2\pi} X_{3,t}(s,t_{0q})ds\right)\right]$$

$$= \lim_{q\to\infty}\left[\frac{2\pi}{M^2q}\frac{1}{2\pi}\left(\frac{C}{2} + \sum_{p=1}^{q-1}\frac{\rho_q}{\sin(\rho_q)}\frac{(1-\cos(\rho_q))Mq}{\tan(\pi/M)} + \frac{C}{2}\right)\right]$$

$$= \lim_{q\to\infty}\left[\frac{C}{M^2q} + \frac{\rho_q}{\sin(\rho_q)}\frac{(1-\cos(\rho_q))(q-1)}{M\tan(\pi/M)}\right],$$

as $q \to \infty$, $\rho_q \to 0$, which implies $\lim_{q\to\infty} \rho_q/\sin(\rho_q)$ goes to 1, and thus, using (2.27) we can write

$$h(2\pi/M^2) - h(0) = \frac{1}{M\tan(\pi/M)} \lim_{q\to\infty} [(1-\cos(\rho_q)q)]$$
$$= \frac{1}{M\tan(\pi/M)} \lim_{q\to\infty} \left[\frac{1-(2\cos^{2/q}(\rho_0/2)-1)}{1/q}\right] = \frac{-4\ln\cos(\rho_0/2)}{M\tan(\pi/M)}.$$

Since $h(2\pi/M^2) - h(0) = c_M(2\pi/M^2)$,

$$c_M = \frac{h(2\pi/M^2)-h(0)}{2\pi/M^2} = \frac{-2\ln\cos(\rho_0/2)}{(\pi/M)\tan(\pi/M)}. \tag{2.45}$$

A similar computation for any time t_{pq} would also show that $h(t_{pq}) - h(0) = c_M t_{pq}$.

Moreover, using expression for ρ_0 in (2.12) and L' Hôpital's rule twice, we can compute

$$\lim_{M\to\infty} c_M = \frac{-2}{\pi} \lim_{M\to\infty} \frac{\ln\cos(\rho_0/2)}{M\tan(\pi/M)} = \frac{-2}{\pi} \lim_{M\to\infty} \frac{\ln(1-a^2\sin^2(\pi/M))}{\tan(\pi/M)/M} = a^2 = 1-b^2,$$

which is in coherence with the fact that a smooth helical curve with torsion b, translates in a vertical direction with a constant speed $1-b^2$, and the case $b=1$, i.e., a straight line is a stationary solution.

2.4 Trajectory of $\mathbf{X}(0,t)$

In this section, we describe the trajectory of a single point $s=0$ located on the helical M-polygon, which constitutes the main difference between the zero-torsion and the nonzero-torsion cases. Recall that in the zero-torsion case, due to the symmetries of the closed M-polygons, the trajectory of one point, i.e., $\mathbf{X}(0,t)$, which at the numerical level was claimed to be a multifractal, lies in a plane [22]. However, for any $\theta_0 > 0$, $\mathbf{X}(0,t)$ is no longer planar, and taking $t \in [0, T_f]$ is not enough to understand its structure, so we consider larger times multiple of T_f. Figure 2.5 corresponds to an M-polygon with $M=6$, $\theta_0 = \pi/5$, i.e., $b = 0.5628\ldots$, $t \in [0, 10\pi/3]$. Observe that $\mathbf{X}(0,t)$ has a helical shape, and exhibits a conspicuous fractal structure that repeats periodically, with some rotation and a vertical movement. In order to further understand this curve, we analyze each component of $\mathbf{X}(0,t)$, by using a Fourier series. In what follows, depending on the choice of the parameter b, we consider two different cases.

2.4.1 Case with $b \in (0, 1)$

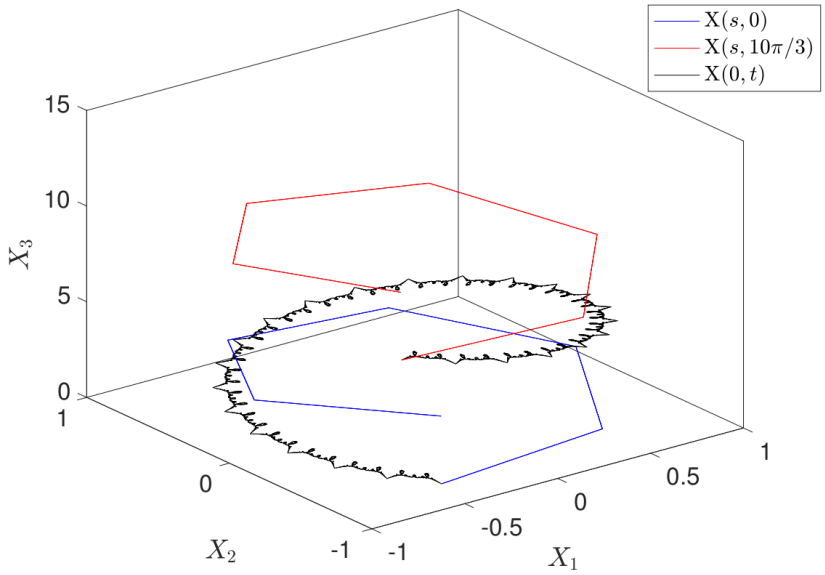

Figure 2.5 Initial polygon $\mathbf{X}(s, 0)$ (blue), for $M = 6$, $\theta_0 = \pi/5$, i.e., $b = 0.5628\ldots$, and its evolution at time $t = 10\pi/3$ (red), together with the curve described by $\mathbf{X}(0, t)$, for $t \in [0, 10\pi/3]$ (black). $\mathbf{X}(0, t)$ has a conspicuous fractal structure which repeats periodically, with some rotation and a vertical movement.

Choice of parameter b

In the case of a planar M-polygon, the curve $\mathbf{X}(0, t)$ has a corner at those values of t, at which the polygonal curve $\mathbf{X}(s, t)$ has a corner at $s = 0$, i.e., at $t = t_{pq}$, with $q \not\equiv 2 \bmod 4$. But for any $\theta_0 > 0$ (or b), due to the lack of space periodicity, for a given time, a corner initially located at $s = 0$, is translated by the Galilean shift. However, if b is chosen in such a way that, at the end of one time period, i.e., at $t = T_f$, the Galilean shift is a rational multiple of the side-length $2\pi/M$ of the corresponding polygonal curve, then in a finite time, $\mathbf{X}(0, t)$ will have a corner. In other words, by demanding that at $t = T_f$, i.e., $p = 1, q = 1$,

$$s_{1,1} = \frac{2\theta_0}{M} = \frac{2\pi}{M}\frac{c}{d} \implies \theta_0 = \frac{\pi c}{d},$$

with $\gcd(c, d) = 1$, $c, d \in \mathbb{N}$, at the end of d (or $d/2$) time periods, the cumulative Galilean shift will become equal to the side-length and $s = 0$ will correspond to a corner.

$\mathbf{X}(0,t)$ having corners depends mainly on the Galilean shift, or, in other words, in order for the curve $\mathbf{X}(0,t)$ to have corners in finite time, b should be chosen in such a way that, at $t = T_f$, the Galilean shift is a rational multiple of the side-length $2\pi/M$ of the corresponding polygonal curve. This can be enforced by taking $\theta_0 = \pi c/d$, with $\gcd(c,d) = 1$, $c, d \in \mathbb{N}$. Then, defining the following multiples of T_f:

$$T_f^{c,d} \equiv \begin{cases} (d/2)T_f \equiv \pi d/M^2, & \text{if } c \cdot d \text{ odd}, \\ d\,T_f \equiv 2\pi d/M^2, & \text{if } c \cdot d \text{ even}, \end{cases} \tag{2.46}$$

the numerical experiments reveal that, at times that are integer multiples of $T_f^{c,d}$, $\mathbf{X}(0,t)$ has a corner, and the three-dimensional fractal structure of $\mathbf{X}(0,t)$ repeats with period $T_f^{c,d}$ (see Figure 2.5). On the other hand, at rational multiples of $T_f^{c,d}$, $\mathbf{X}(0,t)$ has corners of different (smaller) scales.

In order to better understand $\mathbf{X}(0,t)$, we define, in $t \in [0, T_f^{c,d}]$:

$$\begin{cases} z_{1,2}(t) = X_1(0,t) + iX_2(0,t) = R(t)e^{i\nu(t)}, \\ \tilde{X}_3(t) = X_3(0,t) - c_M t, \end{cases}$$

where

$$R(t) = \sqrt{X_1^2(0,t) + X_2^2(0,t)}, \;\; \nu(t) = \arctan(X_2(0,t)/X_1(0,t)),$$

give the polar representation of $z_{1,2}(t)$, and $\tilde{X}_3(t)$ is $X_3(0,t)$ without its vertical height. Since $R(t)$ and $\tilde{X}_3(t)$ are periodic, we can consider their Fourier expansion:

$$R(t) = \sum_{n=-\infty}^{\infty} a_{n,M} e^{2\pi i\, n\, t/T_f^{c,d}}, \quad \tilde{X}_3(t) = \sum_{n=-\infty}^{\infty} \tilde{b}_{n,M} e^{2\pi i\, n\, t/T_f^{c,d}}, \quad t \in [0, T_f^{c,d}].$$

We have approximated the Fourier coefficients $a_{n,M}$ and $\tilde{b}_{n,M}$ using the MATLAB command `fft`, for $M = 6$, $\theta_0 = \pi/5$, $t \in [0, 5\pi/18]$. In the left-hand side of Figure 2.6, we have plotted $R(t)$; and, in the center, the fingerprint plot, i.e., the real part of the approximations of $n\, a_{n,M}$, for $n = 1, 2, \ldots, 2000$.

On the right-hand side, we have plotted $\nu(t)$, which describes the angular movement of $\mathbf{X}(0,t)$ in the XY-plane and can be associated with the phase shift corresponding to the angular movement of a corner initially located at $s = 0$. From its definition, one can suspect that $\nu(t)$ has a multifractal structure, too; hence, computing the phase shift at any rational time appears to be involved and deserves further research. We make some more comments on this in the next section.

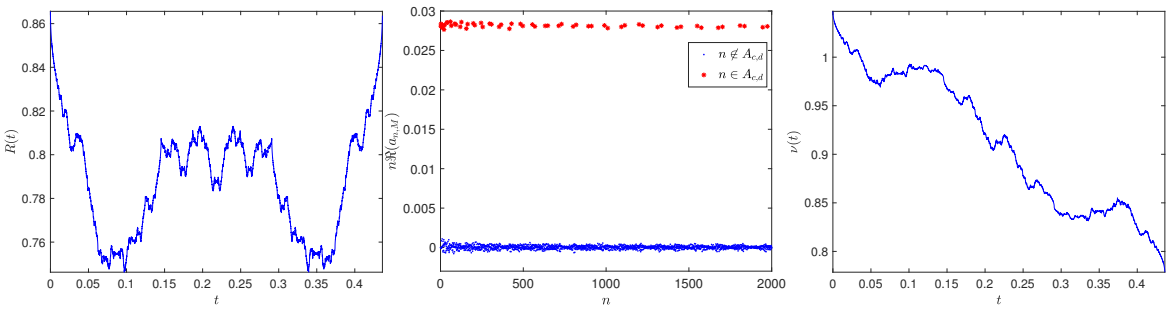

Figure 2.6 Left: $R(t)$, for $t \in [0, T_f^{c,d}]$, $M = 6$, $\theta_0 = \pi/5$, $c = 1$, $d = 5$, $b = 0.5628\ldots$. Center: Approximation of $n\Re(a_{n,M})$, for $n = 1, 2, \ldots, 2000$, where $a_{n,M}$ are the Fourier coefficients of $R(t)$. The dominating points (red starred) are given by (2.47). Right: $\nu(t)$, which seems to have a multifractal structure as well.

We have carried out a careful study of the fingerprints of $R(t)$ and $\tilde{X}_3(t)$, with $t \in [0, T_f^{c,d}]$, for many different values of M, c and d, and have found strong evidence that, when $\theta_0 = c\pi/d$, $\gcd(c, d) = 1$, the dominating points of the fingerprints belong to the following set:

$$A_{c,d} = \begin{cases} \{n(n\,d + c)/2 \,|\, n \in \mathbb{Z}\} \cap \mathbb{N}, & \text{if } c \cdot d \text{ odd}, \\ \{n(n\,d + c) \,|\, n \in \mathbb{Z}\} \cap \mathbb{N}, & \text{if } c \cdot d \text{ even}. \end{cases} \tag{2.47}$$

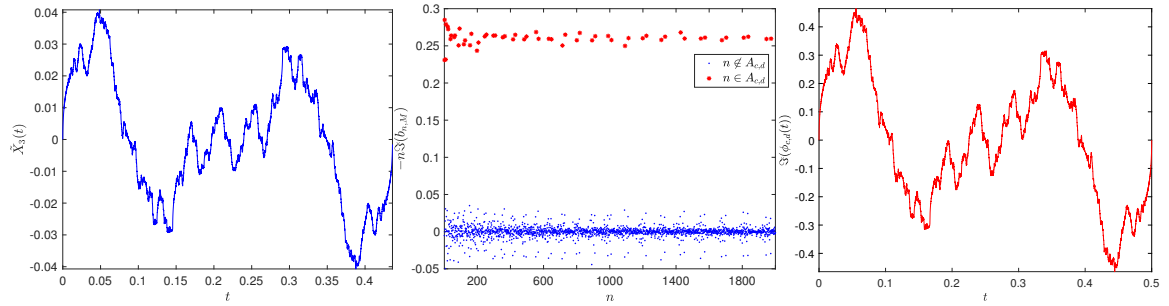

Figure 2.7 Left: $\tilde{X}_3(t)$, for $t \in [0, T_f^{c,d}]$, $M = 6$, $\theta_0 = \pi/5$, $c = 1$, $d = 5$, $b = 0.5628\ldots$. Center: Approximation of $-n\Im(b_{n,M})$, for $n = 1, 2, \ldots, 2000$, where $b_{n,M}$ are the Fourier coefficients of the scaled $\tilde{X}_3(t)$ multiplied by -1. The dominating points (red starred) are given by (2.47). Right: Imaginary part of $\phi_{c,d}(t)$ in (2.48), where the sum is taken over 2^{11} values.

On the other hand, the relation between $\mathbf{X}(0, t)$ for planar M-polygons and Riemann's non-differentiable function suggests comparing $\tilde{X}_3(t)$ in the helical M-polygon

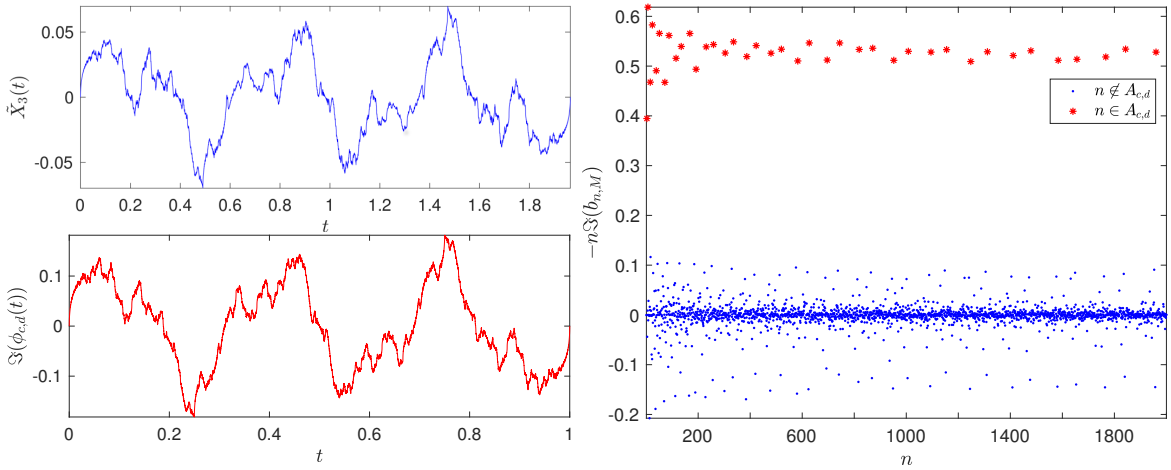

Figure 2.8 For $M = 4, \theta_0 = 2\pi/5$, $N/M = 2^{11}$, left: on the top $\tilde{X}_3(t)$, for $t \in [0, T_f^{c,d}]$, and bottom is $\Im\phi_{c,d}(t)$, $t \in [0,1]$. Right: Approximation of $-n\Im(b_{n,M})$, for $n = 1, 2, \ldots, 2000$, where $b_{n,M}$ are the Fourier coefficients of the scaled $\tilde{X}_3(t)$ multiplied by -1. The dominating points (red starred) are given by (2.47)

case and the imaginary part of

$$\phi_{c,d}(t) = \sum_{k \in A_{c,d}} \frac{e^{2\pi i k t}}{k}, \quad t \in \begin{cases} [0, 1/2], & \text{if } c \cdot d \text{ odd}, \\ [0,1], & \text{if } c \cdot d \text{ even}, \end{cases} \tag{2.48}$$

where $A_{c,d}$ is given by (2.47).

Figure 2.7 is the continuation of Figure 2.6, and hence, all the parameters are identical. On the left-hand side, we have plotted $\tilde{X}_3(t)$; in the center, minus the imaginary part of the approximations of $n\, b_{n,M}$, for $n = 1, 2, \ldots, 2000$, i.e., the fingerprint of the scaled $\tilde{X}_3(t)$; in general, the dominating points appear to be distributed around $1/4$ (when $c \cdot d$ is odd) or $1/2$ (when $c \cdot d$ is even). Finally, on the right-hand side, we have plotted the imaginary part of $\phi_{c,d}(t)$ which, except for a scaling, is visually indistinguishable from the $T_f^{c,d}$-periodic curve $\tilde{X}_3(t)$ on the left-hand side. See also Figure 2.8 where we have considered the parameters $M = 4$, $N/M = 2^{11}$, $c = 2$, $d = 5$, i.e., $\theta_0 = 2\pi/5$ or $b = 0.7265\ldots$. Note that since $c \cdot d$ is even, $\phi_{c,d}(t)$ is periodic for $t \in [0,1]$ and the dominating points in fingerprint plot are distributed about $1/2$. However, due to the smaller value of M, the noise (lower frequencies) in the fingerprint plot is more pronounced.

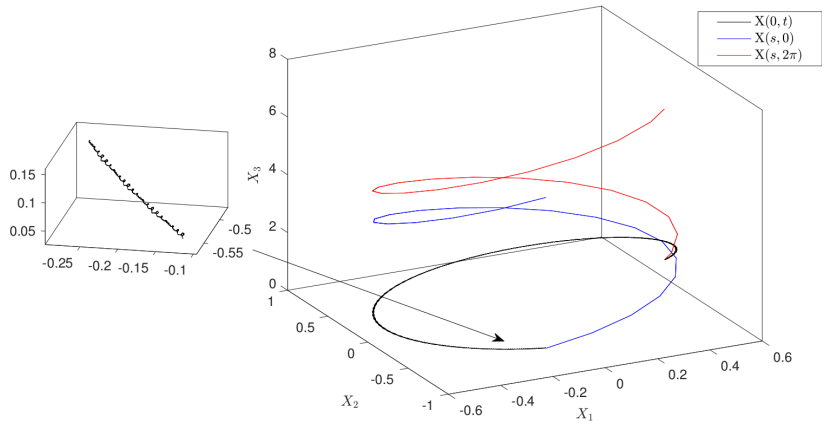

Figure 2.9 Initial polygon $\mathbf{X}(s,0)$ (blue), for $M = 20$, $\theta_0 = \pi/12$, i.e., $b = 0.8312\ldots$, and its evolution at time $t = 2\pi$ (red), together with the curve described by $\mathbf{X}(0,t)$, for $t \in [0, 2\pi]$ (black). $\mathbf{X}(0,t)$ has a conspicuous fractal helical structure, as shown in the zoomed part.

Computation of $\lim_{M\to\infty} \mathbf{X}(0,t)$

As we have seen, when $b \in (0,1)$, the curve $\mathbf{X}(0,t)$ is not periodic, but studying its structure componentwise sheds light on its behavior. We have also considered its time evolution for $M \gg 1$ and sufficiently large values of $T_f^{c,d}$. Figure 2.9 shows $\mathbf{X}(0,t)$, for $M = 20$, $\theta_0 = \pi/12$, $b = 0.8312\ldots, t \in [0, 12\pi/5]$, along with the initial and final helical polygonal curve. The fingerprint of the scaled $\tilde{X}_3(t)$ has been plotted on the left-hand side of Figure 2.10, and it is quite clear that the dominating points converge to $1/2$; indeed, the convergence is stronger than that in the center of Figure 2.7, since we have taken 10^4 points on the x-axis. This and other numerical experiments enable us to conjecture that

$$\lim_{M\to\infty} |n\, b_{n,M}| = \begin{cases} 1/4, & \text{if } n \in A_{c,d} \text{ and } c\cdot d \text{ odd,} \\ 1/2, & \text{if } n \in A_{c,d} \text{ and } c\cdot d \text{ even,} \\ 0, & \text{otherwise.} \end{cases}$$

On the other hand, the curve $\nu(t)$ shown on the right-hand side of Figure 2.10 appears to converge to a straight line. In this regard, we have performed a basic linear fitting $\nu(t) = m\,t + c$ (red), with $c = 1.4133\ldots$, $m = -0.8304\ldots$. Note that the modulus of m can be compared with the value of b, which can also be regarded as the angular velocity of the helical curve $\mathbf{X}$, as it evolves in time. Continuing the discussion from the previous section, we compute the phase shift at time T_f, for a given M and b, by calculating the angle between the tangent vector $\mathbf{T}$ at times $t = 0$ and $t = T_f$. Note

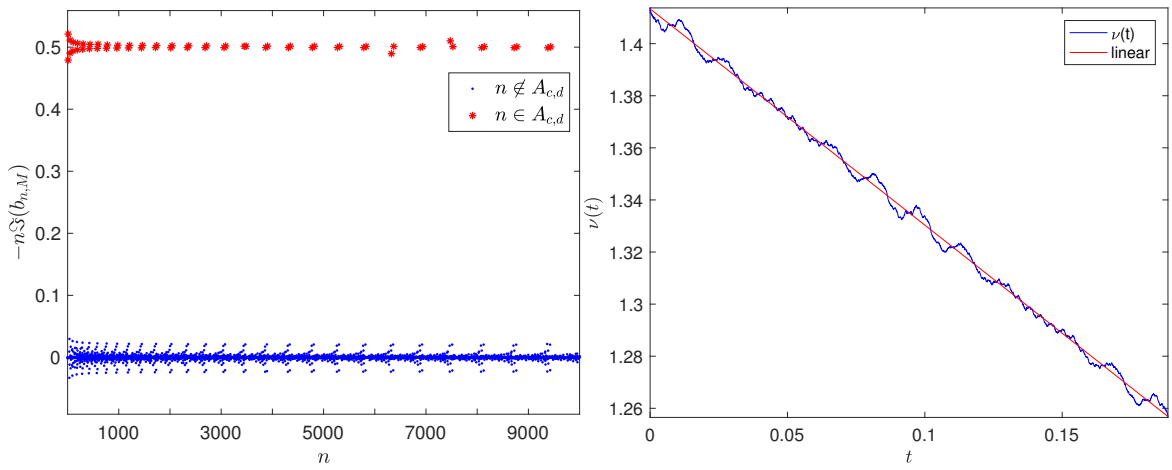

Figure 2.10 Left: fingerprint of the scaled $\tilde{X}_3(t)$, taking $M = 20$, $\theta_0 = \pi/12$, $c = 1$, $d = 12$, $b = 0.8312\ldots$, $t \in [0, T_f^{c,d}]$. The convergence of the dominating points to 0.5 is clearly visible. Right: $\nu(t)$, together with its best fitting line; the slope is $-0.8304\ldots$, and its modulus is close to the value of b.

that the phase shift decreases as M increases, and as $M \to \infty$, it converges to $2\pi b/M^2$. In Figure 2.11, we have compared the corresponding phase shift with the quantity $2\pi b/M^2$, taking $b = 0.4$, $M = 3, 4, \ldots, 20$, $N/M = 7680$. The left-hand side shows the phase shift values for different M values whereas on the right-hand side, we have computed the relative and absolute errors. The results also suggest that, as M grows larger, the amount of both the Galilean and the phase shifts decreases at the end of one time period.

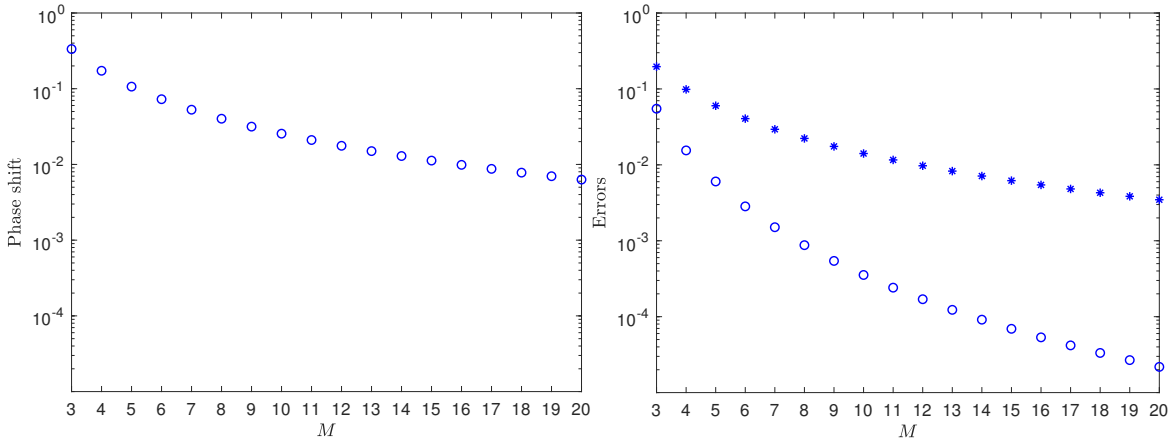

Figure 2.11 Left: Phase shift, for $M = 3, 4, \ldots, 20$, $b = 0.4$, $N/M = 7680$. Right: absolute errors (circled points) and relative errors (starred points) computed by comparing the phase shift with $2\pi b/M^2$, for each M. For a given value of $b > 0$, the phase shift at the end of one time period decreases, as M increases.

2.4.2 Case with $b \to 1^-$

From (2.15), it follows that, as $\theta_0 \to 2\pi/M$, $b \to 1^-$, but in Section 2.2.1, we mentioned that we can have both space and time periodicity only when $\gamma = 1$ (or $\theta_0 = 2\pi/M$). Since, numerically, θ_0 cannot be exactly $2\pi/M$ (or $b = 1$), we have taken $b = 1 - 10^{-5}$, and observed the evolution for M^2 time periods, i.e., until $t = 2\pi$. On the other hand, as b approaches 1, the speed of the center of mass c_M tends to 0, and this implies that the vertical movement (or the third component $X_3(0,t)$, which, after removing the vertical height becomes $2\pi/M$-periodic), is much smaller compared to the other two components. Hence, in order to understand the behavior of $\mathbf{X}(0,t)$ in the XY-plane, we consider the following stereographic projection onto $\mathbb{C}$:

$$z(t) = \frac{X_1(0,t)}{1+\tilde{X}_3(t)} + i\frac{X_2(0,t)}{1+\tilde{X}_3(t)}, \quad t \in [0, 2\pi], \tag{2.49}$$

which is almost 2π-periodic. As done for $b \in (0,1)$, we approximate the Fourier expansion of $z(t)$, and note that the dominating points in its fingerprint correspond to the squares of those integers belong to the set

$$A_M = \{1\} \cup \{n\,M \pm 1 \,|\, n \in \mathbb{N}\}. \tag{2.50}$$

This motivates us to compare $z(t)$ and

$$\phi_M(t) = \sum_{k \in A_M} \frac{e^{2\pi i k^2 t}}{k^2}, \quad t \in [0,1]. \tag{2.51}$$

In order to determine the correct orientation of the almost closed curve $z(t)$, we rotate it clockwise by an angle of $\pi/2 - \pi/M$ radians, and call the resulting curve $z_M(t)$. Figure 2.12 shows $z_M(t)$ (blue) and $\phi_M(t)$ (red), for $M = 3$. Except for a scaling, both curves are visually the same.

In order to strengthen our claim, we take different values of M, $M = 3, 4, \ldots, 15$, and compare them with the corresponding $\phi_M(t)$. In particular, we compute $\phi_M(t) - \lambda_M z_M(t) - \mu_M$, for some $\lambda_M \in \mathbb{R}$ and $\mu_M \in \mathbb{C}$ obtained using a least-square fitting:

$$\lambda_M = \Re\Big(\frac{\text{mean}(z_M^c(t)\cdot\phi^c(t)}{\text{mean}(|z_M^c(t)|^2)}\Big), \quad \mu_M = \text{mean}(\phi_M) - \lambda_M\,\text{mean}(z_M(t)); \tag{2.52}$$

with

$$z_M^c(t) = z_M(t) - \text{mean}(z_M(t)), \quad \phi_M^c(t) = \bar{\phi}_M(t) - \text{mean}(\bar{\phi}_M(t)),$$

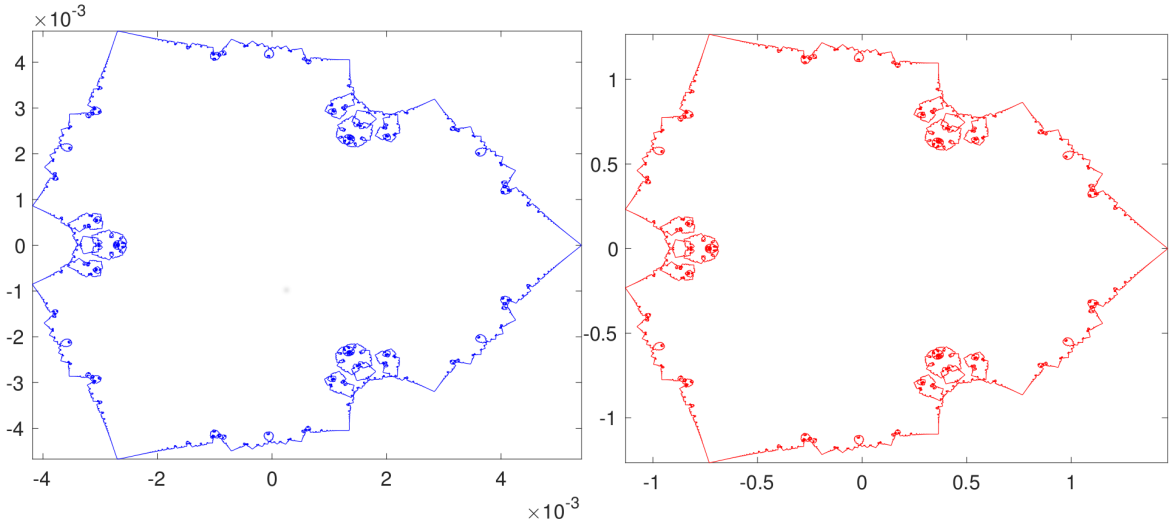

Figure 2.12 Left: Trajectory of a single point $z_M(t)$, for $M = 3$, $N/M = 2^{10}$. Right: $\phi_M(t)$ in (2.51), where $\dim(A_M) = 2^{10}$. Both curves have been computed at $N_t + 1$ points in their respective domain intervals.

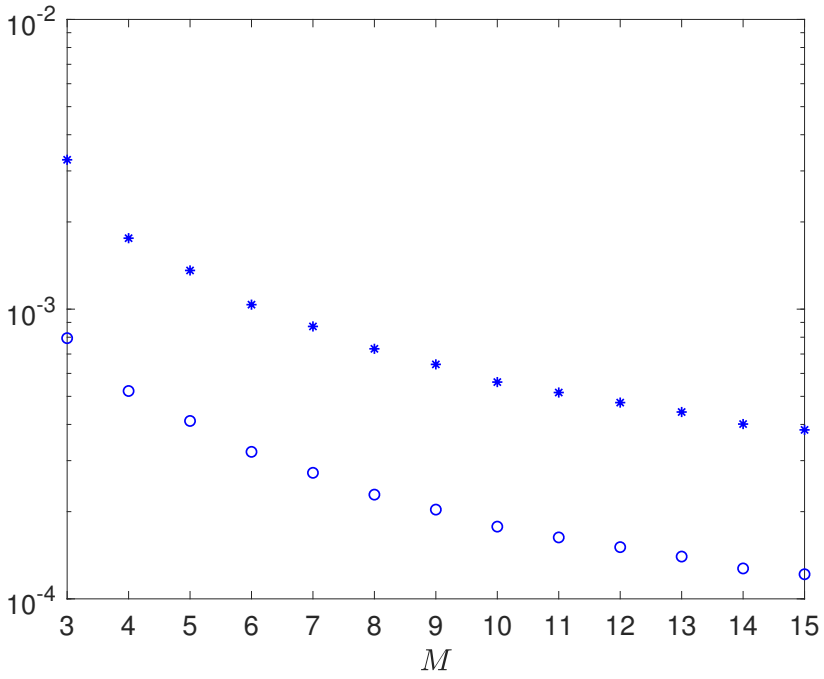

Figure 2.13 Errors $\max_t |(\phi_M - \lambda_M z_M - \mu_M)|$ (circled) and $\max_t |(\phi_M - \lambda_M z_M - \mu_M)/\phi_M|$ (starred), where λ_M and μ_M are computed from (2.52) for $M = 3, 4, \ldots, 15$.

Figure 2.13 shows the absolute error $(\max_t |(\phi_M - \lambda_M z_M - \mu_M)|)$ and relative error $(\max_t |(\phi_M - \lambda_M z_M - \mu_M)/\phi_M|)$ between z_M and ϕ_M. Note that, for different values of M, the time period $t \in [0, 2\pi]$ is the same, so the length of the vector $z_M(t)$ would be $M^2 N_t + 1$, and would vary with M. Therefore, in order to keep a fair comparison among all the M values, we have kept N/M constant, i.e., $N/M = 2^{10}$. As M increases, the length of $z_M(t)$ increases, so we restrict ourselves to the case with $M = 15$, where the length of $z_M(t)$ is $1.3608 \cdot 10^8 + 1$. Moreover, the plot clearly shows that the convergence is quite strong in the sense that, as M increases, the discrepancy between z_M and ϕ_M decreases.

Moreover, the case $M = 4$, $b = 1 - 10^{-5}$ is worth mentioning as well where the set A_M in (2.50) involves only half of the integers, see Figure 2.14 where we have plotted $z_M(t)$ on the left, and $\phi_M(t)$ on the right hand side.

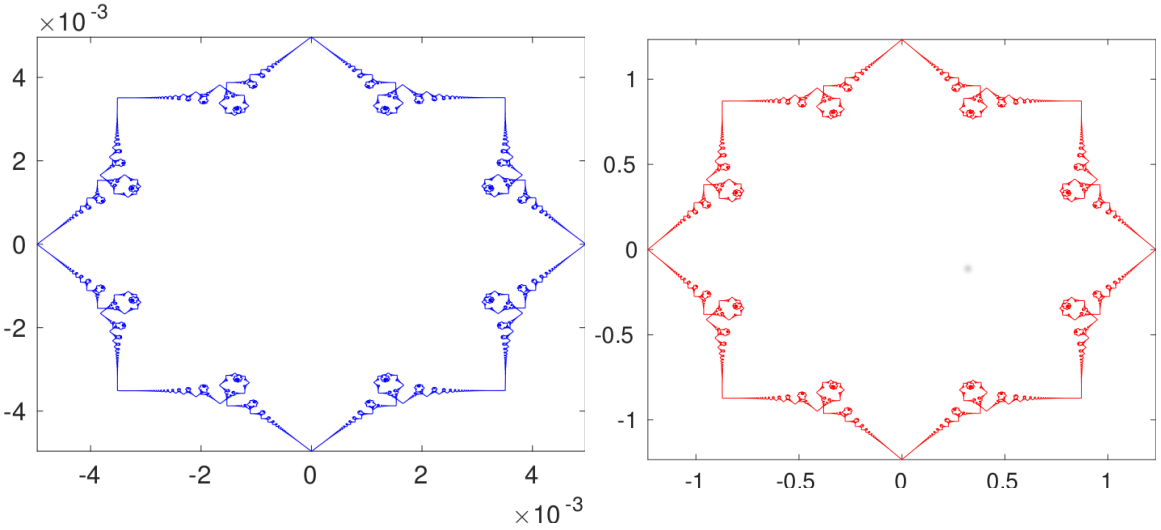

Figure 2.14 Left: Trajectory of a single point $z_M(t)$, for $M = 4$, $N/M = 2^{10}$. Right: $\phi_M(t)$ in (2.51), where $\dim(A_M) = 2^{10}$. Both curves have been computed at $N_t + 1$ points in their respective domain intervals.

Finally, in Figure 2.15, we plot the fingerprint of the scaled $z_M(t)$, for $b = 1 - 10^{-5}$, $t \in [0, 2\pi]$, $M = 3$ (left) and $M = 4$ (right). Observe that, as b tends to 1, the dominating points in the fingerprint approach 1; in other words, we conjecture that

$$\lim_{b \to 1^-} |n\, c_n| = \begin{cases} 1, & \text{if } n \in A_M, \\ 0, & \text{otherwise,} \end{cases}$$

where c_n are the Fourier coefficients of the scaled $z_M(t)$, which implies that the curve z_M converges to ϕ_M, as $b \to 1^-$.

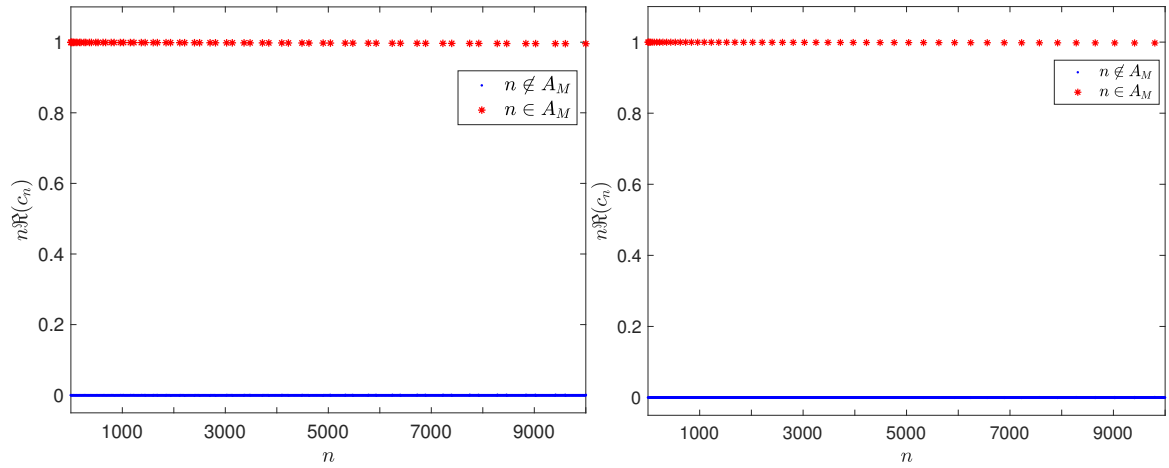

Figure 2.15 Left: Plot of $n\Re(c_n)$ against n, for $M = 3, N/M = 2^{10}$, $b = 1 - 10^{-5}$, $t \in [0, 2\pi]$. The dominating points (red starred) are of the form $k^2 c_{k^2}$, where k is such that $\mathrm{mod}(k \pm 1, M) = 0$; we have taken $k \in \{1, 2, 4, 5, 7, \ldots, 34\}$. Right: Plot of $n\Re(c_n)$ against n, for $M = 4, N/M = 2^{10}$, $b = 1 - 10^{-5}$, $t \in [0, 2\pi]$. The dominating points (red starred) are of the form $k^2 c_{k^2}$, where k is such that $\mathrm{mod}(k \pm 1, M) = 0$; we have taken $k \in \{1, 3, 5, 7, \ldots, 99\}$.

2.5 Behavior of the tangent vector T near irrational times

In the one-corner problem with fixed boundary conditions, and in the planar M-polygon case with periodic boundary conditions a fractal-like phenomenon was observed in the tangent vectors too [22, 24]. This suggests expecting a similar behavior in the case of helical M-polygons. We use the algebraically constructed $\mathbf{T}_{alg}$, which is correct except for a rotation about the z-axis, does not exhibit the Gibbs phenomenon, and can be obtained without numerical simulations.

As in [22], we take rational times t_{pq}, such that q is very large (i.e., t_{pq} can be regarded as an approximation of an irrational time), and there is no pair $(\tilde{p}, \tilde{q})$ where both $\tilde{q}$ and $|p/q - \tilde{p}/\tilde{q}|$ are small. In particular, we take $M = 3$, $t_{pq} = \frac{2\pi}{9}(\frac{1}{4} + \frac{1}{41} + \frac{1}{401}) = \frac{2\pi}{9} \cdot \frac{18209}{65764}$, and note that, as b moves from 0 to 1, the $Mq/2 = 98646$ values of **T** tend to concentrate on the upper half of the sphere, whereas, when $b \approx 1$, they lie very close to its north pole (see the left-hand side of Figure 2.16). On the other hand, the stereographic projection seems to be even more interesting: for $b = 0$, the fractal spiral-like structures appear to be at three or four different scales (see [22, Fig. 8]), but, as b approaches 1, the equally complex structures form a shape resembling a triskelion (see the right-hand side of Figure 2.16).

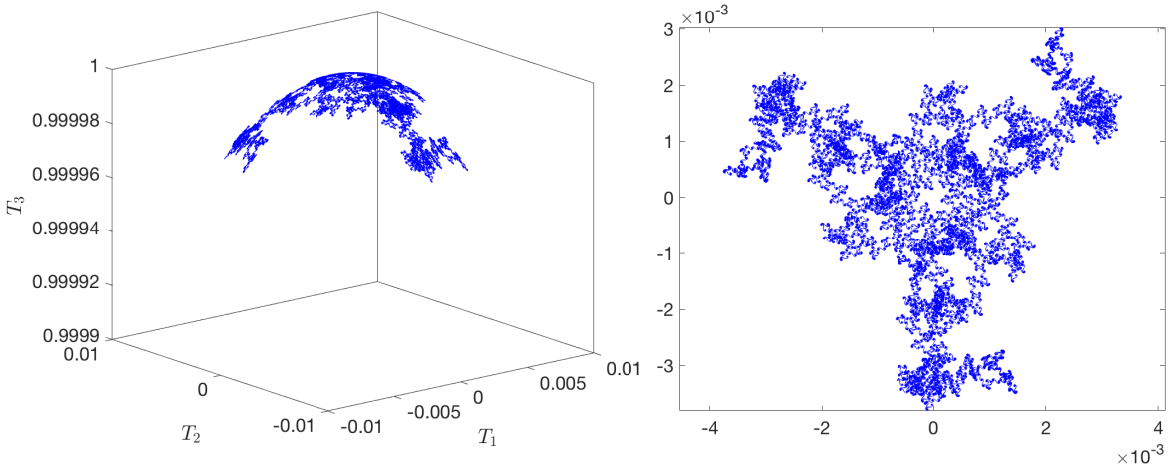

Figure 2.16 Left: $\mathbf{T}_{alg}$, for $M = 3$, $b = 1 - 10^{-5}$, at $t_{pq} = \frac{2\pi}{9}(\frac{1}{4} + \frac{1}{41} + \frac{1}{401}) = \frac{2\pi}{9} \cdot \frac{18209}{65764}$. As b tends to 1, the values of the tangent vector concentrate around the north pole of $\mathbb{S}^2$. Right: The corresponding stereographic projection, which converges to a triskelion with the same scale spirals.

2.6 Numerical relationship between the helical M-polygon and one-corner problems

In this section, we establish the claim that the helical M-polygon problem can be explained as a superposition of M one-corner problems for infinitesimal times, as in [23]. Thus, in order to compare both cases when $\theta_0 > 0$, we obtain the solution of one-corner problem, i.e., the orthonormal basis vectors $\mathbf{T}_{c_\theta}$, $\mathbf{n}_{c_\theta}$, $\mathbf{b}_{c_\theta}$, and the curve $\mathbf{X}_{c_\theta}$, by integrating the Frenet–Serret frame (1.1) with initial conditions (1.21) and (1.22) at $t = t_{1,q}$, $q \gg 1$. We take $c_{\theta,0}$ as defined in (2.19), so the inner angle between the asymptotes of the tangent vectors, i.e., $\lim_{s\to-\infty} \mathbf{T}_{c_\theta}(s) = \mathbf{A}^-$, $\lim_{s\to\infty} \mathbf{T}_{c_\theta}(s) = \mathbf{A}^+$, is equal to the angle between any two adjacent sides of the helical M-polygon with $\mathbf{A}^- = \mathbf{A}^1$, $\mathbf{A}^+ = \mathbf{A}^2$ and $\mathbf{A}^j$, $j = 1, 2$ as in (1.24).

Next, we have to rotate $\mathbf{X}_{c_\theta}$, $\mathbf{T}_{c_\theta}$, $\mathbf{n}_{c_\theta}$ and $\mathbf{b}_{c_\theta}$, in such a way that the rotated vectors $\mathbf{X}_{rot}$ and $\mathbf{T}_{rot}$ match the M-polygon problem, where $\mathbf{X}_{rot} \equiv \mathbf{M} \cdot \mathbf{X}$ and $\mathbf{T}_{rot} \equiv \mathbf{M} \cdot \mathbf{T}$, for a certain rotation matrix $\mathbf{M}$, which is determined by imposing that $\mathbf{T}^-_{rot} = \lim_{s\to-\infty} \mathbf{T}_{rot}(s) = (a\cos(2\pi/M), -a\sin(2\pi/M), b)^T$, $\mathbf{T}^+_{rot} = \lim_{s\to+\infty} \mathbf{T}_{rot}(s) = (a, 0, b)^T$, with $a^2 + b^2 = 1$. In the following lines, we present two algorithms to compute the rotation matrix $\mathbf{M}$.

Algorithm 1

(i) First, project $\mathbf{A}^+$ and $\mathbf{A}^-$ on the plane $z = 0$, which can be done by performing a rotation $\mathbf{M}_1$ about the x-axis(negative) of angle θ_1

$$\nu_1 = \arccos\left(\frac{A_2}{\sqrt{A_2^2 + A_3^2}}\right), \quad \mathbf{M}_1 = \begin{pmatrix} 1 & 0 & 0 \\ 0 & \cos\nu_1 & \sin\nu_1 \\ 0 & -\sin\nu_1 & \cos\nu_1 \end{pmatrix},$$

so that

$$\mathbf{M}_1 \cdot \mathbf{A}^{\pm} = \begin{pmatrix} A_1 \\ \pm\sqrt{A_2^2 + A_3^2} \\ 0 \end{pmatrix}.$$

(ii) Project $\mathbf{T}^-_{rot}(s)$ and $\mathbf{T}^+_{rot}(s)$ also on the plane $z = 0$. Consider the plane where $\mathbf{T}^-_{rot}$ and $\mathbf{T}^+_{rot}$ lie and rotate it in such a way that its normal is parallel to z-axis and passes through the origin. Compute

(a) normal to the initial plane $\hat{\mathbf{n}} = \frac{\mathbf{T}^-_{rot} \wedge_+ \mathbf{T}^+_{rot}}{\|\mathbf{T}^-_{rot} \wedge_+ \mathbf{T}^+_{rot}\|}$,

(b) angle between $\hat{\mathbf{n}}$ and the z-axis and the rotation axis $\hat{\mathbf{u}}_2$

$$\nu_2 = \arccos(\hat{\mathbf{n}} \circ_+ (0,0,1)^T), \ \hat{\mathbf{u}}_2 = \tfrac{\hat{n} \wedge_+ (0,0,1)^T}{\|\hat{n} \wedge_+ (0,0,1)^T\|}.$$

If θ_2 is equal to zero, then the rotation matrix $\mathbf{M}_2$ is an identity matrix, otherwise, $\mathbf{M}_2$ is rotation of angle θ_2 about an axis $\hat{\mathbf{u}}$ such that the vectors $\mathbf{M}_2 \cdot \mathbf{T}^{\pm}_{rot}$ lie on the XY-plane.

(iii) Compute the angle between $\mathbf{M}_1 \cdot \mathbf{A}^{\pm}$ and $\mathbf{M}_2 \cdot \mathbf{T}^{\pm}_{rot}$, and the rotation axis $\hat{\mathbf{u}}_3$

$$\nu_3 = \arccos\left((\mathbf{M}_1 \cdot \mathbf{A}^{\pm}) \circ_+ (\mathbf{M}_2 \cdot \mathbf{T}^{\pm}_{rot})\right), \ \hat{\mathbf{u}}_3 = \tfrac{(\mathbf{M}_1 \cdot \mathbf{A}^{\pm}) \wedge_+ (\mathbf{M}_2 \cdot \mathbf{T}^{\pm}_{rot})}{\|(\mathbf{M}_1 \cdot \mathbf{A}^{\pm}) \wedge_+ (\mathbf{M}_2 \cdot \mathbf{T}^{\pm}_{rot})\|}.$$

With θ_3 and $\hat{u}_3$ we construct the corresponding rotation matrix $\mathbf{M}_3$.

(iv) Hence, $\mathbf{M} = \mathbf{M}_2^{-1} \cdot \mathbf{M}_3 \cdot \mathbf{M}_1$.

In our case, these matrices are

$$\mathbf{M}_1 = \begin{pmatrix} 1 & 0 & 0 \\ 0 & \frac{A_2}{\sqrt{A_2^2+A_3^2}} & \frac{A_3}{\sqrt{A_2^2+A_3^2}} \\ 0 & -\frac{A_3}{\sqrt{A_2^2+A_3^2}} & \frac{A_2}{\sqrt{A_2^2+A_3^2}}, \end{pmatrix}, \ \mathbf{M}_3 = \begin{pmatrix} \cos(\pi/M) & \sin(\pi/M) & 0 \\ -\sin(\pi/M) & \cos(\pi/M) & 0 \\ 0 & 0 & 1 \end{pmatrix},$$

$$\mathbf{M}_2 = \begin{pmatrix} 1+\cos^2(\pi/M)(a\cos(\theta/2-1)) & \cos(\theta/2)\sin(\pi/M-\rho_0/2) & b\cos(\theta/2) \\ \cos(\theta/2)\sin(\pi/M-\rho_0/2) & 1+\sin^2(\pi/M)(a\cos(\theta/2-1)) & -\frac{b}{a}\tan(\rho_0/2) \\ -b\cos(\theta/2) & \frac{b}{a}\tan(\rho_0/2) & a\cos(\theta/2) \end{pmatrix}.$$

Algorithm 2

In this algorithm, we obtain the rotation matrix by using only two intermediate rotations.

(i) Compute the angle ν_1 between $\mathbf{T}^+_{rot}$ and $\mathbf{A}^+$, i.e., $\nu_1 = \arccos(\mathbf{A}^+ \circ_+ \mathbf{T}^+_{rot})$ and axis $\hat{\mathbf{u}} = \frac{\mathbf{A}^+ \wedge_+ \mathbf{T}^+_{rot}}{\|\mathbf{A}^+ \wedge_+ \mathbf{T}^+_{rot}\|}$. If $\nu_1 = 0$ then $\mathbf{M}_1$ is an identity matrix, otherwise $\mathbf{M}_1$ performs a rotation of an angle ν_1 about an axis $\hat{\mathbf{u}}$. Thus, $\mathbf{M}_1 \cdot \mathbf{A}^+ = \mathbf{T}^+_{rot}$.

(ii) Denote $\tilde{\mathbf{A}}^- = \mathbf{M}_1 \cdot \mathbf{A}^-$ and $\tilde{\mathbf{T}}^-_{rot} = \mathbf{M}_1 \cdot \mathbf{T}^-_{rot}$ and ν_2 as the angle they make in the plane whose normal is $\mathbf{T}^+_{rot}$. In other words, $\nu_2 = \arccos\left(\tilde{\mathbf{A}}^-_\perp \circ_+ \tilde{\mathbf{T}}^-_{rot_\perp}\right)$, where $\tilde{\mathbf{A}}^-_\perp = -\mathbf{T}^+_{rot} \wedge_+ (\mathbf{T}^+_{rot} \wedge_+ \tilde{\mathbf{A}}^-)$ and $\tilde{\mathbf{T}}^-_{rot_\perp} = -\mathbf{T}^+_{rot} \wedge_+ (\mathbf{T}^+_{rot} \wedge_+ \tilde{\mathbf{T}}^-_{rot})$ are the orthogonal projection of each vector in the plane orthogonal to $\mathbf{T}^+_{rot}$. Thus, $\mathbf{M}_2$ is a matrix performing a rotation of an angle ν_2 about an axis $\mathbf{T}^+_{rot}$.

(iii) Hence, the desired matrix is $\mathbf{M} = \mathbf{M}_2 \cdot \mathbf{M}_1$.

Thus, we obtain

$$\begin{pmatrix} X_{rot,1} \\ X_{rot,2} \\ X_{rot,3} \end{pmatrix} = \begin{pmatrix} -a\pi/M \\ -\frac{a\pi/M}{\tan(\pi/M)} \\ 0 \end{pmatrix} + \mathbf{M} \cdot \begin{pmatrix} X_{c_0,1} \\ X_{c_0,2} \\ X_{c_0,3} \end{pmatrix}, \quad \begin{pmatrix} T_{rot,1} \\ T_{rot,2} \\ T_{rot,3} \end{pmatrix} = \mathbf{M} \cdot \begin{pmatrix} T_{c_0,1} \\ T_{c_0,2} \\ T_{c_0,3} \end{pmatrix}, \tag{2.53}$$

where $\left(-a\pi/M, -\frac{a\pi/M}{\tan(\pi/M)}, 0\right)^T$ is the location of corner of the helical M-polygon corresponding to $s = 0$, at $t = 0$.

In our numerical simulations, we take $\Delta s = \pi/M^2 q$, and integrate (1.1) by using a fourth-order Runge–Kutta method with initial conditions (1.21) and (1.22) at $t = t_{1,q}$. Then, using the same Δs, we compute the $\mathbf{T}(s, t_{1,q})$ corresponding to the M-polygon problem, for $M = 6$, $\theta_0 = \pi/5$, $q = 502$. We have also compared the evolution of $\mathbf{X}_{rot}(0,t)$ and $\mathbf{X}(0,t)$, where

$$\begin{pmatrix} X_{rot,1}(0,t) \\ X_{rot,2}(0,t) \\ X_{rot,3}(0,t) \end{pmatrix} = \begin{pmatrix} -a\pi/M \\ -\frac{a\pi/M}{\tan(\pi/M)} \\ 0 \end{pmatrix} + 2\sqrt{t}\mathbf{M}c_{\theta,0} \cdot \begin{pmatrix} 0 \\ 0 \\ 1 \end{pmatrix}. \tag{2.54}$$

We note that, when projected on the complex plane, $\mathbf{X}(0,t)$ can be very well approximated by $\mathbf{X}_{rot}(0,t)$ for small values of t such as $t \in [0, t_{1,20}]$. Moreover, there is also a similarity between the third components of both curves; these observations are shown in Figure 2.17.

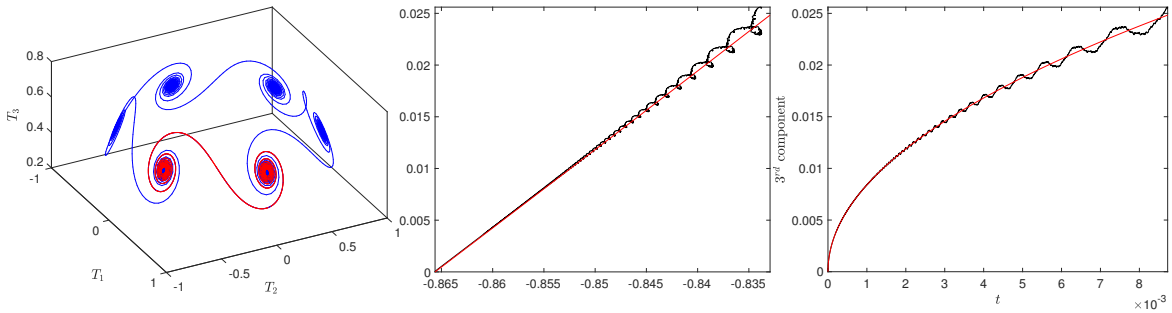

Figure 2.17 Left: $\mathbf{T}$ for the M-polygon problem (blue) and $\mathbf{T}_{rot}$ (red), for $M = 6$, $\theta_0 = \pi/5$, at $t = t_{1,502}$. Center: Comparison between $\mathbf{X}(0,t)$ (black) and $\mathbf{X}_{rot}(0,t)$ (red). Right: Third component $X_3(0,t)$ (black) and $X_{rot,3}(0,t)$ (red), for $t \in [0, t_{1,20}]$.

2.6.1 Approximation of the curvature at the origin

The relationship between the one-corner and the M-polygon problems has deep implications. For instance, in [23], this fact was used to compute the speed of the center of mass through analytical techniques, or, to recover c_0 in (2.26). In what follows, we illustrate again the utility of this approach, to recover (2.19).

Observe that, in the one-corner problem (see [36]), the curvature at $s = 0$ and $t > 0$ is given by $c_0(t) = \sqrt{t}\|\mathbf{T}_s(0,t)\|$; hence, in the case of regular M-polygons, the corresponding formula is $c_{\theta,0}(t_{pq}) = \sqrt{t_{pq}}\|\mathbf{T}_s(0,t_{pq})\|$ at infinitesimal rational times t_{pq}. Following the same steps as in [23], we approximate $\mathbf{T}_s$ using finite differences. Note that, for any given value of q, since $\theta_0 < 2\pi/M$, the Galilean shift satisfies $s_{1,q} < 2\pi/Mq$, and, as a result, $\mathbf{T}(s, t_{1,q})$ is continuous at $s = 0$, $s = -\Delta s$, and $s = \Delta s$, where $\Delta s = 2\pi/Mq$, if q is odd, and $\Delta s = 4\pi/Mq$ if q is even. This fact also implies that

$$\mathbf{T}((-\Delta s + s_{1,q})^-, t_{1,q}) = \mathbf{T}(-\Delta s^-, t_{1,q}), \quad \mathbf{T}((\Delta s + s_{1,q})^-, t_{1,q}) = \mathbf{T}(\Delta s^-, t_{1,q}),$$
$$\mathbf{T}(s_{1,q}^-, t_{1,q}) = \mathbf{T}(0^-, t_{1,q}),$$

Thus, using the algebraic solution $\mathbf{T}_{alg}$ and bearing in mind the previous considerations, we take $q \equiv 2 \bmod 4$, $\Delta s = 4\pi/Mq$, so $c_{\theta,0}$ is approximated as

$$c_{\theta,0} \approx c^q_{\theta,0} \equiv \sqrt{t_{1,q}} \frac{\|\mathbf{T}_{alg}(\frac{4\pi}{Mq}, t_{1,q}) - \mathbf{T}_{alg}(-\frac{4\pi}{Mq}, t_{1,q})\|}{2 \cdot \frac{4\pi}{Mq}}, \quad q \gg 1. \tag{2.55}$$

Recall that

$$\begin{pmatrix} \mathbf{T}_{alg}(\frac{4\pi}{Mq}, t_{1q})^T \\ \mathbf{e}_{1,alg}(\frac{4\pi}{Mq}, t_{1q})^T \\ \mathbf{e}_{2,alg}(\frac{4\pi}{Mq}, t_{1q})^T \end{pmatrix} = \mathbf{R}_{k,m} \begin{pmatrix} \mathbf{T}_{alg}(0, t_{1q})^T \\ \mathbf{e}_{1,alg}(0, t_{1q})^T \\ \mathbf{e}_{2,alg}(0, t_{1q})^T \end{pmatrix}, \quad \text{for } k = 0, m = 1,$$

$$\begin{pmatrix} \mathbf{T}_{alg}(0, t_{1q})^T \\ \mathbf{e}_{1,alg}(0, t_{1q})^T \\ \mathbf{e}_{2,alg}(0, t_{1q})^T \end{pmatrix} = \mathbf{R}_{k,m} \begin{pmatrix} \mathbf{T}_{alg}(-\frac{4\pi}{Mq}, t_{1q})^T \\ \mathbf{e}_{1,alg}(-\frac{4\pi}{Mq}, t_{1q})^T \\ \mathbf{e}_{2,alg}(-\frac{4\pi}{Mq}, t_{1q})^T \end{pmatrix}, \quad \text{for } k = -1, m = q-1,$$

where $\mathbf{R}_{k,m}$ is as in (2.30). Since we need to compute the Euclidean norm of $\mathbf{T}_{alg}(4\pi/Mq, t^-_{1q}) - \mathbf{T}_{alg}(-4\pi/Mq, t^-_{1q})$, we can safely ignore the global rotation of $\mathbf{T}_{alg}$ and assume that $\mathbf{T}_{alg}(0, t_{1q})$, $\mathbf{e}_{1,alg}(0, t_{1q})$, $\mathbf{e}_{2,alg}(0, t_{1q})$ form the identity matrix. Thus,

$$\begin{cases} \mathbf{T}_{alg}\left(\frac{4\pi}{Mq}^-, t_{1q}\right) = \left(\cos(\rho_q), \sin(\rho_q)\cos(\theta_1 + \frac{\theta_0}{q}), \sin(\rho_q)\sin(\theta_1 + \frac{\theta_0}{q})\right)^T \\ \mathbf{T}_{alg}(0^-, t_{1q}) = (1, 0, 0)^T, \\ \mathbf{T}_{alg}\left(-\frac{4\pi}{Mq}^-, t_{1q}\right) = \left(\cos(\rho_q), -\sin(\rho_q)\cos(\theta_{q-1} + \frac{\theta_0}{q}), -\sin(\rho_q)\sin(\theta_{q-1} + \frac{\theta_0}{q})\right)^T, \end{cases}$$

which implies

$$\begin{aligned} \left\|\mathbf{T}_{alg}\left(\frac{4\pi}{Mq}^-, t_{1q}\right) - \mathbf{T}_{alg}\left(-\frac{4\pi}{Mq}^-, t_{1q}\right)\right\| &= \sin(\rho_q)\sqrt{2\left(\left(1 + \cos(\theta_1 - \theta_{q-1} + \frac{2\theta_0}{q}\right)\right)} \\ &= 2\sin(\rho_q)\cos\left(\frac{\theta_1 - \theta_{q-1}}{2} + \frac{\theta_0}{q}\right) \\ &= 2\sin(\rho_q)\cos\left(\frac{\theta_0}{q}\right), \end{aligned} \tag{2.56}$$

where in the last step we have used $\theta_1 = \theta_{q-1}$, which follows from the properties of the generalized Gauß sum: $G(-p, m, q) = G(-p, -m, q) = G(-p, q-m, q)$. Substituting

(2.56) into (2.55) and taking the limit $q \to \infty$,

$$c_{\theta,0} = \lim_{q\to\infty} \sqrt{\frac{2\pi}{M^2 q}} \frac{2\sin(\rho_q)\cos\left(\frac{\theta_0}{q}\right)}{8\pi/Mq} = \lim_{q\to\infty} \sqrt{\frac{q}{8\pi}[1-\cos^2(\rho_q)]}\cos\left(\frac{\theta_0}{q}\right)$$
$$= \lim_{q\to\infty} \sqrt{\frac{q}{8\pi}\left[1-\left(2\cos^{4/q}\left(\frac{\rho_0}{2}\right)-1\right)^2\right]}\cos\left(\frac{\theta_0}{q}\right) = \sqrt{-\frac{2}{\pi}\ln\left(\cos\left(\frac{\rho_0}{2}\right)\right)}.$$

After computing $c_{\theta,0}$ analytically from (2.55), we have also approximated its value numerically, taking $M = 6$, $\theta_0 = \pi/5$, and $q = 1002, 2002, \ldots, 128002$. Table 2.4 shows the discrepancies between the algebraic and numerical values. The results show clearly that, when roughly doubling q, the errors are approximately halved, suggesting a convergence order of $\mathcal{O}(1/q) = \mathcal{O}(t_{1,q})$. We have considered different values of M and

q	$\lvert c_{\theta,0} - c^q_{\theta,0}\rvert$	q	$\lvert c_{\theta,0} - c^q_{\theta,0}\rvert$
1002	$6.8511 \cdot 10^{-5}$	16002	$4.2878 \cdot 10^{-6}$
2002	$3.4280 \cdot 10^{-5}$	32002	$2.1443 \cdot 10^{-6}$
4002	$1.7146 \cdot 10^{-5}$	64002	$1.0720 \cdot 10^{-6}$
8002	$8.5747 \cdot 10^{-6}$	128002	$5.3681 \cdot 10^{-7}$

Table 2.4 $|c_{\theta,0} - c^q_{\theta,0}|$, for $M = 6$, $\theta_0 = \pi/5$. The errors decrease as $\mathcal{O}(1/q) = \mathcal{O}(t_{1,q})$.

θ_0, and the consistency of numerical results give a strong evidence that at a numerical level, for small times, the helical M-polygon problem with nonzero torsion, can be seen as a superposition of M one-corner problems.

2.7 Conclusion

In this chapter, we have investigated the evolution of VFE for an M-sided regular polygon with nonzero torsion in the Euclidean space. In this regard, the problem has been solved numerically and the algebraic solution has been constructed up to a rotation. A precise expression for the speed of the center of mass has been obtained and for any rational time, the angle between any two sides of the new polygon has been determined using a conservation law established in [8]. The numerical solution suggests that due to the presence of nonzero torsion, the time evolution is neither space nor time periodic and this results in a non-planar structure of $\mathbf{X}(0,t)$. However, with a certain choice of torsion, through Fourier analysis at a numerical level, we are able to discover new variants of Riemann's non-differentiable function in the trajectory of

$\mathbf{X}(0,t)$. Finally, we also comment on the relationship between the helical M-polygon and one-corner problems.

Chapter 3

A regular planar l-polygon in the Minkowski space

Time and space are modes by which we think and not conditions in which we live.

Albert Einstein

Contents

3.1 Introduction

Let $\mathbb{R}^{1,2} = \{(x_1, x_2, x_3) : ds^2 = -dx_1^2 + dx_1^2 + dx_1^2\}$ be the three-dimensional Minkowski space, and $\mathbb{H}^2 = \{(x_1, x_2, x_3) : -x_1^2 + x_1^2 + x_1^2 = -1, x_1 > 0\}$ be the unit sphere in it. For an arc-length parameterized initial curve $\mathbf{X_0} : \mathbb{R} \longrightarrow \mathbb{R}^{1,2}$, we consider the geometric flow

$$\mathbf{X}_t = \mathbf{X}_s \wedge_- \mathbf{X}_{ss}, \tag{3.1}$$

where s is the arc-length parameter, t time and the cross product $\wedge_-$ is as in (1.7):

$$\mathbf{a} \wedge_- \mathbf{b} = (-(a_2b_3 - a_3b_2), a_3b_1 - a_1b_3, a_1b_2 - a_2b_1), \ \mathbf{a}, \mathbf{b} \in \mathbb{R}^{1,2}.$$

The time-like tangent vector $\mathbf{T} = \mathbf{X}_s$ solves

$$\mathbf{T}_t = \mathbf{T} \wedge_- \mathbf{T}_{ss}. \tag{3.2}$$

With the generalized curvature κ, torsion τ, through the filament function

$$\psi(s,t) = \kappa(s,t)e^{i\int_0^s \tau(s',t)ds'} = \tilde{\alpha}(s,t) + i\tilde{\beta}(s,t), \tag{3.3}$$

and the parallel-frame

$$\begin{pmatrix} \mathbf{T} \\ \mathbf{e}_1 \\ \mathbf{e}_2 \end{pmatrix}_s = \begin{pmatrix} 0 & \tilde{\alpha} & \tilde{\beta} \\ \tilde{\alpha} & 0 & 0 \\ \tilde{\beta} & 0 & 0 \end{pmatrix} \cdot \begin{pmatrix} \mathbf{T} \\ \mathbf{e}_1 \\ \mathbf{e}_2 \end{pmatrix}, \tag{3.4}$$

where $\mathbf{T}$, $\mathbf{e}_1$, $\mathbf{e}_2$ form a unit orthonormal system, (3.1)–(3.2) are related to the following defocussing type nonlinear Schrödinger equation

$$\psi_t = i\psi_{ss} - \frac{i}{2}\psi(|\psi|^2 + A(t)), \ A(t) \in \mathbb{R}. \tag{3.5}$$

Thanks to the relationship between these three equations, for a given time t, from $\psi(s,t)$, we can obtain $\mathbf{T}(s,t)$ and $\mathbf{X}(s,t)$ up to a rigid movement which can be determined using the symmetries of the problem, and hence, the main idea is to work with (3.5).

In this chapter, we present the binormal motion of the polygonal curves in the Minkowski space $\mathbb{R}^{1,2}$. For an initial datum $\mathbf{X}(s,0)$ as a regular planar l-polygon (to be explained later) with its tangent vector $\mathbf{T}$ in the hyperbolic 2-space $\mathbb{H}^2$, in Section 3.2, we formulate the problem and with appropriate algebraic techniques, construct the solution for rational times. We present different methods to obtain the time evolution of $\mathbf{X}$ and $\mathbf{T}$ numerically. For instance, in Section 3.4, (3.1)–(3.2)

have been solved with a finite difference discretization in space and a fourth-order Runge–Kutta method in time with Dirichlet boundary conditions. On the other hand, in Section 3.5, we employ a Chebyshev discretization in space with implicit methods in time. Moreover, the trajectory of a single point $\mathbf{X}(0,t)$ which resembles the so-called Riemann's non-differentiable function, has also been analyzed numerically.

3.2 A solution of VFE for a regular planar l-polygon

One of the main aims of this chapter is to obtain the solutions of (3.1) and explain their dynamics when a regular planar l-polygon us considered as an initial datum. In this direction, as in the Euclidean case, by assuming uniqueness, we prove the following theorem:

Theorem 5. *Assume that there exists a unique solution of the initial value problem*

$$\mathbf{X}_t = \mathbf{X}_s \wedge_- \mathbf{X}_{ss}, \tag{3.6}$$

with $\mathbf{X}(s,0)$ as a regular planar l-polygon. Then, at a time t_{pq}, a rational multiple of $2\pi/r^2$, i.e., $t_{pq} \equiv (2\pi/r^2)(p/q)$, with $r = 2\pi/l$, $p \in \mathbb{Z}$, $q \in \mathbb{N}$, $\gcd(p,q) = 1$, the solution is a skew l_q-polygon with q times more sides (if q odd) or $q/2$ times more sides (if q even) than the initial polygon. All the new sides have the same length, and the time-like angle l_q between two adjacent sides is constant. Moreover, the polygon at a time t_{pq} is the solution of the generalized Frenet–Serret system

$$\begin{pmatrix} \mathbf{T}(s,t_{pq}) \\ \mathbf{e}_1(s,t_{pq}) \\ \mathbf{e}_2(s,t_{pq}) \end{pmatrix}_s = \begin{pmatrix} 0 & \alpha(s,t_{pq}) & \beta(s,t_{pq}) \\ \alpha(s,t_{pq}) & 0 & 0 \\ \beta(s,t_{pq}) & 0 & 0 \end{pmatrix} \cdot \begin{pmatrix} \mathbf{T} \\ \mathbf{e}_1 \\ \mathbf{e}_2 \end{pmatrix}, \tag{3.7}$$

where $\alpha(s,t_{pq}) + i\beta(s,t_{pq}) = \Psi(s,t_{pq})$, and $\Psi(s,t_{pq})$ is the l-periodic function defined over the period $s \in [0,l)$ as

$$\Psi(s,t_{pq}) = \begin{cases} \dfrac{l_q}{\sqrt{q}} \displaystyle\sum_{m=0}^{q-1} G(-p,m,q)\delta(s - \tfrac{lm}{q}), & \text{if } q \text{ odd}, \\ \dfrac{l_q}{\sqrt{2q}} \displaystyle\sum_{m=0}^{q-1} G(-p,m,q)\delta(s - \tfrac{lm}{q}), & \text{if } q \text{ even}, \end{cases} \tag{3.8}$$

with

$$G(a,b,c) = \sum_{l=0}^{c-1} e^{2\pi i(al^2+bl)/c}, \ a,b \in \mathbb{Z}, c \in \mathbb{Z}\backslash\{0\},$$

being a generalized quadratic Gauß sum.

We will see later that the time-like angle

$$l_q = \begin{cases} 2\,\mathrm{arccosh}(\cosh^{1/q}(l/2)), & \text{if } q \text{ odd}, \\ 2\,\mathrm{arccosh}(\cosh^{2/q}(l/2)), & \text{if } q \text{ even}, \end{cases} \tag{3.9}$$

can be obtained using the conservation law described for the polygonal lines in [8] and in Chapter 2.

3.2.1 Problem definition and formulation

We consider a regular planar polygonal curve with the time-like angle $l > 0$ between any two sides, a constant that is arbitrary. Thus, following the idea of the M-polygon problem in the Euclidean case, we look for a hyperbolic polygon with curvature

$$\kappa(s) = c_0 \sum_{k=-\infty}^{\infty} \delta(s - lk), \ \ s \in \mathbb{R}, \tag{3.10}$$

where s is the arc-length parameter, the argument of the equally spaced Dirac deltas

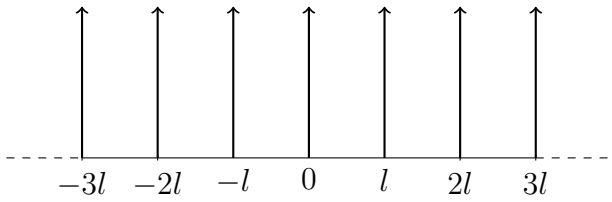

Figure 3.1 A Dirac comb: Dirac deltas equally spaced with an interval l.

corresponds to the location of the corners (Figure 3.1) and the coefficient $c_0 > 0$ is related to l through [21]

$$c_0 = \sqrt{\frac{2}{\pi} \ln\left(\cosh\left(\frac{l}{2}\right)\right)}. \tag{3.11}$$

The expression for $\kappa(s)$ is known as a Dirac comb which is a periodic tempered distribution. Note that in the absence of the torsion, from (3.3), $\psi(s, 0)$ is the curvature of the initial polygonal curve, i.e., $\psi(s, 0) = \kappa(s)$.

Since (3.1)–(3.2) are invariant under hyperbolic rotations[1], without loss of generality, we can assume that the initial planar polygonal curve $\mathbf{X}(s, 0)$ and its tangent vector

[1]We call the rotations in Minkowski 3-space hyperbolic rotations (see Appendix A.) [49]

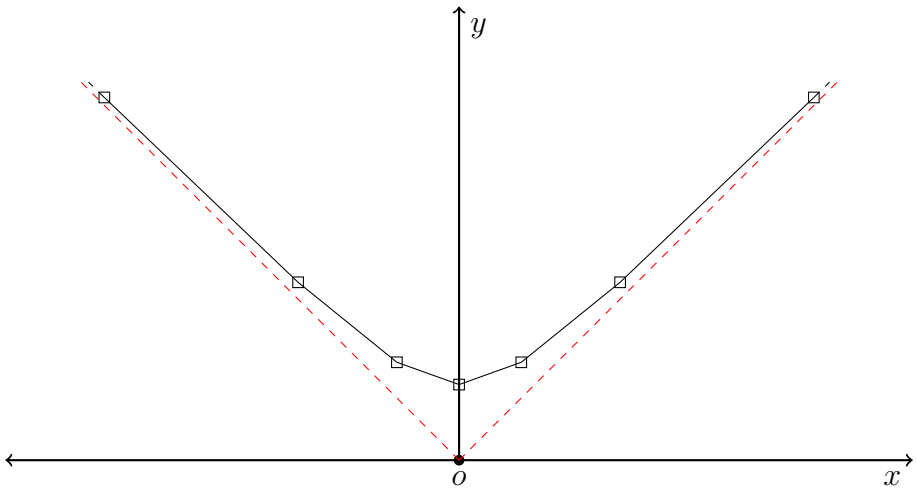

Figure 3.2 A planar l-polygon with $l = 0.75$, with vertices located at $s_n = nl$, $n \in \mathbb{Z}$ (marked with black square), and the asymptotes (in dotted red).

$\mathbf{T}(s,0)$ lie in the XY-plane. Thus, taking OXY as the hyperbolic plane [2], we consider the arc-length parameterized curve $\mathbf{X}(s,0)$ whose vertices are given by

$$\mathbf{X}(s_n,0) = \frac{j(l/2)e^{js_n}}{\sinh(l/2)} \equiv \frac{(l/2)}{\sinh(l/2)} \left(\sinh\left(s_n\right), \cosh\left(s_n\right), 0\right)^T; \tag{3.12}$$

we have used the notation $e^{j\theta} = \cosh(\theta) + j\sinh(\theta)$, with j being the hyperbolic number that satisfies $j^2 = +1$ and $s_n = nl$, $n \in \mathbb{Z}$ [17]. Furthermore, a point $\mathbf{X}(s,0)$, for $s_n < s < s_{n+1}$ lies in the segment that joins $\mathbf{X}(s_n,0)$ and $\mathbf{X}(s_{n+1},0)$ (see Figure 3.2). Since $\mathbf{X}(s_{n+1},0) - \mathbf{X}(s_n,0) = le^{j(s_n+l/2)}$, we obtain the tangent vector

$$\mathbf{T}(s,0) = e^{j(s_n+l/2)} \equiv \left(\cosh\left(l/2+s_n\right), \sinh\left(l/2+s_n\right), 0\right)^T, \tag{3.13}$$

for $s_n < s < s_{n+1}$, which is piecewise constant on the interval (s_n, s_{n+1}). Let us also mention that both $\mathbf{X}(s,0)$ and $\mathbf{T}(s,0)$ are invariant under the hyperbolic rotation

$$\mathbf{H} = \begin{pmatrix} \cosh(l) & \sinh(l) \\ \sinh(l) & \cosh(l) \end{pmatrix}.$$

A simple computation shows that

$$\mathbf{H}^n = \begin{pmatrix} \cosh(nl) & \sinh(nl) \\ \sinh(nl) & \cosh(nl) \end{pmatrix},$$

[2] See Appendix A

which implies that as $|n|$ grows larger, $|\cosh(nl)| \approx |\sinh(nl)| \gg 1$, as a result, the endpoints of the planar l-polygon will converge to the asymptotes of the hyperbola. Since the regular polygonal curve is characterized by only one parameter, i.e., l, we call it as a planar l-polygon. In a recent work, this object has been named as an *elementary t-convex polygon*, characterized by a parameter t [31].

Note that in the Euclidean case, the M-sided polygon can be seen as an approximation of a circle to which it converges as M tends to infinity, whereas in the hyperbolic case, the planar l-polygon converges to a hyperbola as l tends to zero, which is open (see Figure 3.2). Moreover, since one of the main aims of this work is to compute the numerical evolution of these curves, we will consider a finite polygonal curve, which would imply a restriction on the number of sides or vertices. Thus, for an M-sided hyperbolic polygon of length $L = lM$, the vertices are located at

$$\mathbf{X}(s_n, 0) = \frac{j(l/2)e^{js_n}}{\sinh(l/2)} \equiv \frac{(l/2)}{\sinh(l/2)} \left(\sinh(s_n), \cosh(s_n) - \frac{\sinh(L/2)}{M \tanh(l/2)}, 0 \right)^T, \quad (3.14)$$

and the tangent vectors $\mathbf{T}(s, 0)$ are as in (3.13) with $s_n = -L/2 + nl$, $n = 0, 1, 2, \ldots, M$. In the above expression we have taken M even, a similar expression can be obtained for M odd as well. Finally, note that the construction of (3.12) and (3.14) is such that the vertex corresponding to $\mathbf{X}(0, 0)$ lies on the y-axis.

Spatial symmetries of X and T

The invariance of (3.1)–(3.2) under the hyperbolic rotations follows from that of Minkowski cross product under the same. So for a given hyperbolic rotation matrix $\mathbf{R}$ such that $\mathbf{R} \cdot \mathbf{T}(s, 0) = \mathbf{T}(s, 0)$ and $\mathbf{R} \cdot \mathbf{X}(s, 0) = \mathbf{X}(s, 0)$, if the solution is unique, then $\mathbf{R} \cdot \mathbf{X}(s, t) = \mathbf{X}(s, t)$, $\mathbf{R} \cdot \mathbf{T}(s, t) = \mathbf{T}(s, t)$ for all t. In particular, as already mentioned in the previous section, $\mathbf{X}(s, 0)$, $\mathbf{T}(s, 0)$ given by (3.12), (3.13), respectively, are invariant under a rotation of a time-like angle nl about a space-like z-axis for all $n \in \mathbb{Z}$, it can be concluded that $\mathbf{X}(s, t)$ and $\mathbf{T}(s, t)$ are invariant under the same rotations, for all t. In other words, by writing $\mathbf{X} \equiv (X_1, X_2, X_3)^T$, $\mathbf{T} \equiv (T_1, T_2, T_3)^T$, and expressing the rotation in the hyperbolic plane using the hyperbolic number j, we

write for all $n \in \mathbb{N}$ [17],

$$\begin{aligned} X_1(s+nl,t) + jX_2(s+nl,t) &= e^{jnl}(X_1(s,t) + jX_2(s,t)), \\ X_3(s+nl,t) &= X_3(s,t), \\ T_1(s+nl,t) + jT_2(s+nl,t) &= e^{jnl}(T_1(s,t) + jT_2(s,t)), \\ T_3(s+nl,t) &= T_3(s,t). \end{aligned} \tag{3.15}$$

One of the important consequences of these symmetries is that for any time t, for all n, the curve $\mathbf{X}(s+nl,t)$ always lie in the same plane orthogonal to the z-axis.

As in the Euclidean case, (3.1)–(3.2) are mirror invariant, i.e., if $\mathbf{X}(s,t)$ satisfies (3.1), so does $\tilde{\mathbf{X}}(s,t) = (-X_1(-s,t), X_2(-s,t), X_3(-s,t))^T$ and if $\mathbf{X}(s,0) = \tilde{\mathbf{X}}(s,0)$, then $\mathbf{X}(s,t) = \tilde{\mathbf{X}}(s,t)$, for all $t > 0$. Similarly, if $\mathbf{T}(s,t)$ is a solution of (3.2), so is $\tilde{\mathbf{T}}(s,t) = (T_1(-s,t), -T_2(-s,t), -T_3(-s,t))^T$. As a result, $\mathbf{X}(s,t) - \mathbf{X}(-s,t)$ is a positive multiple of $(1,0,0)^T$. This property plays an important role in constructing the algebraic solutions, as we will see later.

Problem formulation

Observe that, by its definition, $\psi(s,0)$ is l-periodic and since NLS equation is invariant with respect to space translations, $\psi(s,t)$ is also l-periodic for all $t \in \mathbb{R}$. On the other hand, $\psi(s,0) = e^{irks}\psi(s,0)$, where $r = 2\pi/l$, $l > 0$, thus, from Galilean invariance $\psi(s,t) = e^{irks - i(rk)^2 t}\psi(s - 2rkt, t)$. Since ψ is periodic, its Fourier coefficients can be computed as

$$\begin{aligned} \hat{\psi}(j,t) &= \frac{1}{l}\int_0^l e^{-2\pi isj/l}\psi(s,t)ds = \frac{1}{l}\int_0^l e^{-irjs}[e^{irks - i(rk)^2 t}\psi(s - 2rkt, t)]ds \\ &= \frac{1}{l}e^{-i(rk)^2 t}\int_0^l e^{-irs(j-k)}\psi(s - 2rkt, t)ds = \frac{1}{l}e^{-i(rk)^2 t}\int e^{-ir(j-k)(y+2rkt)}\psi(y,t)dy \\ &= e^{-i(rk)^2 t - ir(j-k)2rkt}\hat{\psi}(j-k,t), \end{aligned}$$

which holds true for all j, k. By taking $j = k$, we obtain

$$\hat{\psi}(k,t) = e^{-i(rk)^2 t}\hat{\psi}(0,t),$$

as a result, ψ can be expressed as

$$\psi(s,t) = \hat{\psi}(0,t)\sum_{k=-\infty}^{\infty} e^{i(rk)^2 t + i(rk)s}, \tag{3.16}$$

where $\hat{\psi}(0,t)$ is a constant depending on time t and due to the Gauge invariance can be taken real. In this work, without loss of generality, we take it to be real and its value is computed explicitly by using a conservation law to be described later. However, $t=0$ in (3.16) gives

$$\psi(s,0)=\hat{\psi}(0,0)\sum_{k=-\infty}^{\infty}e^{i(rk)s}=\hat{\psi}(0,0)\sum_{k=-\infty}^{\infty}e^{2\pi iks/l}=c_0\sum_{k=-\infty}^{\infty}\delta(s-lk).$$

Using a well-known identity on Dirac comb

$$\frac{1}{F}\sum_{k=-\infty}^{\infty}e^{\pm 2\pi iks/F}=\sum_{n=-\infty}^{\infty}\delta(s-nF), \tag{3.17}$$

and the last expression for $\psi(s,0)$, we obtain $\hat{\psi}(0,0)=c_0/l$. On the other hand, if $\hat{\psi}(0,t)=1$, we get

$$\psi(s,t)=\sum_{k=-\infty}^{\infty}e^{-i(2\pi k/l)^2t+i(2\pi k/l)s}=\theta\left(\frac{s}{l},\frac{4\pi}{l^2}t\right),$$

where $\theta(s,t)$ is the well-known Jacobi theta function, the solution of the free Schrödinger equation for the initial condition given by $\psi(s,0)$ with $c_0=1$. Observe that

$$\begin{aligned}\psi(s,t+(2\pi/r^2))&=\hat{\psi}(0,t)\sum_{k=-\infty}^{\infty}e^{-i(rk)^2(t+\frac{2\pi}{r^2})+i(rk)s}\\&=\hat{\psi}(0,t)\sum_{k=-\infty}^{\infty}e^{-i(rk)^2t}e^{2\pi ik^2}e^{i(rk)s}=\psi(s,t),\end{aligned}$$

implies that $\psi(s,t)$ periodic in time with a period $2\pi/r^2$ or $l^2/2\pi$ which we denote by T_f in this chapter.

3.2.2 The evolution at rational multiples of time $t=T_f$

We evaluate (3.16) at $t=t_{pq}=\frac{2\pi}{r^2}\frac{p}{q}$, $p\in\mathbb{Z}, q\in\mathbb{N}$, $\gcd(p,q)=1$ as

$$\begin{aligned}\psi(s,t_{pq})&=\hat{\psi}(0,t_{pq})\sum_{k=-\infty}^{\infty}e^{-(2\pi i(rk)^2/r^2)(\frac{p}{q})+i(rk)s}\\&=\hat{\psi}(0,t_{pq})\sum_{k=-\infty}^{\infty}e^{-2\pi ik^2(\frac{p}{q})+i(rk)s}=\hat{\psi}(0,t_{pq})\sum_{w=0}^{q-1}\sum_{k=-\infty}^{\infty}e^{-2\pi i(\frac{p}{q})w^2+irws}e^{iqrks}\end{aligned}$$

$$
\begin{aligned}
&= \hat{\psi}(0,t_{pq}) \sum_{w=0}^{q-1} e^{-2\pi i(\frac{p}{q})w^2+irws} \sum_{k=-\infty}^{\infty} e^{2\pi iqks/l} \\
&= \frac{l}{q}\hat{\psi}(0,t_{pq}) \sum_{w=0}^{q-1} e^{-2\pi i(\frac{p}{q})w^2+irws} \sum_{k=-\infty}^{\infty} \delta\left(s-\tfrac{l}{q}k\right) \\
&= \frac{l}{q}\hat{\psi}(0,t_{pq}) \sum_{w=0}^{q-1} e^{-2\pi i(\frac{p}{q})w^2+irw(kl/q)} \sum_{k=-\infty}^{\infty} \delta\left(s-\tfrac{l}{q}k\right) \\
&= \frac{l}{q}\hat{\psi}(0,t_{pq}) \sum_{w=0}^{q-1}\sum_{m=0}^{q-1} e^{-2\pi i(\frac{p}{q})w^2+irwl((qk+m)/q)} \sum_{k=-\infty}^{\infty} \delta\left(s-\tfrac{l}{q}(qk+m)\right) \\
&= \frac{l}{q}\hat{\psi}(0,t_{pq}) \sum_{k=-\infty}^{\infty}\sum_{m=0}^{q-1} \left(\sum_{w=0}^{q-1} e^{-2\pi i(\frac{p}{q})w^2+2\pi iwm/q}\right)\delta\left(s-lk-\tfrac{lm}{q}\right),
\end{aligned}
$$

i.e.,

$$
\psi(s,t_{pq}) = \frac{l}{q}\hat{\psi}(0,t_{pq}) \sum_{k=-\infty}^{\infty}\sum_{m=0}^{q-1} G(-p,m,q)\delta\left(s-lk-\tfrac{lm}{q}\right), \tag{3.18}
$$

where $G(a,b,c)=\sum_{l=0}^{c-1} e^{2\pi i(al^2+bl)/c}$, $a,b,\in\mathbb{Z}$, $c\in\mathbb{Z}\setminus\{0\}$, is a generalised quadratic Gauß sum. Moreover, by using the properties of the Gauß sum, we can write $G(-p,m,q)$ as:

$$
G(-p,m,q) = \begin{cases} \sqrt{q}e^{i\theta_m}, & \text{if } q \text{ odd }, \\ \sqrt{2q}e^{i\theta_m}, & \text{if } q \text{ even} \wedge q/2 \equiv m \bmod 2, \\ 0, & \text{if } q \text{ even} \wedge q/2 \not\equiv m \bmod 2, \end{cases}
$$

for a certain angle θ_m that depends on m (and also p, q). With this, if we consider $k=0$, i.e., $s\in[0,l)$, then,

$$
\psi(s,t_{pq}) = \begin{cases} \dfrac{l}{\sqrt{q}}\hat{\psi}(0,t_{pq}) \displaystyle\sum_{m=0}^{q-1} e^{i\theta_m}\delta\left(s-\tfrac{ml}{q}\right), & \text{if } q \text{ odd}, \\ \dfrac{l}{\sqrt{q/2}}\hat{\psi}(0,t_{pq}) \displaystyle\sum_{m=0}^{q/2-1} e^{i\theta_{2m+1}}\delta\left(s-\tfrac{(2m+1)l}{q}\right), & \text{if } q/2 \text{ odd}, \\ \dfrac{l}{\sqrt{q/2}}\hat{\psi}(0,t_{pq}) \displaystyle\sum_{m=0}^{q/2-1} e^{i\theta_{2m}}\delta\left(s-\tfrac{2ml}{q}\right), & \text{if } q/2 \text{ even}, \end{cases} \tag{3.19}
$$

which implies that at any rational time t_{pq}, a single side of the planar l-polygon at $t=0$, will evolve into q sides if q is odd, and $q/2$ sides if q is even. As it holds true for any $k\in\mathbb{Z}$, the resulting polygon will have q or $q/2$ times more sides than the initial l-polygon. The new Dirac deltas thus formed, are equally spaced, as a result, all the sides of the new polygon are of equal length. Furthermore, the coefficients of Dirac

deltas have equal modulus and are given by

$$c_q = \begin{cases} \frac{l}{\sqrt{q}}\hat{\psi}(0,t_{pq}), & \text{if } q \text{ is odd,} \\ \frac{l}{\sqrt{q/2}}\hat{\psi}(0,t_{pq}), & \text{if } q \text{ is even.} \end{cases} \tag{3.20}$$

In case of a finite length planar l-polygon initially with M sides, given any rational time t_{pq}, from (3.19), it will evolve into Mq-sided polygon for q odd, and $Mq/2$-sided polygon for q even. The angle between any two of its sides will depend on $\hat{\psi}(0,t_{pq})$ which will be determined in the next section.

It is important to mention that except for $t = 0$, $t_{1,2}$ and $t_{1,1}$, the coefficients multiplying the Dirac deltas are not real, as a result, the corresponding polygon is not planar, this fact will later be verified in the numerical results. Remark that, at rational times t_{pq} with $q \equiv 2 \bmod 4$, there is no corner at $s = 0$, for example, when $p = 1$, $q = 2$, the polygonal curve is planar and has the same number of sides as the initial polygon, but rotated by a time-like angle $l/2$ about the z-axis.

Computation of $\hat{\psi}(0,t_{pq})$

Recall that in Chapter 2, we computed $\hat{\psi}(0,t_{pq})$ by using a conservation law established in [8]. Following the discussion in Section 2.2.2, we note that the conservation law holds true in both Euclidean (focusing NLS) and hyperbolic (defocusing NLS) cases. Thus, for $N \in \mathbb{N}$, if the initial data satisfies $\alpha_{k+N}(0) = \alpha_k(0)$ for all k, and the solution is unique, then, it can be concluded that $\tilde{\alpha}_{k+N}(t) = \tilde{\alpha}_k(t)$ for all k and t.

In the regular planar l-polygon case, $\alpha_k(0) = \alpha_{k+1}(0) = c_0$, and at any rational time t_{pq} (taking q odd for now), from (3.19), there are q times more Dirac deltas with coefficients of equal modulus, i.e., c_q. Then, the conservation law becomes

$$c_0^2 = |\alpha_k(0)|^2 = \sum_{k=0}^{q-1} |\alpha_k(t_{pq})|^2 = qc_q^2,$$

as a result, $c_q = c_0/\sqrt{q}$ and

$$\hat{\psi}(0,t_{pq}) = c_0/l = \hat{\psi}(0,0). \tag{3.21}$$

Note that (3.11) holds true whenever there is a singularity formation, for instance, in our case, at rational times t_{pq}. Thus, denoting the time-like angle between any two

tangent vectors by l_q, we have

$$\cosh\left(\frac{l_q}{2}\right) = e^{\pi c_q^2/2} \iff c_q = \sqrt{\frac{2}{\pi}\ln\left(\cosh\left(\frac{l_q}{2}\right)\right)},$$

and since for a given rational time, c_q is the same for all k, the angle l_q is constant for all sides. Furthermore,

$$c_q = \frac{c_0}{\sqrt{q}} \implies \sqrt{\frac{2}{\pi}\ln\left(\cosh\left(\frac{l_q}{2}\right)\right)} = \frac{1}{\sqrt{q}}\sqrt{\frac{2}{\pi}\ln\left(\cosh\left(\frac{l}{2}\right)\right)},$$

i.e.,

$$\cosh\left(\frac{l}{2}\right) = \cosh^q\left(\frac{l_q}{2}\right).$$

After proceeding in the same way for q even, we conclude that

$$l_q = \begin{cases} 2\,\mathrm{arccosh}(\cosh^{1/q}(l/2)), & \text{if } q \text{ odd}, \\ 2\,\mathrm{arccosh}(\cosh^{2/q}(l/2)), & \text{if } q \text{ even}. \end{cases} \tag{3.22}$$

3.2.3 Algebraic solution

In this section, we compute the tangent vector $\mathbf{T}$ and the curve $\mathbf{X}$ algebraically. We follow an approach similar to the one used in [22], and construct the algebraic solution up to a rigid movement which is later determined using the symmetries of the regular planar l-polygon. In principle, we integrate (3.7) with

$$\Psi(s, t_{pq}) = \frac{l_q}{c_q}\psi(s, t_{pq}) = \alpha(s, t_{pq}) + i\beta(s, t_{pq}), \tag{3.23}$$

for q odd, and similarly, for q even, where $\psi(s, t_{pq})$ is as in (3.19). The transformation allows us to integrate the Frenet frame in a way that the coefficients appearing in the semi-skew symmetric matrix[3] are the curvature angle and the torsion angle. In this way, the integration yields the corresponding rotation matrices which describe the geometry of the polygonal curve, as we see in the following lines.

We consider a planar l-polygon with M sides, where without loss of generality, we can take M to be even. The idea is to compute the basis vectors $\mathbf{T}$, $\mathbf{e}_1$, $\mathbf{e}_2$ at any time

[3] See Appendix A for its definition and properties

$t = t_{pq}$ from $\Psi(s, t_{pq}) = (\alpha + i\beta)(s, t_{pq})$. Recall that from (3.19) and (3.23), at any rational time $\Psi(s, t_{pq})$ is a sum of Mq or $Mq/2$ equally spaced deltas in $s \in [-L/2, L/2]$, which implies that the new polygonal curve will have Mq or $Mq/2$ tangent vectors. In order to integrate the frame, we try to understand the transition from one side to the next one, i.e., across one corner, so we consider a Dirac delta located at $s = \tilde{s}$, i.e., $\Psi(\tilde{s}) = (c + id)\delta(\tilde{s})$, so we need to integrate

$$\begin{pmatrix} \mathbf{T} \\ \mathbf{e}_1 \\ \mathbf{e}_2 \end{pmatrix}_s = \begin{pmatrix} 0 & c\delta(s) & d\delta(s) \\ c\delta(s) & 0 & 0 \\ d\delta(s) & 0 & 0 \end{pmatrix} \cdot \begin{pmatrix} \mathbf{T} \\ \mathbf{e}_1 \\ \mathbf{e}_2 \end{pmatrix} = \delta(s)\mathbf{B} \cdot \begin{pmatrix} \mathbf{T} \\ \mathbf{e}_1 \\ \mathbf{e}_2 \end{pmatrix}, \tag{3.24}$$

where

$$\mathbf{B} = \begin{pmatrix} 0 & c & d \\ c & 0 & 0 \\ d & 0 & 0 \end{pmatrix},$$

is a semi-skew symmetric matrix. This system corresponds to $\mathbf{T}(s)$, $\mathbf{e}_1(s)$ and $\mathbf{e}_2(s)$ constant everywhere, except at $s = \tilde{s}$ where there is a vertex. Let us assume that for $s < \tilde{s}$, $\mathbf{T}(s) \equiv \mathbf{T}(\tilde{s}^-)$, $\mathbf{e}_1(s) \equiv \mathbf{e}_1(\tilde{s}^-)$, $\mathbf{e}_2(s) \equiv \mathbf{e}_2(\tilde{s}^-)$ are given, then the goal is to calculate $\mathbf{T}(\tilde{s}^+)$, $\mathbf{e}_1(\tilde{s}^+)$, $\mathbf{e_2}(\tilde{s}^+)$ which correspond to the orthonormal system for $s > \tilde{s}$, $\mathbf{T}(s) \equiv \mathbf{T}(\tilde{s}^+)$, $\mathbf{e}_1(s) \equiv \mathbf{e}_1(\tilde{s}^+)$, $\mathbf{e}_2(s) \equiv \mathbf{e}_2(\tilde{s}^+)$. Then,

$$\begin{pmatrix} \mathbf{T}(\tilde{s}^+)^T \\ \mathbf{e}_1(\tilde{s}^+)^T \\ \mathbf{e}_2(\tilde{s}^+)^T \end{pmatrix} = \exp\left(\mathbf{B}\int_{\tilde{s}^-}^{\tilde{s}^+} \delta(s')ds'\right) \cdot \begin{pmatrix} \mathbf{T}(\tilde{s}^-)^T \\ \mathbf{e}_1(\tilde{s}^-)^T \\ \mathbf{e}_2(\tilde{s}^-)^T \end{pmatrix} = \exp(\mathbf{B}) \cdot \begin{pmatrix} \mathbf{T}(\tilde{s}^-)^T \\ \mathbf{e}_1(\tilde{s}^-)^T \\ \mathbf{e}_2(\tilde{s}^-)^T \end{pmatrix}.$$

By expressing $c + id = le^{i\theta}$, we write the matrix exponential[4], $\exp(\mathbf{B})$

$$= \begin{pmatrix} \cosh(l) & \cos(\theta)\sinh(l) & \sin(\theta)\sinh(l) \\ \cos(\theta)\sinh(l) & 1 + \cos^2(\theta)(\cosh(l) - 1) & \sin(\theta)\cos(\theta)(\cosh(l) - 1) \\ \sin(\theta)\sinh(l) & \sin(\theta)\cos(\theta)(\cosh(l) - 1) & 1 + \cos^2(\theta)(\cosh(l) - 1) \end{pmatrix}, \tag{3.25}$$

which is a hyperbolic rotation matrix performing a rotation of a time-like angle l about a space-like axis $(0, -\sin(\theta), \cos(\theta))^T$.

Consequently, if $\mathbf{T}(\tilde{s}^-)$, $\mathbf{e}_1(\tilde{s}^-)$, $\mathbf{e}_2(\tilde{s}^-)$ form an orthonormal basis in $\mathbb{R}^{1,2}$, then so does $\mathbf{T}(\tilde{s}^+)$, $\mathbf{e}_1(\tilde{s}^+)$, $\mathbf{e}_2(\tilde{s}^+)$. In order to obtain the skew polygon with Mq or $Mq/2$ sides, we need to integrate the system (3.24) Mq or $Mq/2$ times. By taking $\tilde{s} = 0$ and

[4]See Appendix A for its definition and properties

expressing $\Psi(s,t_{pq})=\alpha_k+i\beta_k$ from (3.19) for $s\in[0,l)$,

$$\Psi(s,t_{pq})=\begin{cases}\displaystyle\sum_{m=0}^{q-1}(\alpha_m+i\beta_m)\delta\left(s-\frac{ml}{q}\right), & \text{if } q \text{ odd},\\ \displaystyle\sum_{m=0}^{q/2-1}(\alpha_{2m+1}+i\beta_{2m+1})\delta\left(s-\frac{(2m+1)l}{q}\right), & \text{if } q/2 \text{ odd},\\ \displaystyle\sum_{m=0}^{q/2-1}(\alpha_{2m}+i\beta_{2m})\delta\left(s-\frac{2ml}{q}\right), & \text{if } q/2 \text{ even},\end{cases} \tag{3.26}$$

with

$$\alpha_m+i\beta_m=\begin{cases}l_qe^{i\theta_m}, & \text{if } q \text{ odd},\\ l_qe^{i\theta_m}, & \text{if } q \text{ even}\wedge q/2\equiv m \bmod 2,\\ 0, & \text{if } q \text{ even}\wedge q/2\not\equiv m \bmod 2,\end{cases} \tag{3.27}$$

where l_q is as in (3.22), and thus, the structure of the polygon can be determined at any rational time. As a result, from (3.18), (3.21) and (3.23), we conclude that $\Psi(s,t_{pq})$, $s\in[0,l)$ is given by (3.8) which finishes the proof of Theorem 5.

Furthermore, let us denote (3.25) as $\mathbf{H}_m$ corresponding to $(\alpha_m+i\beta_m)\delta$, i.e., $\mathbf{H}_m$

$$=\begin{pmatrix}\cosh(l_q) & \cos(\theta_m)\sinh(l_q) & \sin(\theta_m)\sinh(l_q)\\ \cos(\theta_m)\sinh(l_q) & 1+\cos^2(\theta_m)(\cosh(l_q)-1) & \sin(\theta_m)\cos(\theta_m)(\cosh(l_q)-1)\\ \sin(\theta_m)\sinh(l_q) & \sin(\theta_m)\cos(\theta_m)(\cosh(l_q)-1) & 1+\sin^2(\theta_m)(\cosh(l_q)-1)\end{pmatrix}, \tag{3.28}$$

and note that, if $(\alpha_m+i\beta_m)=0$, then $\mathbf{H}_m$ is an identity matrix.

If q is odd, then $\mathbf{T}$, $\mathbf{e}_1$, $\mathbf{e}_2$ are piecewise constant in the intervals formed by the discretization $s_j=-(L/2)+j(L/Mq)$, $j=0,1,\dots,Mq$, which in this case, will also correspond to the location of the vertices, and we write

$$\begin{pmatrix}\mathbf{T}(s_1^-)^T\\ \mathbf{e}_1(s_1^-)^T\\ \mathbf{e}_2(s_1^-)^T\end{pmatrix}=\begin{pmatrix}\mathbf{T}(s_0^+)^T\\ \mathbf{e}_1(s_0^+)^T\\ \mathbf{e}_2(s_0^+)^T\end{pmatrix}=\mathbf{H}_0\cdot\begin{pmatrix}\mathbf{T}(s_0^-)^T\\ \mathbf{e}_1(s_0^-)^T\\ \mathbf{e}_2(s_0^-)^T\end{pmatrix},$$

$$\begin{pmatrix}\mathbf{T}(s_2^-)^T\\ \mathbf{e}_1(s_2^-)^T\\ \mathbf{e}_2(s_2^-)^T\end{pmatrix}=\begin{pmatrix}\mathbf{T}(s_1^+)^T\\ \mathbf{e}_1(s_1^+)^T\\ \mathbf{e}_2(s_1^+)^T\end{pmatrix}=\mathbf{H}_1\begin{pmatrix}\mathbf{T}(s_1^-)^T\\ \mathbf{e}_1(s_1^-)^T\\ \mathbf{e}_2(s_1^-)^T\end{pmatrix}=\mathbf{H}_1\mathbf{H}_0\cdot\begin{pmatrix}\mathbf{T}(s_0^-)^T\\ \mathbf{e}_1(s_0^-)^T\\ \mathbf{e}_2(s_0^-)^T\end{pmatrix},$$

$$\begin{pmatrix}\mathbf{T}(s_3^-)^T\\ \mathbf{e}_1(s_3^-)^T\\ \mathbf{e}_2(s_3^-)^T\end{pmatrix}=\begin{pmatrix}\mathbf{T}(s_2^+)^T\\ \mathbf{e}_1(s_2^+)^T\\ \mathbf{e}_2(s_2^+)^T\end{pmatrix}=\mathbf{H}_2\begin{pmatrix}\mathbf{T}(s_2^-)^T\\ \mathbf{e}_1(s_2^-)^T\\ \mathbf{e}_2(s_2^-)^T\end{pmatrix}=\mathbf{H}_2\mathbf{H}_1\mathbf{H}_0\cdot\begin{pmatrix}\mathbf{T}(s_0^-)^T\\ \mathbf{e}_1(s_0^-)^T\\ \mathbf{e}_2(s_0^-)^T\end{pmatrix},$$

and so on. Hence,

$$\begin{pmatrix} \mathbf{T}(s_{k+1}^-)^T \\ \mathbf{e}_1(s_{k+1}^-)^T \\ \mathbf{e}_2(s_{k+1}^-)^T \end{pmatrix} = \begin{pmatrix} \mathbf{T}(s_k^+)^T \\ \mathbf{e}_1(s_k^+)^T \\ \mathbf{e}_2(s_k^+)^T \end{pmatrix} = \mathbf{H}_k \begin{pmatrix} \mathbf{T}(s_k^-)^T \\ \mathbf{e}_1(s_k^-)^T \\ \mathbf{e}_2(s_k^-)^T \end{pmatrix}$$
$$= \mathbf{H}_k\mathbf{H}_{k-1}\dots\mathbf{H}_1\mathbf{H}_0 \cdot \begin{pmatrix} \mathbf{T}(s_0^-)^T \\ \mathbf{e}_1(s_0^-)^T \\ \mathbf{e}_2(s_0^-)^T \end{pmatrix}, \tag{3.29}$$

where $k = 0, 1, \dots, Mq-1$. Moreover, $\mathbf{H}_k$ is periodic modulo q, i.e., $\mathbf{H}_{k+q} \equiv \mathbf{H}_k$. The above expression holds true when $q/2$ is even as well, with the only difference that $\mathbf{H}_k$ with odd indices will be identity matrices. As a result,

$$\begin{pmatrix} \mathbf{T}(s_{2k}^+)^T \\ \mathbf{e}_1(s_{2k}^+)^T \\ \mathbf{e}_2(s_{2k}^+)^T \end{pmatrix} = \mathbf{H}_{2k}\mathbf{H}_{2k-2}\dots\mathbf{H}_2\mathbf{H}_0 \cdot \begin{pmatrix} \mathbf{T}(s_0^-)^T \\ \mathbf{e}_1(s_0^-)^T \\ \mathbf{e}_2(s_0^-)^T \end{pmatrix},$$

and

$$\begin{pmatrix} \mathbf{T}(s_{2k}^+)^T \\ \mathbf{e}_1(s_{2k}^+)^T \\ \mathbf{e}_2(s_{2k}^+)^T \end{pmatrix} \equiv \begin{pmatrix} \mathbf{T}(s_{2k+1}^+)^T \\ \mathbf{e}_1(s_{2k+1}^+)^T \\ \mathbf{e}_2(s_{2k+1}^+)^T \end{pmatrix} \equiv \begin{pmatrix} \mathbf{T}(s_{2k+1}^-)^T \\ \mathbf{e}_1(s_{2k+1}^-)^T \\ \mathbf{e}_2(s_{2k+1}^-)^T \end{pmatrix}, \tag{3.30}$$

for $k = 0, 1, \dots, Mq/2-1$. Similarly, for $q/2$ odd, $\mathbf{H}_k$ with even indices will be identity matrices, which would imply

$$\begin{pmatrix} \mathbf{T}(s_{2k+1}^+)^T \\ \mathbf{e}_1(s_{2k+1}^+)^T \\ \mathbf{e}_2(s_{2k+1}^+)^T \end{pmatrix} = \mathbf{H}_{2k+1}\mathbf{H}_{2k-1}\dots\mathbf{H}_3\mathbf{H}_1 \cdot \begin{pmatrix} \mathbf{T}(s_1^-)^T \\ \mathbf{e}_1(s_1^-)^T \\ \mathbf{e}_2(s_1^-)^T \end{pmatrix},$$

and

$$\begin{pmatrix} \mathbf{T}(s_{2k-1}^+)^T \\ \mathbf{e}_1(s_{2k-1}^+)^T \\ \mathbf{e}_2(s_{2k-1}^+)^T \end{pmatrix} \equiv \begin{pmatrix} \mathbf{T}(s_{2k}^+)^T \\ \mathbf{e}_1(s_{2k}^+)^T \\ \mathbf{e}_2(s_{2k}^+)^T \end{pmatrix} \equiv \begin{pmatrix} \mathbf{T}(s_{2k}^-)^T \\ \mathbf{e}_1(s_{2k}^-)^T \\ \mathbf{e}_2(s_{2k}^-)^T \end{pmatrix}, \tag{3.31}$$

for $k = 0, 1, \dots, Mq/2-1$. It is important to mention that when q is even, the mutual angle l_q for half of the Mq sides is equal to zero which results into a polygon with $Mq/2$ sides, this is clear from (3.30)–(3.31). Furthermore, at any rational time t_{pq}, the

following holds true

$$\begin{pmatrix} \mathbf{T}(\frac{L}{2}^-)^T \\ \mathbf{e}_1(\frac{L}{2}^-)^T \\ \mathbf{e}_2(\frac{L}{2}^-)^T \end{pmatrix} = \mathbf{H}_{Mq-1} \cdot \mathbf{H}_{Mq-2} \cdot \ldots \cdot \mathbf{H}_1 \cdot \mathbf{H}_0 \begin{pmatrix} \mathbf{T}(-\frac{L}{2}^-)^T \\ \mathbf{e}_1(-\frac{L}{2}^-)^T \\ \mathbf{e}_2(-\frac{L}{2}^-)^T \end{pmatrix},$$

and since $\mathbf{H}_k$ is periodic modulo q, by defining

$$\mathbf{H} = \mathbf{H}_{q-1} \cdot \mathbf{H}_{q-2} \cdot \ldots \cdot \mathbf{H}_1 \cdot \mathbf{H}_0,$$

we can write

$$\begin{pmatrix} \mathbf{T}(\frac{L}{2}^-)^T \\ \mathbf{e}_1(\frac{L}{2}^-)^T \\ \mathbf{e}_2(\frac{L}{2}^-)^T \end{pmatrix} = \mathbf{H}^M \begin{pmatrix} \mathbf{T}(-\frac{L}{2}^-)^T \\ \mathbf{e}_1(-\frac{L}{2}^-)^T \\ \mathbf{e}_2(-\frac{L}{2}^-)^T \end{pmatrix}.$$

In summary, for any values of p, q, $\mathbf{T}$, $\mathbf{e}_1$ and $\mathbf{e}_2$ can be determined up to a rigid movement; this holds true for $\mathbf{X}$ as well which is obtained by integrating $\mathbf{T}$. Since we are dealing with a regular polygonal curve, the rigid movement can be computed by making use of its symmetries. Thus, given any rational time t_{pq}, we first compute the rotation matrix $\mathbf{H}_k$, then denoting the piecewise constant orthonormal basis vectors up to a rigid movement by $\tilde{\mathbf{T}}$, $\tilde{\mathbf{e}}_1$, $\tilde{\mathbf{e}}_2$, from (3.29) we have

$$\begin{pmatrix} \tilde{\mathbf{T}}(s_{k+1}^-)^T \\ \tilde{\mathbf{e}}_1(s_{k+1}^-)^T \\ \tilde{\mathbf{e}}_2(s_{k+1}^-)^T \end{pmatrix} = \begin{pmatrix} \tilde{\mathbf{T}}(s_k^+)^T \\ \tilde{\mathbf{e}}_1(s_k^+)^T \\ \tilde{\mathbf{e}}_2(s_k^+)^T \end{pmatrix} = \mathbf{H}_k \begin{pmatrix} \tilde{\mathbf{T}}(s_k^-)^T \\ \tilde{\mathbf{e}}_1(s_k^-)^T \\ \tilde{\mathbf{e}}_2(s_k^-)^T \end{pmatrix}.$$

Without loss of generality we can consider the case $k = 0$ to be an identity matrix:

$$\begin{pmatrix} \tilde{\mathbf{T}}(s_k^-)^T \\ \tilde{\mathbf{e}}_1(s_k^-)^T \\ \tilde{\mathbf{e}}_2(s_k^-)^T \end{pmatrix} = \begin{pmatrix} 1 & 0 & 0 \\ 0 & 1 & 0 \\ 0 & 0 & 1 \end{pmatrix},$$

and using (3.29), we obtain Mq tangent vectors. Moreover, $\tilde{\mathbf{X}}$, i.e., $\mathbf{X}$ up to a rigid movement, can be computed from $\tilde{\mathbf{T}}$ by

$$\tilde{\mathbf{X}}(s_{k+1}) = \tilde{\mathbf{X}}(s_k) + \frac{l}{q}\tilde{\mathbf{T}}(s_k^+), \tag{3.32}$$

for $k = 0, 1, \ldots, Mq-1$, and $\tilde{\mathbf{X}}(s_0)$ can be assigned any value, for example, $\tilde{\mathbf{X}}(s_0) = (0,0,0)^T$, and thus, we obtain the $Mq+1$ vertices of the hyperbolic polygon. Next, we determine the correct rotation by using the symmetries of the curve $\mathbf{X}$ as described in Section 3.2.1. In this regard, first, to align the polygon orthogonal to the z-axis, we use the fact that for any time t, $\mathbf{X}(-L/2+lk)$, for $k = 0, 1, \ldots, M$ lie in the XY-plane. The aligned curve is rotated about the z-axis in such a way that $\mathbf{X}(l) - \mathbf{X}(-l)$ is a positive multiple of $(1,0,0)^T$. One way the aforementioned procedure can be done efficiently is the following:

(i) Compute the unit time-like vectors $\mathbf{w}^+ = \frac{\tilde{\mathbf{X}}(l)-\tilde{\mathbf{X}}(0)}{\|\tilde{\mathbf{X}}(l)-\tilde{\mathbf{X}}(0)\|_0}$, $\mathbf{w}^- = \frac{\tilde{\mathbf{X}}(-l)-\tilde{\mathbf{X}}(0)}{\|\tilde{\mathbf{X}}(-l)-\tilde{\mathbf{X}}(0)\|_0}$.

(ii) Compute the unit space-like vector $\hat{\mathbf{u}} = \frac{\mathbf{w}^+ \wedge_- \mathbf{w}^-}{\|\mathbf{w}^+ \wedge_- \mathbf{w}^-\|_0}$.

(iii) If space-like vectors $\hat{\mathbf{u}}$ and $\hat{\mathbf{z}} = (0,0,1)^T$,

   (a) span a time-like vector subspace, i.e., $\hat{\mathbf{u}} \circ_- \hat{\mathbf{z}} > \|\hat{\mathbf{u}}\|_0 \|\hat{\mathbf{z}}\|_0$, then the time-like angle $\nu_1 = \operatorname{arccosh}\left(\frac{\hat{\mathbf{u}} \circ_- \hat{\mathbf{z}}}{\|\mathbf{u}\|_0 \|\mathbf{z}\|_0}\right)$, and $\hat{\mathbf{v}} = \hat{\mathbf{u}} \wedge_- \hat{\mathbf{z}}$ is a space-like vector,

   (b) span a space-like vector subspace, i.e., $\hat{\mathbf{u}} \circ_- \hat{\mathbf{z}} < \|\hat{\mathbf{u}}\|_0 \|\hat{\mathbf{z}}\|_0$, then the space-like angle $\nu_1 = \arccos\left(\frac{\hat{\mathbf{u}} \circ_- \hat{\mathbf{z}}}{\|\mathbf{u}\|_0 \|\mathbf{z}\|_0}\right)$, and $\hat{\mathbf{v}} = \hat{\mathbf{u}} \wedge_- \hat{\mathbf{z}}$ is a time-like vector,

   (c) span a light-like vector subspace, i.e., $\hat{\mathbf{u}} \circ_- \hat{\mathbf{z}} = \|\hat{\mathbf{u}}\|_0 \|\hat{\mathbf{z}}\|_0$, then $\nu_1 = 0$, and $\mathbf{L}_1$ is an identity matrix,

   then, $\mathbf{L}_1$ is a matrix performing a rotation of angle ν_1 about the axis $\hat{\mathbf{v}}/\|\hat{\mathbf{v}}\|_0$ [51].

(iv) Compute time-like vectors $\mathbf{w}^+_{rot} = \mathbf{L}_1 \cdot \mathbf{w}^+$, $\mathbf{w}^-_{rot} = \mathbf{L}_1 \cdot \mathbf{w}^-$, and $\mathbf{w} = \frac{\mathbf{w}^+_{rot} - \mathbf{w}^-_{rot}}{\|\mathbf{w}^+_{rot} - \mathbf{w}^-_{rot}\|_0}$. Then, $\nu_2 = \operatorname{arccosh}(\mathbf{w} \circ_- (1,0,0)^T)$ is the time-like angle, and $\mathbf{L}_2$ is the corresponding rotation about the axis given by $\frac{\mathbf{w} \wedge_- (1,0,0)}{\|\mathbf{w} \wedge_- (1,0,0)\|_0}$,

(v) Compute the desired rotation $\mathbf{L} = \mathbf{L}_2 \cdot \mathbf{L}_1$, and $\mathbf{T} = \mathbf{L} \cdot \tilde{\mathbf{T}}$, $\mathbf{X} = \mathbf{L} \cdot \tilde{\mathbf{X}}$.

Thus, we obtain $\mathbf{X}$, $\mathbf{T}$ in a correct orientation. Although, the computation of $\mathbf{T}$ is done, to determine $\mathbf{X}$ completely, we need to specify the movement of its center of mass which is computed in the next section.

3.3 Numerical solution

As mentioned previously, to compute the numerical evolution, we consider a planar l-polygon of length L that is now characterized by two parameters, i.e., l and M such that $L = l \cdot M$. For our purpose, we take M even, so that the initial curve $\mathbf{X}(s,0)$,

$s \in [-L/2, L/2]$, will have a vertex located at $s = 0$ and the symmetries described in Section 3.2.1. This also allows us to capture the time evolution of a single point, i.e., $\mathbf{X}(0, t)$. Note that as we truncate the l-polygon, the role of boundary conditions in the numerical scheme becomes very important. As with M we are approximating an infinite long polygon, naturally, more accurate results are obtained for a large value of L. However, for a fixed M, due to the exponential growth of the Euclidean norm of tangent vector $\mathbf{T}$, a large value of l causes the solution to blow up in a short time making the numerical scheme unstable. This was also observed in the one-corner problem where a large value of c_0 lead to similar effects [24]. On the other hand, a large value of M restricts us to consider small values of l.

Having said that, we solve (3.1)–(3.2) numerically for the initial data as in (3.13)–(3.14) for $s \in [-L/2, L/2]$. There have been several papers dedicated to the numerical treatment of (3.1)–(3.2) [15, 22, 24]. For instance, in the case of the Euclidean regular M-polygons, the coupled system is solved with a pseudo-spectral method in space and a fourth-order Runge–Kutta method in time [22, 25]. In the hyperbolic case, due to the lack of spatial periodicity in $\mathbf{X}$, $\mathbf{T}$, the same numerical treatment is not possible. In the following lines, we consider different numerical schemes and discuss the time evolution of l-polygon problem.

3.4 Finite difference discretization

We divide the interval $[-L/2, L/2]$ into $N + 1$ equally spaced nodes

$$s_j = -L/2 + jL/N, \ j = 0, 1, \ldots, N, \tag{3.33}$$

with a fixed step size $h = L/N$. For any well-defined function $u(s, \cdot)$, we let $u_j = u(s_j, \cdot)$, and consider the following fourth-order approximation of its first derivative

$$u_s(s_j, \cdot) = D^{+-}u_j + \mathcal{O}(h^4),$$

where $D^{+-}u_j =$

$$\frac{1}{12h}\times\begin{cases}-25u_j+48u_{j+1}-36u_{j+2}+16u_{j+3}-3u_{j+4}, & j=0,\\ -3u_{j-1}-10u_j+18u_{j+1}-6u_{j+2}+u_{j+3}, & j=1,\\ u_{j-2}-8u_{j-1}+8u_{j+1}-u_{j+2}, & j=2,\ldots,N-2,\\ -u_{j-3}+6u_{j-2}-18u_{j-1}+10u_j+3u_{j+1}, & j=N-1,\\ 3u_{j-4}-16u_{j-3}+36u_{j-2}-48u_{j-1}+25u_j, & j=N,\end{cases} \tag{3.34}$$

similarly,

$$u_{ss}(s_j,\cdot)=F^{+-}u_j+\mathcal{O}(h^4),$$

is the approximation for the second derivative, where $F^{+-}u_j =$

$$\frac{1}{12h^2}\times\begin{cases}45u_j-154u_{j+1}+214u_{j+2}-156u_{j+3}+61u_{j+4}-10u_{j+5}, & j=0,\\ 10u_{j-1}-15u_j-4u_{j+1}+14u_{j+2}-6u_{j+3}+u_{j+4}, & j=1,\\ -u_{j-2}+16u_{j-1}-30u_j+16u_{j+1}-u_{j+2}, & j=2,\ldots,N-2,\\ u_{j-4}-6u_{j-3}+14u_{j-2}-4u_{j-1}-15u_j+10u_{j+1}, & j=N-1,\\ -10u_{j-5}+61u_{j-4}-156u_{j-3}+214u_{j-2}-154u_{j-1}+45u_j, & j=N.\end{cases} \tag{3.35}$$

Note that in the above approximations, for the inner points we have used a fourth-order central difference scheme. To maintain the same order of accuracy over all the discretized domain, for the boundary and its neighboring points, we employ a fourth-order forward/backward difference scheme. Furthermore, (3.34)–(3.35) correspond to a system of simultaneous linear equations which can be expressed in a matrix form. Denoting $\mathbf{u}=\{u_0,u_1,\ldots,u_{N-1},u_N\}^T$, we write (3.34)–(3.35) as

$$\begin{cases}\mathbf{u}_s=\mathbf{D}\cdot\mathbf{u},\\ \mathbf{u}_{ss}=\mathbf{F}\cdot\mathbf{u},\end{cases}$$

respectively, where $\mathbf{D}$, $\mathbf{F}$ are $(N+1)\times(N+1)$ band matrices. On the other hand, the time interval $[0,T_f]$ has been discretized into N_t+1 equally spaced time steps $t_k=k\Delta t$, $k=0,1,\ldots,N_t$, with $\Delta t=T_f/N_t$.

3.4.1 Fixed boundary conditions for T

We consider the following initial-boundary value problem,

$$\begin{cases} \mathbf{X}_t(s,t) = \mathbf{X}_s(s,t) \wedge_- \mathbf{X}_{ss}(s,t) = \mathbf{T}(s,t) \wedge_- \mathbf{T}_s(s,t), \\ \mathbf{T}_t(s,t) = \mathbf{T}(s,t) \wedge_- \mathbf{T}_{ss}(s,t), \\ \mathbf{T}(-L/2,t) = \mathbf{T}^-, \\ \mathbf{T}(+L/2,t) = \mathbf{T}^+, \ s \in [-L/2, L/2], \ t \in [0, T_f], \end{cases} \tag{3.36}$$

with initial conditions $\mathbf{X}(s,0)$, $\mathbf{T}(s,0)$ as given in (3.13), (3.14), respectively, and

$$\begin{cases} \mathbf{T}^- = (\cosh(l/2 - L/2), \sinh(l/2 - L/2), 0)^T, \\ \mathbf{T}^+ = (\cosh(l/2 + L/2), \sinh(l/2 + L/2), 0)^T. \end{cases}$$

By using the space discretization mentioned above, we integrate (3.36) numerically by using the fourth-order Runge–Kutta method in time. We write

$$\mathbf{T}_j^{(n)} \equiv \mathbf{T}^{(n)}(s_j) \equiv \mathbf{T}(s_j, t^n), \ \mathbf{X}_j^{(n)} \equiv \mathbf{X}^{(n)}(s_j) \equiv \mathbf{X}(s_j, t^n),$$

where $\mathbf{X}_j^{(0)}$ can be computed from (3.14) by using a linear interpolation and $\mathbf{T}(s_j, \cdot) = \mathbf{T}(s, \cdot)$ for $s_j \le s < s_{j+1}$, if $s < 0$, and $s_j < s \le s_{j+1}$, if $s > 0$. Thus, we obtain N values of piecewise constant tangent vector, each corresponding to respective N segments. Moreover, since (3.36) is solved only for $\mathbf{T}$, so to keep the consistency in dimensions we obtain its $N+1$ values in the following way:

$$\begin{aligned} &\tilde{\mathbf{T}}_0^{(0)} = \mathbf{T}_0^{(0)}, \ \tilde{\mathbf{T}}_{j+1}^{(0)} = \tfrac{1}{2}\left(\mathbf{T}_j^{(0)} + \mathbf{T}_{j+1}^{(0)}\right), \ j = 0, 1, \ldots, N-2, \\ &\tilde{\mathbf{T}}_N^{(0)} = \mathbf{T}_{N-1}^{(0)}, \ \mathbf{T}_j^{(0)} = \tfrac{\tilde{\mathbf{T}}_j}{\|\tilde{\mathbf{T}}_j\|_0}. \end{aligned}$$

With this, we calculate

$$\begin{aligned} \mathbf{X}_j^{(n+1)} &= \mathbf{X}_j^{(n)} + \tfrac{\Delta t}{6}(\mathbf{A}_j^X + \mathbf{B}_j^X + \mathbf{C}_j^X + \mathbf{D}_j^X), \ j = 0, 1, 2, \ldots, N, \\ \tilde{\mathbf{T}}_j &= \mathbf{T}_j^{(n)} + \tfrac{\Delta t}{6}(\mathbf{A}_j^T + \mathbf{B}_j^T + \mathbf{C}_j^T + \mathbf{D}_j^T), \\ \mathbf{T}_j^{(n+1)} &= \tfrac{\tilde{\mathbf{T}}_j}{\|\tilde{\mathbf{T}}_j\|_0}, \ j = 1, 2, \ldots, N-1, \end{aligned}$$

where,

$$\mathbf{A}_j^X = \mathbf{T}_j^{(n)} \wedge_- D^{+-}\mathbf{T}_j^{(n)}, \ \mathbf{A}_j^T = \mathbf{T}_j^{(n)} \wedge_- F^{+-}\mathbf{T}_j^{(n)}, \ \mathbf{T}_j^{(A)} = \mathbf{T}_j^{(n)} + \tfrac{\Delta t}{2}\mathbf{A}_j^T,$$

N	Δs	Δt_{max}
256	$3.7500 \cdot 10^{-2}$	$7.441010326374327 \cdot 10^{-4}$
512	$1.8750 \cdot 10^{-2}$	$1.866312036256753 \cdot 10^{-4}$
1024	$9.3750 \cdot 10^{-3}$	$4.661983686987983 \cdot 10^{-5}$
2048	$4.6875 \cdot 10^{-3}$	$1.165021950245675 \cdot 10^{-5}$
4096	$2.3437 \cdot 10^{-3}$	$2.912999110940176 \cdot 10^{-6}$

Table 3.1 Δt_{max} for $L = 9.6$, $T_f = 5.7296 \cdot 10^{-2}$.

$$\mathbf{B}_j^X = \mathbf{T}_j^{(A)} \wedge_- D^{+-}\mathbf{T}_j^{(A)},\ \mathbf{B}_j^T = \mathbf{T}_j^{(A)} \wedge_- F^{+-}\mathbf{T}_j^{(A)},\ \mathbf{T}_j^{(B)} = \mathbf{T}_j^{(n)} + \tfrac{\Delta t}{2}\mathbf{B}_j^T,$$

$$\mathbf{C}_j^X = \mathbf{T}_j^{(B)} \wedge_- D^{+-}\mathbf{T}_j^{(B)},\ \mathbf{C}_j^T = \mathbf{T}_j^{(B)} \wedge_- F^{+-}\mathbf{T}_j^{(B)},\ \mathbf{T}_j^{(C)} = \mathbf{T}_j^{(n)} + \Delta t\mathbf{C}_j^T,$$

$$\mathbf{D}_j^X = \mathbf{T}_j^{(C)} \wedge_- D^{+-}\mathbf{T}_j^{(C)},\ \mathbf{D}_j^T = \mathbf{T}_j^{(C)} \wedge_- F^{+-}\mathbf{T}_j^{(C)},$$

and for the boundary conditions,

$$\mathbf{T}_0^{(n)} \equiv \mathbf{T}^-,\ \mathbf{T}_N^{(n)} \equiv \mathbf{T}^+,\ n = 0, 1, \ldots, N_t.$$

Remark that in order to avoid the accumulation of rounding errors, we renormalize $\mathbf{T}$ at every (including intermediate) time steps which also guarantees that $\mathbf{T}_j^{(n)} \in \mathbb{H}^2$, for all j and n.

Stability

From the numerical scheme described above, it is clear that Δt is a function of Δs. We have computed numerically the value of Δt_{max}, i.e., the maximum value of Δt, for which $\|\mathbf{T}\|$ calculated using (3.37) does not blow up, or, in other words, the numerical scheme is stable. We have taken $M = 16$, $l = 0.6$, $L = 9.6$, $t \in [0, T_f]$, where $T_f = 5.7296 \cdot 10^{-2}$. The values of different Δs, Δt_{max} have been recorded in Table 3.1, and it is quite clear that $\Delta t/\Delta s^2 \approx 0.5302\ldots$, in other words, $\Delta t = \mathcal{O}(\Delta s^2)$.

Accuracy

Denoting the numerical solution as $\mathbf{T}_{num}(s,t)$, $\mathbf{X}_{num}(s,t)$, we have $\mathbf{T}_{num}(s,t) = \mathbf{T}(s,t) + \mathcal{O}(\Delta s^4) + \mathcal{O}(\Delta t^4)$. It is important to note that since the initial data for tangent vector $\mathbf{T}$ is piecewise constant, a fourth-order accuracy in space is not achieved; however, we check the accuracy with respect to the time variable. In this direction, we have taken the parameters $M = 16, l = 0.6, L = 9.6$, and different values of time

n	$\|\mathbf{T}(\cdot,\Delta t)-\mathbf{T}(\cdot,\Delta t/2)\|$	$\log_2\left(\frac{\|\mathbf{T}(\cdot,\Delta t)-\mathbf{T}(\cdot,\Delta t/2)\|}{\|\mathbf{T}(\cdot,\Delta t/2)-\mathbf{T}(\cdot,\Delta t/4)\|}\right)$
0	$2.026166725776559\cdot 10^{-2}$	0.334849613949231
1	$1.606480288566086\cdot 10^{-2}$	1.501570043593869
2	$5.673587765826951\cdot 10^{-3}$	3.701771082277862
3	$4.360272628143871\cdot 10^{-4}$	4.002635528750734
4	$2.720196570405965\cdot 10^{-5}$	4.006625209898787
5	$1.692333374158203\cdot 10^{-6}$	4.003533506536733

Table 3.2 The order of accuracy for the Runge–Kutta method in time with fixed boundary conditions on tangent vector $\mathbf{T}$ for $M=16$, $l=0.6$, computed using (3.37), with $\Delta t = 2^{-n}\cdot 1.8189\cdot 10^{-4}$.

steps, i.e., $\Delta t = 2^{-n}\cdot 1.8189\cdot 10^{-4}$, $n=0,1,\ldots,7$, $N=2^5M$, $\Delta s = 1.875\cdot 10^{-2}$, $T_f = 5.7296\cdot 10^{-2}$. Table 3.2 shows the corresponding error values for the tangent vector $\mathbf{T}$, and $\|\cdot\|$ is given by

$$\|\mathbf{T}\| = \left[\frac{1}{N+1}\sum_{j=0}^{N}\left(-T_{1,j}^2+T_{2,j}^2+T_{3,j}^2\right)\right]^{1/2}, \tag{3.37}$$

where $T_{i,j}=T_i(s_j,\cdot)$.

Center of mass

The numerical experiments show that apart from the formation of new corners at the rational times, the planar l-polygon performs a vertical movement too. In order to measure the latter, we compute the center of mass of the polygonal curve by calculating the mean of $\mathbf{X}$:

$$\mathbf{X}^{mean}(t) = \frac{1}{L}\int_{-L/2}^{L/2}\mathbf{X}(s,t)ds.$$

With the discretization (3.33), we approximate the above integral numerically by using the trapezoidal rule

$$\int_{-L/2}^{L/2}\mathbf{X}(s,t)ds \approx \frac{\Delta s}{2}\left[\mathbf{X}(s_0,t)+2\sum_{j=1}^{N-1}\mathbf{X}(s_j,t)+\mathbf{X}(s_N,t)\right].$$

We analyze this quantity componentwise, and by using the spatial symmetries mentioned in Section 3.2.1, we note that the first component is equal to zero and by denoting the

second and third component by $X_{2,0}^{mean}$ and $X_{3,0}^{mean}$, respectively, we have

$$X_{2,0}^{mean}(t) = \frac{1}{N}\sum_{j=0}^{N-1} X_2(s_j,t),\ X_{3,0}^{mean}(t) = \frac{1}{N}\sum_{j=0}^{N-1} X_3(s_j,t), \tag{3.38}$$

We can further simplify and write $X_{3,0}^{mean}(t)$

$$\begin{aligned}
&= \frac{1}{N}\sum_{j=0}^{N-1} X_3(s_j,t)\\
&= \frac{1}{N}\Big[X_3(s_0,t) + \ldots + X_3(s_{N/M-1},t) + \ldots + X_3(s_{N-N/M+1},t) + \ldots + X_3(s_N,t)\Big]\\
&= \frac{M}{N}\sum_{j=0}^{N/M-1} X_3(s_j,t).
\end{aligned} \tag{3.39}$$

For the numerical simulations, we take $M = 96$, $N/M = 2^9$, $l = 0.1$, $t \in [0, T_f]$, $N_t = 80640$, and note that $X_{1,0}^{mean}(t)$ is equal to zero; however, $X_{2,0}^{mean}(t)$, $X_{3,0}^{mean}(t)$ are nonzero and exhibit certain structures in their trajectories. In order to understand that, first we consider $X_{3,0}^{mean}(t)$ which determines the position of the center of mass along the z-axis, in other words, the vertical height of the polygonal curve $\mathbf{X}(s,t)$. After performing numerical simulations for different values of M and l, we observe that $X_{3,0}^{mean}(t)$ can be very well approximated by means of a constant multiplied by t. To be precise,

$$X_{3,0}^{mean}(t) \approx \frac{X_{3,0}^{mean}(T_f)}{T_f} t = c_l^{num}\ t, \tag{3.40}$$

where c_l^{num} is the mean speed computed numerically. However, in Chapter 4, we will obtain an exact expression for the mean speed of l-polygon:

$$c_l = \frac{4\ln\cosh(l/2)}{l\sqrt{1-\operatorname{sech}^2(l/2)}}, \tag{3.41}$$

which depends only on l.

At this point, it is important to mention that during the numerical evolution we notice that the inner points of the $\mathbf{T}$, and thus those of $\mathbf{X}$, are far more accurate than the ones close to the boundary. For instance, see Figure 3.3 where we have plotted the absolute difference between the numerical and algebraic solutions of the third component of $\mathbf{T}$. Clearly, the error is much lesser for the inner points, as a result, it becomes important to observe the evolution for them as well. With this motivation, in

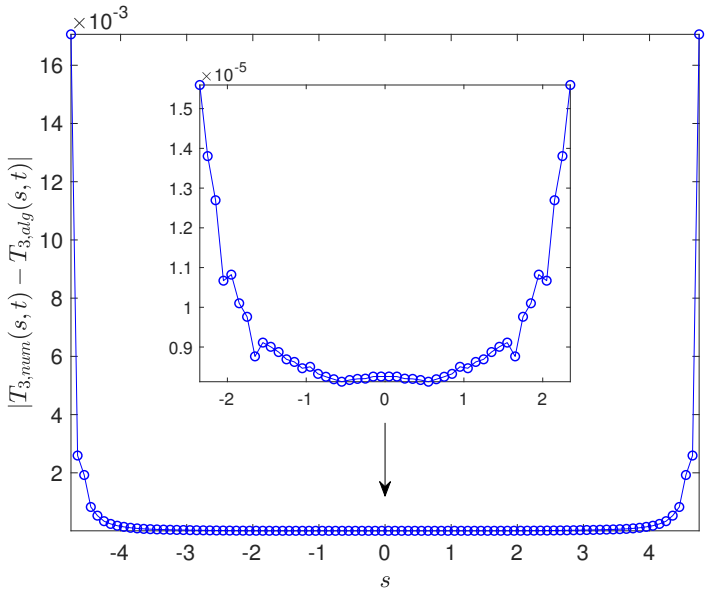

Figure 3.3 The absolute difference between the numerical and algebraic solution of the third component of tangent vector at time $t = T_f$, for $M = 96, l = 0.1, N/M = 2^9, s \in [-L/2, L/2]$. The values represented by blue circles, are computed using the mean of N/M values for each side. The magnified part shows that the error in the inner points, i.e., when $s \in [-L/4, L/4]$, is much lesser than the outer ones.

order to make a reasonable choice of the "inner points", we define

$$X_{3,r}^{mean}(t) = \frac{1}{N_r} \sum_{j=2rN/M}^{N-2rN/M-1} X_3(s_j, t), \ r = 0, 1, \ldots, M/4 - 1, \tag{3.42}$$

for $N_r = N - (4rN/M)$, i.e., the mean of $X_3(s_j, t)$ for $s_j \in [-L/2 + 2rl, L/2 - 2rl]$. For each r, we compute $\max_n(|X_{3,r}^{mean}(t^{(n)}) - c_l t^{(n)}|)$, i.e., the maximum difference between $X_{3,r}^{mean}(t)$ and its linear approximation $c_l t$. From Figure 3.4 it is quite clear that error is smaller when the nodes closer to boundary are avoided; the figure is the continuation of Figure 3.3, hence all parameters are identical. It also shows that after certain values of r, the error does not vary much, as a result, without loss of generality, we can take $r = M/8$ which would imply $s_j \in [-L/4, L/4]$, i.e., $j = N/4 + 1, N/4 + 2, \ldots, 3N/4$. Note that although $X_{3,0}^{mean}(t^{(n)})$ can be computed using only N/M values, but due to the unevenness of errors discussed above, we will use $N/2$ elements.

In order to further strengthen the claim of (3.40), we compute $\max_n(|X_{3,r}^{mean}(t^{(n)}) - c_l t^{(n)}|)$ for different values of l and fixed r. Since a regular planar l-polygon is characterized by the parameter l, the speed of center of mass depends only on it; however, with parameter M, we are approximating the infinitely long planar l-polygon. In this

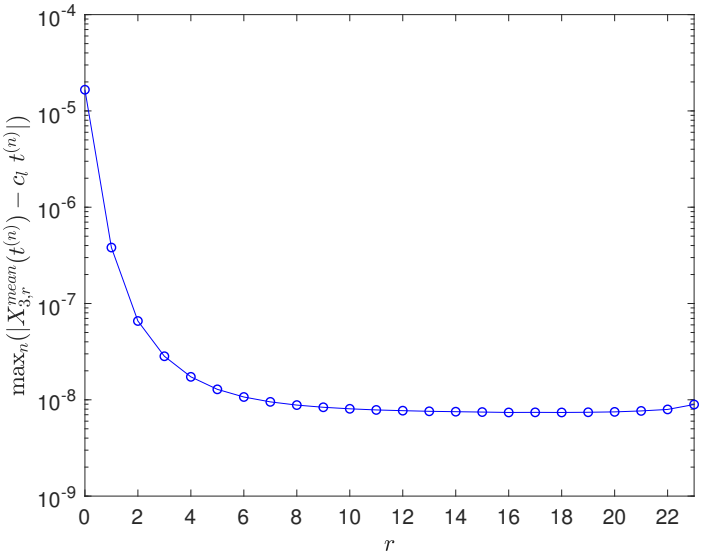

Figure 3.4 $\max_n(|X_{3,r}^{mean}(t^{(n)}) - c_l t^{(n)}|)$ for $M = 96, l = 0.1, N/M = 2^9$, where the mean of $X_3(s_j, t^{(n)})$ has been computed using $4rN/M$ values such that $s_j \in [-L/2 + 2rl, L/2 - 2rl]$, $r = 0, 1, 2, \ldots, M/4 - 1$, $c_l = 1.000416458444891$. Clearly, the error is much lesser when inner points are considered.

regard, Table 3.3 shows the discrepancy for a fixed value of l, N/M and different values of M, where c_l is computed using (3.41). It is quite clear that the better results are obtained for larger values of M. Recall that the choice of M also determines the values of l for which the numerical method is stable. Therefore, for further simulations, we have taken a moderately large value, i.e., $M = 96$ and different values of l and N/M. For $l = 0.025, 0.050, 0.1, 0.12, 0.15$, and $N/M = 2^6, 2^7, 2^8, 2^9$, the corresponding errors have been stored in Table 3.4. Moreover, every time the number of points is doubled, the errors decrease by a factor little less than two, hence, suggesting that they behave as $\mathcal{O}((N/M)^{-1})$. The table also shows the value of c_l for each l which is very close to 1, as a result, we have shown the difference between the two. Clearly, c_l decreases with l and converges to 1 as l goes to zero, i.e., $\mathbf{X}(s, 0)$ tends to a hyperbola.

M	$N/M = 2^7$	M	$N/M = 2^7$
24	$1.0476 \cdot 10^{-8}$	96	$1.2481 \cdot 10^{-10}$
48	$7.5024 \cdot 10^{-10}$	192	$8.8182 \cdot 10^{-11}$

Table 3.3 $\max_n(|X_{3,r}^{mean}(t^{(n)}) - c_l t^{(n)}|)$, $l = 0.025$, $c_l = 1.000026040853303$, and different L, M values where $X_{3,r}^{mean}(t^{(n)})$ is computed for $r = M/8$. It is evident that better results are obtained for large M values.

In order to complete the discussion, we compute $X_{3,r}^{mean}(t)$ for $r = 0$, i.e., using all N elements and compute the errors as before. Figure 3.5 shows the corresponding plot for $X_{3,0}^{mean}(t)$ which is also linear, but due to the presence of larger errors near the boundary, the slope of the curve c_l^{num} differs a lot from the expected value. Moreover, refining the grid also does not improve the results much, as seen in Table 3.5, thus showing that the approximation, when all the points are considered, is not as good as compared to the inner points.

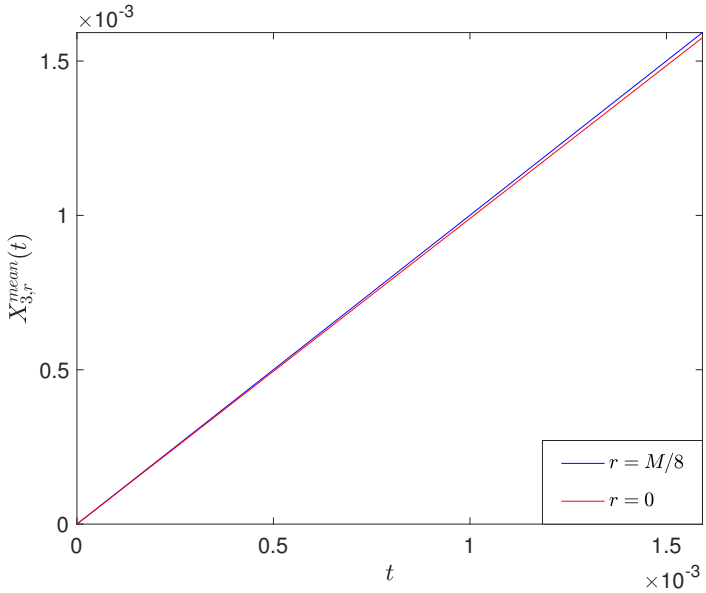

Figure 3.5 $X_{3,r}^{mean}(t)$ as a function of t, for $M = 96$, $N/M = 2^9$, $l = 0.1$, $t \in [0, T_f]$ for $r = 0$ (red), $c_l^{num} = 0.9899904240867042$, and $r = M/8$ (blue), $c_l^{num} = 1.000412194733485$.

l	$N/M = 2^6$	$N/M = 2^7$	$N/M = 2^8$	$N/M = 2^9$	$(c_l - 1)$
0.15	$2.0578 \cdot 10^{-7}$	$1.1334 \cdot 10^{-7}$	$6.3398 \cdot 10^{-8}$	$3.7051 \cdot 10^{-8}$	$9.3645 \cdot 10^{-4}$
0.12	$8.4311 \cdot 10^{-8}$	$4.6133 \cdot 10^{-8}$	$2.6124 \cdot 10^{-8}$	$1.5543 \cdot 10^{-8}$	$5.9957 \cdot 10^{-4}$
0.1	$4.0669 \cdot 10^{-8}$	$2.2237 \cdot 10^{-8}$	$1.2801 \cdot 10^{-8}$	$7.7110 \cdot 10^{-9}$	$4.1646 \cdot 10^{-4}$
0.05	$2.5460 \cdot 10^{-9}$	$1.5103 \cdot 10^{-9}$	$9.2425 \cdot 10^{-10}$	$6.1407 \cdot 10^{-10}$	$1.0415 \cdot 10^{-4}$
0.025	$1.6008 \cdot 10^{-10}$	$1.2481 \cdot 10^{-10}$	$8.8786 \cdot 10^{-11}$	$7.1406 \cdot 10^{-11}$	$2.6040 \cdot 10^{-5}$

Table 3.4 The error $\max_n(|X_{3,r}^{mean}(t^{(n)}) - c_l t^{(n)}|)$ for $M = 96$ and different N/M, l and corresponding c_l values, where $X_{3,r}^{mean}(t^{(n)})$ is computed using (3.42) for $r = M/8$.

Next, we compute $X_{2,r}^{mean}(t)$, which appears to be nonzero unlike the first component and its Euclidean counterpart. In this regard, for the same parameters, i.e., $M = 96$, $l = 0.1$, $N/M = 2^9$, we plot $X_{2,r}^{mean}(t)$ for $r = 0, M/8, M/4$ in Figure 3.6. Observe that

l	$N/M = 2^6$	$N/M = 2^7$	$N/M = 2^8$	$N/M = 2^9$
0.15	$3.7545 \cdot 10^{-5}$	$3.7455 \cdot 10^{-5}$	$3.7405 \cdot 10^{-5}$	$3.7377 \cdot 10^{-5}$
0.12	$2.3973 \cdot 10^{-5}$	$2.3936 \cdot 10^{-5}$	$2.3915 \cdot 10^{-5}$	$2.3904 \cdot 10^{-5}$
0.1	$1.6626 \cdot 10^{-5}$	$1.6609 \cdot 10^{-5}$	$1.6599 \cdot 10^{-5}$	$1.6593 \cdot 10^{-5}$
0.05	$4.1476 \cdot 10^{-6}$	$4.1465 \cdot 10^{-6}$	$4.1459 \cdot 10^{-6}$	$4.1456 \cdot 10^{-6}$
0.025	$1.0364 \cdot 10^{-6}$	$1.0363 \cdot 10^{-6}$	$1.0362 \cdot 10^{-6}$	$1.0362 \cdot 10^{-6}$

Table 3.5 The error $\max_n(|X_{3,r}^{mean}(t^{(n)}) - c_l t^{(n)}|)$ for $M = 96$ and different N/M, l and corresponding c_l values, where $X_{3,r}^{mean}(t^{(n)})$ is computed using (3.42) for $r = 0$.

when the inner sides are considered the shape of the curve changes and appears to be periodic when $r = M/4$. Let us mention that unlike $X_{3,r}^{mean}$ where changing r value does not change its value up to the numerical errors, the value of $X_{2,r}^{mean}$ does depend on the r value. However, in this experiment our aim is to observe the qualitative behavior of its evolution rather than the quantitative one.

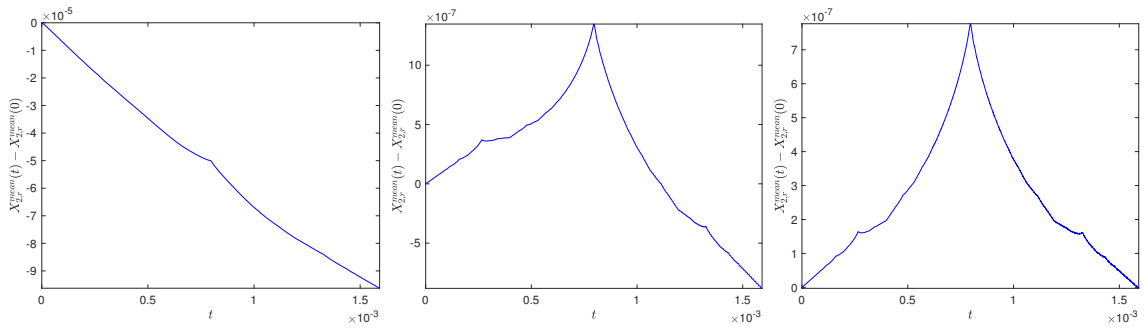

Figure 3.6 $X_{2,r}^{mean}(t) - X_{2,r}^{mean}(0)$ for $M = 96$, $N/M = 2^9$, $l = 0.1$, $t \in [0, T_f]$, using $r = 0$ (left), i.e., N points, for $r = M/8$ (center), i.e., $N/2$ points and $r = M/4$ (right), i.e., $4N/M$ points.

Furthermore, using the approach in Chapter 2 and [23, Section 4], we can compute $\mathbf{X}^{mean}$ using the algebraic solution and thus, avoid the numerical errors completely. In that direction, we compute

$$\mathbf{X}^{mean}(t) = \int_0^t \text{mean}(\mathbf{X}_t)(t')dt' = \int_0^t \left[\frac{1}{L}\int_{-L/2}^{L/2} \mathbf{X}_t(s,t')ds\right] dt', \tag{3.43}$$

and for any rational time t_{pq}, the first integral is precisely given by

$$\int_{-L/2}^{L/2} \mathbf{X}_t(s,t_{pq})ds = \frac{l_q}{\sinh(l_q)} \sum_{k=0}^{Mq-1} \mathbf{T}_k \wedge_- \mathbf{T}_{k+1}, \tag{3.44}$$

where $\mathbf{T}_k = \mathbf{T}(s_k^+, \cdot)$.

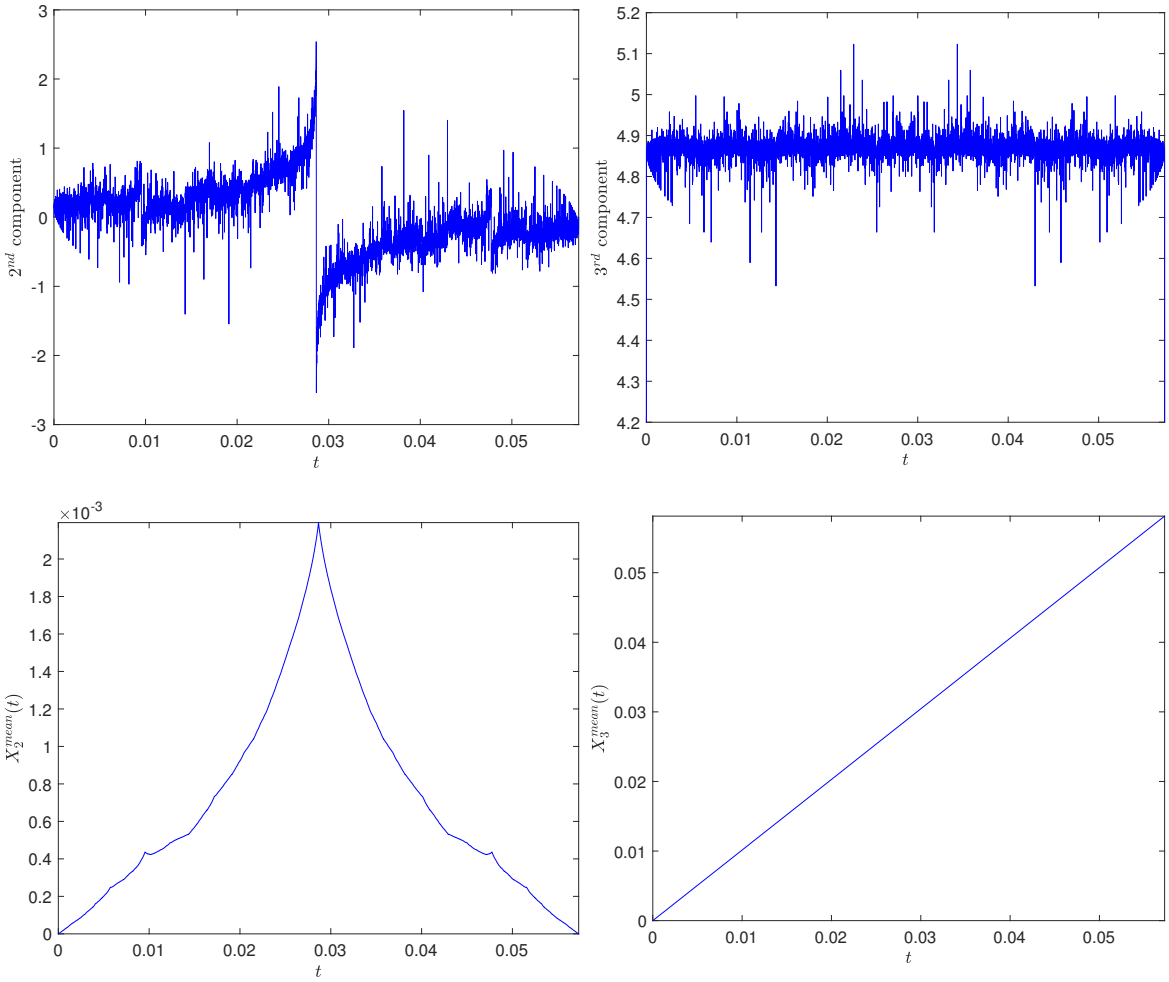

Figure 3.7 Second and third components of (3.43) and (3.44) computed for $M = 8$, $l = 0.6$, $q = 7560$. Clearly, with an integration with respect to time, the oscillations disappear and we obtain a periodic curve and a straight line respectively.

Hence, by approximating the integral with respect to time in (3.43) by a third-order method, for a large q, we can compute the movement of the center of mass. Unlike in the Euclidean case, we do not obtain a precise expression for the components of $\mathbf{X}^{mean}$, however, it certainly allows us to compute them using the algebraic solution $\mathbf{T}_{alg}$ which is free from numerical errors. In this regard, we have taken $M = 8$, $l = 0.6$, $q = 7560$ and the interval $[0, T_f]$ has been divided into q equally spaced segments. We have plotted the integral (3.44) whose first component is zero and the rest of the two components seem to be very oscillatory in nature as seen in the Euclidean case (Figure 2.4). However, after integrating in time, the oscillations completely disappear and we

obtain the second component as a periodic curve and the third component as a straight line with a slope converging to c_l with q, as observed previously (see Figure 3.7).

l	$N/M = 2^6$	$N/M = 2^7$	$N/M = 2^8$	$N/M = 2^9$	$N/M = 2^{10}$
0.2	$4.0442 \cdot 10^{-2}$	$3.2678 \cdot 10^{-2}$	$2.6665 \cdot 10^{-2}$	$2.2341 \cdot 10^{-2}$	$1.9248 \cdot 10^{-2}$
0.15	$2.2711 \cdot 10^{-2}$	$1.8066 \cdot 10^{-2}$	$1.4479 \cdot 10^{-2}$	$1.1974 \cdot 10^{-2}$	$1.0171 \cdot 10^{-2}$
0.12	$1.5620 \cdot 10^{-2}$	$1.2359 \cdot 10^{-2}$	$9.8698 \cdot 10^{-3}$	$8.4188 \cdot 10^{-3}$	$7.2017 \cdot 10^{-3}$
0.1	$1.1894 \cdot 10^{-2}$	$9.3896 \cdot 10^{-3}$	$7.5154 \cdot 10^{-3}$	$6.4954 \cdot 10^{-3}$	$5.5810 \cdot 10^{-3}$
0.05	$5.0056 \cdot 10^{-3}$	$3.9380 \cdot 10^{-3}$	$3.2342 \cdot 10^{-3}$	$2.8058 \cdot 10^{-3}$	$2.4328 \cdot 10^{-3}$
0.025	$2.3853 \cdot 10^{-3}$	$1.8751 \cdot 10^{-3}$	$1.5517 \cdot 10^{-3}$	$1.3476 \cdot 10^{-3}$	$1.1716 \cdot 10^{-3}$

Table 3.6 The error $\max_{j,n} \|\mathbf{X}_{num}(s_j, t^{(n)}) - (0, X_2^{mean}(t^{(n)}), c_l t^{(n)}) - \mathbf{X}_{alg}(s_j, t^{(n)})\|$, for $j = N/4+1, \ldots, 3N/4+1$, $n = 0, 1, \ldots, 1260$, $M = 48$ and different N/M, l.

Comparison between the numerical and algebraic solution

Having learnt about the movement of the center of mass of the polygonal curve, we compare the numerical solution $\mathbf{T}_{num}$, $\mathbf{X}_{num}$, with their algebraic counterparts which we denote by $\mathbf{T}_{alg}$, $\mathbf{X}_{alg}$. Since $\mathbf{X}_{alg}$ has been constructed up to a rigid movement, to compare it with $\mathbf{X}_{num}$, we subtract its movement in the YZ-plane. In other words, we compute $\max_{j,n} \|\mathbf{X}_{num}(s_j, t^{(n)}) - (0, X_{2,r}^{mean}(t^{(n)}), c_l\ t^{(n)}) - \mathbf{X}_{alg}(s_j, t^{(n)})\|$, where $\|\cdot\|$ is the Euclidean distance, $t^{(n)} = (n/N_t)T_f$, $n = 0, 1, \ldots, N_t$, $s_j = -L/2 + jL/N$, $j = 0, 1, \ldots, N+1$, and c_l is computed using (3.41). For the numerical simulations, we have taken a fixed value of $M = 48$, and different values of l and N/M. Note that during the algebraic construction of $\mathbf{X}_{alg}$, we obtain the vertices of the polygonal curve for a given time; however, the in-between points, i.e., $\mathbf{X}_{alg}(s_j, \cdot)$ have been computed by using the linear interpolation. It is important to mention that given the size of discretization, it can be computationally impossible to compare the solutions at all $N_t + 1$ time instants, therefore, we have considered 1260 different time instants. Moreover, as done before, we have computed the errors for $r = M/8$ or $N/2+1$ points, and $r = 0$, i.e., all $N+1$ points which have been stored in Table 3.6, 3.7, respectively. As seen in the case of approximation of $X_{3,r}^{mean}(t)$, we note that the magnitude of errors is lesser when only inner points are considered, moreover, they decrease by a certain factor when the discretization is made finer. Although the convergence is slow, keeping in the mind that $\max \|\mathbf{X}_{alg}\| \gg 1$, the results are satisfactory and show that as N grows larger, the numerical solution converges to the algebraic one. It also gives strong evidence the $\mathbf{X}_{num}$ is periodic or at least quasi-periodic in time with a period T_f.

The comparison between the two can be further appreciated if we add the movement in the YZ-plane to $\mathbf{X}_{alg}(s,\cdot)$, and plot it along with $\mathbf{X}_{num}(s,\cdot)$, for instance, see Figure 3.10. Bearing in mind that we have fixed the boundary conditions for $\mathbf{T}_{num}$, the error towards the endpoints of $\mathbf{X}_{num}$ is visible when compared with $\mathbf{X}_{alg}$ on the left-hand side. At the same time, the difference between the figures is almost indistinguishable as we move away from the boundaries, for instance, see Figure 3.11 where we have plotted only the inner points.

l	$N/M = 2^6$	$N/M = 2^7$	$N/M = 2^8$	$N/M = 2^9$	$N/M = 2^{10}$
0.2	$6.9820 \cdot 10^{-1}$	$6.9650 \cdot 10^{-1}$	$6.9647 \cdot 10^{-1}$	$6.9486 \cdot 10^{-1}$	$6.9437 \cdot 10^{-1}$
0.15	$2.6192 \cdot 10^{-1}$	$2.6154 \cdot 10^{-1}$	$2.6165 \cdot 10^{-1}$	$2.6132 \cdot 10^{-1}$	$2.6125 \cdot 10^{-1}$
0.12	$1.4835 \cdot 10^{-1}$	$1.4826 \cdot 10^{-1}$	$1.4828 \cdot 10^{-1}$	$1.4818 \cdot 10^{-1}$	$1.4818 \cdot 10^{-1}$
0.1	$1.0043 \cdot 10^{-1}$	$1.0041 \cdot 10^{-1}$	$1.0040 \cdot 10^{-1}$	$1.0038 \cdot 10^{-1}$	$1.0037 \cdot 10^{-1}$
0.05	$3.3170 \cdot 10^{-2}$	$3.3198 \cdot 10^{-2}$	$3.3215 \cdot 10^{-2}$	$3.3218 \cdot 10^{-2}$	$3.3213 \cdot 10^{-2}$
0.025	$1.4688 \cdot 10^{-2}$	$1.4704 \cdot 10^{-2}$	$1.4712 \cdot 10^{-2}$	$1.4715 \cdot 10^{-2}$	$1.4714 \cdot 10^{-2}$

Table 3.7 The error $\max_{j,n} \|\mathbf{X}_{num}(s_j, t^{(n)}) - (0, X_2^{mean}(t^{(n)}), c_l t^{(n)}) - \mathbf{X}_{alg}(s_j, t^{(n)})\|$, for $j = 1, \ldots, N+1$, $n = 0, 1, \ldots, 1260$, $M = 48$ and different N/M, l.

Regarding the numerical solution of tangent vector $\mathbf{T}_{num}$, Figure 3.8 shows its first component for $M = 48$, $l = 0.2$, $N/M = 2^{11}$, at different rational times. In the zoomed part, we see that at half time period, i.e., $t = t_{1,2}$, the tangent vector is continuous at $s = 0$ (red), hence showing that the curve $\mathbf{X}$ does not have a vertex at that time. Besides that, the oscillations arising due to the numerical approximation of a piecewise constant function are more prominent towards the boundary which also contribute to a larger error value as commented before. At the end of one time period, we obtain the tangent vector up to the numerical errors (yellow), which is same as at the initial time, thus showing the time periodicity of $\mathbf{T}_{num}$.

Figure 3.9 shows all three components of the tangent vector for both numerical and algebraic solutions at one-third of the time period, i.e., $t = t_{1,3}$. It is quite clear that there are three times more segments and apart from the numerical oscillations, the two figures are comparable. Since $M = 48$, therefore, at $t = t_{1,3}$, there will be $Mq = 144$ tangent vectors, and thus we have

$$\mathbf{T}_{alg,1} = \begin{pmatrix} 6.0854 \cdot 10^{1} \\ -6.0846 \cdot 10^{1} \\ -5.7735 \cdot 10^{-2} \end{pmatrix}, \quad \mathbf{T}_{alg,2} = \begin{pmatrix} 5.4978 \cdot 10^{1} \\ -5.4969 \cdot 10^{1} \\ 0 \end{pmatrix}, \quad \mathbf{T}_{alg,3} = \begin{pmatrix} 4.9836 \cdot 10^{1} \\ -4.9825 \cdot 10^{1} \\ 5.7735 \cdot 10^{-2} \end{pmatrix}, \tag{3.45}$$

and the rest can be computed by rotating $\mathbf{T}_{alg,1}$, $\mathbf{T}_{alg,2}$, $\mathbf{T}_{alg,3}$ by a time-like angle l

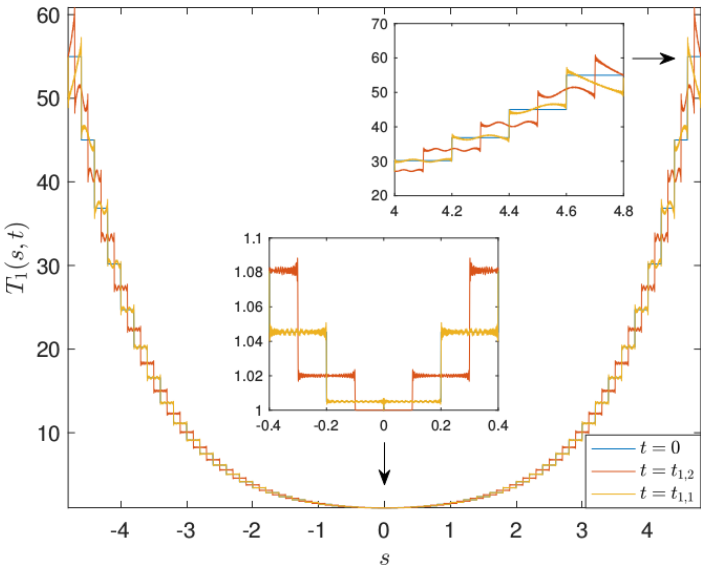

Figure 3.8 The first component of $\mathbf{T}_{num}(s,t)$ for $M=48$, $l=0.2$, $N/M=2^{11}$ at initial, half and final time period.

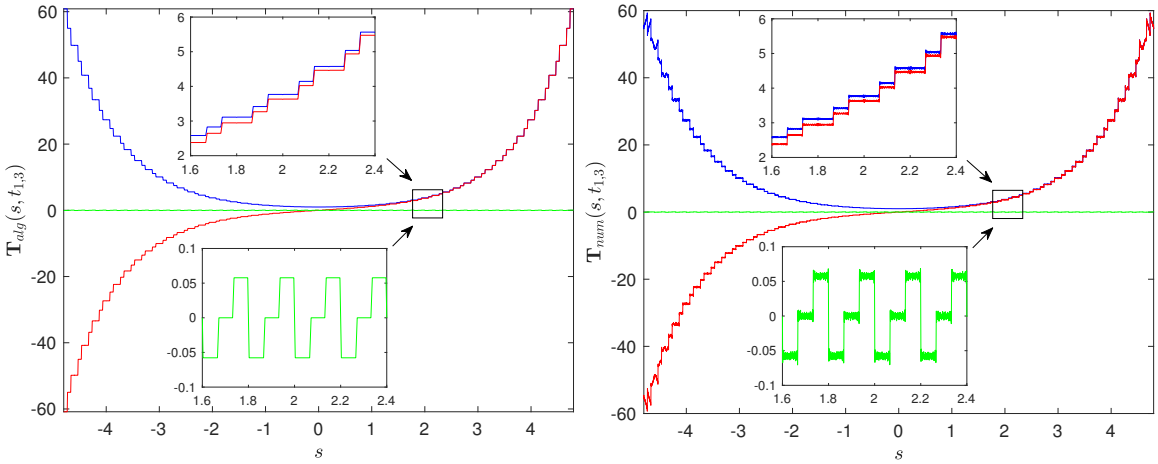

Figure 3.9 $\mathbf{T}_{num}(s,t)$ (left) and $\mathbf{T}_{alg}$ (right) at $t=t_{1,3}$ $l=0.2$, $M=48$, $N/M=2^{11}$.

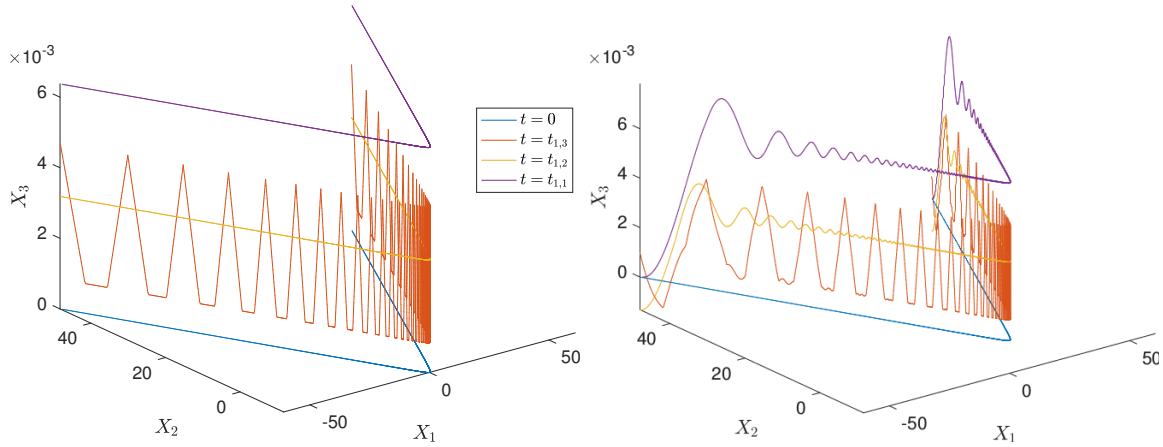

Figure 3.10 $\mathbf{X}_{alg}(s, t_{pq})$ (left) and $\mathbf{X}_{num}(s, t_{pq})$ (right) for $M = 48, l = 0.2$, $N/M = 2^{11}$ at different rational times t_{pq}. The errors towards the boundary points of $\mathbf{X}_{num}$ is quite prominent, however, as we move away the difference between the two figures is almost indistinguishable.

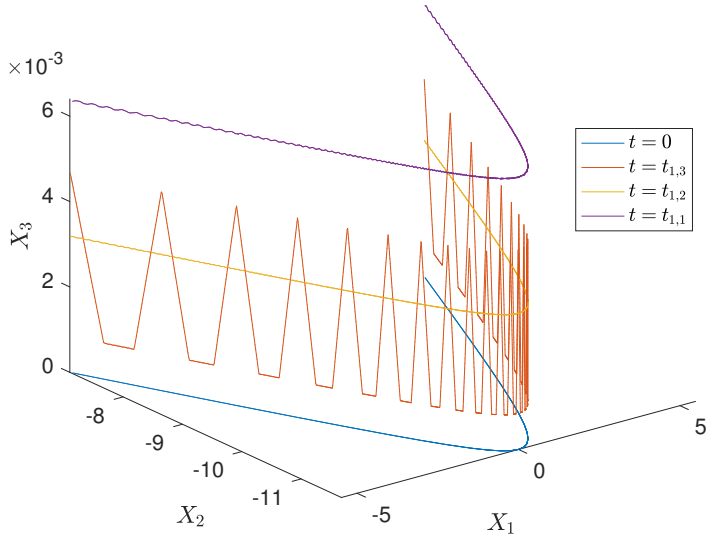

Figure 3.11 $\mathbf{X}_{num}(s, t_{pq})$ (right) for $M = 96, l = 0.1$, $N/M = 2^{11}$ at different rational times t_{pq} when inner points, i.e., s_j for $j = N/4 + 1, \ldots, 3N/4$ are considered.

about a space-like z-axis in the counter-clockwise direction consecutively. For instance, the ones on the left-hand side of $s = 0$ are obtained by a hyperbolic rotation of an angle $L/2 - l$ about the z-axis

$$\mathbf{T}_{alg,70} = \begin{pmatrix} 1.0217 \\ -2.0156 \cdot 10^{-1} \\ -5.7735 \cdot 10^{-2} \end{pmatrix}, \mathbf{T}_{alg,71} = \begin{pmatrix} 1.0050 \\ -1.0017 \cdot 10^{-1} \\ 0 \end{pmatrix}, \mathbf{T}_{alg,72} = \begin{pmatrix} 1.0017 \\ -1.1093 \cdot 10^{-4} \\ 5.7735 \cdot 10^{-2} \end{pmatrix}. \tag{3.46}$$

In order to compare them with the corresponding numerical solution, we take the mean of each segment and compute the absolute difference. Thus, with a discretization $N/M = 2^{11}$, the maximum absolute and relative errors with (3.45) are $\mathcal{O}(1)$, $\mathcal{O}(10^{-1})$, and $\mathcal{O}(10^{-5})$, $\mathcal{O}(10^{-2})$ for (3.46), which, in our opinion, given the nature of the problem, is reasonably good.

Trajectory of $\mathbf{X}(0, t)$

The choice of initial data (i.e., even number of sides for $\mathbf{X}$) allows us to capture the time evolution of $\mathbf{X}(0, t)$ numerically. Due to the mirror symmetries of $\mathbf{X}$ explained in the Section 3.2.1, the z-axis and $\mathbf{X}(-L/2 + kl/2, t)$ for $k = 0, 1, \ldots, 2M$ always lie in the same plane for all $t \geq 0$, where an even value of k corresponds to the vertices and an odd value to the middle point of the sides. In the following lines, we consider only the evolution of vertices, and with parameters $M = 48$, $N/M = 2^{11}$, $l = 0.2$, numerical simulations show that $\mathbf{X}(0, t)$ lies in the YZ-plane, whereas $\mathbf{X}(-L/2 + lk, t)$ for $k = 0, 1, 2, \ldots, M$ lie in a plane which is the YZ-plane rotated by a hyperbolic angle $L/2 - lk$ with respect to the z-axis in the counterclockwise direction. We have already seen that the inner points are the most accurate ones, thus, we consider $\mathbf{X}(0, t)$, project it onto the complex plane and define

$$z(t) = -X_2(0, t) + iX_3(0, t), \ t \in [0, T_f], \tag{3.47}$$

or, in general, for any vertex, i.e., $k = 0, 1, \ldots, M$

$$z(t) = -\left[e^{j(L/2-lk)}(X_1 + jX_2)(-L/2 + lk, t)\right] + iX_3(-L/2 + lk, t), \tag{3.48}$$

where we have used notation involving the hyperbolic number j.

Figure 3.12 shows the plot for $z(t)$ (left) which reminds us of the one observed in the Euclidean case [22]. Although, we are able to capture the trajectory of $\mathbf{X}(0, t)$, but due to lack of numerical accuracy, the corners of $z(t)$ are not as sharp as observed in the

Euclidean case (for instance, $z(t)$ towards the end of the time period). In our opinion, up to some extent, this can be explained with the following reasons. It is quite clear that the accuracy improves as N/M value increases, and we have also seen that more accurate results are obtained for larger values of M. Therefore, a large of N yields better numerical results. In the Euclidean case, due to the symmetries, it was possible to work with just one side of the polygonal curve, i.e., only N/M points; and the efficient `fft` algorithm in MATLAB makes the computation cost to be of $\mathcal{O}((N/M)\log(N/M))$. However, in our case, due to the fixed boundary conditions, we work with all the sides of the planar l-polygon and thus, the derivatives are computed using $(N+1)\times(N+1)$ dimensional finite difference matrices. Naturally, the computational time is much longer and from a numerical point of view, the problem is more challenging.

Having said that, in Figure 3.13, we plot the trajectory $z(t)$ for $M = 192$, $l = 0.025$, $N/M = 2^{11}$, i.e., $N = 393216$, and the corners can be well appreciated there. On

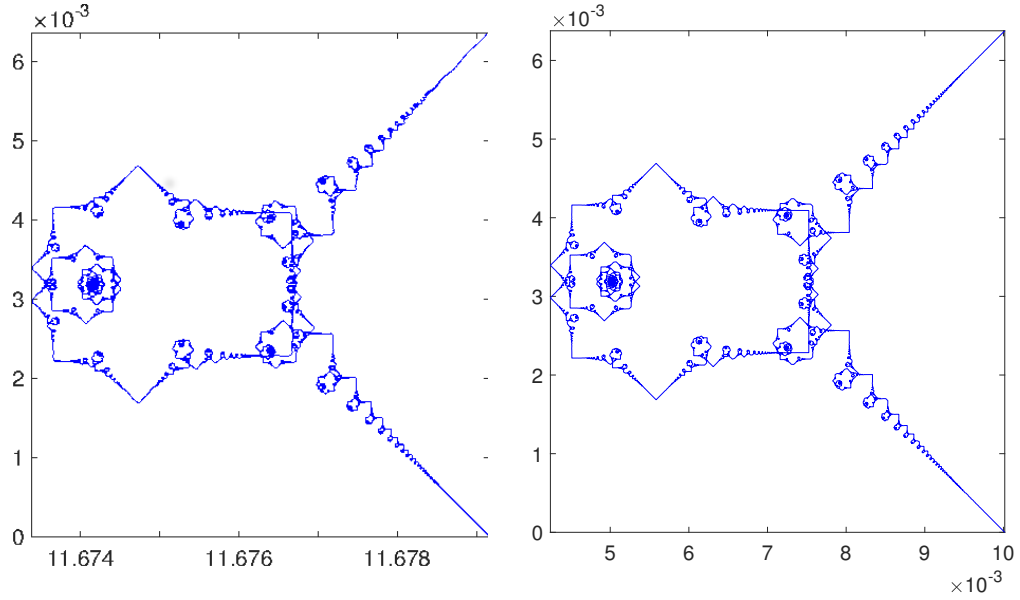

Figure 3.12 $z(t)$ (left) for $M = 48$, $l = 0.2$, $N/M = 2^{11}$, and $z_{alg}(t)$ (right) for $l = 0.2$ where the interval $[0, T_f]$ is divided into 7561 points.

the other hand, by plotting it componentwise we note that the second component of $\mathbf{X}(0,t)$ is periodic in time while the third component becomes periodic after removing the constant vertical movement, see Figure 3.14. Consequently, for a given value of l, we define

$$z_l(t) = z(t) - ic_l\, t,\ t \in [0, T_f], \tag{3.49}$$

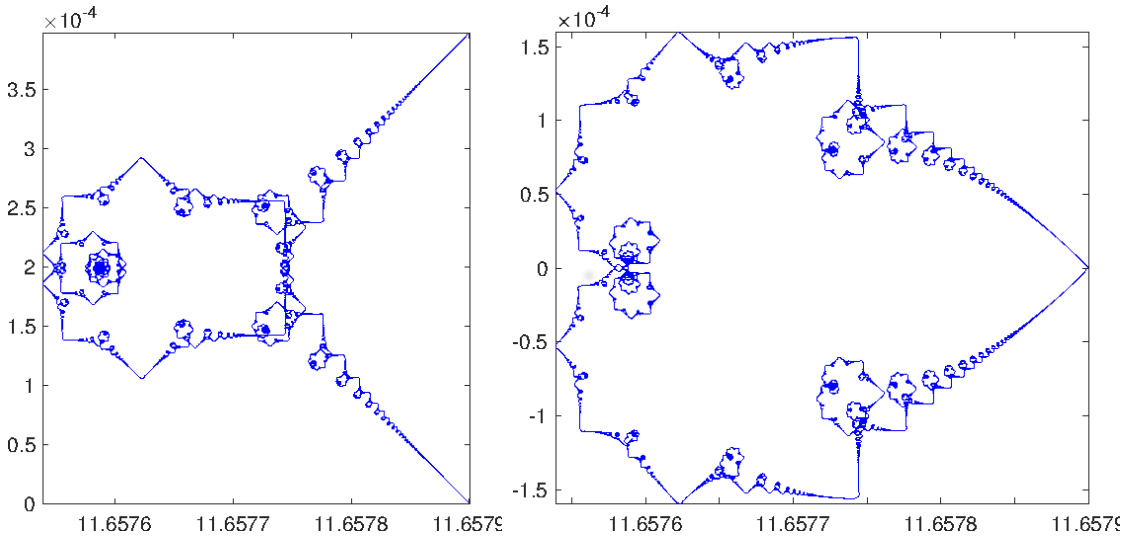

Figure 3.13 $z(t)$ (left) and $z_l(t)$ (right) for $M = 192$, $l = 0.05$, $N/M = 2^{11}$.

which is T_f-periodic and is shown in Figure 3.13 for $M = 192$, $l = 0.05$. The multifractal structure of $z_l(t)$ can be compared with the graph of

$$\phi(t) = \sum_{k=1}^{\infty} \frac{e^{i\pi k^2 t}}{i\pi k^2}, \ t \in [0, 2]. \tag{3.50}$$

$\phi(t)$ appeared in [30] where its real part

$$f(t) = \sum_{k=1}^{\infty} \frac{\sin(\pi k^2 t)}{\pi k^2},$$

also called Riemann's non-differentiable function, was considered.

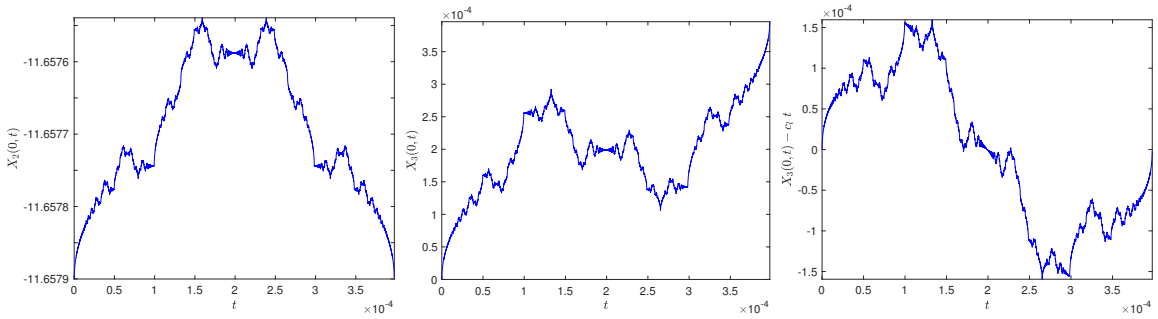

Figure 3.14 $M = 192$, $l = 0.05$, $N/M = 2^{11}$, $X_2(0,t)$ (left), $X_3(0,t)$ (center) and $X_3(0,t) - c_l\ t$, i.e., third component after removing the vertical height.

Remember that in the numerical simulations, with a large value of M, the value of l needs to be chosen small, hence, we obtain the $z_l(t)$ only for certain values of l.

However, the computation of the algebraic solution $\mathbf{X}_{alg}$ does not depend on M which is also free from numerical errors. As a result, we can consider any value of l(bearing in mind that due to the exponential growth of $\mathbf{X}$ and $\mathbf{T}$, l can not be very large), and compute $z(t)$ algebraically. Since $\mathbf{X}_{alg}$ is determined up to a movement in the YZ-plane, after adding the trajectory along the y-axis to the planar curve $\mathbf{X}_{alg}(0,t)$ can be compared with $\phi(t)$. Furthermore, as we also know the exact value of c_l, by adding the vertical height for all the times, we can obtain $z(t)$ algebraically. In other words, we have

$$\begin{cases} z_{l,alg}(t) = -(X_{2,alg}(0,t) + X_{2,alg}^{mean}(t)) + iX_{3,alg}(0,t), \\ z_{alg}(t) = z_{l,alg}(t) + ic_l t, \ t \in [0, T_f], \end{cases} \tag{3.51}$$

with $X_{2,alg}^{mean}(t)$ being the mean of the second component which can be obtained using (3.43) as explained before. We also redefine the previous definition of $\phi(t)$ and write

$$\phi(t) = \sum_{k=1}^{\infty} \frac{e^{2\pi i k^2 t}}{k^2}, \ t \in [0,1]. \tag{3.52}$$

From now on, our purpose of working with $\mathbf{X}(0,t)$ will be two fold. First, we would like to see its dependence on the parameter l and second, compare its structure with the one in the Euclidean case. We begin by plotting z_{alg} for $l = 0.2$ and compare it with the one computed numerically, see Figure 3.12. One can note that except for a horizontal translation, both figures are identically the same.

Having done that, to compare z_{alg} with its Euclidean counterpart, we choose the value of l such that the corresponding parameter c_0 is kept the same in both cases. More precisely, from (1.26)

$$\left[\tfrac{2}{\pi} \ln\left(\cosh\left(\tfrac{l}{2}\right)\right)\right]^{1/2} = \left[-\tfrac{2}{\pi} \ln\left(\cos\left(\tfrac{\pi}{M}\right)\right)\right]^{1/2} \iff l = 2\,\mathrm{arccosh}\left(\sec\left(\tfrac{\pi}{M}\right)\right), \tag{3.53}$$

where M is the number of sides of the Euclidean planar M-polygon.

Figure 3.15 shows $z_{l,alg}(t)$ (blue) for different values of l such that $M = 3, 4, 5, 6$ and 10 and $\phi(t)$ (red) where the respective intervals for t have been divided into 7561 points. It can be noted that except for a scaling, $z_{l,alg}$ corresponding to the value $M = 10$ looks very close to ϕ (red). In order to further compare them, we employ two different approaches. First, as done in Chapter 2, we consider $\phi - \lambda_l z_{l,alg} - \mu_l$ where $\lambda_l \in \mathbb{R}$ and $\mu \in \mathbb{C}$ have been computed from least squares fitting method. In

particular,

$$\lambda_l = \Re\left(\frac{\text{mean}(z^c_{l,alg}(t)\cdot\phi^c(t))}{\text{mean}(|z^c_{l,alg}(t)|^2)}\right), \quad \mu_l = \text{mean}(\phi) - \lambda_l\,\text{mean}(z_{l,alg}(t)); \tag{3.54}$$

with

$$z^c_{l,alg}(t) = z_{l,alg}(t) - \text{mean}(z_{l,alg}(t)), \quad \phi^c(t) = \bar{\phi}(t) - \text{mean}(\bar{\phi}(t)),$$

where the mean has been computed for $N_t + 1$ points. In this regard, we choose the

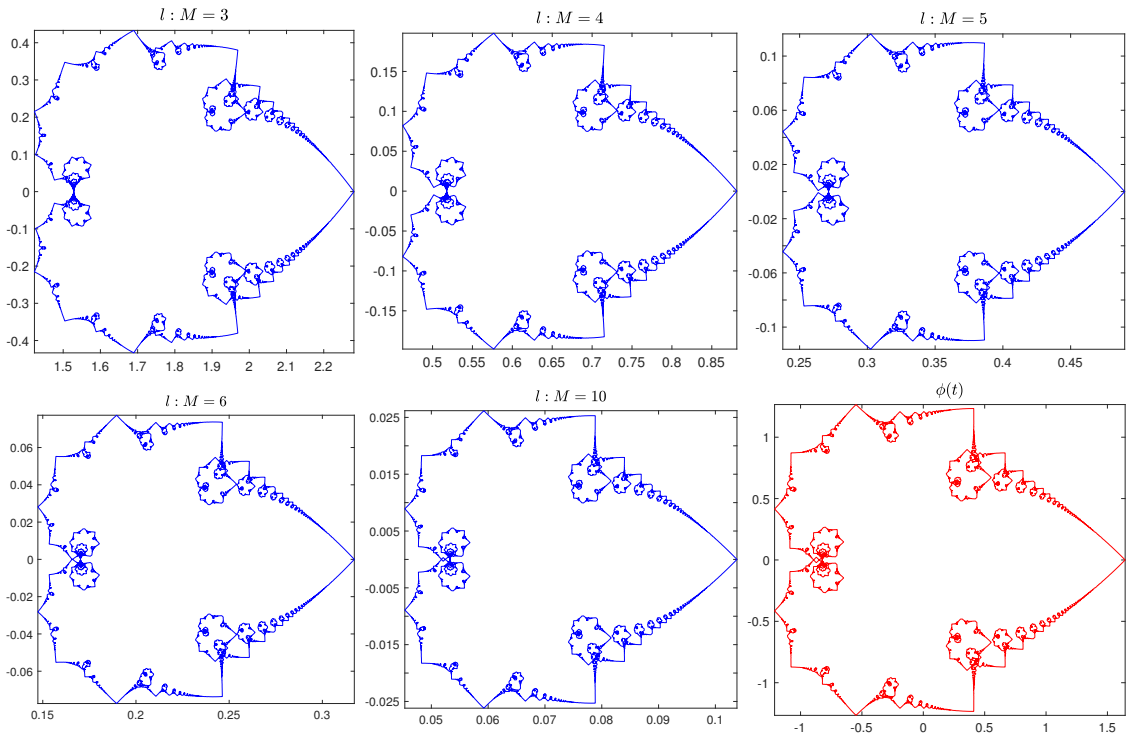

Figure 3.15 $z_l(t)$ (blue) for different values of l computed using (3.53) for $M = 3, 4, 5, 6$ and 10, and $\phi(t)$ (red); parameter t takes its value in the respective intervals which are divided into 7561 points.

value of l from (3.53) for $M = 3, 4, \ldots, 20$ and Table 3.8 shows the absolute error $\max_t |(\phi(t) - \lambda_l z_{l,alg}(t) - \mu_l)|$ and relative error $\max_t |(\phi(t) - \lambda_l z_{l,alg}(t) - \mu_l)/\phi(t)|$, where maximum is taken over 7560 values and sum for $\phi(t)$ has been computed for $k = 1, 2, \ldots, 2^{11}$. It is quite clear that as l gets smaller, the two errors decrease, thus, showing that $z_{l,alg}$ converges to ϕ.

l	$\|\phi(t) - \lambda_l z_l(t) - \mu_l\|_{L^\infty}$	$(\|\phi(t) - \lambda_l z_l(t) - \mu_l)/\phi(t)\|_{L^\infty}$
2.6639	$2.372149809891611 \cdot 10^{-1}$	$2.103146176364024 \cdot 10^{-1}$
1.7627	$1.202137911333187 \cdot 10^{-1}$	$1.069015846447526 \cdot 10^{-1}$
1.3485	$7.395129681674713 \cdot 10^{-2}$	$6.553706601060941 \cdot 10^{-2}$
1.0986	$5.037950918821697 \cdot 10^{-2}$	$4.443542112256472 \cdot 10^{-2}$
0.9293	$3.663493700302557 \cdot 10^{-2}$	$3.213089943830340 \cdot 10^{-2}$
0.8064	$2.789087911280586 \cdot 10^{-2}$	$2.430407039076064 \cdot 10^{-2}$
0.7127	$2.197342077064023 \cdot 10^{-2}$	$1.900794506510361 \cdot 10^{-2}$
0.6389	$1.777857413459586 \cdot 10^{-2}$	$1.525374219018601 \cdot 10^{-2}$
0.5791	$1.472276688206210 \cdot 10^{-2}$	$1.249405615271557 \cdot 10^{-2}$
0.5297	$1.246933387993874 \cdot 10^{-2}$	$1.040521660507873 \cdot 10^{-2}$
0.4881	$1.072191965674805 \cdot 10^{-2}$	$8.785609255857535 \cdot 10^{-3}$
0.4526	$9.339284815580278 \cdot 10^{-3}$	$7.504212131235847 \cdot 10^{-3}$
0.4220	$8.226335556448189 \cdot 10^{-3}$	$6.472826985297105 \cdot 10^{-3}$
0.3952	$7.317114759958195 \cdot 10^{-3}$	$5.630289048039735 \cdot 10^{-3}$
0.3717	$6.564693662811320 \cdot 10^{-3}$	$4.933085043817143 \cdot 10^{-3}$
0.3508	$5.934935939585980 \cdot 10^{-3}$	$4.373662840752222 \cdot 10^{-3}$
0.3322	$5.402525137486635 \cdot 10^{-3}$	$3.944858964309793 \cdot 10^{-3}$
0.3155	$4.948361852601247 \cdot 10^{-3}$	$3.579444073336197 \cdot 10^{-3}$

Table 3.8 The maximum errors between $\phi(t) = \sum_{k=1}^{\infty} \frac{e^{2i\pi k^2 t}}{k^2}$ and $z_{l,alg}(t)$. $\phi(t)$ has been computed for $k = 1, 2, \ldots, 2048$ and both $\phi(t)$ and $z_{l,alg}(t)$ have been evaluated at 7561 points.

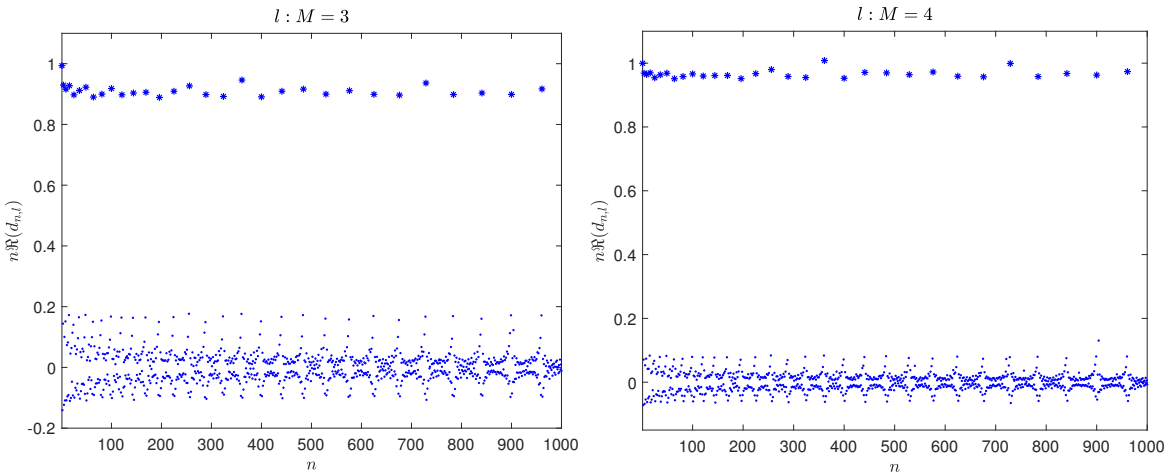

Figure 3.16 Fingerprint of $z_{l,alg}^{scaled}(t)$ for different values of l which are chosen using (3.53) for $M = 3, 4$.

Furthermore, using the fact that $z_{l,alg}(t)$ is T_f-periodic, we express the scaled $z_{l,alg}$ in terms of its Fourier expansion

$$z_{l,alg}^{scaled}(t) = \sum_{n=-\infty}^{\infty} d_{n,l}\, e^{2\pi i n t/T_f},\ t \in [0, T_f],$$

where $z_{l,alg}^{scaled}(t) = \lambda_l z_{l,alg}(t) + \mu_l$, and compute its fingerprint plot. This approach was also employed in Chapter 2 where the Fourier coefficients $d_{n,l}$ are approximated numerically by using the `fft` algorithm in MATLAB. Figures 3.16, 3.17 show the fingerprint for l in (3.53) such that $M = 3, 4, 5$ and 10. We observe that the dominating points (represented by blue stars) of $nd_{n,l}$ correspond to the squares of n whose value gets closer to 1 as l becomes smaller. On the other hand, the rest of the points (noise) approach to zero for smaller value of l; in other words, as l tends to zero, the dominating points converge to 1 whereas the rest of them to zero. As a result, we conjecture that

$$\lim_{l\to 0} |n\, d_{n,l}| = \begin{cases} 1, & \text{if } n = k^2, k \in \mathbb{Z}, \\ 0, & \text{otherwise}, \end{cases}$$

which also shows convergence of $z_{l,alg}^{scaled}$ to ϕ, as l tends to zero.

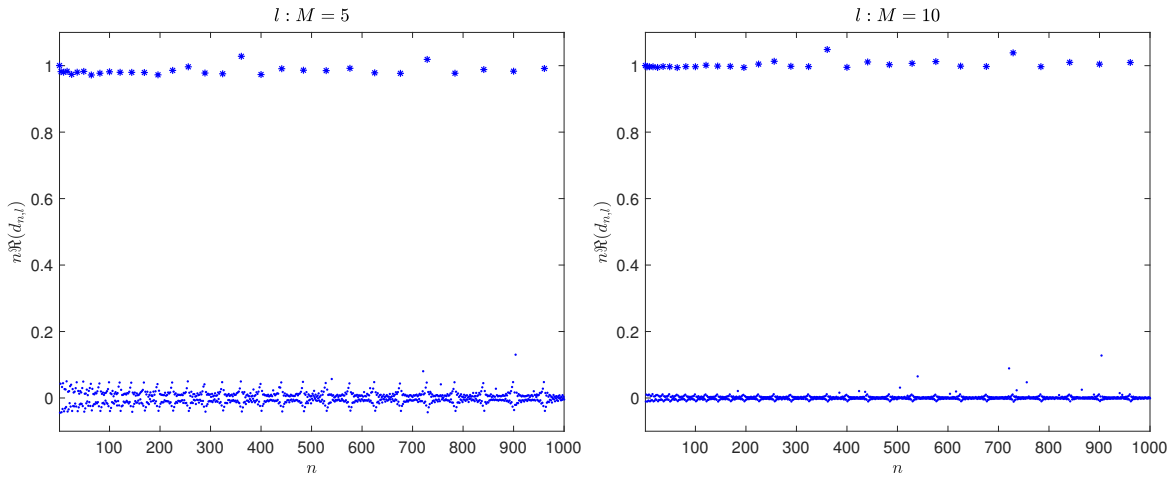

Figure 3.17 Fingerprint of $z_{l,alg}^{scaled}(t)$ for different values of l which are chosen using (3.53) for $M = 5, 10$.

Behavior of the tangent vector T near irrational times

Having seen the evolution of the regular M-polygons in the Euclidean case at rational times t_{pq} with $q \gg 1$, we are motivated to do the same for a planar l-polygon [22, 25].

In this direction, we consider the algebraic solution $\mathbf{T}_{alg}$ that is free from the numerical errors and has been determined completely in the previous section.

Recall that given any rational time t_{pq}, the polygonal curve $\mathbf{X}$ has q or $q/2$ times more sides and the tangent vector $\mathbf{T}$ has q or $q/2$ times more jumps. With this, first we consider t_{pq} with a *small* q and examine the evolution at $t = t_{pq} + \epsilon$, $|\epsilon| \ll 1$. We take $\epsilon = \frac{T_f}{q'}$, $q' \gg 1$, and with $\gcd(q, q') = 1$, $\frac{p}{q} + \frac{1}{q'} = \frac{pq'+1}{qq'}$, therefore, at $t_{pq} + \epsilon$, there will be qq' or $qq'/2$ times more sides. Figure 3.18 shows the stereographic projection of $\mathbf{T}_{alg}$ onto $\mathbb{C}$ for $M = 8$, $l = 0.6$, $p = 1$, $q = 3$, $q' = 7999$. One can observe the 24 spiral-like structures whose center correspond to the values of $\mathbf{T}$ at $t = T_f/3$. Moreover, it is important to mention that these are not really spirals, but 8×23997 tangent vectors that closely resemble to a curve with 24 spirals. These spirals can be compared with the Cornu spiral which also appeared in [21, 22].

As a next step, we consider the rational times t_{pq} with a *large* q such that there is no pair $\tilde{p}, \tilde{q}$, with both $\tilde{q}$ and $|\frac{p}{q} - \frac{\tilde{p}}{\tilde{q}}|$ small. In particular, for the same parameters as before, we have taken $t = \left(\frac{1}{3} + \frac{1}{31} + \frac{1}{301}\right) T_f = \frac{10327}{27993} T_f$. The corresponding stereographic projection of $\mathbf{T}_{alg}$ is shown in Figure 3.18 where one can observe the spiral structures at a smaller scale, thus exhibiting a fractal-like phenomenon.

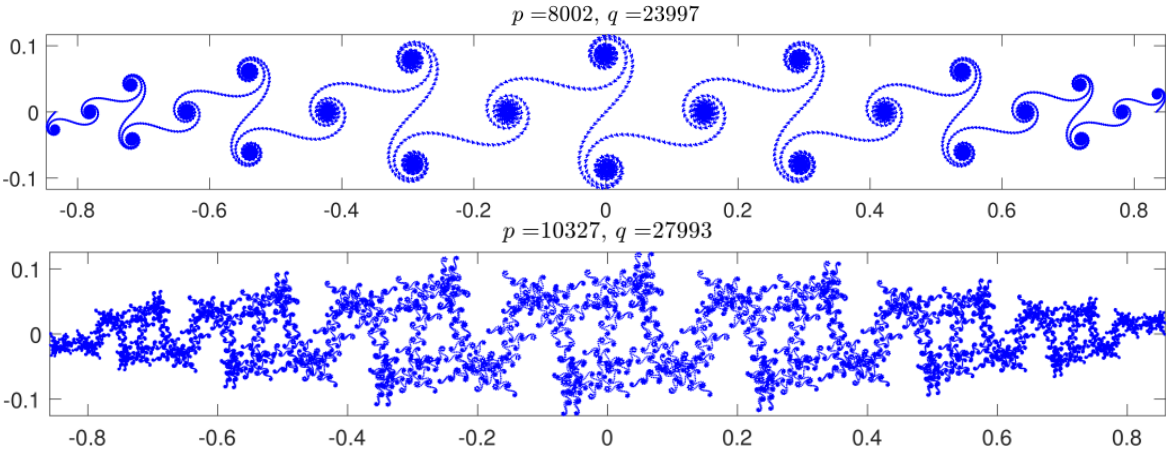

Figure 3.18 The stereographic projection of $\mathbf{T}_{alg}(s, t_{pq})$, at two different values of t_{pq} for $M = 8$, $l = 0.6$.

3.4.2 Fixed boundary conditions for X

As a next approach, we fix the boundary condition for $\mathbf{X}$ and consider the following initial-boundary value problem,

$$\begin{cases} \mathbf{X}_t(s,t) = \mathbf{X}_s(s,t) \wedge_- \mathbf{X}_{ss}(s,t), \ s \in [-L/2, L/2], \\ \mathbf{X}(-L/2,t) = \mathbf{X}^-, \ \mathbf{X}(+L/2,t) = \mathbf{X}^+, \ t \in [0, T_f], \end{cases} \tag{3.55}$$

with initial conditions $\mathbf{X}(s,0)$ given by (3.12) and

$$\begin{cases} \mathbf{X}^- = \frac{(l/2)}{\sinh(l/2)} \left(-\sinh\left(L/2\right), \cosh\left(L/2\right), 0\right)^T, \\ \mathbf{X}^+ = \frac{(l/2)}{\sinh(l/2)} \left(\sinh\left(L/2\right), \cosh\left(L/2\right), 0\right)^T, \end{cases}$$

and the tangent vector can be computed at any time using $\mathbf{T}(s,t) = \mathbf{X}_s(s,t)$.

Thus, by using the finite difference space discretization mentioned above, we integrate (3.55) numerically by using a fourth-order Runge–Kutta method in time. Using the notations the same as before

$$\mathbf{T}_j^{(n)} \equiv \mathbf{T}^{(n)}(s_j) \equiv \mathbf{T}(s_j, t^n), \ \mathbf{X}_j^{(n)} \equiv \mathbf{X}^{(n)}(s_j) \equiv \mathbf{X}(s_j, t^n),$$

we calculate

$$\mathbf{X}_j^{(n+1)} = \mathbf{X}_j^{(n)} + \tfrac{\Delta t}{6}(\mathbf{A}_j^X + \mathbf{B}_j^X + \mathbf{C}_j^X + \mathbf{D}_j^X), \ j = 0, 1, 2, \ldots, N,$$

where

$$\begin{aligned} \mathbf{A}_j^X &= D^{+-}\mathbf{X}_j^{(n)} \wedge_- F^{+-}\mathbf{X}_j^{(n)}, \ \mathbf{X}_j^{(A)} = \mathbf{X}_j^{(n)} + \tfrac{\Delta t}{2}\mathbf{A}_j^X, \\ \mathbf{B}_j^X &= D^{+-}\mathbf{X}_j^{(A)} \wedge_- F^{+-}\mathbf{X}_j^{(A)}, \ \mathbf{X}_j^{(B)} = \mathbf{X}_j^{(n)} + \tfrac{\Delta t}{2}\mathbf{B}_j^X, \\ \mathbf{C}_j^X &= D^{+-}\mathbf{X}_j^{(B)} \wedge_- F^{+-}\mathbf{X}_j^{(B)}, \ \mathbf{X}_j^{(C)} = \mathbf{X}_j^{(n)} + \Delta t\mathbf{C}_j^X, \\ \mathbf{D}_j^X &= D^{+-}\mathbf{X}_j^{(C)} \wedge_- F^{+-}\mathbf{X}_j^{(C)}, \end{aligned}$$

with the boundary conditions

$$\mathbf{X}_0^{(n)} \equiv \mathbf{X}^-, \ \mathbf{X}_N^{(n)} \equiv \mathbf{X}^+,$$

N	Δs	Δt_{max}
256	$3.7500 \cdot 10^{-2}$	$7.441010326374327 \cdot 10^{-4}$
512	$1.8750 \cdot 10^{-2}$	$1.860252581593582 \cdot 10^{-4}$
1024	$9.3750 \cdot 10^{-3}$	$4.654409383678499 \cdot 10^{-5}$
2048	$4.6875 \cdot 10^{-3}$	$1.164548364087039 \cdot 10^{-5}$
4096	$2.3437 \cdot 10^{-3}$	$2.912110775760220 \cdot 10^{-6}$

Table 3.9 Δt_{max} for $L = 9.6$, $T_f = 5.7296 \cdot 10^{-2}$.

n	$\|\mathbf{X}(\cdot, \Delta t) - \mathbf{X}(\cdot, \Delta t/2)\|$	$\log_2 \left(\frac{\|\mathbf{X}(\cdot,\Delta t) - \mathbf{X}(\cdot,\Delta t/2)\|}{\|\mathbf{X}(\cdot,\Delta t/2) - \mathbf{X}(\cdot,\Delta t/4)\|} \right)$
1	$3.833657201833302 \cdot 10^{-4}$	0.634443131578382
2	$2.469601403923588 \cdot 10^{-4}$	3.515912027538592
3	$2.158896791826083 \cdot 10^{-5}$	4.035430655460087
4	$1.316576831285029 \cdot 10^{-6}$	4.029028353939669
5	$8.064692640601389 \cdot 10^{-8}$	4.015343036826833

Table 3.10 The order of accuracy for the Runge–Kutta method in time with fixed boundary conditions on tangent vector $\mathbf{X}$ for $M = 16$, $l = 0.6$, computed using (3.37), with $\Delta t = 2^{-n} \cdot 1.818913635335947 \cdot 10^{-4}$.

and

$$\mathbf{T}_j^{(n)} = D^{+-}\mathbf{X}_j^{(n)}, \ n = 0, 1, \ldots, N_t.$$

Note that $\mathbf{T}^{(n)}$ thus obtained may not have a unit norm for all n, and normalizing it at every time instant will not affect the solution $\mathbf{X}^{(n)}$.

Stability

From the discretization defined before, it is clear that Δt is a function of Δs. We have computed numerically the value of Δt_{max}, maximum value of Δt, for which the numerical scheme is stable. We have taken $M = 16$, $l = 0.6$, $L = 9.6$, $t \in [0, T_f]$, where $T_f = 5.7296 \cdot 10^{-2}$. The values of different Δs, Δt_{max} have been recorded in the table 3.9, and it is quite clear that $\Delta t/\Delta s^2 \approx 0.5301\ldots$, in other words, $\Delta t = \mathcal{O}(\Delta s^2)$.

Accuracy

Denoting the numerical solution as $\mathbf{T}_{num}(s,t)$, $\mathbf{X}_{num}(s,t)$, we have $\mathbf{X}_{num}(s,t) = \mathbf{X}(s,t) + \mathcal{O}(\Delta s^4) + \mathcal{O}(\Delta t^4)$. It is important to note that since the initial data for the curve $\mathbf{X}$ is piecewise differentiable, as a result, a fourth-order accuracy in space is not achieved, nevertheless, we check the accuracy with respect to the time variable. In this

direction, we have taken the parameters $M = 16, l = 0.6, L = 9.6$, and different values of time steps, i.e., $\Delta t = 2^{-n} \cdot 1.8189 \cdot 10^{-4}$, $n = 1, \ldots, 7$, $N = 2^5 M$, $\Delta s = 1.875 \cdot 10^{-2}$, $T_f = 5.7296 \cdot 10^{-4}$. Table 3.2 shows the corresponding error values for the tangent vector $\mathbf{T}$ where $\|\cdot\|$ is as in (3.37).

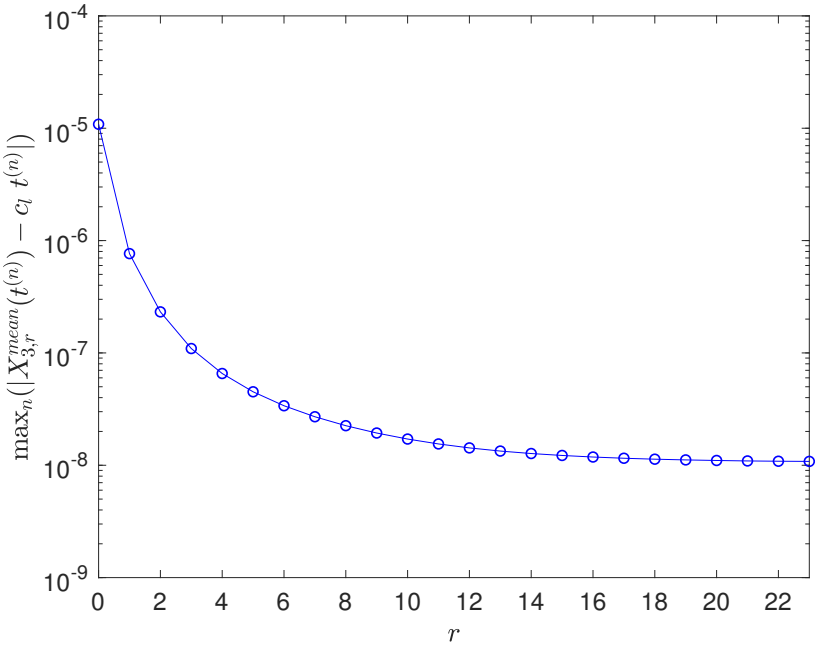

Figure 3.19 The error $\max_n(|X_{3,r}^{mean}(t^{(n)}) - c_l t^{(n)}|)$ for $M = 96, l = 0.1, N/M = 2^9$, where the mean of $X_3(s_j, t^{(n)})$ has been computed using $4rN/M$ values such that $s_j \in [-L/2 + 2rl, L/2 - 2rl]$, $r = 0, 1, 2, \ldots, M/4 - 1$. Results when boundary conditions on $\mathbf{X}$ are considered.

Numerical results

We have performed the same numerical experiments with the same parameters as done in the previous section, and the observations are the following

1. The third component of the center of mass, i.e., $X_3^{mean}(t)$ is linear as noticed before. Figure 3.19 shows that choosing inner points for $\mathbf{X}$ yields more accurate results where we have taken $M = 96$, $l = 0.1$, $N/M = 2^9$. As a next step, we compute the error $\max_n(|X_{3,r}^{mean}(t^{(n)}) - c_l t^{(n)}|)$ for all N and $N/2$ (inner) points for $M = 96$, $l = 0.025, 0.05, 0.1, 0.12, 0.15$, and different discretization, i.e., $N/M = 2^n$, $N_t = 5040 \cdot 4^{n-7}$, $n = 7, 8, 9, 10$, and present the results in Tables 3.11, 3.12, respectively. The errors clearly show the agreement between the numerical and algebraic approach.

l	$N/M = 2^7$	$N/M = 2^8$	$N/M = 2^9$	$N/M = 2^{10}$
0.15	$9.3160 \cdot 10^{-8}$	$6.1953 \cdot 10^{-8}$	$4.8137 \cdot 10^{-8}$	$4.0215 \cdot 10^{-8}$
0.12	$3.9341 \cdot 10^{-8}$	$2.8732 \cdot 10^{-8}$	$2.5508 \cdot 10^{-8}$	$2.5558 \cdot 10^{-8}$
0.1	$2.0118 \cdot 10^{-8}$	$1.5477 \cdot 10^{-8}$	$1.4274 \cdot 10^{-8}$	$1.1907 \cdot 10^{-8}$
0.05	$2.0160 \cdot 10^{-9}$	$2.1002 \cdot 10^{-9}$	$2.6505 \cdot 10^{-9}$	$2.6784 \cdot 10^{-9}$
0.025	$3.1577 \cdot 10^{-10}$	$4.1408 \cdot 10^{-10}$	$6.0336 \cdot 10^{-10}$	$6.4325 \cdot 10^{-10}$

Table 3.11 The error $\max_n(|X_{3,r}^{mean}(t^{(n)}) - c_l t^{(n)}|)$ for $M = 96$ and different N/M, l, where $X_{3,r}^{mean}(t^{(n)})$ is computed using (3.42) for $r = M/8$, i.e., $N/2$ points and fixed boundary condition on $\mathbf{X}$.

l	$N/M = 2^7$	$N/M = 2^8$	$N/M = 2^9$	$N/M = 2^{10}$
0.15	$2.4371 \cdot 10^{-5}$	$2.4396 \cdot 10^{-5}$	$2.4403 \cdot 10^{-5}$	$2.4371 \cdot 10^{-5}$
0.12	$1.5609 \cdot 10^{-5}$	$1.5617 \cdot 10^{-5}$	$1.5614 \cdot 10^{-5}$	$1.5585 \cdot 10^{-5}$
0.1	$1.0845 \cdot 10^{-5}$	$1.0848 \cdot 10^{-5}$	$1.0852 \cdot 10^{-5}$	$1.0858 \cdot 10^{-5}$
0.05	$2.7132 \cdot 10^{-6}$	$2.7126 \cdot 10^{-6}$	$2.7125 \cdot 10^{-6}$	$2.7126 \cdot 10^{-6}$
0.025	$6.7841 \cdot 10^{-7}$	$6.7819 \cdot 10^{-7}$	$6.7810 \cdot 10^{-7}$	$6.7808 \cdot 10^{-7}$

Table 3.12 The error $\max_n(|X_{3,r}^{mean}(t^{(n)}) - c_l t^{(n)}|)$ for $M = 96$ and different N/M, l, where $X_{3,r}^{mean}(t^{(n)})$ is computed using (3.42) for $r = 0$, i.e., N points and fixed boundary condition on $\mathbf{X}$.

2. $X_{2,r}^{mean}(t)$ for $M = 96$, $l = 0.1$, $N/M = 2^9$, has been plotted in Figure 3.20 which can be compared with Figure 3.6, especially when the inner points are considered.

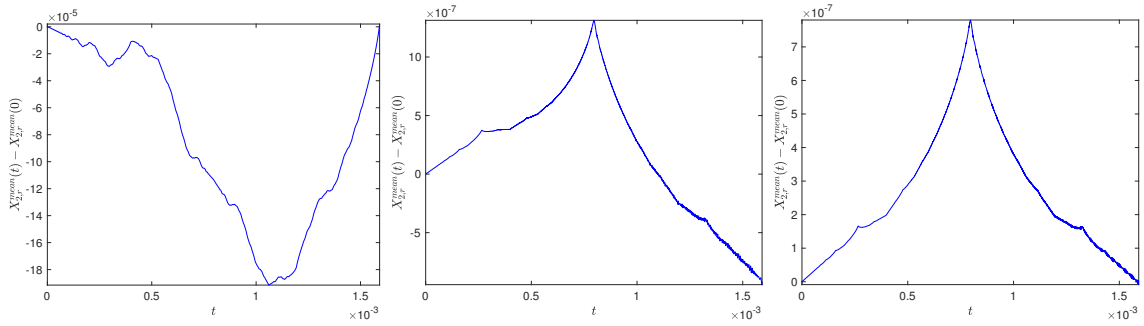

Figure 3.20 $X_{2,r}^{mean}(t) - X_{2,r}^{mean}(0)$ for $M = 96$, $N/M = 2^9$, $l = 0.1$, $t \in [0, T_f]$, using $r = 0$ (left), i.e., N points, for $r = M/8$ (center), i.e., $N/2$ points and $r = M/4$ (right), i.e., $4N/M$ points, for fixed boundary conditions of $\mathbf{X}$.

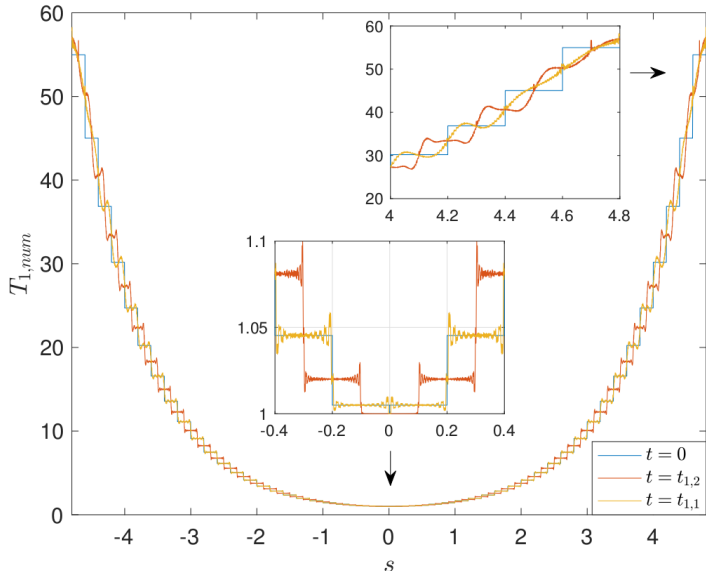

Figure 3.21 The first component of $\mathbf{T}_{num}(s,t)$ for $M = 48$, $l = 0.2$, $N/M = 2^{11}$ at initial, half and final time period for fixed boundary condition of $\mathbf{X}$.

3. We have also plotted the first component of tangent vector $\mathbf{T}$ at initial, final and at half of the time period in Figure 3.21, and in the magnified part it is quite clear that the information at the boundary is not captured well; moreover, when compared with Figure 3.8, the oscillations are bigger.

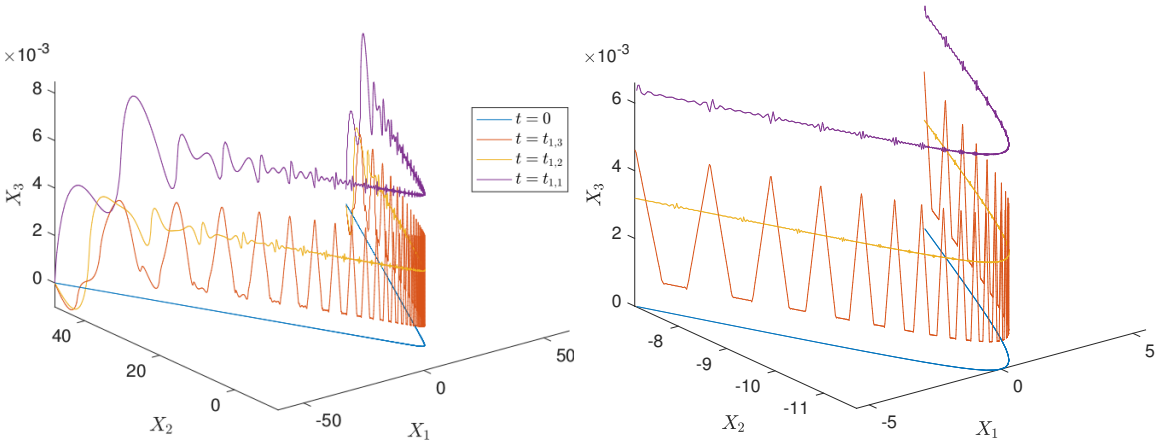

Figure 3.22 $\mathbf{X}_{num}(s, t_{pq})$ for $M = 48, l = 0.2$, $N/M = 2^{11}$ at different rational times t_{pq} for fixed boundary conditions on $\mathbf{X}$. The error towards the boundary points of $\mathbf{X}_{num}$ is quite prominent, however, as we move away the difference between the two figures is almost indistinguishable.

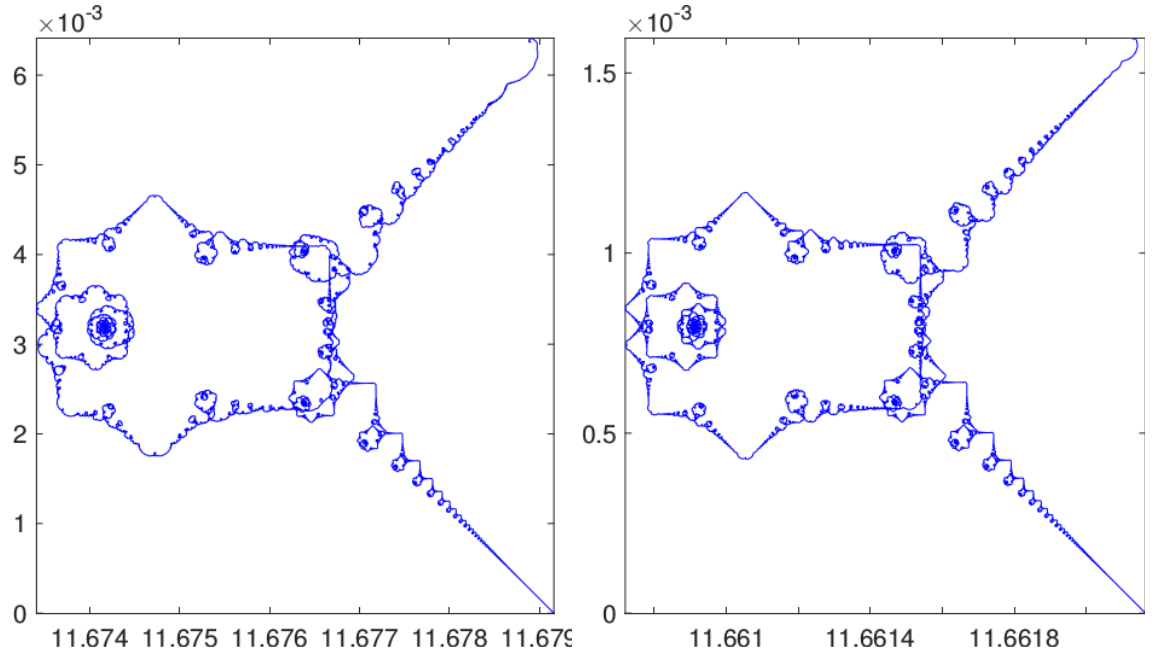

Figure 3.23 $z(t)$ for $M = 48$, $l = 0.2$ (left), and $M = 96$, $l = 0.1$ (right), $N/M = 2^{11}$.

4. The evolution of $\mathbf{X}$ at different rational times is shown in Figure 3.22. We have plotted all the points (left) and inner points (right) at $t = 0, t_{1,3}, t_{1,2}, T_f$ which can be compared with Figures 3.10, 3.11.

5. Although we do not see much difference at a visual level in $\mathbf{X}$, $\mathbf{T}$ obtained from the two approaches (i.e., fixed boundary condition for $\mathbf{X}$ and $\mathbf{T}$), the trajectory $\mathbf{X}(0,t)$ seems to show the imperfection more than the previous case. For example, when compared Figure 3.23 with Figure 3.12, both for $M = 48$, $l = 0.2$, $N/M = 2^{11}$, and one can clearly see that as time progresses, the corners of $\mathbf{X}(0,t)$ gets more rounded. This can partially be explained by the noting that in the case of fixed boundary condition for $\mathbf{T}$, it is normalized at every time instant, whereas in the current scenario, we only work with $\mathbf{X}$, so renormalizing $\mathbf{T}$ does not affect $\mathbf{X}$. Consequently, the error propagation is faster. During our simulations, we keep track of $\|\mathbf{T}(\cdot, t^{(n)})\|_0^2 + 1$, for instance, for the parameters mentioned above, $\max_n(\|\mathbf{T}(\cdot, t^{(n)})\|_0^2 + 1) = 5.875199227447503 \cdot 10^{-4}$. Figure 3.24 shows $z(t)$ and $z_l(t)$ for $M = 192$, $l = 0.05$, $N/M = 2^{11}$, and it can be seen that the corners are less rounded, but definitely not better than the previous approach (for example, see Figure 3.13); moreover, $\max_n, (\|\mathbf{T}(\cdot, t^{(n)})\|_0^2 + 1) = 5.958725168397905 \cdot 10^{-5}$.

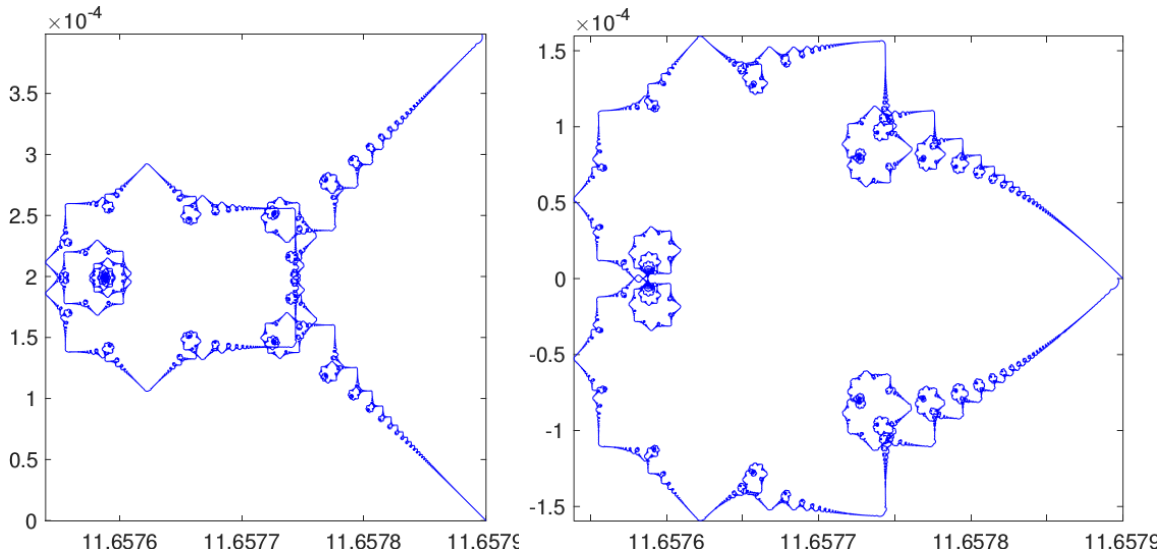

Figure 3.24 $z(t)$ (left) and $z_l(t)$ (right) for $M = 192, l = 0.05$, $N/M = 2^{11}$.

Thus, having compared the two ways of fixing the boundary condition with finite difference space discretization, it seems very clear that the better results are obtained when the end points for $\mathbf{T}$ are fixed. Recall that this was also a suitable choice when the numerical study for the one-corner problem was done in [15, 24].

3.5 Chebyshev spectral discretization

We noticed that in the Euclidean case, due to the periodicity of tangent vector $\mathbf{T}$, a pseudo-spectral discretization with trigonometric basis functions is very useful. In the hyperbolic case, this not being the case, we have tried the finite difference discretization which combined with fourth-order Runge–Kutta method gave reasonably good results. However, due to their spectral accuracy, we are tempted to try the Chebyshev spectral discretization which was remarkably accurate and efficient in the case of one-corner problem [24].

We have seen in the previous section that working (i.e., fixing boundary conditions) with the tangent vector $\mathbf{T}$ gives relatively better results, as a result, we follow the same approach in this section as well. We will consider the Chebyshev spectral collocation method [16, 59] with nodes s_j

$$s_j = (L/2)\cos(j\pi/N), \ j = 0, 1, \ldots, N, \tag{3.56}$$

and approximate the tangent vector $\mathbf{T}$ by a polynomial of the form

$$\mathbf{T}(s,t) \approx \sum_{k=0}^{N} a_k(t) U_k(s/L), \ \forall t \geq 0,$$

where $U_k(s) = \cos(k \arccos(s))$ is the Chebyshev polynomial of degree k.

Furthermore, due to the unequal distribution of Chebyshev points, we need to reparameterize the initial data $\mathbf{T}(s,0)$, $\mathbf{X}(s,0)$, at the same time bearing in mind that the sides of the planar l-polygon have equal (hyperbolic) length. We consider M equally sized intervals $[\tilde{s}_k, \tilde{s}_{k+1}]$, where $\tilde{s}_k = -L/2 + kL/M$, $k = 0, 1, \ldots, M-1$ and divide the interval $[-L/2, L/2]$ into $N+1$ points given by (3.56). Thus, for given M piecewise constant tangent vector $\mathbf{T}_k \equiv \mathbf{T}(s,0)$ for $s \in [\tilde{s}_k, \tilde{s}_{k+1}]$, one way to obtain $\mathbf{T}(s_j, 0)$ could be the following:

1. Compute the count/density d_k of Chebyshev nodes s_j's belonging to interval $[\tilde{s}_k, \tilde{s}_{k+1})$ for $k = 0, 1, \ldots, M/2 - 1$. Due to the symmetry of s_j's, the remaining d_k values can be computed as $d_{M-k-1} = d_k$, such that $\sum_{k=0}^{M-1} d_k = N$.

2. Compute $\mathbf{T}(s_{\tilde{j}}, 0) = \mathbf{T}_k$, for $\tilde{j} = j - 1 + \sum_{r=0}^{k} d_{r-1}$, $j = 1, 2, \ldots, d_k$, $k = 0, 1, \ldots, M/2 - 1$, $d_{-1} = 0$; and $\mathbf{T}(s_{\tilde{j}}, 0) = \mathbf{T}_k$, for $\tilde{j} = j + \sum_{r=0}^{k} d_{r-1}$, $j = 1, 2, \ldots, d_k$, $k = M/2, M/2 + 1, \ldots, M - 1$.

3. Note that $\mathbf{T}(s_{N/2},0)$ is yet to be evaluated, so from N values of $\mathbf{T}(s_j,0)$, $N+1$ values can be obtained by

$$\begin{aligned}
\tilde{\mathbf{T}}(s_0,0) &= \mathbf{T}(s_0,0),\\
\tilde{\mathbf{T}}(s_{j+1},0) &= \tfrac{1}{2}\left[\mathbf{T}(s_j,0)+\mathbf{T}(s_{j+1},0)\right],\ j=0,1,\ldots,N/2-2,\\
\tilde{\mathbf{T}}(s_{N/2},0) &= \tfrac{1}{2}\left[\mathbf{T}(s_{N/2-1},0)+\mathbf{T}(s_{N/2+1},0)\right],\\
\tilde{\mathbf{T}}(s_j,0) &= \tfrac{1}{2}\left[\mathbf{T}(s_j,0)+\mathbf{T}(s_{j+1},0)\right],\ j=N/2+1,N/2+2,\ldots,N-1,\\
\tilde{\mathbf{T}}(s_N,0) &= \mathbf{T}(s_N,0),\\
\mathbf{T}(s_j,0) &= \tfrac{\tilde{\mathbf{T}}}{\|\tilde{\mathbf{T}}\|_0}.
\end{aligned}$$

After having obtained $\mathbf{T}(s,0)$, using Chebyshev integration, $\mathbf{X}(s,0)$ can be obtained up to a constant which can be determined from the mean of $\mathbf{X}(s,0)$.

3.5.1 Working with the equation for T

With the initial data mentioned above, we first compute the evolution of (3.1)–(3.2) using the Chebyshev space discretization and a fourth-order Runge–Kutta method in time. As the latter is an explicit scheme, the stability of the numerical method imposes a restriction of $\Delta t=\mathcal{O}(\Delta s^2)$. On the other hand, due to their unequal distribution and clustering towards the boundary, for N Chebyshev nodes in the given interval, the minimum step size $\Delta s=\mathcal{O}(1/N^2)$ implies $\Delta t=\mathcal{O}(1/N^4)$ and hence, makes the method computationally undesirable. The implementation of this scheme is same as the one explained in Section 3.4.1 with the only change that the finite difference matrices[5] have been replaced by their Chebyshev counterparts.

As a next approach, for the integration in time, we use multi-stage methods. The main idea is to work with $\mathbf{T}$ and develop a numerical scheme where the higher-order derivative term in (3.2) can be treated implicitly, thereby eliminating severe restrictions on Δt. In this regard, by denoting $\mathbf{F}_N$ as the Chebyshev second-order differentiation matrix and writing

$$\mathbf{T}^n \equiv \begin{pmatrix} T_1^n \\ T_2^n \\ T_3^n \end{pmatrix},\ \text{where } T_k^n = \begin{pmatrix} T_k^n(s_0) \\ T_k^n(s_1) \\ \vdots \\ T_k^n(s_{N-1}) \\ T_k^n(s_N) \end{pmatrix}\ k=1,2,3,$$

[5] See [59, Theorem 7] for their expression and further details.

corresponds to a $(N+1)$-dimensional column vector, we begin with a first-order method and discretize (3.2) as

$$\begin{aligned}\frac{\mathbf{T}^{n+1}-\mathbf{T}^n}{\Delta t} &= \mathbf{T}^n \wedge_- \mathbf{T}^{n+1}_{ss} = \mathbf{T}^n \wedge_- \mathbf{F}_N\ \mathbf{T}^{n+1} = \begin{pmatrix} T_2^n T_{3,ss}^{n+1} - T_3^n T_{2,ss}^{n+1} \\ -T_1^n T_{3,ss}^{n+1} + T_3^n T_{1,ss}^{n+1} \\ -T_1^n T_{2,ss}^{n+1} + T_2^n T_{1,ss}^{n+1} \end{pmatrix} \\ &= \begin{pmatrix} 0 & T_3^n \mathbf{F}_N & -T_2^n \mathbf{F}_N \\ T_3^n \mathbf{F}_N & 0 & -T_1^n \mathbf{F}_N \\ -T_2^n \mathbf{F}_N & T_1^n \mathbf{F}_N & 0 \end{pmatrix} \begin{pmatrix} T_1^{n+1} \\ T_2^{n+1} \\ T_2^{n+1} \end{pmatrix}.\end{aligned} \tag{3.57}$$

To implement the fixed boundary condition on $\mathbf{T}$, i.e., $T_k(s_0,\cdot) = T_k^+$ and $T_k(s_N,\cdot) = T_k^-$ for $k = 1,2,3$, we first decompose $\mathbf{F}_N = (f_{i,j})$, $i,j = 0,1,\ldots,N$ into

$$f^+ = \begin{pmatrix} f_{1,0} \\ f_{2,0} \\ \vdots \\ f_{N-2,0} \\ f_{N-1,0} \end{pmatrix}, \tilde{\mathbf{F}}_N = \begin{pmatrix} f_{1,1} & f_{1,2} & \cdots & f_{1,N-1} \\ f_{2,1} & f_{2,2} & \cdots & f_{2,N-1} \\ \vdots & \vdots & \ddots & \vdots \\ f_{N-2,1} & f_{N-2,2} & \cdots & f_{N-2,N-1} \\ f_{N-1,1} & f_{N-1,2} & \cdots & f_{N-1,N-1} \end{pmatrix}, f^- = \begin{pmatrix} f_{1,N} \\ f_{2,N} \\ \vdots \\ f_{N-2,N} \\ f_{N-1,N} \end{pmatrix}, \tag{3.58}$$

where the first and the final row of $\mathbf{F}_N$ have been discarded and $\tilde{\mathbf{F}}_N$ is $(N-1)\times(N-1)$ matrix. For the inner grid points, i.e., $i = 1,2,\ldots,N-1$, we can write

$$T_3^n \mathbf{F}_N T_2^{n+1} = \begin{pmatrix} T_{3,1}^n \\ T_{3,2}^n \\ \vdots \\ T_{3,N-2}^n \\ T_{3,N-1}^n \end{pmatrix} \left[T_{2,0}^{n+1} f^+ + T_{2,N}^{n+1} f^- + \tilde{\mathbf{F}}_N \begin{pmatrix} T_{2,1}^{n+1} \\ T_{2,2}^{n+1} \\ \vdots \\ T_{2,N-2}^{n+1} \\ T_{2,N-1}^{n+1} \end{pmatrix} \right] = T_3^n T_{2,bd} + T_3^n \tilde{\mathbf{F}}_N T_2^{n+1},$$

where $T_{2,bd} = T_{2,0}^{n+1} f^+ + T_{2,N}^{n+1} f^-$ is $(N-1)$-dimensional column vector. With this, (3.57) becomes

$$\frac{\mathbf{T}^{n+1}-\mathbf{T}^n}{\Delta t} = \begin{pmatrix} T_3^n T_{2,bd} - T_2^n T_{3,bd} \\ T_3^n T_{1,bd} - T_1^n T_{3,bd} \\ -T_2^n T_{1,bd} + T_1^n T_{2,bd} \end{pmatrix} + \underbrace{\begin{pmatrix} 0 & T_3^n \tilde{\mathbf{F}}_N & -T_2^n \tilde{\mathbf{F}}_N \\ T_3^n \tilde{\mathbf{F}}_N & 0 & -T_1^n \tilde{\mathbf{F}}_N \\ -T_2^n \tilde{\mathbf{F}}_N & T_1^n \tilde{\mathbf{F}}_N & 0 \end{pmatrix}}_{\tilde{\mathbf{F}}} \begin{pmatrix} T_1^{n+1} \\ T_2^{n+1} \\ T_3^{n+1} \end{pmatrix},$$

or,

$$(\mathbf{I}_{N-1} - \Delta t\tilde{\mathbf{F}}) \begin{pmatrix} T_1^{n+1} \\ T_2^{n+1} \\ T_3^{n+1} \end{pmatrix} = \Delta t \begin{pmatrix} T_3^n T_{2,bd} - T_2^n T_{3,bd} \\ T_3^n T_{1,bd} - T_1^n T_{3,bd} \\ -T_2^n T_{1,bd} + T_1^n T_{2,bd} \end{pmatrix} + \begin{pmatrix} T_1^n \\ T_2^n \\ T_3^n \end{pmatrix}, \tag{3.59}$$

where $T_{k,bd} = T_{k,0}^{n+1} f^+ + T_{k,N}^{n+1} f^-$ and $\tilde{\mathbf{F}}$ is $(3N-3)\times(3N-3)$ dimensional matrix. Thus, we have system of $3N-3$ equations and $3N-3$ unknowns, i.e., $T_k^{n+1}(s_j)$, $k = 1, 2, 3$, $j = 1, 2, \ldots, N-1$. Moreover, for Δt sufficiently small, $\mathbf{I}_{N-1} - \Delta t\tilde{\mathbf{F}}$ is invertible, hence, the system has a unique solution. From $\mathbf{T}$, we compute

$$\mathbf{X}_t(0, t^n) = (\mathbf{T} \wedge_- \mathbf{T}_{ss})(0, t^n),$$

from which $\mathbf{X}(0, t)$ can be computed by an integration with respect to time where we can use a fourth-order method. With this, and integrating $\mathbf{X}_s = \mathbf{T}$, we obtain $\mathbf{X}(\cdot, t^n)$ for $n = 1, 2, \ldots, N_t$.

As the numerical results show that the first-order method is unconditionally stable, we move forward to implement a second-order method which is known as second-order semi-implicit backward differentiation formula (SBDF) [2]. Thus, using the notations same as above, (3.2) can be discretized as

$$\frac{1}{2\Delta t}\left(3\mathbf{T}^{n+1} - 4\mathbf{T}^n + \mathbf{T}^{n-1}\right) = \left[(2\mathbf{T}^n - \mathbf{T}^{n-1}) \wedge_- \mathbf{T}_{ss}^{n+1}\right],$$

which in turn can be expressed as

$$\begin{aligned} &\frac{1}{2\Delta t}\left(3\mathbf{T}^{n+1} - 4\mathbf{T}^n + \mathbf{T}^{n-1}\right) = \\ &\quad = \begin{pmatrix} C_3^n T_{2,bd} - C_2^n T_{3,bd} \\ C_3^n T_{1,bd} - C_1^n T_{3,bd} \\ -C_2^n T_{1,bd} + C_1^n T_{2,bd} \end{pmatrix} + \underbrace{\begin{pmatrix} 0 & C_3^n\tilde{\mathbf{F}}_N & -C_2^n\tilde{\mathbf{F}}_N \\ C_3^n\tilde{\mathbf{F}}_N & 0 & -C_1^n\tilde{\mathbf{F}}_N \\ -C_2^n\tilde{\mathbf{F}}_N & C_1^n\tilde{\mathbf{F}}_N & 0 \end{pmatrix}}_{\tilde{\mathbf{F}}} \begin{pmatrix} T_1^{n+1} \\ T_2^{n+1} \\ T_3^{n+1} \end{pmatrix}, \end{aligned}$$

or,

$$\left(3\mathbf{I}_{N-1} - 2\Delta t\tilde{\mathbf{F}}\right) \begin{pmatrix} T_1^{n+1} \\ T_2^{n+1} \\ T_3^{n+1} \end{pmatrix} = 2\Delta t \begin{pmatrix} C_3^n T_{2,bd} - C_2^n T_{3,bd} \\ C_3^n T_{1,bd} - C_1^n T_{3,bd} \\ -C_2^n T_{1,bd} + C_1^n T_{2,bd} \end{pmatrix} + 4 \begin{pmatrix} T_1^n \\ T_2^n \\ T_3^n \end{pmatrix} - \begin{pmatrix} T_1^{n-1} \\ T_2^{n-1} \\ T_3^{n-1} \end{pmatrix}, \tag{3.60}$$

where $C_k^n = 2T_k^n - T_k^{n-1}$, $T_{k,bd} = T_{k,0}^{n+1} f^+ + T_{k,N}^{n+1} f^-$, $k = 1, 2, 3$ are $(N-1)$-dimensional column vectors. As before, we solve a system of $N-1$ equations, and since $3\mathbf{I}_{N-1} - 2\Delta t\tilde{\mathbf{F}}$

is invertible independent of the choice of Δt, the method is unconditionally stable. It is important to mention that for the initialization, two initial data are needed, as $\mathbf{T}(\cdot, t^0)$ is given, we obtain $\mathbf{T}(\cdot, t^1)$ by using the first-order method combined with a fourth-order Richardson extrapolation.

Continuing in this direction, we proceed to construct a third-order method and discretize (3.2) as

$$\frac{1}{\Delta t}\left(\frac{11}{6}\mathbf{T}^{n+1} - 3\mathbf{T}^{n} + \frac{3}{2}\mathbf{T}^{n-1} - \frac{1}{3}\mathbf{T}^{n-2}\right) = \left[(3\mathbf{T}^{n} - 3\mathbf{T}^{n-1} + \mathbf{T}^{n-2}) \wedge_{-} \mathbf{T}_{ss}^{n+1}\right].$$

After introducing the boundary conditions as done above, we note that the method is not numerically stable. We have also tried replacing the implicit part with an extrapolation, i.e.,

$$\frac{1}{\Delta t}\left(\frac{11}{6}\mathbf{T}^{n+1} - 3\mathbf{T}^{n} + \frac{3}{2}\mathbf{T}^{n-1} - \frac{1}{3}\mathbf{T}^{n-2}\right) = \left[(4\mathbf{T}^{n} - 6\mathbf{T}^{n-1} + 4\mathbf{T}^{n-2} - \mathbf{T}^{n-3}) \wedge_{-} \mathbf{T}_{ss}^{n+1}\right].$$

However, this also does not resolve the problem. Thus, we can obtain only a second-order method in time.

3.5.2 Working with the stereographic projection form

In [24], solving the stereographic projection of (3.2) with a Chebyshev spectral discretization combined with second-order semi-implicit backward differentiation formula (SBDF) was found to be very efficient and accurate [2]. Following their approach, we consider the stereographic projection of $\mathbf{T} = (T_1, T_2, T_3)^T$ onto $\mathbb{C}$,

$$z = x + iy \equiv (x, y) \equiv \left(\frac{T_2}{1 + T_1}, \frac{T_3}{1 + T_1}\right), \tag{3.61}$$

where $\mathbf{T}$ is projected from $(-1, 0, 0)^T$ into $\mathbb{R}^2$, identifying $\mathbb{R}^2$ with $\mathbb{C}$ [10]. In the Euclidean case, since $\mathbf{T} \in \mathbb{S}^2$, there is a point on the sphere, $(-1, 0, 0)^T$, corresponding to which there is no point in $\mathbb{C}$, as a result, there is a bijection between $\mathbb{S}^2 - \{(-1, 0, 0)^T\}$ and $\mathbb{R}^2$. However, in the hyperbolic case, $\mathbf{T} \in \mathbb{H}^2$, there is a bijection between $\mathbb{D}$ and $\mathbb{H}^2$, where

$$\mathbb{D} = \{(x, y) \in \mathbb{R}^2 \mid x^2 + y^2 < 1\},$$

is also known as Poincaré disc. Consequently, the tangent vector can be recovered by

$$\mathbf{T} = (T_1, T_2, T_3)^T \equiv \left(\frac{1 + x^2 + y^2}{1 - x^2 - y^2}, \frac{2x}{1 - x^2 - y^2}, \frac{2y}{1 - x^2 - y^2}\right)^T.$$

Next, by differentiating (3.61), using (3.2) we obtain that z solves the following nonlinear Schrödinger equation

$$z_t = iz_{ss} + \frac{2i\bar{z}}{1-|z|^2} z_s^2.$$

By using Chebyshev spectral discretization, we approximate z by a polynomial of the form

$$z(s,t) \approx \sum_{k=0}^{N} a_k(t) U_k(s/L),$$

where $U_k(s) = \cos(k \arccos(s))$ is the Chebyshev polynomial of degree k. For the time evolution, we have considered a semi-implicit second-order backward differentiation formula (SBDF)

$$\frac{1}{2\Delta t}\left[3z^{n+1} - 4z^n + z^{n-1}\right] = iz_{ss}^{n+1} + 2\mathcal{N}(z^n, t^n) - \mathcal{N}(z^{n-1}, t^{n-1}), \tag{3.62}$$

where $\mathcal{N}(z,\cdot) = \frac{2i\bar{z}}{1-|z|^2} z_s^2$. Thus, we solve

$$\begin{cases} z_t = iz_{ss} - \frac{2i\bar{z}}{1+|z|^2} z_s^2, \\ z(s,0) = \left(\frac{\sinh(l/2+s_n)}{1+\cosh(l/2+s_n)}, 0\right), \\ z(-L/2,t) = \left(\frac{\sinh(l/2-L/2)}{1+\cosh(l/2-L/2)}, 0\right), \\ z(+L/2,t) = \left(\frac{\sinh(l/2+L/2)}{1+\cosh(l/2+L/2)}, 0\right). \end{cases} \tag{3.63}$$

One of the main advantages of working with the semi-implicit backward differentiation formula is that treating the second-order derivative term z_{ss} implicitly helps in reducing the restrictions on Δt. Besides that, by working with this form the resulting linear system from the above formulation is less computationally expensive due to the size of the underlying matrix which is $(N-1) \times (N-1)$, as compared with (3.60) where we need to solve $(3N-3) \times (3N-3)$ size matrices.

In [24], the main idea to compute the numerical solution for a certain time $0 < t \ll 1$; however, in the present case, we are interested in $\mathbf{X}$ and $\mathbf{T}$ at all times, for which second-order scheme is not desired. Furthermore, using a higher order scheme such as a third-order and a fourth-order SBDF methods also do not yield satisfactory results. Hence, it can be concluded that the pseudo-spectral discretization does not help us in obtaining better results than the finite difference approach, in particular, a higher

order method in time. The latter is important for our purpose as we are interested in the behavior of $\mathbf{X}$ at all times, for instance, $\mathbf{X}(0,t)$.

3.6 Conclusion

In this chapter, we have discussed the evolution of VFE in the Minkowski space for a regular planar l-polygon characterized by a parameter $l > 0$. It has been observed that the evolution at a theoretical level can be compared with that in the Euclidean case; however, the numerical treatment is quite different and challenging. In this regard, we have found that both from the computational cost and the accuracy point of view a finite difference discretization with fixed boundary conditions for tangent vector $\mathbf{T}$ yields the best results. We have also commented on several other numerical methods that we have tried. On the other hand, to study the trajectory $\mathbf{X}(0,t)$, we have worked with the algebraic solution and shown that it converges to Riemann's non-differentiable function as the parameter l tends to zero. In the rest of this work, we will refer to this problem as *l-polygon problem*.

Chapter 4

Connection between the l-polygon problem and one-corner problem in the Minkowski space

We are like islands in the sea,
separate on the surface but
connected in the deep.

William James

Contents

4.1 Introduction

Given the parameter $c_0 > 0$, let us denote the solutions of the one-corner problem as

$$\mathbf{X}_{c_0},\ \mathbf{T}_{c_0},\ \mathbf{n}_{c_0},\ \mathbf{b}_{c_0},$$

which are obtained by integrating $\mathbf{X}_s = \mathbf{T}$, and the Frenet–Serret frame

$$\begin{pmatrix}\mathbf{T}\\ \mathbf{n}\\ \mathbf{b}\end{pmatrix}_s = \begin{pmatrix}0 & c_0/\sqrt{t} & 0\\ c_0/\sqrt{t} & 0 & s/2t\\ 0 & -s/2t & 0\end{pmatrix}\begin{pmatrix}\mathbf{T}\\ \mathbf{n}\\ \mathbf{b}\end{pmatrix},\ s\in\mathbb{R}, \tag{4.1}$$

with initial conditions

$$\begin{cases}\mathbf{X}(0,t) = 2c_0\sqrt{t}(0,0,1)^T,\ \mathbf{T}(0,t) = (1,0,0)^T,\\ \mathbf{n}(0,t) = (0,1,0)^T,\ \mathbf{b}(0,t) = (0,0,1)^T.\end{cases} \tag{4.2}$$

Recall that the self-similar solutions

$$\mathbf{X}_{c_0}(s,t) = \sqrt{t}\mathbf{X}_{c_0}(s/\sqrt{t},1),\ t>0,$$

form a one-parameter family of curves with c_0 as its curvature at $t=1$ and converge to two non-parallel straight lines as t approaches zero. This was proved in [21, Theorem 1], where it was also shown that $\mathbf{X}_{c_0}$ is smooth for all $t>0$. Moreover, the following asymptotics of $\mathbf{X}_{c_0}$ at $t=1$ were obtained:

$$\mathbf{X}_{c_0}(s,1) = \mathbf{A}^{\pm}\left(s-\frac{2c_0^2}{s}\right) - \frac{4c_0}{s^2}\mathbf{n} + \mathcal{O}\left(\frac{1}{s^3}\right),\ s\to\pm\infty, \tag{4.3}$$

where $\mathbf{A}^{\pm}$ are unit time-like vectors as in (1.24) with $\mathbf{A}^- = \mathbf{A}^1$, $\mathbf{A}^+ = \mathbf{A}^2$. Note that none of the components of $\mathbf{X}_{c_0}(s,1)$ is Lebesgue integrable on $\mathbb{R}$, but if we define

$$\mathbf{e}_0 := \frac{\mathbf{A}^-\wedge_-\mathbf{A}^+}{\|\mathbf{A}^-\wedge_-\mathbf{A}^+\|_0} = \left(0, -\frac{A_3}{\sqrt{A_2^2+A_3^2}}, \frac{A_2}{\sqrt{A_2^2+A_3^2}}\right)^T, \tag{4.4}$$

then, $\mathbf{e}_0\circ_-\mathbf{A}^{\pm} = 0$, as a result, in (4.3), we get rid of the term with $\mathbf{A}^{\pm}$ and $\mathbf{e}_0\circ_-\mathbf{X}_{c_0}$ is finite. Hence, it can be integrated as

$$\int_{-\infty}^{\infty}\mathbf{e}_0\circ_-\mathbf{X}_{c_0}(s,1)ds = \frac{2\pi c_0^2}{\sqrt{1-e^{-\pi c_0^2}}}. \tag{4.5}$$

One of the main outcomes of this chapter is the computation of the above integral. In this regard, first, in Section 4.2, we establish a numerical relationship between the l-polygon and one-corner problems in the Minkowski space. Later, through its application, in Section 4.3, we obtain an expression for the mean speed c_l of the l-polygon with which it propagates in the vertical direction. This is done analytically by computing (4.5) in Theorem 6, and later numerically in Section 4.4. Explicit expressions for the components of $\mathbf{A}^{\pm}$ have been determined in Section 4.5, and in Section 4.6, we comment on the evolution of the linear momentum of the planar l-polygon.

Let us also mention that we denote the numerical solutions of the l-polygon problem by $\mathbf{T}_l$ and $\mathbf{X}_l$, and this chapter follows the approach of [23] where the Euclidean case was considered.

4.2 Numerical connection between the l-polygon problem and the one-corner problem

In this section, we show numerically that the l-polygon problem in the Minkowski space can be explained as a superposition of several one-corner problems at infinitesimal small times. Recall that while solving the l-polygon problem numerically, we consider a regular planar l-polygon with M sides; thus, bearing in mind that the orientation of initial data in each case is in agreement with the other, we solve both the problems for time $t = t_{1,q}$, $q \gg 1$. In other words, we solve the one-corner problem numerically such that the hyperbolic angle at the corner $s = 0$ is equal to that of the l-polygon problem and this can be done by choosing the parameter

$$c_0 = \sqrt{\frac{2}{\pi} \ln\left(\cosh\left(\frac{l}{2}\right)\right)}. \tag{4.6}$$

Also recall that

$$\lim_{s\to-\infty} \mathbf{T}_{c_0} = \mathbf{A}^{-} = (A_1, -A_2, -A_3)^T, \ \lim_{s\to\infty} \mathbf{T}_{c_0} = \mathbf{A}^{+} = (A_1, A_2, A_3)^T,$$

so the curve $\mathbf{X}_{c_0}$ and the orthonormal basis vectors $\mathbf{T}_{c_0}$, $\mathbf{n}_{c_0}$ and $\mathbf{b}_{c_0}$ should be rotated in such a way that for a hyperbolic rotation matrix $\mathbf{H}$, $\mathbf{X}_{rot} \equiv \mathbf{H} \cdot \mathbf{X}_{c_0}$, $\mathbf{T}_{rot} \equiv \mathbf{H} \cdot \mathbf{T}_{c_0}$, match their counterparts in the l-polygon problem. The matrix $\mathbf{H}$ can be computed by enforcing the condition that $\lim_{s\to\pm\infty} \mathbf{T}_{rot}(s)$ correspond to the tangent vector of

the planar l-polygon at $s = 0^{\pm}$, $t = 0$, i.e.,

$$\begin{cases} \lim\limits_{s\to-\infty} \mathbf{T}_{rot}(s) = \left(\cosh\left(l/2\right), -\sinh\left(l/2\right), 0\right)^T, \\ \lim\limits_{s\to\infty} \mathbf{T}_{rot}(s) = \left(\cosh\left(l/2\right), \sinh\left(l/2\right), 0\right)^T. \end{cases}$$

Thus, we have

$$\mathbf{H} = \begin{pmatrix} 1 & 0 & 0 \\ 0 & \frac{A_2}{\sqrt{A_2^2+A_3^2}} & \frac{A_3}{\sqrt{A_2^2+A_3^2}} \\ 0 & \frac{-A_3}{\sqrt{A_2^2+A_3^2}} & \frac{A_2}{\sqrt{A_2^2+A_3^2}} \end{pmatrix}, \tag{4.7}$$

which can be explicitly computed by using the expressions[1] for A_1, A_2, A_3

$$\begin{aligned} A_2 &= \frac{2}{\pi c_0} e^{\pi c_0^2/4} \sinh(\pi c_0^2/2) \Re\left\{\Upsilon\right\}, \\ A_3 &= \frac{2}{\pi c_0} e^{\pi c_0^2/4} \sinh(\pi c_0^2/2) \Im\{\Upsilon\}, \end{aligned} \tag{4.8}$$

with $\Upsilon = e^{i\pi/4}\Gamma(1 - ic_0^2/4)\Gamma(1/2 + ic_0^2/4)$, and $A_2^2 + A_3^2 = e^{\pi c_0^2} - 1$. Furthermore,

$$\begin{aligned} \mathbf{X}_{rot} \equiv \begin{pmatrix} X_{rot,1} \\ X_{rot,2} \\ X_{rot,3} \end{pmatrix} &= \mathbf{H} \cdot \begin{pmatrix} X_{c_0,1} \\ X_{c_0,2} \\ X_{c_0,3} \end{pmatrix} + \frac{l/2}{\sinh(l/2)} \begin{pmatrix} 0 \\ \left(1 - \frac{\sinh(L/2)}{M\tanh(l/2)}\right) \\ 0 \end{pmatrix}, \\ \mathbf{T}_{rot} \equiv \begin{pmatrix} T_{rot,1} \\ T_{rot,2} \\ T_{rot,3} \end{pmatrix} &= \mathbf{H} \cdot \begin{pmatrix} T_{c_0,1} \\ T_{c_0,2} \\ T_{c_0,3} \end{pmatrix}, \end{aligned} \tag{4.9}$$

where $(0, \frac{l/2}{\sinh(l/2)}\left(1 - \frac{\sinh(L/2)}{M\tanh(l/2)}\right), 0)^T$ corresponds to the location of the corner at $t = 0$, $s = 0$ for the planar l-polygon in (3.14).

4.2.1 Numerical experiments

In the following lines, we describe the numerical method for the comparison between the two problems. Depending on whether q is even or odd, for the l-polygon problem, we compute the algebraic solution $\mathbf{T}_{alg}(s, t_{1,q})$ at those $s = s_k \in [-l/2, l/2]$, $l > 0$, which belong to the middle points of the sides of the corresponding skew hyperbolic polygon. In this direction, depending on q, we consider the following discretization:

[1] See Section 4.5 for their computation

q	Error	q	Error	q	Error
501	$1.4912 \cdot 10^{-2}$	500	$7.0958 \cdot 10^{-3}$	502	$6.7851 \cdot 10^{-3}$
1001	$1.1146 \cdot 10^{-2}$	1000	$5.0360 \cdot 10^{-3}$	1002	$5.2768 \cdot 10^{-3}$
2001	$7.8673 \cdot 10^{-3}$	2000	$3.5493 \cdot 10^{-3}$	2002	$3.7201 \cdot 10^{-3}$
4001	$5.5824 \cdot 10^{-3}$	4000	$2.5417 \cdot 10^{-3}$	4002	$2.6345 \cdot 10^{-3}$
8001	$3.9579 \cdot 10^{-3}$	8000	$1.8155 \cdot 10^{-3}$	8002	$1.8638 \cdot 10^{-3}$
16001	$2.8044 \cdot 10^{-3}$	16000	$1.2935 \cdot 10^{-3}$	16002	$1.3181 \cdot 10^{-3}$
32001	$1.9862 \cdot 10^{-3}$	32000	$9.1986 \cdot 10^{-4}$	32002	$9.3214 \cdot 10^{-4}$
64001	$1.4064 \cdot 10^{-3}$	64000	$6.5340 \cdot 10^{-4}$	64002	$6.5944 \cdot 10^{-4}$
128001	$9.9583 \cdot 10^{-4}$	128000	$4.6400 \cdot 10^{-4}$	128002	$4.6694 \cdot 10^{-4}$

Table 4.1 The errors $\max_k(\|\mathbf{T}_{alg}(s_k, t_{1,q}) - \mathbf{T}_{rot}(s_k, t_{1,q})\|)$ for different values of q, $l = 0.6$, decrease as $\mathcal{O}(1/\sqrt{q}) = \mathcal{O}(\sqrt{t_{1,q}})$.

(i) when $q \equiv 1 \bmod 2$:
we choose $s_k = l(2k-1)/2q$, $k = -(q-1)/2, \ldots, (q+1)/2$, $\Delta s = s_{k+1} - s_k = l/q$. For example, for $q = 101$, $k = -50, \ldots, 51$ and $s_{-50} = -l/2$, $\ldots$, $s_0 = -l/2q$, $s_1 = l/2q$, $\ldots$, $s_{51} = l/2$;

(ii) when $q \equiv 0 \bmod 4$:
$s_k = l(2k-1)/q$, $k = -q/4+1, \ldots, q/4$, $\Delta s = 2l/q$. For example, for $q = 100$, $k = -24, \ldots, 25$, and $s_{-24} = -49l/100q$, $\ldots$, $s_0 = -l/q$, $s_1 = l/q$, $\ldots$, $s_{25} = 49l/100q$. Note that in this and the above case, $s = 0$ corresponds to a corner of the skew l-polygon;

(iii) when $q \equiv 2 \bmod 4$:
$s_k = 2lk/q$, $k = -(q-2)/4, \ldots, (q-2)/4$, $\Delta s = 2l/q$. For example, $q = 102$, $k = -25, \ldots, 25$, $s_{-25} = -50l/100$, $\ldots$, $s_0 = 0$, $\ldots$, $s_{25} = 50l/100$. In this case, there is no corner at $s = 0$.

On the other hand, by discretizing the interval $[-l/2, l/2]$ into $2^4q + 1$ points with a step size $\Delta s = l/2^4q$, we solve the one-corner problem numerically, i.e., at time $t = t_{1,q}$, we integrate (4.1) by using a fourth-order Runge–Kutta method with initial conditions (4.2). In this way, $\mathbf{T}_{c_0}(s, t_{1,q})$ can be computed for the same $s = s_k$ as mentioned above and then, from (4.7), we obtain $\mathbf{T}_{rot}(s, t_{1,q})$.

For our numerical simulations, we have taken $M = 8, l = 0.6$ and different values of q. Figure 4.1 shows the errors $\log_{10}(\|\mathbf{T}_{alg}(s_k, t_{1,q}) - \mathbf{T}_{rot}(s_k, t_{1,q})\|)$ for different values of q where $\|\cdot\|$ is the Euclidean distance and we compute it for each s_k. The minimum errors are shown in red color which are attained at very small values of s. Table 4.1

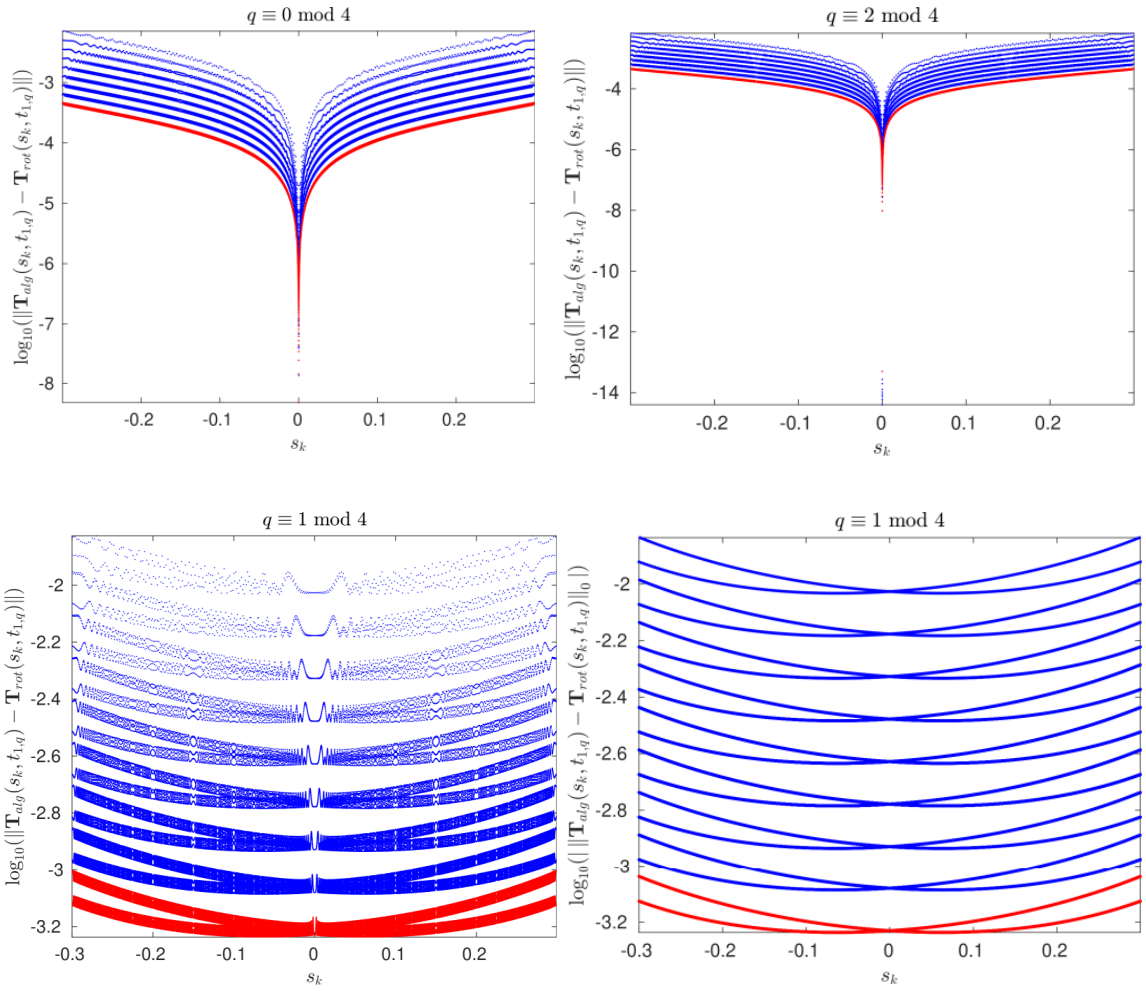

Figure 4.1 The error $\log_{10}(\|\mathbf{T}_{alg}(s_k,t_{1,q}) - \mathbf{T}_{rot}(s_k,t_{1,q})\|)$ for different q values, for $l = 0.6$, $q \equiv 0 \bmod 4$, $q \equiv 2 \bmod 4$, $q \equiv 1 \bmod 4$ and $\log_{10}(|\,\|\mathbf{T}_{alg}(s_k,t_{1,q}) - \mathbf{T}_{rot}(s_k,t_{1,q})\|_0\,|)$ for $q \equiv 1 \bmod 4$. The minimum values obtained for the largest q are shown in red color.

show the errors $\max_k(\|\mathbf{T}_{alg}(s_k, t_{1,q}) - \mathbf{T}_{rot}(s_k, t_{1,q})\|)$ for the same values of q. It is clear from the table that the maximum of error values decreases by a factor of square root of two, every time when q is (approximately) doubled, in other words, it decreases as $\mathcal{O}(1/\sqrt{q}) = \mathcal{O}(t_{1,q})$. Note that the minimum error value is attained at smallest values of $s = |s_k|$.

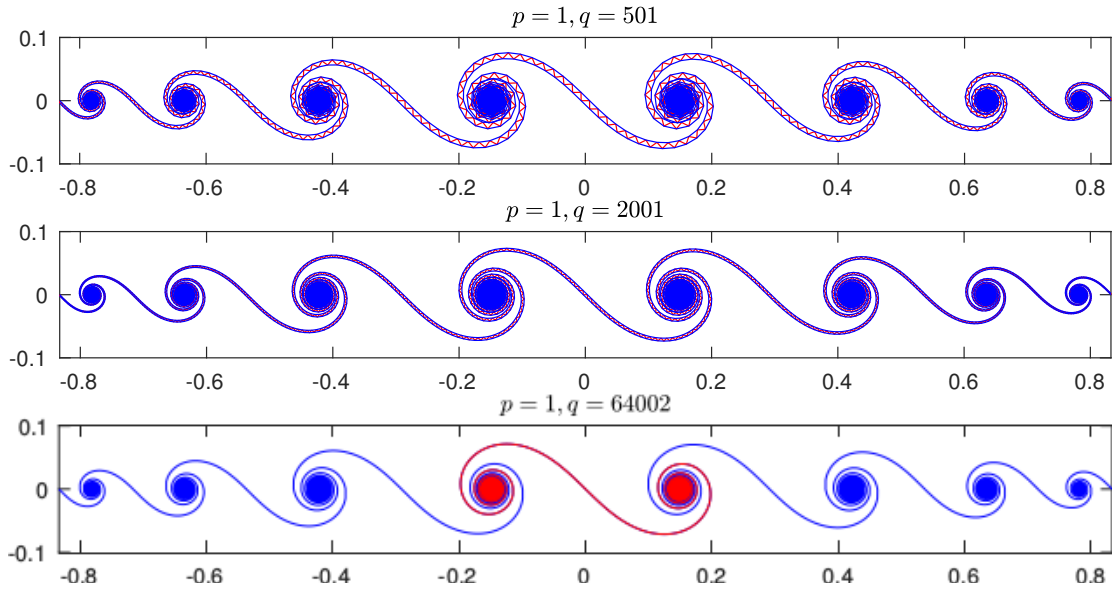

Figure 4.2 The stereographic projection of $\mathbf{T}_{alg}(s, t_{pq})$ for $M = 8, l = 0.6$, $p = 1$, $q = 501, 2001, 64002$.

Nonetheless, for q odd, the plot of $\log_{10}(\|\mathbf{T}_{alg}(s_k, t_{1,q}) - \mathbf{T}_{rot}(s_k, t_{1,q})\|)$ seems to have a different shape when compared with the other two cases. This peculiar phenomenon was also observed in the Euclidean case ([23, Figure 2]) and could be explained by computing $\mathbf{T}_{alg}(s_k, t_{1,q})$ for q odd. For instance, Figure 4.2 shows $\mathbf{T}_{alg}$ for $q = 501$ where $Mq = 8 \times 501$ points (red) appear to form a curve with a sawtooth effect. However, if we plot only the alternate points (blue), we obtain two smooth curves with the sawtooth structure in-between; and as q increases, the structure gets smaller approximately by a factor of one half when q is taken approximately four times bigger as seen in Figure 4.2 where $q = 2001$. This can be further appreciated in the fourth subfigure where we measure the discrepancy between the two curves using $\|\cdot\|_0$ instead of $\|\cdot\|$.

On the other hand, for q even, we obtain a very regular curve as in Figure 4.2 where for $q = 64002$ we have plotted $\mathbf{T}_{alg}$(blue) and $\mathbf{T}_{rot}$(red) together; it is quite clear that the two curves look almost identical. Moreover, for $q/2$ odd, since the tangent

q	Absolute Error	Relative Error
502	$4.452708337809863 \cdot 10^{-5}$	$2.650223938013458 \cdot 10^{-4}$
1002	$2.230639580691474 \cdot 10^{-5}$	$1.327662619091869 \cdot 10^{-4}$
2002	$1.116394232367202 \cdot 10^{-5}$	$6.644708106650881 \cdot 10^{-5}$
4002	$5.584661008195546 \cdot 10^{-6}$	$3.323955032925001 \cdot 10^{-5}$
8002	$2.793003139017758 \cdot 10^{-6}$	$1.662377864527374 \cdot 10^{-5}$
16002	$1.396670628817098 \cdot 10^{-6}$	$8.312895552983875 \cdot 10^{-6}$
32002	$6.983755935496827 \cdot 10^{-7}$	$4.156687515401240 \cdot 10^{-6}$
64002	$3.491995678728266 \cdot 10^{-7}$	$2.078413818533916 \cdot 10^{-6}$
128002	$1.746068324925965 \cdot 10^{-7}$	$1.039248861829102 \cdot 10^{-6}$

Table 4.2 The errors for the approximation of c_0 using (4.10) decrease as $\mathcal{O}(1/q)$ where $c_0 = 0.1680125318446675$, $l = 0.6$.

vector is continuous at $s = 0$, it is also possible to approximate the coefficient c_0, as we will see in the following lines.

Approximation of curvature at the origin

Recall that in the one-corner problem, for any time $t > 0$, $c_0 = \sqrt{t}\,\|\mathbf{T}_s(0,t)\|_0$, so in the case of a planar l-polygon at $t = t_{1,q}$, this becomes $c_0 = \sqrt{t_{1,q}}\,\|\mathbf{T}_s(0,t_{1,q})\|_0$, where we approximate the derivative terms using a finite difference. Thus, without loss of generality we can choose $q \equiv 2 \bmod 4$, in this way, $\mathbf{T}$ is continuous at $s = 0$ and $s = \pm\Delta s$ for $\Delta s = 2l/q$, we can write

$$\mathbf{T}_s(0,t_{1,q}) = \lim_{\Delta s \to 0} \frac{\mathbf{T}_{alg}(\Delta s, t_{1,q}) - \mathbf{T}_{alg}(-\Delta s, t_{1,q})}{2\Delta s},$$

and

$$c_0 = \lim_{\substack{q\to\infty \\ q\equiv 2 \bmod 4}} \sqrt{t_{1,q}} \frac{\|\mathbf{T}_{alg}(2l/q, t_{1,q}) - \mathbf{T}_{alg}(-2l/q, t_{1,q})\|_0}{4l/q}. \tag{4.10}$$

The absolute and relative errors for the above mentioned approximation (4.10) are given in Table 4.2 and it's quite clear that as q increases, the error decreases as $\mathcal{O}(1/q) = \mathcal{O}(t_{1,q})$. On the other hand, recall that at time $t_{1,q}$ for q even, there are $q/2$ times more sides with mutual time-like angle l_q, as a result, from the hyperbolic rotation matrix (3.28)

$$\mathbf{H}_m = \begin{pmatrix} \cosh(l_q) & \cos(\theta_m)\sinh(l_q) & \sin(\theta_m)\sinh(l_q) \\ \cos(\theta_m)\sinh(l_q) & 1+\cos^2(\theta_m)(\cosh(l_q)-1) & \sin(\theta_m)\cos(\theta_m)(\cosh(l_q)-1) \\ \sin(\theta_m)\sinh(l_q) & \sin(\theta_m)\cos(\theta_m)(\cosh(l_q)-1) & 1+\sin^2(\theta_m)(\cosh(l_q)-1) \end{pmatrix},$$

we can write

$$\begin{pmatrix} \mathbf{T}_{alg}(2l/q,t_{1,q})^T \\ \mathbf{e}_{1,alg}(2l/q,t_{1,q})^T \\ \mathbf{e}_{2,alg}(2l/q,t_{1,q})^T \end{pmatrix} = \mathbf{H}_1 \begin{pmatrix} \mathbf{T}_{alg}(0,t_{1,q})^T \\ \mathbf{e}_{1,alg}(0,t_{1,q})^T \\ \mathbf{e}_{2,alg}(0,t_{1,q})^T \end{pmatrix},$$

and

$$\begin{pmatrix} \mathbf{T}_{alg}(-2l/q,t_{1,q})^T \\ \mathbf{e}_{1,alg}(-2l/q,t_{1,q})^T \\ \mathbf{e}_{2,alg}(-2l/q,t_{1,q})^T \end{pmatrix} = \mathbf{H}_{q-1}^{-1} \begin{pmatrix} \mathbf{T}_{alg}(0,t_{1,q})^T \\ \mathbf{e}_{1,alg}(0,t_{1,q})^T \\ \mathbf{e}_{2,alg}(0,t_{1,q})^T \end{pmatrix}.$$

Since we are interested only in the Minkowski norm of $\mathbf{T}_{alg}(2l/q,t_{1,q}) - \mathbf{T}_{alg}(-2l/q,t_{1,q})$, we can discard the global rotation and thus, without loss of generality, by taking

$$\begin{pmatrix} \mathbf{T}_{alg}(0,t_{1,q})^T \\ \mathbf{e}_{1,alg}(0,t_{1,q})^T \\ \mathbf{e}_{2,alg}(0,t_{1,q})^T \end{pmatrix} = \begin{pmatrix} 1 & 0 & 0 \\ 0 & 1 & 0 \\ 0 & 0 & 1 \end{pmatrix},$$

we get

$$\begin{cases} \mathbf{T}_{alg}(2l/q,t_{1,q}) = (\cosh(l_q), \cos(\theta_1)\sinh(l_q), \sin(\theta_1)\sinh(l_q))^T, \\ \mathbf{T}_{alg}(-2l/q,t_{1,q}) = (\cosh(l_q), -\cos(\theta_{q-1})\sinh(l_q), -\sin(\theta_{q-1})\sinh(l_q))^T, \end{cases}$$

and $\|\mathbf{T}_{alg}(2l/q,t_{1,q}) - \mathbf{T}_{alg}(-2l/q,t_{1,q})\|_0$

$$\begin{aligned} &= \left\|(0, (\cos(\theta_1)+\cos(\theta_{q-1}))\sinh(l_q), (\sin(\theta_1)+\sin(\theta_{q-1}))\sinh(l_q))^T\right\|_0 \\ &= \sinh(l_q)\sqrt{2+2(\cos(\theta_1)\cos(\theta_{q-1})+\sin(\theta_1)\sin(\theta_{q-1}))} \\ &= \sinh(l_q)\sqrt{2(1+\cos(\theta-\theta_{q-1}))} = 2\sinh(l_q), \end{aligned}$$

where in the last step, we have used the fact that $\theta_1 = \theta_{q-1}$ which is immediate from the properties of generalized Gauß sums: $G(-p,m,q) = G(-p,-m,q) = G(-p,q-m,q)$ and $m=1$, gives the desired result. Thus, substituting the above expression in (4.10), with $T_f = l^2/2\pi$ gives

$$\begin{aligned} c_0 &= \lim_{q\to\infty} \sqrt{\frac{T_f}{q}}\frac{q}{4l} 2\sinh(l_q) = \lim_{q\to\infty}\sqrt{\frac{q}{2\pi}}\frac{\sinh(l_q)}{2} \\ &= \lim_{q\to\infty}\frac{1}{2}\sqrt{\frac{q}{2\pi}(\cosh^2(l_q)-1)} = \lim_{q\to\infty}\frac{1}{2}\sqrt{\frac{q}{2\pi}\left[\left(2\cosh^{4/q}(l/2)-1\right)^2-1\right]}, \end{aligned}$$

using L'Hôpital's rule, we obtain

$$c_0 = \lim_{q\to\infty} \frac{1}{2}\left[\frac{8}{\pi}\left(2\cosh^{4/q}(l/2)-1\right)e^{\frac{4}{q}\ln\cosh(l/2)}\ln\cosh(l/2)\right]^{1/2} = \sqrt{\frac{2}{\pi}\ln\cosh(l/2)}.$$

Recall that l is the angle between time-like vectors $\mathbf{A}^+$ and $\mathbf{A}^-$

$$\cosh(l) = \mathbf{A}^+ \circ_- \mathbf{A}^- = -1 + 2A_1^2,$$

thus, we recover

$$e^{\pi c_0^2/2} = \cosh(l/2) = \sqrt{\frac{1+\cosh(l)}{2}} = A_1.$$

Furthermore, we compare the time evolution of a one point in both the problems and thus, we compute $\mathbf{X}_l(0,t)$ and $\mathbf{X}_{rot}(0,t)$ for $t \in [0, t_{1,20}]$. In this regard, we have

$$\begin{aligned}\mathbf{X}_{rot}(0,t) \equiv \begin{pmatrix} X_{rot,1}(0,t) \\ X_{rot,2}(0,t) \\ X_{rot,3}(0,t)\end{pmatrix} &= \mathbf{H}\cdot\begin{pmatrix} X_{c_0,1}(0,0) \\ X_{c_0,2}(0,0) \\ X_{c_0,3}(0,0)\end{pmatrix} + \frac{l/2}{\sinh(l/2)}\begin{pmatrix} 0 \\ \left(1-\frac{\sinh(L/2)}{M\tanh(l/2)}\right) \\ 0\end{pmatrix} \\ &= 2c_0\sqrt{t}\begin{pmatrix} 0 \\ \frac{A_3}{\sqrt{A_2^2+A_3^2}} \\ \frac{A_2}{\sqrt{A_2^2+A_3^2}}\end{pmatrix} + \frac{l/2}{\sinh(l/2)}\begin{pmatrix} 0 \\ \left(1-\frac{\sinh(L/2)}{M\tanh(l/2)}\right) \\ 0\end{pmatrix}.\end{aligned} \tag{4.11}$$

Figure 4.3 shows the trajectories for $t \in [0, t_{1,20}]$, i.e., for small times. Both $\mathbf{X}_l(0,t)$ and $\mathbf{X}_{rot}(0,t)$ lie in the YZ-plane, and when plotted together it is clear in Figure 4.3 that $\mathbf{X}_l(0,t)$ (blue) can be approximated by a straight line (red) with a slope A_2/A_3. On the other hand, if we plot the third components $X_{l,3}(0,t)$, $X_{rot,3}(0,t)$ for small times, then the former (left) appears to grow along the curve $2c_0\sqrt{t}A_2/\sqrt{A_2^2+A_3^2}$ as shown in Figure 4.3 (right).

For our numerical simulations, we have taken $M = 8$, $l = 0.6$, but the results hold true for any $M \geq 2$, where the choice of M to be even was made to take advantage of the symmetries of the planar l-polygon. Thus, there is strong numerical evidence that for small times the l-polygon problem can be seen a superposition of several one-corner problems. In the following section, we utilize this fact to compute an exact expression for the speed of the center of mass c_l of the planar l-polygon.

Finally, remark that the quantity A_2/A_3 also determines the angle φ which the curve $\mathbf{X}_{rot}(0,t)$ makes with the plane containing $\mathbf{X}_{rot}(s,0)$. Interestingly, φ is also the angle corresponding to the corner of $z_l(t)$ located at $t = 0$ which holds true in the

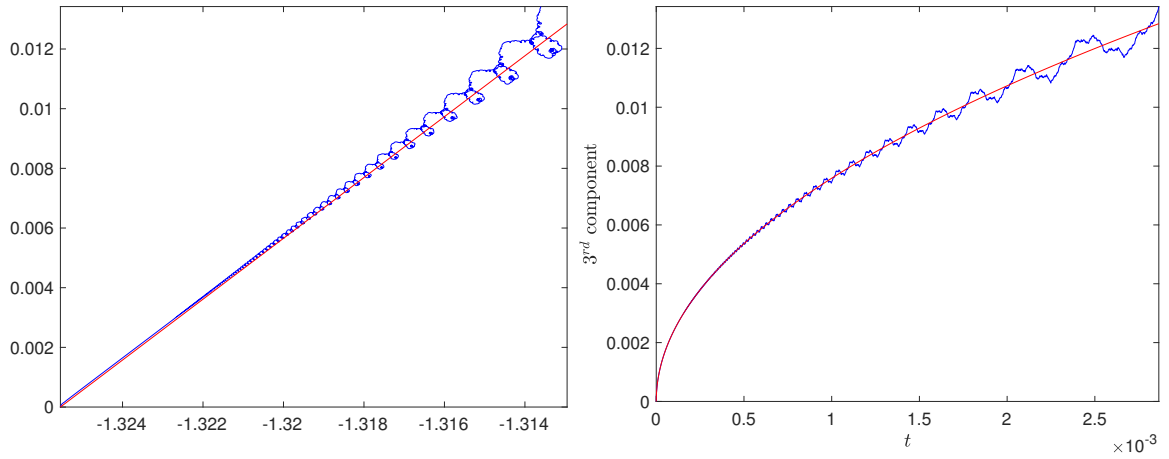

Figure 4.3 Left side $\mathbf{X}(0,t)$, $t \in [0, t_{1,20}]$ for $M = 8$, $l = 0.6$ and on the right side the third component versus time t for the l-polygon (blue) and one-corner (red) problems.

Euclidean case as well. To compare both cases simultaneously, from (3.53) we obtain c_0 for $M = 3, 4, \ldots, 20$ and compute A_2/A_3 using (4.8) in the hyperbolic case and using [36, (57)] for the Euclidean case. The values thus obtained have been plotted in Figure 4.4 where it can be seen that A_2/A_3 is greater (smaller) than the one in hyperbolic (Euclidean) case and tends to one as c_0 becomes smaller. In fact, from (4.8), $A_2(0)/A_3(0) = 1$. Thus, for a given c_0, φ is more (less) than $\pi/2$ and converges to $\pi/2$ in the limit, as in the case of Riemann's non-differentiable function. Moreover, for any $c_0 > 0$ in the hyperbolic case, its value can be precisely given as

$$\varphi = \arctan\left(\frac{A_2}{A_3}\right) = \arctan\left(\frac{\Re\{\Upsilon\}}{\Im\{\Upsilon\}}\right) = \arg(i\bar{\Upsilon}), \tag{4.12}$$

with $\Upsilon = e^{i\pi/4}\Gamma(1 - ic_0^2/4)\Gamma(1/2 + ic_0^2/4)$. By using the following

$$\frac{\Gamma(z_1)\Gamma(z_2)}{\Gamma(z_1 + z_2)} = B(z_1, z_2),$$

where $B(\cdot,\cdot)$ is the beta function, we can write

$$\Upsilon = e^{i\pi/4}B(1 - ic_0^2/4, 1/2 + ic_0^2/4)\Gamma(3/2) = \frac{\sqrt{\pi}}{2}\, e^{i\pi/4}B(1 - ic_0^2/4, 1/2 + ic_0^2/4).$$

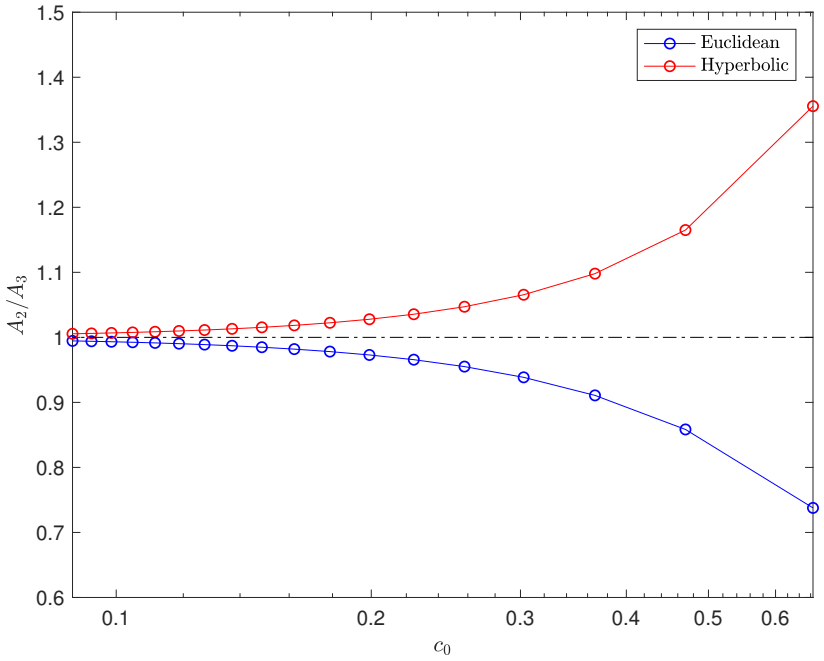

Figure 4.4 Semilogarithmic plot of A_2/A_3 as function of c_0 in both Euclidean and Hyperbolic cases. Clearly, as c_0 tends to zero, A_2/A_3 approaches to one marked with dashed dotted line.

4.3 Analytical computation of c_l using one-corner problem

In Chapter 3, during the numerical evolution of the planar l-polygon, we observed that the trajectory of its center of mass lies in the YZ-plane. More precisely, for the arc-length parameterized curve $\mathbf{X}_l$ with length L,

$$\mathbf{X}_l^{mean}(t) = \frac{1}{L}\int_{-L/2}^{L/2} \mathbf{X}_l(s,t)ds = (0, y(t), c_l t),$$

where the second component $y(t)$ was found to be T_f-periodic and a linear behavior was noted in the third component. In this section, we consider only the third component:

$$c_l t = X_{3,l}^{mean}(t) = \frac{1}{N}\sum_{j=0}^{N-1} X_{l,3}(s_j,t) = \frac{M}{N}\sum_{j=0}^{N/M-1} X_{l,3}(s_j,t),$$

where the equality on the right-hand side follows from (3.39) and implies that computing the mean over the interval $[-L/2, L/2]$ is equivalent to that over $[-l/2, l/2]$. In other

words,

$$c_l t = \frac{1}{l}\int_{-l/2}^{l/2} X_{l,3}(s,t)\ ds,\ \forall t > 0,$$

which we can be rewritten as

$$c_l = \frac{1}{lt}\int_{-l/2}^{l/2} X_{l,3}(s,t)\ ds,\ \forall t > 0,$$

and it holds true especially when $t \to 0$. At this point, it is important to recall from the previous section that, at infinitesimal times, the l-polygon problem can be described as a superposition of several one-corner problems, as a result, we claim that

$$c_l = \lim_{t\to 0}\frac{1}{lt}\int_{-l/2}^{l/2} X_{rot,3}(s,t)\ ds.$$

Moreover, by using the self-similarity of $\mathbf{X}_{rot}$:

$$\mathbf{X}_{rot}(s,t) = \sqrt{t}\mathbf{X}_{rot}(s/\sqrt{t},1),\ t > 0,$$

we can express

$$c_l = \lim_{t\to 0}\frac{1}{l\sqrt{t}}\int_{-l/2}^{l/2} X_{rot,3}(s,1)\ ds.$$

A simple change of variable $s/\sqrt{t} \to s$ gives

$$c_l = \lim_{t\to 0}\frac{1}{l}\int_{-l/2\sqrt{t}}^{l/2\sqrt{t}} X_{rot,3}(s,1)\ ds,$$

and passing the limit allows us to conjuncture that

$$c_l = \frac{1}{l}\int_{-\infty}^{\infty} X_{rot,3}(s)\ ds,$$

where we have used $X_{rot}(s) = X_{rot,3}(s,1)$. As a result, we have the following result

Theorem 6.

$$\int_{-\infty}^{\infty} X_{rot}(s)\ ds = \frac{2\pi c_0^2}{\sqrt{1-e^{-\pi c_0^2}}}. \tag{4.13}$$

With this, we obtain c_l in terms of c_0 and also l, i.e.,

$$c_l = \frac{2\pi c_0^2}{l\sqrt{1-e^{-\pi c_0^2}}} = \frac{4\ln\cosh(l/2)}{l\sqrt{1-\operatorname{sech}^2(l/2)}} = -\frac{\ln(1-\tanh^2(l/2))}{(l/2)\tanh(l/2)}. \tag{4.14}$$

Observe that because of the definition of X_{rot} in (4.9), and its initial value in (4.2), we have

$$\int_{-\infty}^{\infty} X_{rot}(s)ds > 0. \tag{4.15}$$

4.3.1 Proof of Theorem 6

Since the proof is mainly based on the one-corner problem, we take $t = 1$ and use the following notation for the variables. We write $\mathbf{X}(s) = \mathbf{X}_{c_0}(s, 1)$, $\mathbf{T}(s) = \mathbf{T}_{c_0}(s, 1)$, $\mathbf{n}(s) = \mathbf{n}_{c_0}(s, 1)$, $\mathbf{b}(s) = \mathbf{b}_{c_0}(s, 1)$, which implies $\mathbf{X}_{c_0}(s, t) = \sqrt{t}\mathbf{X}(s/\sqrt{t})$, $\mathbf{T}_{c_0}(s, t) = \mathbf{T}(s/\sqrt{t})$, $\mathbf{n}_{c_0}(s, t) = \mathbf{n}(s/\sqrt{t})$, $\mathbf{b}_{c_0}(s, t) = \mathbf{b}(s/\sqrt{t})$. The non-bold letters $X(s)$, $T(s)$, $n(s)$, $b(s)$ will be used to refer any component of their bold counterparts.

Differentiating $X(s)$ three times and using the Frenet–Serret formulas, we obtain the ODE [21]

$$X'''(s) = T''(s) = c_0 n'(s) = c_0^2 T(s) + \frac{s}{2} c_0 b(s). \tag{4.16}$$

Moreover, differentiating $\mathbf{X}_{c_0}(s, t) = \sqrt{t}\mathbf{X}(s/\sqrt{t})$ both sides with respect to t gives

$$\mathbf{X}_{c_0,t}(s, t) = \mathbf{X}_{c_0,s} \wedge_{-} \mathbf{X}_{c_0,ss} = \frac{c_0}{\sqrt{t}}\mathbf{T}_{c_0} \wedge_{-} \mathbf{n}_{c_0} = \frac{c_0}{\sqrt{t}}\mathbf{b}_{c_0}(s, t) = \frac{c_0}{\sqrt{t}}\mathbf{b}(s/\sqrt{t}),$$
$$\left(\sqrt{t}\mathbf{X}(s/\sqrt{t})\right)_t = \frac{1}{2\sqrt{t}}\mathbf{X}(s/\sqrt{t}) - \frac{s}{2t}\mathbf{X}_s(s/\sqrt{t}).$$

Combining the above two equations

$$\frac{c_0}{\sqrt{t}}\mathbf{b}(s/\sqrt{t}) = \frac{1}{2\sqrt{t}}\mathbf{X}(s/\sqrt{t}) - \frac{s}{2t}\mathbf{X}_s(s/\sqrt{t}),$$

which at $t = 1$ is

$$c_0 b(s) = \frac{1}{2}X(s) - \frac{s}{2}X'(s). \tag{4.17}$$

Hence, from (4.16)-(4.17),

$$X'''(s) + \left(-c_0^2 + \frac{s^2}{4}\right)X'(s) - \frac{s}{4}X(s) = 0, \tag{4.18}$$

which has three linearly independent solutions and from [21, Theorem 1], we note that the solution grows linearly as $s \to \infty$. Next, by denoting the Fourier transform of $X(s)$ as $\hat{X}(\xi)$:

$$\hat{X}(\xi) = \frac{1}{\sqrt{2\pi}}\int_{-\infty}^{\infty} X(s)e^{-is\xi}ds, \;\; X(s) = \frac{1}{\sqrt{2\pi}}\int_{-\infty}^{\infty} \hat{X}(\xi)e^{is\xi}d\xi, \tag{4.19}$$

and from the properties of Fourier transform such as

$$[s^n X(s)]^\wedge = i^n \frac{d^n}{d\xi^n}\hat{X}(\xi), \quad \left[\frac{d^n}{ds^n}X(s)\right]^\wedge = (i\xi)^n \hat{X}(\xi),$$

we learn that $\hat{X}(\xi)$ is a solution of

$$\xi\hat{X}''(\xi) + 3\hat{X}'(\xi) + 4\xi^3\hat{X}(\xi) + 4c_0^2\xi\hat{X}(\xi) = 0. \tag{4.20}$$

Note that (4.20) holds true for any component of $\hat{\mathbf{X}}$, especially for $\hat{X}_{rot}$ which from (4.9), is a linear combination of components of $\hat{\mathbf{X}}$. On the other hand, $\xi = 0$ is a regular singular point of (4.20) whose indicial equation

$$r(r-1) + 3r = 0, \tag{4.21}$$

has $r_1 = 0$, $r_2 = -2$ as its two roots that differ by an integer. As a result, by using the Frobenius-Fuch theorem, we obtain

$$\begin{cases} \hat{X}_{r_1}(\xi) = \sum_{n=0}^{\infty} a_n \xi^{2n}, \text{ for } r = r_1, \\ \hat{X}_{r_2}(\xi) = c\hat{X}_{r_1}(\xi)\ln|\xi| + |\xi|^{-2}\sum_{n=0}^{\infty} b_n\xi^{2n}, \text{ for } r = r_2, \end{cases} \tag{4.22}$$

for some constant c and the coefficients a_n, b_n which can be determined through recursive relations. Note that $\hat{X}_{r_1}(\xi)$ is even and analytic, whereas $\hat{X}_{r_2}(\xi)$ is even and behaves close to the origin as $\frac{d^2}{d\xi^2}\ln|\xi|$. Therefore, following the discussion in [36], at the origin the odd solution has to be like δ'. For the proof of Theorem 6, we will be considering only the analytic solution, i.e., $\hat{X}_{r_1}(\xi)$.

Thus, by transforming the problem into the Fourier space, proving Theorem 6 is equivalent to arriving at an expression for $\hat{X}_{rot}(0)$ since

$$\sqrt{2\pi}\hat{X}_{rot}(0) = \int_{-\infty}^{\infty} X_{rot}(s)\, ds. \tag{4.23}$$

In this regard, we introduce $\widehat{W}(\xi^2) = \xi^2\hat{X}(\xi)$, and with $\eta = \xi^2 > 0$, $\widehat{W}(\eta) = \eta\hat{X}(\sqrt{\eta})$. Also note that, $\xi^2\delta'(\xi) = 0$ and $\xi^2\frac{d^2}{d\xi^2}\ln|\xi| = -1$, as a result, $\widehat{W}(\xi)$ exists at $\xi = 0$ and is bounded around it. As a next step, we look for the equation that $\widehat{W}(\xi)$ satisfies, and

in this regard, we differentiate $\widehat{W}(\eta)$ and write

$$\widehat{W}'(\eta) = \frac{\sqrt{\eta}}{2}\hat{X}'(\sqrt{\eta}) + \frac{1}{\eta}\widehat{W}(\eta),$$
$$\widehat{W}''(\eta) = \frac{1}{4}\hat{X}''(\sqrt{\eta}) + \frac{1}{2\eta}\left(\widehat{W}'(\eta) - \frac{1}{\eta}\widehat{W}(\eta)\right) + \frac{1}{\eta}\widehat{W}'(\eta) - \frac{1}{\eta^2}\widehat{W}(\eta),$$

substituting $\hat{X}'$, $\hat{X}''$ from above in (4.20), gives

$$\widehat{W}''(\eta) + \left(1 + \frac{c_0^2}{\eta}\right)\widehat{W}(\eta) = 0. \tag{4.24}$$

Observe that $\eta = 0$ is a regular singular point for the above equation and the corresponding indicial equation $r(r-1) = 0$ has $r_1 = 1$ and $r_2 = 0$ as its roots. Thus, by using Frobenious-Fuch theorem as before, we write

$$\begin{cases} \widehat{W}_{r_1}(\eta) = \sum_{n=0}^{\infty} d_n \eta^{n+1}, \text{ for } r = r_1, \\ \widehat{W}_{r_2}(\eta) = c\widehat{W}_{r_1}(\eta)\ln|\eta| + \sum_{n=0}^{\infty} e_n \eta^n, \text{ for } r = r_2, \end{cases} \tag{4.25}$$

where the coefficients d_n and e_n can be determined through recursive relations. It is important to mention that (4.24) is a special case of a well-known equation called Coulomb wave equation (see [48, Section 33.2(i)]) and its solution $\widehat{W}(\eta)$ is known as Coulomb wave function.

Furthermore, when $r = 0$ in (4.21), the corresponding solution (omitting the subscript) $\hat{X}(\xi)$ is analytic and $\hat{X}(0)$ is finite. Consequently, $\widehat{W}(\eta) = \eta\hat{X}(\sqrt{\eta})$ is analytic for $\eta \geq 0$ and $\widehat{W}(0) = 0$. Also,

$$\hat{X}(0) = \lim_{\xi\to 0}\hat{X}(\xi) = \lim_{\xi\to 0}\frac{\widehat{W}(\xi^2)}{\xi^2} = \lim_{\xi\to 0}\frac{2\xi\widehat{W}'(\xi^2)}{2\xi} = \widehat{W}'(0). \tag{4.26}$$

With this, we state our first result

Lemma 1. *(a) Given $\widehat{W}(0) = 0$, if $\widehat{W}(\eta)$ is a solution of (4.24), then it is analytic for $\eta \geq 0$. Moreover, $|\widehat{W}(\eta)|$ and $|\widehat{W}'(\eta)|$ are bounded for $\eta \in [0, \infty)$.*

(b) Given $\widehat{W}(0) \neq 0$, if $\widehat{W}(\eta)$ is a solution of (4.24), then $|\widehat{W}(\eta)|$ is bounded for $\eta \in [0, \infty]$, whereas $|\widehat{W}'(\eta)|$ is bounded for $\eta \in [\epsilon, \infty)$ for all $\epsilon > 0$. Furthermore,

for η small and positive,

$$\widehat{W}'(\eta) = -c_0^2 \widehat{W}(0) \ln(\eta) + \mathcal{O}(1).$$

Proof. Following the above discussion, when $\widehat{W}(0) = 0$, $\widehat{W}(\eta)$ is analytic, and the remaining claim can be proved by defining the energy

$$E(\eta) = (\widehat{W}')^2(\eta) + \left(1 + \frac{c_0^2}{\eta}\right) \widehat{W}^2(\eta), \quad \forall \eta > 0.$$

Its derivative

$$\begin{aligned} E'(\eta) &= 2\widehat{W}'(\eta) \left(\widehat{W}'' + \left(1 + \frac{c_0^2}{\eta}\right) \widehat{W}(\eta)\right) - \frac{c_0^2}{\eta^2} \widehat{W}^2(\eta) \\ &= -\frac{c_0^2}{\eta^2} \widehat{W}^2(\eta) \leq 0, \end{aligned}$$

which implies that $E(\eta)$ is a decreasing function for all $\eta > 0$, and

$$0 < E(\eta) \leq E(\eta_0), \ \forall \eta \geq \eta_0 > 0,$$

where

$$\begin{aligned} \lim_{\eta_0 \to 0^+} E(\eta_0) &= (\widehat{W}')^2(0) + \widehat{W}^2(0) + \lim_{\eta_0 \to 0^+} \frac{c_0^2}{\eta} \widehat{W}^2(\eta) \\ &= (\widehat{W}')^2(0) + \lim_{\eta_0 \to 0^+} 2c_0^2 \widehat{W}(\eta_0) \widehat{W}'(\eta_0) = (\widehat{W}')^2(0). \end{aligned}$$

Thus, $|E(\eta)| \leq (\widehat{W}')^2(0)$ for all $\eta \geq 0$, as a result, $|\widehat{W}(\eta)|$ and $|\widehat{W}'(\eta)|$ are bounded in $[0, \infty)$.

On the other hand, when $\widehat{W}(0) \neq 0$, the analytic solution $\widehat{W}(\eta)$ remains bounded for the interval $[0, \infty)$, but as $\eta \to 0$, $E(\eta) \to \infty$, so, $\widehat{W}'(\eta)$ is not bounded at $\eta = 0$. However, its behavior near the origin can be deduced by looking at the case $r = -2$ in (4.25). Also, by writing

$$\begin{aligned} \widehat{W}'(\eta) &= \widehat{W}'(1) - \int_\eta^1 \widehat{W}''(\tilde{\eta}) d\tilde{\eta} \\ &= \widehat{W}'(1) + \int_\eta^1 \left(1 + \frac{c_0^2}{\tilde{\eta}}\right) \widehat{W}(\tilde{\eta}) d\tilde{\eta} \end{aligned}$$

and using the fact that $\widehat{W}(\eta)$ is bounded around zero, i.e., $\widehat{W}(\eta) = \widehat{W}(0)+\mathcal{O}(1),\ \eta \to 0$, the result follows. □

Let us mention that from now on we will be dealing with the case when $\widehat{W}$ is analytic, i.e., when $\widehat{W}(0) = 0$. In the following lines, we present few more results which compose the proof of Theorem 6. In short, they are the following:

(i) equation for W when $\widehat{W}(0) = 0$,

(ii) expression for $\widehat{W}'(0)$ in terms of $W(0)$,

(iii) asymptotics for $\widehat{W}(\eta)$, $\eta \gg 1$,

(iv) asymptotics of $\widehat{W}(\eta)$ in terms of $W(0)$,

(v) equation for $(-\mathbf{n} + i\mathbf{b})^\wedge$ and the conclusion.

Equation for W when $\widehat{W}(0) = 0$

Given that

$$\widehat{W}(\eta) = \frac{1}{\sqrt{2\pi}} \int_{-\infty}^{\infty} W(t) e^{-it\eta}, \quad \eta \geq 0, \tag{4.27}$$

solves (4.24), we want to look for the equation which $W(t)$, a tempered distribution, satisfies. In this regard, we consider (4.24) and compute

$$\left[\eta \widehat{W}'' + (\eta + c_0^2)\widehat{W}\right]^\vee = 0.$$

Next, by using the following properties of inverse Fourier transform:

$$\left[(i\xi)^n \widehat{W}(\xi)\right]^\vee = \frac{d^n W(t)}{dt^n}, \quad \left[i^n \frac{d^n \widehat{W}(\xi)}{d\xi^n}\right]^\vee = t^n W(t),$$

and substituting in the above equation, we obtain

$$(1 - t^2)W'(t) - (2t - ic_0^2)W(t) = 0. \tag{4.28}$$

Another simple computation gives

$$W(t) = \frac{W(0)}{1 - t^2} \left|\frac{t+1}{t-1}\right|^{-ic_0^2/2}, \tag{4.29}$$

which solves (4.28) and is regular for all $t \neq \pm 1$. Furthermore, we express $W(t) = W(0)f_+(t)f_-(t)$ where

$$f_+(t) = \frac{|1+t|^{-ic_0^2/2}}{1+t}, \ f_-(t) = \frac{|1-t|^{ic_0^2/2}}{1-t},$$

satisfy

$$\begin{cases} (1+t)f'_+(t) = -f_+(t)(ic_0^2/2+1), \\ (1-t)f'_-(t) = -f_-(t)(ic_0^2/2-1), \end{cases}$$

respectively. Note that $f_+(t)$ is regular for all $t \geq 0$ and $f_-(t)$ is regular for all $t \leq 0$, and $f_\pm(0) = 1$.

Lemma 2. *Assume that $W(t)$ is given as in (4.29), then,*

$$\int_0^\infty W(t)dt = 0, \ \int_{-\infty}^0 W(t)dt = 0,$$

and, hence, $\widehat{W}(0) = 0$.

Proof. Let us define

$$W_+(t) = \begin{cases} 0, & t < 0, \\ W(t), & t \geq 0, \end{cases} \tag{4.30}$$

and $W_-(t) = W(t) - W_+(t)$, thus, $\widehat{W}(\eta) = \widehat{W}_+(t) + \widehat{W}_-(t)$. So, at $\eta = 0$, we have

$$\widehat{W}_-(0) = \frac{1}{\sqrt{2\pi}} \int_{-\infty}^0 \frac{Y(0)}{1-t^2} \left|\frac{1-t}{1+t}\right|^{ic_0^2/2} dt = \frac{W(0)}{\sqrt{2\pi}} \int_{-\infty}^0 (1+t)^{-ic_0^2/2-1} f_-(t)dt,$$

and integration by parts yields

$$\widehat{W}_-(0) = \frac{2W(0)}{ic_0^2\sqrt{2\pi}} \left[\int_{-\infty}^0 f'_-(t) \, |1+t|^{-ic_0^2/2} \, dt - 1\right], \tag{4.31}$$

similarly,

$$\widehat{W}_+(0) = \frac{2W(0)}{ic_0^2\sqrt{2\pi}} \left[\int_0^\infty f'_+(t) \, |1-t|^{ic_0^2/2} \, dt + 1\right], \tag{4.32}$$

where the last two integrals are absolutely convergent. Hence, rewriting $\widehat{W}_-(0)$ as

$$\begin{aligned}\widehat{W}_-(0) &= \frac{2W(0)}{ic_0^2\sqrt{2\pi}} \lim_{\epsilon\to 0}\left[\left(\int_{-\infty}^{-1-2\epsilon/(1-\epsilon)} + \int_{-1+2\epsilon/(1+\epsilon)}^{0}\right) f'_-|1+t|^{-ic_0^2/2}dt - 1\right] \\ &= \frac{2W(0)}{ic_0^2\sqrt{2\pi}} \lim_{\epsilon\to 0}\left[\Delta_\epsilon + \frac{ic_0^2}{2}\left(\int_{-\infty}^{-1-2\epsilon/(1-\epsilon)} + \int_{-1+2\epsilon/(1+\epsilon)}^{0}\right) f_+(t)f_-(t)dt\right],\end{aligned}$$

where $\Delta_\epsilon = \left|\frac{2\epsilon}{1-\epsilon}\right|^{-ic_0^2/2} \frac{|2+2\epsilon/(1-\epsilon)|^{ic_0^2/2}}{2+2\epsilon/(1-\epsilon)} - \left|\frac{2\epsilon}{1+\epsilon}\right|^{-ic_0^2/2} \frac{|2-2\epsilon/(1+\epsilon)|^{ic_0^2/2}}{2-2\epsilon/(1+\epsilon)}$ tends to zero as $\epsilon \to 0$, and thus, we obtain

$$\widehat{W}_-(0) = \frac{1}{\sqrt{2\pi}} \lim_{\epsilon\to 0}\left[\left(\int_{-\infty}^{-1-2\epsilon/(1-\epsilon)} + \int_{-1+2\epsilon/(1+\epsilon)}^{0}\right) W(t)dt\right].$$

Next, we perform change of variables

$$u = \frac{1-t}{1+t},\ t = \frac{1-u}{1+u},\ dt = -\frac{2du}{(1+u)^2},$$

so that

$$W(t(u)) = \frac{1}{4u}W(0)(1+u)^2|u|^{ic_0^2/2}.$$

Consequently,

$$\widehat{W}_-(0) = -\frac{W(0)}{\sqrt{2\pi}} \lim_{\epsilon\to 0}\left[\left(\int_{-1}^{-1/\epsilon} + \int_{1/\epsilon}^{1}\right) \frac{|u|^{ic_0^2/2}}{2u}du\right] = 0.$$

By following the same steps, one can show that $\widehat{W}_+ = 0$, and we conclude that $\widehat{W}(0) = 0$. □

Expression for $\widehat{W}'(0)$ in terms of $W(0)$

From (4.26), we can write

$$\begin{aligned}\widehat{W}'(0) &= \lim_{\eta\to 0}\widehat{W}'(\eta) = \lim_{\eta\to 0}\frac{-i}{\sqrt{2\pi}}\int_{-\infty}^{\infty} tW(t)e^{-it\eta}dt \\ &= \lim_{\eta\to 0}\frac{iW(0)}{\sqrt{2\pi}}\int_{-\infty}^{\infty}\frac{t}{t^2-1}\left|\frac{t+1}{t-1}\right|^{-ic_0^2/2} e^{-it\eta}dt = \frac{W(0)}{\sqrt{2\pi}}\lim_{\eta\to 0} J(\eta),\end{aligned}$$

with $J(\eta) = i\int_{-\infty}^{\infty} \frac{t}{t^2-1}\left|\frac{t+1}{t-1}\right|^{-ic_0^2/2} e^{-it\eta}dt$, $\eta > 0$. By rewriting

$$\begin{aligned} J(\eta) &= \frac{ie^{i\eta}}{2}\int_{-\infty}^{\infty}\frac{1}{t}\left|\frac{t}{t-2}\right|^{-ic_0^2/2} e^{-it\eta}dt + \frac{ie^{-i\eta}}{2}\int_{-\infty}^{\infty}\frac{1}{t}\left|\frac{t+2}{t}\right|^{-ic_0^2/2} e^{-it\eta}dt \\ &= \frac{ie^{i\eta}}{2}\int_{-\infty}^{\infty}\frac{1}{t}\left[(\cos(t\eta) - i\sin(t\eta))\left(\left|\frac{t}{t-2}\right|^{-ic_0^2/2} + \left|\frac{t+2}{t}\right|^{-ic_0^2/2}\right)\right]dt \\ &= \frac{ie^{i\eta}}{2}\left(J_1(\eta) - iJ_2(\eta)\right), \end{aligned} \tag{4.33}$$

where

$$\begin{cases} J_1(\eta) = \displaystyle\int_{-\infty}^{\infty}\frac{1}{t}\cos(t\eta)\left(\left|\frac{t}{t-2}\right|^{-ic_0^2/2} + \left|\frac{t+2}{t}\right|^{-ic_0^2/2}\right)dt, \\ J_2(\eta) = \displaystyle\int_{-\infty}^{\infty}\frac{1}{t}\sin(t\eta)\left(\left|\frac{t}{t-2}\right|^{-ic_0^2/2} + \left|\frac{t+2}{t}\right|^{-ic_0^2/2}\right)dt. \end{cases}$$

Moreover, by following the same steps of Lemma 3.6 and 3.7 in [23], we get

$$\begin{cases} \lim_{\eta\to 0} J_1(\eta) = -i2\pi\tan(c_0^2\pi/4), \\ \lim_{\eta\to 0} J_2(\eta) = 2\pi. \end{cases}$$

Consequently, from (4.33)

$$\lim_{\eta\to 0} J(\eta) = \frac{i}{2}\left[-i2\pi\tanh\left(\frac{\pi c_0^2}{4}\right) - i2\pi\right] = \pi\left(1+\tanh\left(\frac{\pi c_0^2}{4}\right)\right),$$

and thus,

$$\widehat{W}'(0) = W(0)\sqrt{\frac{\pi}{2}}\left(1+\tanh\left(\frac{\pi c_0^2}{4}\right)\right) = W(0)\frac{\sqrt{2\pi}}{1+e^{-\pi c_0^2/2}}. \tag{4.34}$$

Asymptotics for $\widehat{W}(\eta)$, $\eta \gg 1$

Since the coefficients appearing in (4.24) are scalars, we can write $\widehat{W}(\eta)$ using its real and imaginary part as

$$\widehat{W}(\eta) = \Re(\widehat{W}(\eta)) + i\Im(\widehat{W}(\eta)).$$

Naturally, both $\Re(\widehat{W})(\eta)$ and $\Im(\widehat{W}(\eta))$ solve (4.24). Next, we define

$$F(\eta) = \Re(\widehat{W}(\eta)) + i\Re(\widehat{W}'(\eta)),$$

so that

$$\begin{aligned} F'(\eta) &= \Re(\widehat{W}'(\eta)) + i\Re(\widehat{W}''(\eta)) = \Re(\widehat{W}'(\eta)) + i\left[-\left(1+\frac{c_0^2}{\eta}\right)\Re(\widehat{W}(\eta))\right] \\ &= -i[\Re(\widehat{W}(\eta)) + i\Re(\widehat{W}'(\eta))] - i\frac{c_0^2}{\eta}\Re(\widehat{W}(\eta)) \\ &= -iF(\eta) - i\frac{c_0^2}{2\eta}(F(\eta)+\bar{F}(\eta)) = -iF(\eta)\left(1+\frac{c_0^2}{\eta}\right) - i\frac{c_0^2}{2\eta}\bar{F}(\eta), \end{aligned}$$

i.e.,

$$F'(\eta) + iF(\eta)\left(1+\frac{c_0^2}{\eta}\right) = -i\frac{c_0^2}{2\eta}\bar{F}(\eta). \tag{4.35}$$

With the integration factor $e^{i\varphi(\eta)}$, with $\varphi(\eta) = \eta - \frac{c_0^2}{2}\ln|\eta|$, we can write

$$\left(F(\eta)e^{i\varphi(\eta)}\right)' = -\frac{ic_0^2}{2\eta}\bar{F}(\eta)e^{i\varphi(\eta)} \implies G'(\eta) = -\frac{ic_0^2}{2\eta}e^{2i\varphi(\eta)}\bar{G}(\eta),$$

for $G(\eta) = e^{i\varphi(\eta)}F(\eta)$. And by writing $G(\eta) = F^\infty + g(\eta)$, we obtain the equation for $g(\eta)$:

$$\begin{aligned} g'(\eta) &= -\frac{ic_0^2}{2\eta}e^{2i\varphi(\eta)}(\bar{F}^\infty + \bar{g}(\eta)) \\ &= -\frac{ic_0^2}{2\eta}e^{2i\varphi(\eta)}\bar{F}^\infty - \frac{ic_0^2}{2\eta}e^{2i\varphi(\eta)}\bar{g}(\eta). \end{aligned}$$

Next, by integrating the last equation from $[\eta, \tilde{\eta}]$ and following the same steps as in [23, Section 3.2.1] and passing the limit in $\tilde{\eta}$, we obtain

$$F(\eta) = F^\infty e^{-i\varphi(\eta)} - \frac{c_0^2}{4\eta}\bar{F}^\infty e^{i\varphi(\eta)} + \frac{ic_0^4}{8\eta}F^\infty e^{-i\varphi(\eta)} + \mathcal{O}\left(\frac{1}{\eta^2}\right). \tag{4.36}$$

Differentiating the last expression and using (4.35) yields

$$(F(\eta) - F^\infty e^{-i\varphi(\eta)})' = -\frac{ic_0^2}{4\eta}\bar{F}^\infty e^{i\varphi(\eta)} + \frac{c_0^4}{8\eta}F^\infty e^{-i\varphi(\eta)} + \mathcal{O}\left(\frac{1}{\eta^2}\right). \tag{4.37}$$

From (4.36), we also obtain $F^\infty = \lim_{\eta\to\infty} F(\eta)e^{i\varphi(\eta)}$ where $F(\eta)$ consists of the real parts of $\widehat{W}$ and $\widehat{W}'$. Furthermore, the aforementioned procedure also holds true for $F(\eta)$ defined using the corresponding imaginary parts, i.e., $F(\eta) = \Im(\widehat{W}(\eta)) + i\Im(\widehat{W}'(\eta))$. Thus, combining both parts, the result is valid for $F(\eta) = \widehat{W}(\eta) + i\widehat{W}'(\eta)$ with $F^\infty = \lim_{\eta\to\infty}[e^{i\varphi(\eta)}(\widehat{W}(\eta) + i\widehat{W}'(\eta))]$.

Lemma 3. *Let $F(\eta) = \widehat{W}(\eta) + i\widehat{W}'(\eta)$ be even, with $\widehat{W}(0) = 0$. Then, for $|s| \gg 1$,*

$$\frac{1}{\sqrt{2\pi}}\int_{-\infty}^{\infty} F(\xi^2)e^{is\xi}d\xi = \frac{1}{\sqrt{2\pi}}\int_{-\infty}^{\infty} F^{\infty}e^{i(s\xi - c_0^2\ln|\xi| - \xi^2)}d\xi + \mathcal{O}\left(\frac{1}{|s|}\right).$$

The proof follows using the same steps as in [23, Lemma 3.4].

Asymptotics of $\widehat{W}(\eta)$ in terms of $W(0)$

In order to compute the asymptotics of $\widehat{W}(\eta)$, we consider (4.27) and divide the integral over different intervals while bearing in mind that $\widehat{W}(t)$ is regular for $t^2 \neq 1$. In this regard, let us define the test function ϕ such that $\text{supp}(\phi) = \{t : |t^2 - 1| \leq 1/2\}$ and $\phi(t) = 1$ when $|t^2 - 1| < 1/4$. Thus, we express

$$\begin{aligned}\widehat{W}(\eta) &= \frac{1}{\sqrt{2\pi}}\int_{-\infty}^{\infty}\phi(t)W(t)e^{-it\eta}d\eta + \frac{1}{\sqrt{2\pi}}\int_{-\infty}^{\infty}(1-\phi(t))W(t)e^{-it\eta}d\eta \\ &= \widehat{W}_{11}(\eta) + \widehat{W}_{12}(\eta),\end{aligned}$$

where $\widehat{W}_{12}(\eta)$ corresponds to the integral over the region $|t^2 - 1| > 1/4$. Next, by defining the differential operator D as $Df(t) = (i\eta)^{-1}(df/dt)$ with D^t as its transpose $D^t f(t) = -(d/dt)(f/i\eta)$, then $D^N(e^{i\eta t}) = e^{i\eta t}, \forall N$, we write

$$\begin{aligned}\widehat{W}_{12}(\eta) &= \frac{\widehat{W}(0)}{\sqrt{2\pi}}\int_{-\infty}^{\infty}(1-\phi(t))\frac{1}{1-t^2}e^{-i\frac{c_0^2}{2}\ln\left|\frac{t+1}{t-1}\right|}D(e^{-it\eta})dt \\ &= -\frac{\widehat{W}(0)}{\sqrt{2\pi}}\frac{1}{i\eta}\int_{-\infty}^{\infty}\left((1-\phi(t))\frac{1}{1-t^2}e^{-i\frac{c_0^2}{2}\ln\left|\frac{t+1}{t-1}\right|}\right)' e^{-it\eta}dt.\end{aligned}$$

Expanding the integrand and using $|t^2 - 1| > 1/4$, yields

$$|\widehat{W}_{12}(\eta)| \leq \frac{c}{\eta},$$

for some constant c, and with this we have $\widehat{W}_{12}(\eta) = \mathcal{O}(1/\eta)$, when $\eta \gg 1$. On the other hand, $\widehat{W}_{11}(\eta)$ can be further simplified by dividing the integral as

$$\begin{aligned}\widehat{W}_{11}(\eta) &= \frac{1}{\sqrt{2\pi}}\left(\int_{|t-1|<1} + \int_{|t+1|<1} + \int_{|t|>2}\right)\phi(t)W(t)e^{-it\eta}dt \\ &= S_1(\eta) + S_2(\eta) + 0.\end{aligned}$$

Using $W(t)$ from (4.29), followed by a change of variable, for $\eta \gg 1$, we write the asymptotics of $S_1(\eta)$ as

$$S_1(\eta) = -\frac{W(0)}{2\sqrt{2\pi}} e^{-i\eta - i(c_0^2/2)\ln|2\eta|} \int_{-\infty}^{\infty} \frac{|t|^{ic_0^2/2}}{t} e^{-it} dt + \mathcal{O}\left(\frac{1}{\eta}\right),$$

and similarly,

$$S_2(\eta) = \frac{W(0)}{2\sqrt{2\pi}} e^{i\eta + i(c_0^2/2)\ln|2\eta|} \int_{-\infty}^{\infty} \frac{|t|^{-ic_0^2/2}}{t} e^{-it} dt + \mathcal{O}\left(\frac{1}{\eta}\right).$$

Moreover, by using the fact that $W(0)$ is real, we have $S_2(\eta) = -\bar{S}_1(\eta)$. As a result,

$$\begin{aligned}\widehat{W}_{11}(\eta) &= S_1(\eta) - \bar{S}_2(\eta) = 2\Im(S_1)(\eta) \\ &= -\frac{W(0)}{\sqrt{2\pi}} \Im\left(e^{-i\eta - i(c_0^2/2)\ln|2\eta|} \int_{-\infty}^{\infty} \frac{|t|^{ic_0^2/2}}{t} e^{-it} dt\right) + \mathcal{O}\left(\frac{1}{\eta}\right).\end{aligned}$$

Next, consider the integral in the above expression

$$\varsigma = \int_{-\infty}^{\infty} \frac{|t|^{ic_0^2/2}}{t} e^{-it} dt = -2i \int_0^{\infty} \frac{|t|^{ic_0^2/2}}{t} \sin t dt = 2\sinh(\pi c_0^2/4)\Gamma(ic_0^2/2),$$

where the last equality can be obtained by solving the integral using Mathematica®. We write $\varsigma = |\varsigma| e^{i\arg(\varsigma)}$, where $|\varsigma| = (2/c_0)\sqrt{\pi \tanh(\pi c_0^2/4)}$ can be computed using $|\Gamma(iy)|^2 = \pi/(y\sinh(\pi y)), y \in \mathbb{R}$. With this,

$$\widehat{W}(\eta) = -W(0)\frac{\sqrt{2}}{c_0} \tanh^{1/2}\left(\frac{\pi c_0^2}{4}\right) \Im\left(e^{-i\eta - i(c_0^2/2)\ln|2\eta| + i\arg(\varsigma)}\right) + \mathcal{O}\left(\frac{1}{\eta}\right),$$

and

$$\limsup_{\eta\to\infty} \widehat{W}(\eta) = |W(0)|\frac{\sqrt{2}}{c_0} \tanh^{1/2}\left(\frac{\pi c_0^2}{4}\right) = \frac{|W(0)|}{c_0}\left(\frac{2(1 - e^{-\pi c_0^2/2})}{1 + e^{-\pi c_0^2/2}}\right)^{1/2}. \tag{4.38}$$

Equation for $(-\mathbf{n} + i\mathbf{b})\hat{}(\xi)$ and the conclusion

We compute the expression for $\mathbf{n}(\xi)$ and $\mathbf{b}(\xi)$ by using the Frenet–Serret formulas:

$$\begin{gathered}\mathbf{T}' = c_0\mathbf{n}(s) \implies i\xi\hat{\mathbf{T}}(\xi) = c_0\hat{\mathbf{n}}(\xi), \\ \text{i.e., } -\xi^2\hat{\mathbf{X}}(\xi) = -\widehat{\mathbf{W}}(\xi^2) = -\widehat{\mathbf{W}}(\eta) = c_0\hat{\mathbf{n}}(\xi) \implies \widehat{\mathbf{W}}(\eta) = -c_0\hat{\mathbf{n}}(\xi),\end{gathered}$$

similarly,

$$c_0\mathbf{b}' = -c_0(s/2)\mathbf{n} = -(s/2)\mathbf{X}''$$
$$\implies ic_0\xi\hat{\mathbf{b}}(\xi) = -\frac{i}{2}\frac{d}{d\xi}(-\xi^2\hat{\mathbf{X}}(\xi)) = \frac{i}{2}\frac{d}{d\xi}\widehat{\mathbf{W}}(\xi^2) = i\xi\widehat{\mathbf{W}}'(\xi^2) \implies \widehat{\mathbf{W}}'(\eta) = c_0\hat{\mathbf{b}}(\xi).$$

Thus, we have

$$c_0(-\mathbf{n} + i\mathbf{b})^\wedge(\xi) = \widehat{\mathbf{W}}(\eta) + i\widehat{\mathbf{W}}'(\eta).$$

Using $\mathbf{e}_0$ in (4.4), and $X_{rot} = \mathbf{e}_0 \cdot \mathbf{X}$, we have

$$\widehat{W}_{rot}(\eta) = \widehat{W}_{rot}(\xi^2) = \xi^2\hat{X}_{rot}(\xi^2) = \xi^2(\mathbf{e}_0 \cdot \mathbf{X}) = -\mathbf{e}_0 \cdot c_0\hat{\mathbf{n}}(\xi),$$

and since $\mathbf{e}_0$ is a constant vector, $\widehat{W}_{rot}(\eta)$ satisfies (4.24) and

$$\begin{aligned}\widehat{W}_{rot}(0) &= -\mathbf{e}_0 \cdot c_0\hat{\mathbf{n}}(0) = -\mathbf{e}_0 \cdot \left(\frac{1}{\sqrt{2\pi}}\int_{-\infty}^{\infty} c_0\mathbf{n}(s)ds\right) \\ &= -\mathbf{e}_0 \cdot \left(\frac{1}{\sqrt{2\pi}}(\mathbf{T}(\infty) - \mathbf{T}(-\infty))\right) = \frac{1}{\sqrt{2\pi}}\mathbf{e}_0 \cdot (0, 2A_2, 2A_3) = 0,\end{aligned}$$

as a result, from the part (i) of Lemma 1, $\widehat{W}'_{rot}(0)$ exists and is finite. Next, we write

$$F_{rot}(\eta) = \widehat{W}_{rot}(\eta) + i\widehat{W}'_{rot}(\eta) = c_0\mathbf{e}_0 \cdot (-\hat{\mathbf{n}} + i\hat{\mathbf{b}})(\xi),$$

and note that $\mathbf{e}_0 \cdot \mathbf{T}$ is odd, whereas $\mathbf{e}_0 \cdot \mathbf{n}$ and $\mathbf{e}_0 \cdot \mathbf{b}$ are even, so, by using Lemma 3 for $F_{rot}(\eta)$, we get

$$\begin{aligned}c_0\mathbf{e}_0 \cdot (-\mathbf{n} + i\mathbf{b})(s) &= \frac{1}{\sqrt{2\pi}}\int_{-\infty}^{\infty} F_{rot}(\xi^2)e^{is\xi}d\xi \\ &= \frac{1}{\sqrt{2\pi}}F_{rot}^{\infty}\int_{-\infty}^{\infty} e^{i(s\xi - c_0^2\ln|\xi| - \xi^2)}d\xi + \mathcal{O}\left(\frac{1}{|s|}\right), \ |s| \gg 1.\end{aligned}$$

Consider the integral on the right hand side of the above equality as

$$\begin{aligned}\int_{-\infty}^{\infty} e^{i(s\xi - c_0^2\ln|\xi| - \xi^2)}d\xi &= \frac{1}{\sqrt{2\pi}}e^{is^2/4}\int_{-\infty}^{\infty} e^{-i(\xi - s/2)^2}e^{-ic_0^2\ln|\xi|}d\xi \\ &= \frac{1}{\sqrt{2\pi}}e^{is^2/4}e^{-ic_0^2\ln|s/2|}\int_{-\infty}^{\infty} e^{i\xi^2}d\xi + \mathcal{O}\left(\frac{1}{|s|}\right) \\ &= \frac{1}{\sqrt{2\pi}}e^{is^2/4}e^{-ic_0^2\ln|s/2|}\sqrt{i\pi} + \mathcal{O}\left(\frac{1}{|s|}\right),\end{aligned}$$

where the second equality follows from [7, Lemma 2.1]. With this, we obtain

$$c_0\mathbf{e}_0\cdot(-\mathbf{n}+i\mathbf{b})(s)=\sqrt{i/2}|F^{\infty}_{rot}|e^{is^2/4-ic_0^2\ln|s/2|+i\arg(F^{\infty}_{rot})}+\mathcal{O}\left(\frac{1}{|s|}\right),\ |s|\gg 1, \quad (4.39)$$

and

$$\lim_{s\to\infty} c_0\mathbf{e}_0\cdot(-\mathbf{n}+i\mathbf{b})(s)=c_0\mathbf{e}_0\cdot(-\mathbf{n}+i\mathbf{b})(\infty).$$

Next,

$$|c_0\mathbf{e}_0\cdot(-\mathbf{n}+i\mathbf{b})(\infty)|^2=c_0^2(\mathbf{e}_0\cdot\mathbf{n}(\infty))^2+(\mathbf{e}_0\cdot\mathbf{b}(\infty))^2,$$

and note that

$$\mathbf{e}_0\cdot\mathbf{T}(\infty)=\left(0,-\frac{A_3}{\sqrt{A_2^2+A_3^2}},\frac{A_2}{\sqrt{A_2^2+A_3^2}}\right)\cdot(A_1,A_2,A_3)=0,$$

which implies that the unit space-like vectors $\mathbf{e}_0,\mathbf{n},\mathbf{b}$ satisfy

$$\mathbf{e}_0\cdot\mathbf{n}=1,\ \mathbf{e}_0\cdot\mathbf{b}=0;$$

consequently,

$$|c_0\mathbf{e}_0\cdot(-\mathbf{n}+i\mathbf{b})(\infty)|^2=c_0^2.$$

Thus, from the above expression and (4.39), we have

$$|F^{\infty}_{rot}|=\sqrt{2}c_0,$$

and since $F^{\infty}_{rot}=\lim\limits_{\eta\to\infty}e^{i\varphi(\eta)}(\widehat{W}_{rot}+i\widehat{W}'_{rot})(\eta)$,

$$\limsup_{\eta\to\infty}\widehat{W}_{rot}(\eta)=\sqrt{2}c_0,$$

which by using (4.38) gives

$$|W_{rot}(0)|=c_0^2\left(\frac{1+e^{-\pi c_0^2/2}}{1-e^{-\pi c_0^2/2}}\right)^{1/2}.$$

Recall that our main objective is to compute $\widehat{W}'_{rot}(0)$ which from (4.34) and above expression is given by

$$\widehat{W}'_{rot}(0) = W_{rot}(0)\frac{\sqrt{2\pi}}{1+e^{-\pi c_0^2/2}} = c_0^2\left(\frac{2\pi}{1-e^{-\pi c_0^2}}\right)^{1/2}.$$

Thus, from (4.23) and (4.26), we conclude

$$\int_{-\infty}^{\infty} X_{rot}(s)\, ds = \sqrt{2\pi}\hat{X}_{rot}(0) = \sqrt{2\pi}\widehat{W}'_{rot}(0) = \frac{2\pi c_0^2}{\sqrt{1-e^{-\pi c_0^2}}}.$$

4.4 Numerical computation of $\int_{-\infty}^{\infty} X_{rot}(s)ds$

In this section, we compute the integral $\int_{-\infty}^{\infty} X_{rot}(s)ds$ numerically and verify the expression given in (4.13). The main idea is to solve the following initial value problem at $t = 1$ using the approach in [23]:

$$\begin{cases} \mathbf{X}'''(s) + \left(\frac{s^2}{4} - c_0^2\right)\mathbf{X}'(s) - \frac{s}{4}\mathbf{X}(s) = 0 \\ \mathbf{X}(0) = 2c_0(0,0,1)^T, \\ \mathbf{X}'(0) = (0,0,1)^T, \\ \mathbf{X}''(0) = c_0(0,1,0)^T. \end{cases}$$

Then, from (4.11), $X_{rot} \equiv X_{3,rot}$ satisfies

$$\begin{cases} X'''_{rot}(s) + \left(\frac{s^2}{4} - c_0^2\right)X'_{rot}(s) - \frac{s}{4}X_{rot}(s) = 0 \\ X_{rot}(0) = 2c_0A_2/\sqrt{A_2^2+A_3^2}, \\ X'_{rot}(0) = 0, \\ X''_{rot}(0) = -c_0A_3/\sqrt{A_2^2+A_3^2}. \end{cases} \tag{4.40}$$

Moreover, by taking $\tilde{X}_{rot}(s) = X_{rot}(-s)$, we note that

$$\begin{aligned} -X_{rot}(-s)''' + \left(\frac{(-s)^2}{4} - c_0^2\right)(-X'_{rot}(-s)) - \frac{(-s)}{4}X_{rot}(-s) \\ = \tilde{X}_{rot}(s)''' + \left(\frac{s^2}{4} - c_0^2\right)\tilde{X}'_{rot}(s) - \frac{s}{4}\tilde{X}_{rot}(s) = 0, \end{aligned}$$

i.e., $\tilde{X}_{rot}(s)$ is also a solution of (4.40). Since $\tilde{X}_{rot}(0) = X_{rot}(0)$, $\tilde{X}'_{rot}(0) = X'_{rot}(0)$, $\tilde{X}''_{rot}(0) = X''_{rot}(0)$, hence, $X_{rot}(s)$ is an even function. As a result,

$$\int_{-\infty}^{\infty} X_{rot}(s)ds = 2\int_{0}^{\infty} X_{rot}(s)ds = 2\lim_{s\to\infty}\int_{0}^{s} X_{rot}(\tilde{s})d\tilde{s} = 2\lim_{s\to\infty} I_{rot}(s),$$

which solves

$$\begin{cases} I^{(4)}_{rot}(s) + (s^2/4 - c_0^2)\, I''_{rot}(s) - (s/4) I'_{rot}(s) = 0 \\ I_{rot}(0) = 0, \quad I'_{rot}(0) = 2c_0 A_2/\sqrt{A_2^2 + A_3^2}, \\ I''_{rot}(0) = 0, \quad I'''_{rot}(0) = -c_0 A_3/\sqrt{A_2^2 + A_3^2}. \end{cases} \tag{4.41}$$

Thus, the problem reduces to computing $I_{rot}(s)$ and in order to do it numerically, we introduce

$$\begin{aligned} &I_1(s) = I_{rot}(s),\ I_2(s) = I'_{rot}(s) = I'_1(s), \\ &I_3(s) = I''_{rot}(s) = I'_2(s),\ I_4(s) = I'''_{rot}(s) = I'_3(s), \end{aligned}$$

and rewrite (4.41) as

$$\begin{pmatrix} I_1(s) \\ I_2(s) \\ I_3(s) \\ I_4(s) \end{pmatrix}' = \begin{pmatrix} 0 & 1 & 0 & 0 \\ 0 & 0 & 1 & 0 \\ 0 & 0 & 0 & 1 \\ 0 & \frac{s}{4} & -\left(c_0^2 + \frac{s^2}{4}\right) & 0 \end{pmatrix} \begin{pmatrix} I_1(s) \\ I_2(s) \\ I_3(s) \\ I_4(s) \end{pmatrix} = \begin{pmatrix} I_2(s) \\ I_3(s) \\ I_4(s) \\ \frac{s}{4} I_2(s) - \left(c_0^2 + \frac{s^2}{4}\right) I_3(s) \end{pmatrix}, \tag{4.42}$$

with initial conditions

$$\begin{cases} I_1(0) = 0, \quad I_2(0) = 2c_0 A_2/\sqrt{A_2^2 + A_3^2}, \\ I_3(0) = 0, \quad I_4(0) = -c_0 A_3/\sqrt{A_2^2 + A_3^2}. \end{cases} \tag{4.43}$$

We solve (4.42)-(4.43) numerically by using a fourth-order Runge–Kutta method by taking $s \in [0, L/2]$, where the interval has been discretized into $N+1$ equally spaced nodes $s_n = n\Delta s$, $\Delta s = (L/2)/N$, $n = 0, 1, 2, \ldots, N$. For our numerical simulations, we have taken $L = 2000$, $N = 10^6$ and $c_0 = 0.1680125318446675$ corresponding to $l = 0.6$. The left side of Figure (4.5) shows the semilogarithmic plot of the approximation of $I_{rot}(s)$ which as s gets larger converges to a value that can be given in a closed form

by the expression in Theorem 6:

$$\lim_{s\to\infty} I_{rot}(s) = \frac{1}{2}\int_{-\infty}^{\infty} X_{rot}(s)ds = \frac{\pi c_0^2}{\sqrt{1-e^{-\pi c_0^2}}}.$$

The algebraic value of the integral for given c_0 is 0.3044205299096596, and using that we compute the error for the numerical solution. On the right-hand side of Figure 4.5, we have plotted it on a logarithmic scale which clearly decreases as s grows. Moreover, the above mentioned behavior remains consistent for different values of c_0, i.e., l as well, which gives a numerical proof of the Theorem 6.

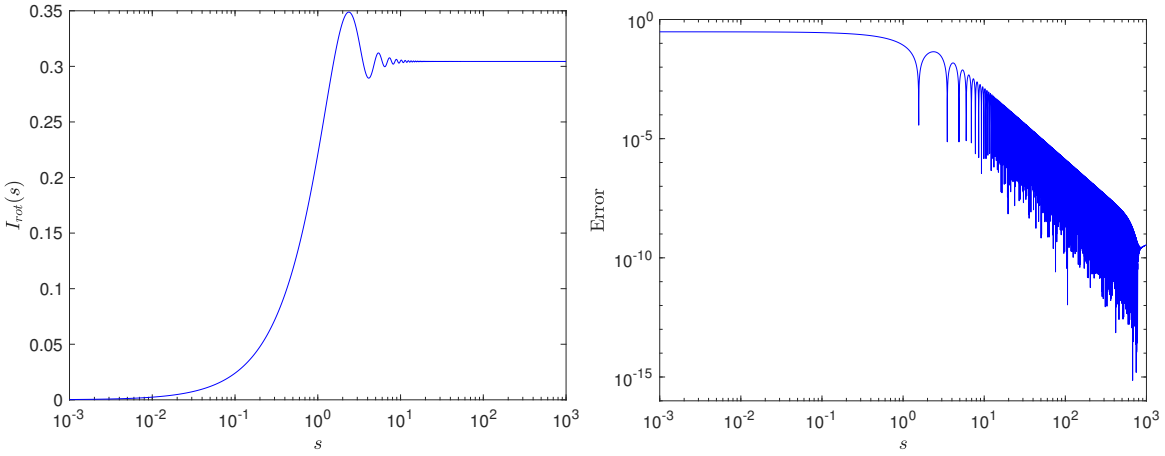

.

Figure 4.5 Left: Semilogarithmic plot for $I_{rot}(s)$ for $s_{max} = 1000$, $c_0 = 0.1680125318446675$. Right: Logarithmic plot of error $|I_{rot}(s) - \pi c_0^2/\sqrt{1-e^{-\pi c_0^2}}|$

4.5 Expression for $\mathbf{A}^{\pm} = (A_1, \pm A_2, \pm A_3)^T$

For the one-corner problem in the Euclidean case, a precise expression for each of the components of tangent vector $\mathbf{A}^{+} = (A_1, A_2, A_3)^T$ was given in [36], and later using a similar approach, an expression for A_1 was obtained in the hyperbolic case [21]. In the following lines, we re-derive A_1 by means of the Laplace transform using a completely different approach, and continuing the computations in [21], we calculate A_2 and A_3 whose knowledge was found to be extremely useful in Section 4.2.

4.5.1 Computation of A_1 using the Laplace transform

Unlike the last section, where we used the analytic (even) solution of (4.20) to compute the speed of center for mass, we consider the odd solution which behaves like δ' near the origin and can be expressed as

$$\hat{\chi}(\xi) = b_0\delta' + b_1\,\mathrm{sgn}(\xi) + b_2\,\mathrm{sgn}(\xi)\xi + \dots.$$

Differentiating it gives

$$\begin{aligned}\hat{\chi}'(\xi) &= b_0\delta'' + (2b_1 + 2b_2\xi)\delta + b_2\,\mathrm{sgn}(\xi) + \dots,\\ \hat{\chi}''(\xi) &= b_0\delta''' + (2b_1 + 2b_2\xi)\delta' + 4b_2\delta + \dots,\end{aligned}$$

and substituting above terms in (4.20) yields the first few coefficients such as

$$b_0 = 1,\ b_1 = -c_0^2,\ b_2 = -c_0^4/(1 - 4c_0^2).$$

If we write the first component of $\hat{\mathbf{X}}(\xi)$ as $\hat{X}_1(\xi) = -iA_1\hat{\chi}(\xi)$, and define

$$\widehat{W}_1(\eta) = \widehat{W}_1(\xi^2) = \xi^2\hat{X}_1(\xi),\ \eta > 0,$$

which solves

$$\widehat{W}'' + \widehat{W}\left(1 + \frac{c_0^2}{\eta}\right) = 0 \Leftrightarrow \eta\widehat{W}'' + \eta\widehat{W} + c_0^2\widehat{W} = 0,$$

then,

$$\widehat{W}_1(0) = 0,\ \widehat{W}_1'(0) = \lim_{\eta\to 0}\frac{\widehat{W}_1(\eta)}{\eta} = iA_1c_0^2. \tag{4.44}$$

Next, let's define the Laplace transform of $\widehat{W}_1(\eta)$ as

$$\mathcal{L}(t) = \mathcal{L}\{\widehat{W}_1(\eta)\} = \int_0^\infty \widehat{W}_1(\eta)e^{-t\eta}d\eta,\ t > 0, \tag{4.45}$$

and consider

$$\mathcal{L}\left\{\eta\widehat{W}'' + \eta\widehat{W} + c_0^2\widehat{W}\right\} = 0. \tag{4.46}$$

By using the following properties of the Laplace transform:

$$\begin{aligned}\mathcal{L}\{\widehat{W}^m(\eta)\} = t^m\mathcal{L}\{\widehat{W}(\eta)\} - t^{m-1}\widehat{W}(0) - t^{m-2}\widehat{W}'(0) - \cdots\\ - t\widehat{W}^{m-2}(0) - \widehat{W}^{m-1}(0),\end{aligned}$$

$$\mathcal{L}\{\eta^m \widehat{W}(\eta)\} = (-1)^m \frac{d^m}{dt^m}\mathcal{L}\{\widehat{W}(\eta)\},\ m = 1, 2, \ldots,$$

(4.46) becomes

$$\begin{aligned} &-[t^2\mathcal{L}(t) - t\mathcal{L}(0) - \mathcal{L}'(0)]' - \mathcal{L}'(t) + c_0^2\mathcal{L}(t) = 0 \\ \Longrightarrow\ &t^2\mathcal{L}'(t) + 2t\mathcal{L}(t) + \mathcal{L}'(t) - c_0^2\mathcal{L}(t) = 0. \end{aligned} \tag{4.47}$$

Moreover,

$$\mathcal{L}(0) = \int_0^\infty \widehat{W}_1(\eta)d\eta = 2\int_0^\infty \xi\widehat{W}_1(\xi^2)d\xi = 2\int_0^\infty \xi^3\hat{X}_1(\xi)d\xi = \int_{-\infty}^\infty \xi^3\hat{X}_1(\xi)d\xi,$$

where in the last equality we have used the fact that $\hat{X}_1$ is odd. Using the differentiation property of the Fourier transform, we obtain

$$\mathcal{L}(0) = iX_1'''(s)|_{s=0} = ic_0T_1'(0) = ic_0^2. \tag{4.48}$$

Consider again (4.45) and write

$$\mathcal{L}(t) = \int_0^\infty \widehat{W}_1(\eta)e^{-t\eta}d\eta = \frac{1}{t}\int_0^\infty \widehat{W}_1'(\eta)e^{-t\eta}d\eta = \frac{\widehat{W}_1'(0)}{t^2} + \frac{1}{t^2}\int_0^\infty \widehat{W}_1''(\eta)e^{-t\eta}d\eta,$$

i.e.,

$$t^2\mathcal{L}(t) = \widehat{W}_1'(0) + \int_0^\infty \widehat{W}_1''e^{-t\eta}d\eta,$$

which as $t \to \infty$ becomes

$$\lim_{t\to\infty} t^2\mathcal{L}(t) = \widehat{W}'(0). \tag{4.49}$$

Hence, from (4.47)-(4.48), we have the following initial value problem:

$$\begin{cases} \mathcal{L}'(t) + \frac{2t}{1+t^2}\mathcal{L}(t) - \frac{c_0^2}{1+t^2}\mathcal{L}(t) = 0, \\ \mathcal{L}(0) = ic_0^2, \end{cases} \tag{4.50}$$

and after solving it, we get

$$\mathcal{L}(t) = \frac{\mathcal{L}(0)}{1+t^2}e^{c_0^2\arctan(t)},$$

which in turn gives

$$\lim_{t\to\infty} t^2\mathcal{L}(t) = \lim_{t\to\infty} \frac{\mathcal{L}(0)t^2}{1+t^2}e^{c_0^2\arctan(t)} = ic_0^2e^{\pi c_0^2/2}.$$

Thus, from (4.44), (4.49) and the last equation, we conclude

$$ic_0^2 A_1 = \widehat{W}'(0) = ic_0^2 e^{c_0^2\pi/2} \implies A_1 = e^{\pi c_0^2/2}.$$

The above approach works for the Euclidean case as well, hence, following the same steps, one can arrive at the corresponding expression for A_1.

4.5.2 Computation of A_2 and A_3

Writing the time-like tangent vector $\mathbf{T}$, space-like normal and binormal vector $\mathbf{n}$, $\mathbf{b}$ componentwise, $\mathbf{T} \equiv (T_j)$, $\mathbf{n} \equiv (n_j)$, $\mathbf{b} \equiv (b_j)$, we have

$$|n_j|^2 + |b_j|^2 - |T_j|^2 = \begin{cases} -1 & \text{if } j = 1, \\ 1, & \text{if } j = 2, 3, \end{cases}$$

with initial conditions

$$\mathbf{T}(0) = (1, 0, 0)^T, \ \mathbf{n}(0) = (0, 1, 0)^T, \ \mathbf{b}(0) = (0, 0, 1)^T.$$

On the other hand, from [21, Theorem 1]

$$A_j = \lim_{s\to\infty} T_j(s), \ j = 1, 2, 3$$

and from [21, (51)]

$$T_j(s) = i(1 + \theta_j\bar{\vartheta}_j)(s), \ j = 2, 3, \tag{4.51}$$

where θ_j and ϑ_j satisfy

$$\begin{cases} \theta_j'' + i(s/2)\theta_j' - (c_0^2/4)\theta_j = 0 \\ \vartheta_j'' + i(s/2)\vartheta_j' - (c_0^2/4)\vartheta_j = 0 \\ \theta_j'\bar{\vartheta}_j' - (c_0^2/4)\theta_j\bar{\vartheta}_j = E_j, \end{cases} \tag{4.52}$$

and can be represented as

$$\begin{cases} \theta_j(s) = (a_{1,j}\beta_1(s) + a_{2,j}\beta_2(s)), \\ \vartheta_j(s) = (b_{1,j}\beta_1(s) + b_{2,j}\beta_2(s)). \end{cases} \tag{4.53}$$

Moreover, E_j can be chosen as $c_0^2/2$ and $\beta_1(s)$, $\beta_2(s)$ are as in [21, (55)]. With this, our first goal is to compute $a_{1,j}, a_{2,j}, b_{1,j}, b_{2,j}$.

In this regard, differentiating (4.53) gives

$$\begin{cases} \theta_j'(s) = (a_{1,j}\beta_1'(s) + a_{2,j}\beta_2'(s)), \\ \vartheta_j'(s) = (b_{1,j}\beta_1'(s) + b_{2,j}\beta_2'(s)), \end{cases} \tag{4.54}$$

and for $j = 2, 3$, the asymptotics of $\theta_j(s)$ and $\vartheta_j(s)$ are given by

$$\begin{cases} \theta_j(s) = (a_{1,j}\gamma_1 + a_{2,j}\gamma_2)e^{-i\frac{c_0^2}{2}\log s} + \mathcal{O}(1/s), \ s \to \infty, \\ \vartheta_j(s) = (b_{1,j}\gamma_1 + b_{2,j}\gamma_2)e^{-i\frac{c_0^2}{2}\log s} + \mathcal{O}(1/s), \ s \to \infty. \end{cases} \tag{4.55}$$

So, for $j = 2$, we write

$$E_2 = \theta_2'\bar{\vartheta}_2' - (c_0^2/4)\theta_2\bar{\vartheta}_2 = c_0^2/2,$$

and

$$T_2(0) = i(1 + \theta_2(0)\bar{\vartheta}_2(0)) = 0, \implies \theta_2(0)\bar{\vartheta}_2(0) = -1,$$

as a result,

$$\theta_2'(0)\bar{\vartheta}_2(0) = c_0^2/4. \tag{4.56}$$

Also, recall that from [21, (52)-(53)]

$$n_j = (i/c_0)(\theta_j\bar{\vartheta}_j' + \theta_j'\bar{\vartheta}_j), \ b_j = (1/c_0)(\theta_j\bar{\vartheta}_j' - \theta_j'\bar{\vartheta}_j),$$

and

$$n_j - ib_j = (2i/c_0)\theta_j\bar{\vartheta}_j', \tag{4.57}$$

so for $j = 2$, $1 = (2i/c_0)\theta_2(0)\bar{\vartheta}'(0)$. If we choose $\theta_2(0) = 1$, then by using (4.51), (4.56),(4.57), we obtain

$$\begin{cases} \theta_2'(0) = ic_0/2, \\ \bar{\vartheta}_2(0) = -1, \bar{\vartheta}_2'(0) = -ic_0/2. \end{cases} \tag{4.58}$$

Thus, by evaluating (4.53), (4.54) at $s = 0$, and using the fact that $\beta_1(0) = -\beta_2(0)$, $\beta_1'(0) = \beta_2'(0)$, and (4.58), we get

$$\begin{cases} (a_{1,2} - a_{2,2})\beta_1(0) = 1, \ (a_{1,2} + a_{2,2})\beta_1'(0) = ic_0/2, \\ (b_{1,2} - b_{2,2})\beta_1(0) = -1, \ (b_{1,2} + b_{2,2})\beta_1'(0) = ic_0/2, \end{cases} \tag{4.59}$$

which in turn gives

$$\begin{cases} a_{1,2} = \frac{ic_0\beta_1 + 2\beta_1'}{4\beta\beta_1'}, \ a_{2,2} = \frac{ic_0\beta_1 - 2\beta_1'}{4\beta\beta_1'}, \\ b_{1,2} = \frac{ic_0\beta_1 - 2\beta_1'}{4\beta\beta_1'}, \ b_{2,2} = \frac{ic_0\beta_1 + 2\beta_1'}{4\beta\beta_1'}, \end{cases} \tag{4.60}$$

where $\beta_1 = \beta_1(0)$, $\beta_1' = \beta_1'(0)$. Similarly, for $j = 3$, by taking $E_3 = c_0^2/2$, $\theta_3(0) = i$ and after performing same steps as before

$$\begin{cases} a_{1,3} = i\frac{-c_0\beta_1 + 2\beta_1'}{4\beta\beta_1'}, \ a_{2,3} = -i\frac{c_0\beta_1 + 2\beta_1'}{4\beta\beta_1'}, \\ b_{1,3} = -i\frac{c_0\beta_1 + 2\beta_1'}{4\beta\beta_1'}, \ b_{2,3} = i\frac{-c_0\beta_1 + 2\beta_1'}{4\beta\beta_1'}. \end{cases} \tag{4.61}$$

Remember that our aim is to compute A_j, which from (4.51) and (4.55) implies computing

$$\lim_{s\to\infty} \theta_j(s)\bar{\vartheta}_j(s) = (a_{1,j}(s)\gamma_1 + a_{2,j}(s)\gamma_2)\left(\overline{b_{1,j}(s)\gamma_1 + b_{2,j}(s)\gamma_2}\right), \ j = 2, 3.$$

So, for $j = 2$, using (4.60), $\lim_{s\to\infty} \theta_2(s)\bar{\vartheta}_2(s)$

$$\begin{aligned} &= (a_{1,2}\gamma_1 + a_{2,2}\gamma_2)\left(\overline{b_{1,2}\gamma_1 + b_{2,2}\gamma_2}\right) \\ &= \left(\frac{ic_0}{4\beta_1'}(\gamma_1 + \gamma_2) + \frac{1}{2\beta_1}(\gamma_1 - \gamma_2)\right)\overline{\left(\frac{ic_0}{4\beta_1'}(\gamma_1 + \gamma_2) - \frac{1}{2\beta_1}(\gamma_1 - \gamma_2)\right)}, \end{aligned} \tag{4.62}$$

where

$$\begin{aligned} \gamma_1 &= 2e^{-\pi c_0^2/4}\Gamma(1 + ic_0^2/2), \quad \gamma_2 = -2e^{\pi c_0^2/4}\Gamma(1 + ic_0^2/2), \\ \beta_1 &= 2e^{-\pi c_0^2/8}\Gamma(1 + ic_0^2/4), \quad \beta_1' = -(c_0^2/2)e^{i\pi/4}e^{-\pi c_0^2/8}\Gamma(1/2 + ic_0^2/4). \end{aligned}$$

Next, by taking

$$u = \frac{ic_0}{4\beta_1'}(\gamma_1 + \gamma_2), \ v = \frac{1}{2\beta_1}(\gamma_1 - \gamma_2),$$

(4.62) becomes

$$\lim_{s\to\infty} \theta_2(s)\bar{\vartheta}_2(s) = (u + v)(\bar{u} - \bar{v}) = |u|^2 - |v|^2 + v\bar{u} - u\bar{v}. \tag{4.63}$$

By using the following identities for $y \in \mathbb{R}$:

$$\begin{aligned} |\Gamma(1+iy)|^2 &= y^2|\Gamma(iy)|^2, \quad |\Gamma(iy)|^2 = \frac{\pi}{y\sinh \pi y}, \\ |\Gamma(1/2+iy)|^2 &= \frac{\pi}{\cosh \pi y}, \quad \overline{\Gamma(1+iy)} = \Gamma(1-iy), \end{aligned} \tag{4.64}$$

we can compute

$$\begin{aligned} |\gamma_1-\gamma_2|^2 &= 4|\Gamma(1+ic_0^2/2)|^2(e^{\pi c_0^2/4+e^{-\pi c_0^2/4}})^2 \\ &= 2\pi c_0^2\frac{(e^{\pi c_0^2/4+e^{-\pi c_0^2/4}})^2}{\sinh(\pi c_0^2/2)} = 4\pi c_0^2\frac{(1+e^{-\pi c_0^2/2})^2}{1-e^{-\pi c_0^2}}, \end{aligned}$$

and similarly,

$$|\gamma_1+\gamma_2|^2 = 4\pi c_0^2\frac{(1-e^{-\pi c_0^2/2})^2}{1-e^{-\pi c_0^2}},\ |\beta_1'|^2 = \frac{\pi c_0^2}{4}\frac{e^{-\pi c_0^2/4}}{\cosh(\pi c_0^2/4)},\ |\beta_1|^2 = \pi c_0^2\frac{e^{-\pi c_0^2/4}}{\sinh(\pi c_0^2/4)},$$

which gives

$$|u|^2 = \frac{(1-e^{-\pi c_0^2/2})^2\cosh(\pi c_0^2/4)}{e^{-\pi c_0^2/4}(1-e^{-\pi c_0^2})},\ |v|^2 = \frac{(1+e^{-\pi c_0^2/2})^2\sinh(\pi c_0^2/4)}{e^{-\pi c_0^2/4}(1-e^{-\pi c_0^2})}.$$

On the other hand,

$$v\bar{u} = \frac{(\gamma_1-\gamma_2)}{2\beta_1}\overline{\frac{ic_0}{4\beta_1'}(\gamma_1+\gamma_2)},$$

where

$$(\gamma_1-\gamma_2)\overline{(\gamma_1+\gamma_2)} = -4c_0^2\pi,$$

can be easily computed by using the properties of Gamma function stated above, and

$$\beta_1\bar{\beta}_1' = -c_0^2e^{-\pi c_0^2/4}e^{-i\pi/4}\Gamma(1+ic_0^2/4)\Gamma(1/2-ic_0^2/4).$$

Thus, we have

$$v\bar{u} = -\frac{i\pi c_0}{2}\frac{e^{\pi c_0^2/4}e^{i\pi 4}}{\Gamma(1+ic_0^2/4)\Gamma(1/2-ic_0^2/4)},$$

and

$$\begin{aligned} v\bar{u}-u\bar{v} &= -i\pi c_0e^{\pi c_0^2/4}\frac{\Re\{e^{i\pi/4}\Gamma(1-ic_0^2/4)\Gamma(1/2+ic_0^2/4)\}}{|\Gamma(1-ic_0^2/4)|^2|\Gamma(1/2-ic_0^2/4)} \\ &= -\frac{2i}{\pi c_0}e^{\pi c_0^2/4}\sinh(\pi c_0^2/2)\Re\{e^{i\pi/4}\Gamma(1-ic_0^2/4)\Gamma(1/2+ic_0^2/4)\}. \end{aligned}$$

Combining this and the expression for $|u|^2$ and $|v|^2$, from (4.63) we write

$$\begin{aligned} A_2 &= \lim_{s\to\infty} T_2(s) = \lim_{s\to\infty} T_2(s)(1+\theta_2(s)\bar{\vartheta}_2(s)) \\ &= 1 + |a|^2 - |b|^2 + b\bar{a} - a\bar{b} \\ &= \frac{2}{\pi c_0} e^{\pi c_0^2/4} \sinh(\pi c_0^2/2) \Re\{e^{i\pi/4}\Gamma(1 - ic_0^2/4)\Gamma(1/2 + ic_0^2/4)\}, \end{aligned}$$

and after performing similar steps for $j = 3$ and using (4.61), one can arrive at

$$A_3 = \frac{2}{\pi c_0} e^{\pi c_0^2/4} \sinh(\pi c_0^2/2) \Im\{e^{i\pi/4}\Gamma(1 - ic_0^2/4)\Gamma(1/2 + ic_0^2/4)\}.$$

4.6 Transfer of linear momentum

In case of a 3D fluid modeled by Euler equations and having a regular vorticity ω that vanishes at infinity with an appropriate rate, the fluid impulse

$$\int_{\mathbb{R}^3} x \wedge_+ \omega(x,t)\, dx,$$

remains conversed in time (see [46, p. 24]). For the motion of vortex filaments under LIA, since the vorticity is assumed to be concentrated along the curve $\mathbf{X}$, the corresponding quantity is

$$\mathcal{M}(t) = \int_{-\infty}^{\infty} \mathbf{X}(s,t) \wedge_+ \mathbf{T}(s,t)\, ds,$$

which is called the linear momentum. The connection of this quantity with the fluid impulse was shown in [52], and that it remains conserved for the closed regular curves, was proved in [1].

Recently in [7, Appendix], for the self-similar solutions of VFE, the linear momentum was obtained as

$$\mathcal{M}(t) = |t|c_0(\mathbf{A}^+ - \mathbf{A}^-) = 2c_0|t|(0, A_2, A_3),$$

which decays as t decreases until it vanishes at the singularity formation time and grows again after crossing $t = 0$; hence, it is not preserved. The reason for this can be associated with the behavior of the filament at infinity. Later in [23], for the regular planar M-sided closed polygons, it was found that $\mathcal{M}(t)$ remains conserved; however, when it is computed only for one side of the M-polygon, a characteristic intermittent behavior was observed.

This motivates us to investigate the case of planar l-polygon in the Minkowski space which are open. In this regard, we write the linear momentum for regular planar l-polygon as

$$\mathcal{M}_l(t) = \int_{-\infty}^{\infty} \rho_l(s,t)\, ds, \tag{4.65}$$

where $\rho_l(s,t) = \mathbf{X}_l(s,t) \wedge_- \mathbf{T}_l(s,t)$. We compute this quantity numerically, and for this, we consider an l-polygon $\mathbf{X}_l$ with M sides. Using Lemma 6.1 in [23] for $\mathbf{X}_l$, at any rational time t_{pq}, $\mathbf{X}_l(s,t_{pq}) \wedge_- \mathbf{T}_l(s,t_{pq})$ is constant for $s \in (s_j, s_{j+1})$, $s_j = -L/2 + jL/(Mq)$, $j = 0,1,\ldots,Mq-1$, $L = Ml$. Thus, (4.65) can be computed exactly as

$$\mathcal{M}_l(t_{pq}) = \frac{l}{q} \sum_{j=0}^{Mq-1} \mathbf{X}_l(s_j,t_{pq}) \wedge_- \mathbf{T}_l(s_j^+,t_{pq}), \tag{4.66}$$

which is valid for both q even and odd.

For our numerical simulations, we have taken $M = 96$, $l = 0.1$, $N/M = 2^{11}$, which show that the first component of $\mathcal{M}_l(t)$ is identically equal to zero, whereas the shape of second component reminds us of Figure 9 in [23] and third component resembles to the real part of the Riemann's function, i.e., $\phi(t)$ (see Figure 4.6).

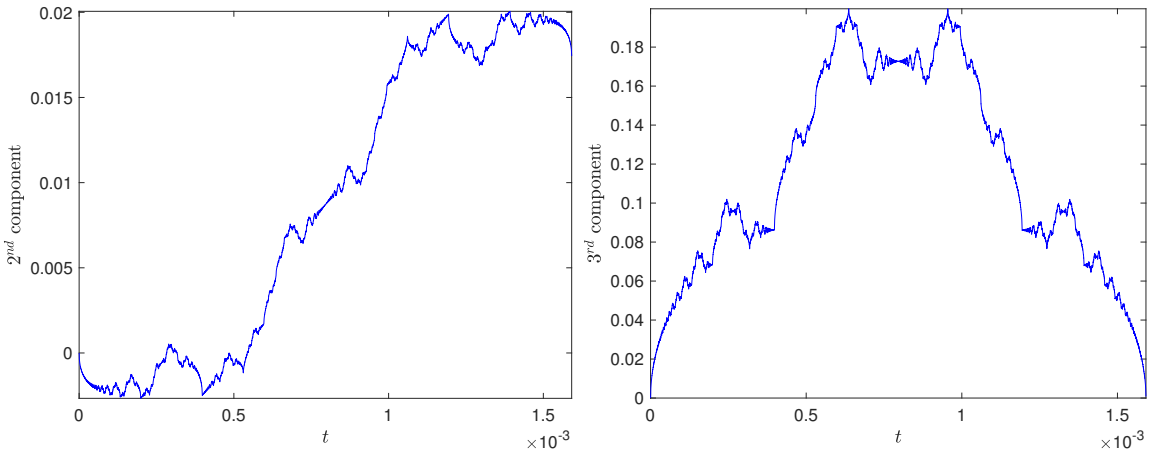

Figure 4.6 Left: Second component of $\mathcal{M}(t^{(n)})$, and right: Third component of $\mathcal{M}(t^{(n)})$-$\mathcal{M}(t^{(0)})$ for $M = 96$, $l = 0.1$, $N/M = 2^{11}$ computed by considering only the inner points as done in Chapter 3

As a next step, we observe the dependence of $\mathcal{M}_l(t)$ on the parameter l. Recall the discussion on $\mathbf{X}(0,t)$ in Section 3.4.1, where for the same purpose, we worked with the algebraic solution that was obtained up to a movement in the YZ-plane. In that case,

we compute

$$\int_{-L/2}^{L/2} \mathbf{X}_{alg}(s,t_{pq}) \wedge_{-} \mathbf{T}_{alg}(s,t_{pq})\ ds = \frac{l}{q} \sum_{j=0}^{Mq-1} \mathbf{X}_{alg}(s_j,t_{pq}) \wedge_{-} \mathbf{T}_{alg}(s_j^{+},t_{pq}).$$

In this regard, we have plotted the second and third components of $\mathcal{M}(t^{(n)})$ for $n = 0, 1, \ldots, 9242$, for $M = 48$, $l = 0.1$, which are both periodic in time. Furthermore,

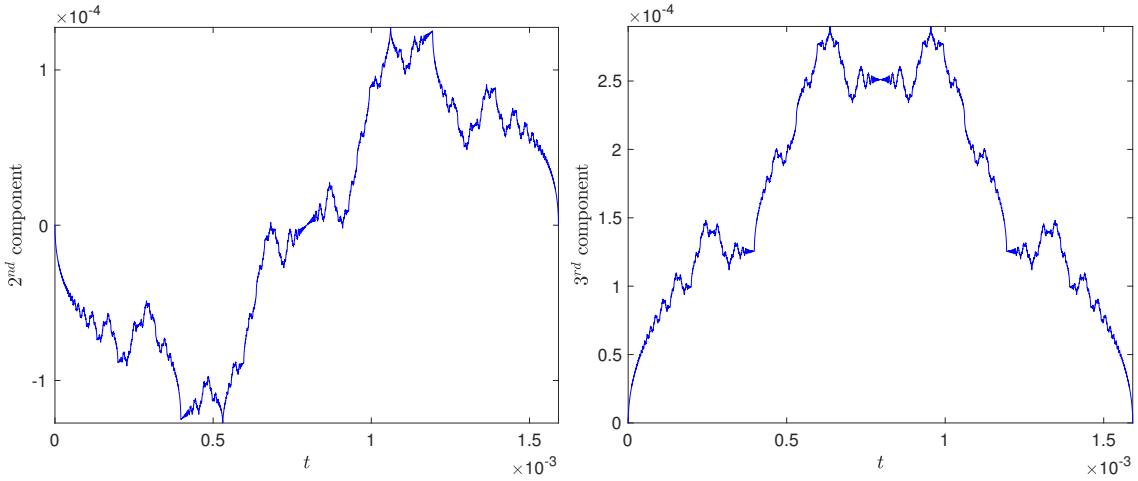

Figure 4.7 Left: Second component of $\mathcal{M}(t^{(n)})$, and right: third component of $\mathcal{M}(t^{(n)})$-$\mathcal{M}(t^{(0)})$ for $n = 0, 1, \ldots, 2 \cdot 4621$, for $M = 48$, $l = 0.1$ and $\mathcal{M}_3(t^{(0)}) = 5.008337500992375 \cdot 10^{-4}$.

note that in the previous sections we claimed that the l-polygon problem in the Minkowski space can be seen as a superposition of several one-corner problems. Bearing this in mind, we compute $\mathcal{M}_l(t)$ only for one side and observe the behavior of quantity

$$\int_0^l \rho_l(s,t)\ ds,$$

which we compute by using the algebraic solution as

$$\int_0^l \mathbf{X}_{alg}(s,t_{pq}) \wedge_{-} \mathbf{T}_{alg}(s,t_{pq})\ ds = \frac{l}{q} \sum_{j=0}^{q-1} \mathbf{X}_{alg}(s_j,t_{pq}) \wedge_{-} \mathbf{T}_{alg}(s_j^{+},t_{pq}). \tag{4.67}$$

For the same choice of parameters mentioned above, we find that first component of (4.67) is no more equal to zero, on the other hand, except for a scaling, the second and third components do not change their shape when compared with their counterparts in (4.66). Thus, an intermittent behavior is observed in all three components. Observe that the first and second components are identically same up to

a sign and scaling. To be precise, the scaling factor in the above-mentioned case is 20.016663875654110. As a next step, we have considered the l-polygon of fixed length

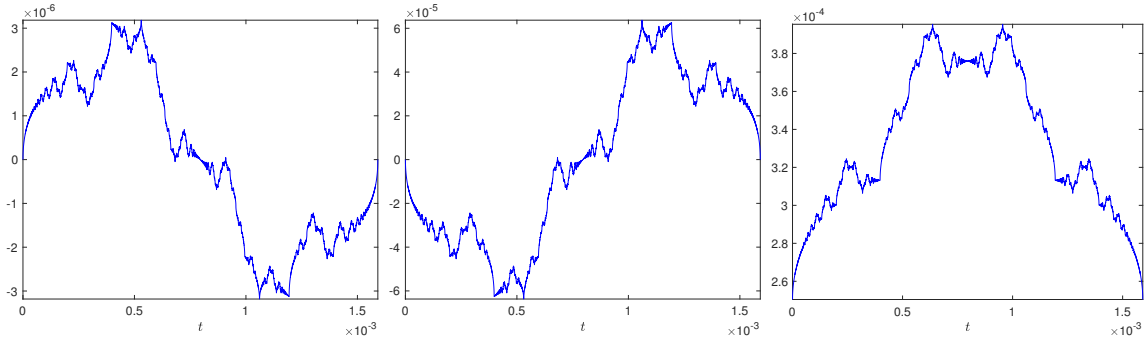

Figure 4.8 First, second and third component of $\mathcal{M}(t^{(n)})$ computing using one side, $n = 0, 1, \ldots, 2 \cdot 4621$, $M = 48, l = 0.1$. Observe that the first and second components are identically same up to a sign and scaling. To be precise, the scaling factor in the above mentioned case is -20.016663875654110.

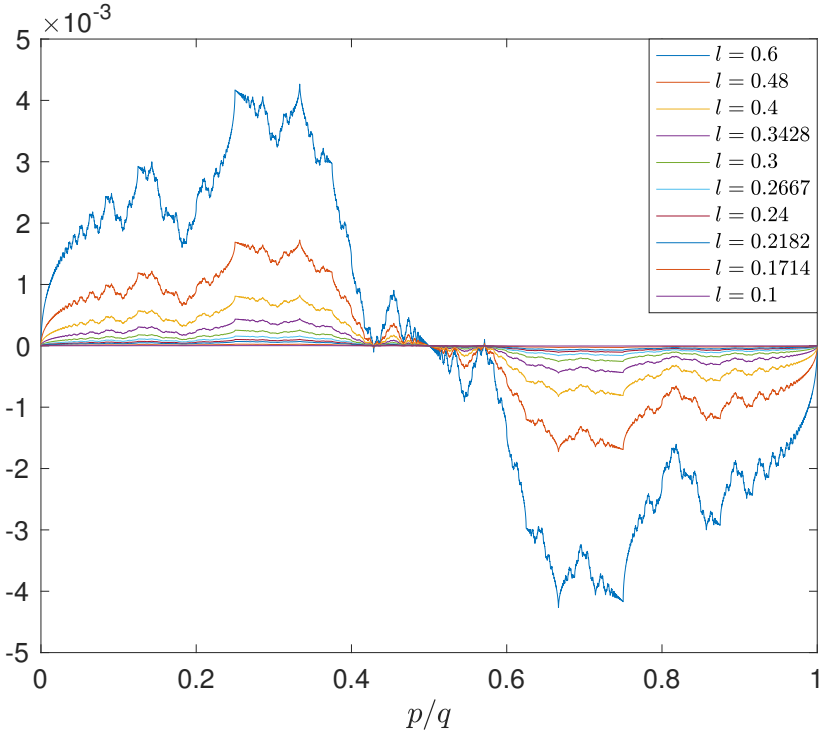

Figure 4.9 The first component of $\mathcal{M}(t^{(n)})$ computing using one side, $n = 0, 1, \ldots, 2 \cdot 4621$, for different M and l values such that $L = 4.8$.

L, and different number of sides and angles between them. In particular, we have taken $L = 4.8$, and $M = 8, 10, 12, 14, 16, 18, 20, 22, 28, 48$, i.e., $l = 0.6, 0.48, 0.4, 0.3428 \ldots$,

$0.3, 0.2667\ldots, 0.24, 0.2182\ldots, 0.1714\ldots, 0.1$, respectively, so that $L = lM$; Figure 4.9 shows the first component of (4.67) for each of them. Note that except for a scaling, the curves in Figure 4.9 can compared with the imaginary part of ϕ in (3.50).

4.7 Conclusion

In Chapter 3, it was observed that the planar l-polygon propagates in the vertical direction with a constant speed c_l. In this chapter, by establishing a relationship between the l-polygon and one-corner problems, we have given an exact expression for c_l. The components of the tangent vector at time zero for the one-corner problem have been determined, as a result, a precise mathematical expression is provided for each of them. Moreover, we have also examined the behavior of the linear momentum for the planar l-polygon which displays an intermittent behavior.

Chapter 5

Conclusions and Future work

5.1 Conclusions

The main protagonist of this memoir has been the vortex filament equation (VFE), a subject in fluid literature that has gained a substantial attention recently. The equation is also known as the binormal flow or localized induction approximation (LIA) and it describes the time evolution of a vortex filament curve. In this thesis, we have studied the evolution of regular polygonal curves according to VFE. Recent work on regular planar M-sided polygons as an initial data shows that the numerical evolution captures certain properties of the real fluid, for instance, the axis-switching phenomenon. On the other hand, due to its relationship with the so-called Schrödinger map and nonlinear Schrödinger (NLS) equation, we have a piecewise continuous initial data for the tangent vectors and an infinite sum of Dirac deltas at the level of the NLS equation. As a result, studying the problem from an analytical point of view also becomes important.

With this motivation, we have extended the previous case of regular planar M-polygons in two different ways. First, by considering helical M-polygons, i.e., introducing a nonzero torsion in the Euclidean planar polygons and secondly, with planar l-polygons in the hyperbolic space, called the Minkowski 3-space. Assuming uniqueness, we have successfully investigated both the cases by observing that the dynamics at later times exhibits a Talbot effect. That is to say, at rational multiples of the period new polygons appears whose number of sides depends on the parity of the denominator and this has been confirmed with both algebraic and numerical techniques. We have also found that the time evolution preserves several quantities of the binormal flow and the symmetries of the regular polygons help us in obtaining some of these. The speed of the center of mass with which the polygonal curve moves in the vertical direction, is one such example. In fact, the symmetries also come to our aid in reducing the

computation cost of the numerical method in the Euclidean case, however, this has not been the case in the hyperbolic setting. Furthermore, in the trajectory of a single point, i.e., $\mathbf{X}(0,t)$, we have discovered new variants of the Riemann's non-differentiable function which is multifractal and of great interest from a mathematical point of view. Let us not forget that the motivation to work with the polygonal curves also comes from the one-corner problem. In this work, through numerical experiments, we have observed that for infinitesimal times, the multiple-corner problem can be seen as a superposition of several one-corner problems.

As a conclusion, we see that these new solutions (i.e., polygonal curves) of VFE can be used to illustrate numerically that the smooth solutions given by helices and straight lines in the Euclidean space and hyperbolas in the Minkowski space, share the same instability as the one already established for circles. This is accomplished by showing the existence of variants of the Riemann's function that are as close to smooth curves as desired when measured in the right topology. This topology is motivated by some recent results on the well-posedness of VFE, which proves that the self-similar solutions of VFE have finite renormalized energy [8, 9].

5.2 Future work

In this section, we present some ideas on the work done in this thesis that could be of interest in the future.

In **Chapter 2**, for a given value of sides M and torsion b, along with the trajectory of a single point $\mathbf{X}(0,t)$, we analyzed the evolution of a regular helical M-polygon both algebraically and numerically. Moreover, given any rational time t_{pq}, the aperiodic evolution gives rise to two terms, i.e., Galilean shift s_{pq} and phase shift, which capture the movement of a corner along the polygonal curve and the XY-plane, respectively. Bearing this in mind, it might be interesting to look at the time evolution of a corner for a given time period. In this direction, we have computed the trajectory of $\mathbf{X}(s_{pq}, t_{pq})$ for $p = 0, 1, \ldots, q$, $M = 6$, $b = 0.4$, $N/M = 2q$, where $q = 2099$ has been taken as a prime number. Figure 5.1 shows the first, second and third components of $\mathbf{X}(s_{pq}, t_{pq})$, which in turn has been shown on the left hand side of Figure 5.2. These plots remind us of the trajectory $\mathbf{X}(0,t)$ in the zero-torsion case, whose presence can further be seen after a certain rotation performed manually on $\mathbf{X}(s_{pq}, t_{pq})$; one can also compare the case $M = 3$, $b = 0.4$, plotted on the right hand side of the Figure 5.2 with [22, Figure 2]. Giving a precise expression or an algorithm to compute this rotation seems

to be challenging and could be of immense help in determining the algebraic solution completely.

In [39], it was shown that the Riemann's function ϕ as in (3.50) satisfies

$$\phi(t) = \phi(t_{pq}) + e^{i\pi m/4} q^{-1/2} (t - t_{pq})^{1/2} + \text{lower-order terms},$$

with $p, q \in \mathbb{Z}$, $q > 0$, $\gcd(p, q) = 1$, $m \equiv m(t_{pq}) \in \mathbb{Z}/8\mathbb{Z}$. This identity was proved in [30, Theorem 4.2] which also implies that the Hölder exponent of ϕ is $1/2$, i.e.,

$$|\phi(t) - \phi(t_{pq})| = q^{-1/2} |t - t_{pq}|^{1/2} + \text{lower-order terms}.$$

In our opinion, it could be interesting to compute the Hölder exponent and relevant properties for the ϕ_M and $\phi_{c,d}$ which were discovered in the evolution of helical M-polygons.

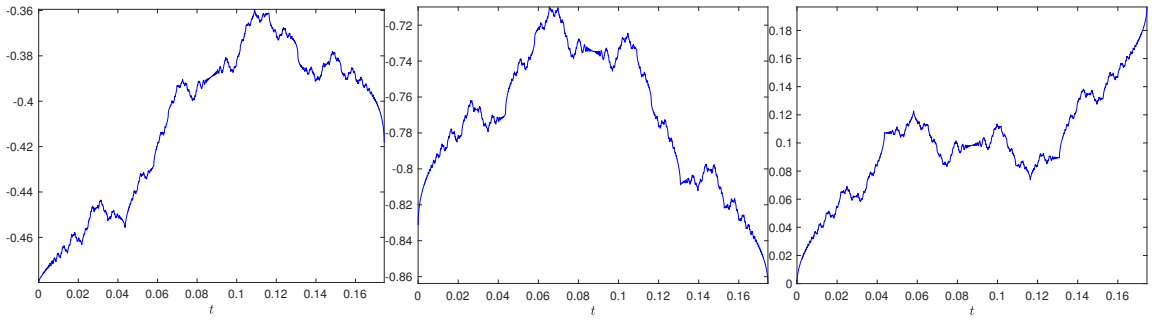

Figure 5.1 The first (left), second (center) and third (right) component of $\mathbf{X}(s_{pq}, t_{pq})$ for $M = 6$, $b = 0.4$, $N/M = 2q$, $q = 2099$ for one time period.

In **Chapter 3**, during the numerical evolution of hyperbolic l-polygon, we found that a fourth-order finite difference space discretization with the same order explicit Runge–Kutta method in time gave the best results. We also tried a pseudo-spectral discretization with Chebyshev polynomials as basis functions, but due to their unequal distribution near the boundary, an explicit method in time was undesirable. As a result, we went on to work with the implicit methods and were successful in obtaining a second-order semi-implicit backward differentiation formula for both Schrödinger map equation and its stereographic projection. However, not only these methods are of lower-order for our purpose, due to the denseness of the Chebyshev differentiation matrices, the resulting system is also computationally expensive to solve. Thus, finding an efficient higher-order method in time could be advantageous. On the other hand, the second component of the trajectory of the center of mass of the l-polygon was found to have a periodic structure. We think that it might be interesting to learn more

about it as a function and its properties. Finally, we would also like to address the case of an arbitrary polygon in the Minkowski space.

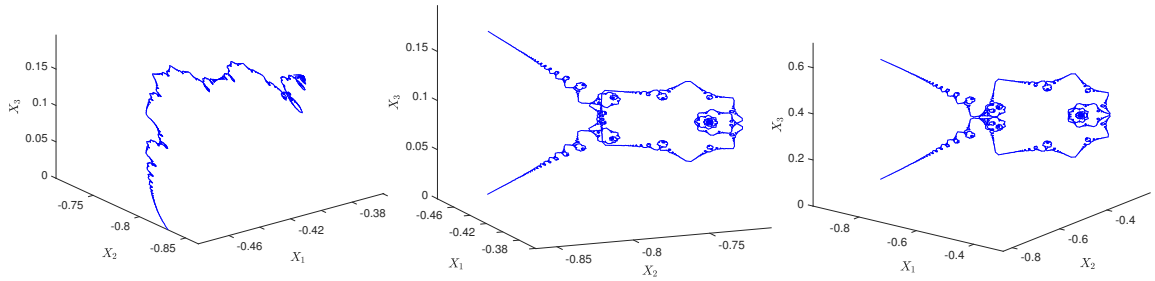

Figure 5.2 Left: $\mathbf{X}(s_{pq}, t_{pq})$ for $M = 6$, $b = 0.4$, $N/M = 2q$, $q = 2099$ for one time period; center: $\mathbf{X}(s_{pq}, t_{pq})$ after a certain rotation, right: After a rotation $\mathbf{X}(s_{pq}, t_{pq})$ for $M = 3$, $b = 0.4$.

In **Chapter 4**, we gave an expression for the angle φ which the curve $\mathbf{X}_{rot}(0, t)$ makes with the plane containing $\mathbf{X}_{rot}(s, 0)$. Thus, for a given $c_0 > 0$, from (4.8) we have

$$\varphi = \arctan\left(\frac{A_2}{A_3}\right) = \arctan\left(\frac{\Re\{\Upsilon\}}{\Im\{\Upsilon\}}\right) = \arg(i\bar{\Upsilon}), \tag{5.1}$$

with

$$\Upsilon = e^{i\pi/4} B(1 - ic_0^2/4, 1/2 + ic_0^2/4)\Gamma(3/2) = \frac{\sqrt{\pi}}{2}\, e^{i\pi/4} B(1 - ic_0^2/4, 1/2 + ic_0^2/4),$$

where $B(\cdot, \cdot)$ is the beta function.

We are curious to know if the above expression can be reduced to a more simplified form.

Helical polygons in the Minkowski space

Having addressed the helical polygons in the Euclidean case, it becomes natural to consider its counterpart in the hyperbolic space. As mentioned in Section 1.4, in the Minkowski space, the torsion can be introduced in two different ways, hence, following that discussion, we expect hyperbolic and circular helical polygons. In the following lines, we state some essential points to investigate each of the two cases.

Circular helical polygon

The arc-length parameterized regular circular helical polygon is characterized by parameters M and b which correspond to the number of its sides and torsion, respectively.

In this case, the parameter b is also the first component of the 2π-periodic tangent vector $\mathbf{T}(s,0)$ as shown in Figure 1.4. So, we write

$$\mathbf{T}(s,0)=\left(b, a\cos\left(\frac{2\pi k}{M}\right), a\sin\left(\frac{2\pi k}{M}\right)\right)^T \equiv (b, ae^{2\pi ik/M}), \qquad s_k<s<s_{k+1}, \quad (5.2)$$

where $s_k = 2\pi k/M$ for $k=0,1,...,M-1$, $b>1, a^2-b^2=-1$. The corresponding curve $\mathbf{X}(s,0)$ is a circular helical polygon whose vertices at s_k are given by

$$\mathbf{X}(s_k,0)=\left(bs_k, \frac{a\pi\sin(\pi(2k-1)/M)}{M\sin(\pi/M)}, -\frac{a\pi\cos(\pi(2k-1)/M)}{M\sin(\pi/M)}\right)^T, \qquad (5.3)$$

so that for any $s\in(s_k,s_{k+1})$, the corresponding point $\mathbf{X}(s,0)$ lies on the line segment joining $\mathbf{X}(s_k,0)$ and $\mathbf{X}(s_{k+1},0)$. Moreover, the time-like curvature angle ρ_0 and space-like torsion angle θ_0 are given by

$$\rho_0 = 2\,\mathrm{arcsinh}\left(a\sin\left(\frac{\pi}{M}\right)\right),\ \theta_0 = 2\arctan\left(b\tan\left(\frac{\pi}{M}\right)\right),$$

which do not depend on k values and satisfy

$$\cos\left(\frac{\theta_0}{2}\right)\cosh\left(\frac{\rho_0}{2}\right)=\cos\left(\frac{\pi}{M}\right).$$

On the other hand, at the level of NLS equation, the initial datum is the following:

$$\psi_\theta(s,0)=c_{\theta,0}e^{i\gamma s}\sum_{k=-\infty}^{\infty}\delta(s-2\pi k/M),$$

where $\gamma = M\theta_0/2\pi$ and $c_{\theta,0}=\sqrt{\frac{2}{\pi}\ln\left(\cosh\left(\frac{\rho_0}{2}\right)\right)}$.

Hyperbolic helical polygon

When the parameter b corresponds to the third component of the tangent vector $\mathbf{T}(s,0)$ as in Figure 1.3, the regular hyperbolic helical polygon is characterized by parameter l and b, where l is its side-length. Thus, we have

$$\mathbf{T}(s,0)=\left(a\cosh\left(\frac{l}{2}+s_k\right), a\sinh\left(\frac{l}{2}+s_k\right), b\right)^T \equiv (ae^{j(l/2+s_k)}), \qquad s_k<s<s_{k+1}, \quad (5.4)$$

where $s_k = kl$ for $k \in \mathbb{Z}$, $b > 1, a^2 - b^2 = -1$. The corresponding curve $\mathbf{X}(s,0)$ is a hyperbolic helical polygon whose vertices at s_k are given by

$$\mathbf{X}(s_k,0) = \frac{l/2}{\sinh(l/2)} \left(a\sinh(s_k), a\cosh(s_k), b\right)^T, \tag{5.5}$$

so that for any $s \in (s_k, s_{k+1})$, the corresponding point $\mathbf{X}(s,0)$ lies on the line segment joining $\mathbf{X}(s_k,0)$ and $\mathbf{X}(s_{k+1},0)$. The time-like curvature angle and space-like torsion angle are given by

$$\rho_0 = 2\,\mathrm{arcsinh}\left(a\sinh\left(\frac{l}{2}\right)\right), \ \theta_0 = 2\arctan\left(b\tanh\left(\frac{l}{2}\right)\right),$$

which satisfy

$$\cos\left(\frac{\theta_0}{2}\right)\cosh\left(\frac{\rho_0}{2}\right) = \cosh\left(\frac{\pi}{M}\right).$$

Moreover, the initial datum for the NLS equation is

$$\psi_\theta(s,0) = c_{\theta,0}e^{i\gamma s}\sum_{k=-\infty}^{\infty}\delta(s-lk),$$

where $\gamma = \theta_0/l$, and $c_{\theta,0}$ is as given above.

With this knowledge by following the steps as in Chapter 2, for a given rational time t_{pq}, $\psi(s,t_{pq})$ can be obtained which also gives an expression for the Galilean shift for both types of helical polygons. Later, by integrating generalized Frenet–Serret formula (3.7), we can construct $\mathbf{X}$ and $\mathbf{T}$ up to a rigid movement. Furthermore, for a given rational time t_{pq}, the mutual angle between any two sides of the new helical polygon is constant and given by

$$\rho_q = \begin{cases} 2\,\mathrm{arccosh}\left(\cosh^{1/q}(\rho_0/2)\right), & \text{if } q \text{ odd}, \\ 2\,\mathrm{arccosh}\left(\cosh^{2/q}(\rho_0/2)\right), & \text{if } q \text{ even}. \end{cases} \tag{5.6}$$

On the other hand, for the numerical evolution, we can employ the same methods as discussed in Chapter 2 and 3. Hence, similar conclusions as in Chapter 2, are expected to be drawn about the trajectory of $\mathbf{X}(0,t)$. Since we can construct the algebraic solution up to a rotation, the evolution near the irrational times can also be investigated for both kinds of helical polygons. We also plan to address their relationship with the one-corner problem.

Finally, giving a theoretical proof to (2.27), (3.22), (5.6) would also be interesting. In this direction, we have started with an approach involving quaternions both in the Euclidean and hyperbolic cases.

Appendix A

Basic concepts and supporting computations

A.1 Basics of the hyperbolic geometry

In this section, we state some basic definitions and concepts in the hyperbolic geometry, that have been essential in this Ph.D. thesis [45, 51].

A.1.1 The Minkowski space

The Minkowski space denoted by $\mathbb{R}^{1,2}$ is a three-dimensional Euclidean space defined with the inner product:

$$u \circ_{-} v = -u_1 v_1 + u_2 v_2 + u_3 v_3, \tag{A.1}$$

where $u = (u_1, u_2, u_3)$, $v = (v_1, v_2, v_3)$ and $\langle \cdot, \cdot \rangle_0$ is called the *Lorentzian* or *Minkowski inner product*. Sometimes it is also expressed as

$$u \circ_{-} v = u_1 v_1 + u_2 v_2 - u_3 v_3, \tag{A.2}$$

in that case, the Minkowski space is denoted by $\mathbb{R}^{2,1}$. The structure of $\circ_{-}$ allows it to take both negative and non-positive values which implies that it is not positive-definite. The inner product gives rise to the *Minkowski norm*:

$$\|u\|_0 = \sqrt{u \circ_{-} u} = \sqrt{-u_1^2 + u_2^2 + u_3^2}. \tag{A.3}$$

By defining a vector $\overline{u} = (u_2, u_3) \in \mathbb{R}^{1,1}$, we have $u = (u_1, \overline{u})$ and then, we can also write

$$\|u\|_0^2 = -u_1^2 + |\overline{u}|^2, \tag{A.4}$$

The set of $u \in \mathbb{R}^{1,2}$ such that $\|u\|_0 = 0$ is the *hypercone* C^2 defined by $|u_1| = |\overline{u}|$. The hypercone C^2 is called *light cone* of $\mathbb{R}^{1,2}$. Thus, depending on the value of $\|\cdot\|_0$ a vector $u \in \mathbb{R}^{1,2}$ can be characterized in three ways:

- Light-like when $\|u\|_0 = 0$ (light cone),
- Space-like when $\|u\|_0 > 0$ (exterior of the light cone),
- Time-like when $\|u\|_0$ is imaginary (interior of the light cone). A time-like vector u is called positive/future (resp. negative/past) iff $u_1 > 0$ (resp. $u_1 < 0$). Both interior and exterior of C^2 in $\mathbb{R}^{1,2}$ are the open subsets of $\mathbb{R}^{1,2}$.

The first property also implies that the Minkowski norm $\|\cdot\|_0$ is a pseudo-norm as a light-like vector need not necessarily be a zero vector.

Hyperbolic plane

Given a and b real numbers,

$$z = a + jb,$$

is a *hyperbolic number* where j satisfies $j^2 = +1$ and is not a real number [17]. A collection of all such z is identified as *hyperbolic plane*. Just like in the case of complex plane, the addition and multiplication operations are defined as

$$\begin{aligned}(a + jb) + (c + jd) &= a + c + j(b + d),\\ (a + jb)(c + jd) &= (ac + bd) + j(ad + bc).\end{aligned}$$

Every hyperbolic number has a *conjugate hyperbolic number*

$$\bar{z} = a - jb.$$

Consequently, the *modulus* can be defined as

$$|z| = \sqrt{z\bar{z}} = \sqrt{a^2 - b^2},$$

which can be real, purely imaginary or equal to zero for $z \neq 0$. [54, Chapter 1, p.30]

A.1.2 The hyperbolic 2-space

The curvature of a sphere of radius r in $\mathbb{R}^3$ is $1/r^2$, a positive constant and for a hyperbolic 2-space, it is negative. The duality between spherical and hyperbolic geometry tells that hyperbolic 2-space should be a sphere of imaginary radius. As we have seen that under the notion of (A.3) imaginary lengths are possible, a *hyperbolic 2-space* can be defined as a collection of time-like vectors with unit magnitude:

$$F^2 = \{u \in \mathbb{R}^{1,2} : \|u\|_0^2 = -1\}. \tag{A.5}$$

Since a time-like vector has two components, F^2 is disconnected and is characterized as a union of two (positive and negative) sheets. The subset of all u in F^2 such that $u_1 > 0$ (resp. $u_1 < 0$) is called the positive/future (resp. negative/past) sheet of F^2. The *hyperboloid model* $\mathbb{H}^2$ of hyperbolic 2-space is defined as the positive sheet of F^2:

$$\mathbb{H}^2 = \{u \in \mathbb{R}^{1,2} : \|u\|_0^2 = -1, u_1 > 0\}, \tag{A.6}$$

which is the analogue of a unit sphere in the Euclidean case.

Definition 1. *Two vectors u and v in $\mathbb{R}^{1,2}$ are **Lorentz orthonormal** if and only if $u \circ_- v = 0$.*

Theorem 7. *Given two nonzero Lorentz orthogonal vectors u and v in $\mathbb{R}^{1,2}$, if u is time-like then v is space-like.*

Definition 2. *A vector subspace V of $\mathbb{R}^{1,2}$ is said to be*

1. ***time-like** if and only if V has a time-like vector,*
2. ***space-like** if and only if every nonzero vector in V is space-like, or*
3. ***light-like** otherwise.*

Definition 3 (Time-like angle between time-like vectors). *Let u and v be positive(negative) time-like vectors in $\mathbb{R}^{1,2}$. Then, the **Lorentzian time-like angle** between u and v is defined as a unique nonnegative real number $\eta(u, v)$ such that*

$$u \circ_- y = \|u\|_0 \|v\|_0 \cosh \eta(u, v) \tag{A.7}$$

Note that $\eta(u, v) = 0$ iff u and v are positive scalar multiple of each other.

Definition 4. *For u and v in $\mathbb{R}^{1,2}$, the **Lorentzian cross product** of u and v is defined as*

$$u \wedge_- v = \tilde{I}(u \wedge_+ v), \tag{A.8}$$

where

$$\tilde{I} = \begin{pmatrix} -1 & 0 & 0 \\ 0 & 1 & 0 \\ 0 & 0 & 1 \end{pmatrix}. \tag{A.9}$$

Note that $u \wedge_- v$ is Lorentz orthogonal to both u and v:

$$u \circ_- (u \wedge_- v) = u \circ_- \tilde{I}(u \wedge_+ y) = u \circ_+ (u \wedge_+ v) = 0,$$
$$v \circ_- (u \wedge_- v) = v \circ_- \tilde{I}(u \wedge_+ y) = v \circ_+ (u \wedge_+ v) = 0.$$

Theorem 8. *Given u and v linearly independent space-like vectors in $\mathbb{R}^{1,2}$, the following are equivalent:*

1. *The vectors u and v satisfy the inequality $|u \circ_- v| < \|u\|_0 \|v\|_0$.*
2. *The vector subspace V spanned by u and v is space-like.*

Definition 5 (The space-like angle between space-like vectors)**.** *Let u and v be space-like vectors in $\mathbb{R}^{1,2}$ that span a space-like vector space. Then, the **Lorentzian space-like angle** between u and v is defined as a unique real number $\eta(u, v)$ between 0 and π such that*

$$u \circ_- v = \|u\|_0 \|v\|_0 \cos \eta(u, v). \tag{A.10}$$

Observe that $\eta(u, v) = 0$ if and only if u and v are positive scalar multiples of each other, $\eta(u, v) = \pi/2$ if and only if u and v are Lorentz orthogonal and $\eta(u, v) = \pi$ if and only if u and v are negative scalar multiples of each other.

Theorem 9. *Given u and v linearly independent space-like vectors in $\mathbb{R}^{1,2}$, the following are equivalent:*

1. *The vectors u and v satisfy the inequality $|u \circ_- v| > \|u\|_0 \|v\|_0$.*
2. *The vector subspace V spanned by u and v is time-like.*

Definition 6 (The time-like angle between space-like vectors)**.** *Let u and v be space-like vectors in $\mathbb{R}^{1,2}$ that span a time-like vector space. Then, the **Lorentzian time-like angle** between u and v is defined as a unique positive real number $\eta(u, v)$ such that*

$$|u \circ_- v| = \|u\|_0 \|v\|_0 \cosh \eta(u, v). \tag{A.11}$$

Theorem 10. *Given u and v linearly independent space-like vectors in $\mathbb{R}^{1,2}$, the following are equivalent:*

1. *The vectors u and v satisfy the inequality $|u \circ_- v| = \|u\|_0 \|v\|_0$.*

2. *The vector subspace V spanned by u and v is light-like.*

Definition 7 (The angle between space-like and time-like vectors)**.** *Let u be space-like and v be time-like vectors in $\mathbb{R}^{1,2}$. Then, the* ***Lorentzian time-like angle*** *between u and v is defined as a unique nonnegative real number $\eta(u, v)$ such that*

$$|u \circ_- v| = \|u\|_0 \|v\|_0 \sinh \eta(u, v). \tag{A.12}$$

A.2 Rotation matrices in the Minkowski space

In this section, based on the work in [49], we describe the rotations in the Minkowski space $\mathbb{R}^{1,2}$.

Recall that in the Euclidean case, given a rotation axis $\mathbf{u} = (a, b, c)$ and rotation angle θ, using the Rodrigues' formula, the corresponding rotation matrix can be obtained as

$$e^{\theta A} = I + \sin(\theta)A + (1 - \cos(\theta))A^2,$$

where

$$A = \begin{pmatrix} 0 & -c & b \\ c & 0 & -a \\ -b & a & 0 \end{pmatrix},$$

is the skew-symmetric matrix and I is the identity matrix in $\mathbb{R}^3$.

In the Minkowski space depending on the rotation axis whether it is space-like or time-like, this formula takes different forms. Thus, for a rotation axis $\mathbf{u} = (a, b, c)$ and a rotation angle θ,

- if rotation axis is time-like:

$$e^{\theta B} = I + \sin(\theta)B + (1 - \cos(\theta))B^2, \tag{A.13}$$

- if rotation axis is space-like:

$$e^{\theta B} = I + \sinh(\theta)B + (1 - \cosh(\theta))B^2, \tag{A.14}$$

where

$$B = \begin{pmatrix} 0 & c & -b \\ c & 0 & -a \\ -b & a & 0 \end{pmatrix},$$

is the semi-skew symmetric matrix that satisfies $\tilde{I}B\tilde{I} = -B^T$ and $\tilde{I}$ is as in (A.9).

Properties of a hyperbolic rotation matrix

Let's denote the hyperbolic rotation matrix by $\mathbf{H}$, then

- $\mathbf{H}$ is called semi-orthogonal matrix if $\mathbf{H}u \circ_- \mathbf{H}u = u \circ_- u$ for $u \in \mathbb{R}^{1,2}$. This property also implies that semi-orthogonal matrices preserve the length of the vectors in the Minkowski space-time. Moreover, column (rows) of the semi-orthogonal matrix form an orthonormal basis of $\mathbb{R}^{1,2}$.
- $\mathbf{H}$ is a semi-orthogonal matrix if and only if $\mathbf{H}^T\tilde{I}\mathbf{H} = \tilde{I}$.
- Invariance of the Minkowski cross product:

$$\mathbf{H}(v_1 \wedge_- v_2) = \mathbf{H}v_1 \wedge_- \mathbf{H}v_2, \ \forall v_1, v_2 \in \mathbb{R}^{1,2}.$$

- Given rotation $\mathbf{H}$, through (A.13)–(A.14), the corresponding semi-skew symmetric matrix can be retrieved as

$$B = \frac{\mathbf{H} - \tilde{I}\mathbf{H}^T\tilde{I}}{2\sinh(\theta)}, \quad \text{or} \quad B = \frac{\mathbf{H} - \tilde{I}\mathbf{H}^T\tilde{I}}{2\sin(\theta)}.$$

A.3 A brief introduction to the pseudo-spectral methods

Let us consider the following initial value problem,

$$\begin{cases} u_t = \mathcal{N}(u, u_s, u_{ss}, t), \ s \in [-L/2, L/2], \ t > 0, \\ u(s, 0) = u_0(s), \end{cases} \tag{A.15}$$

where the solution $u(s,t)$ satisfies certain boundary conditions and on the right hand side, $\mathcal{N}$ is function of u, its derivatives with respect to s which in turn takes its values in a compact interval of length L. By defining the operator $\mathcal{D} = \partial_t - \mathcal{N}$, (A.15) becomes

$\mathcal{D}u = 0$. The main idea behind spectral methods is to approximate the solution $u(s,t)$ by a finite sum

$$u_N(s,t) = \sum_{k=0}^{N} a_k(t)\phi_k(s),$$

where $a_k(t)$ are the expansion coefficients which need to be determined once the choice of basis functions $\phi_k(s)$, $k = 0, 1, \ldots$ have been made. In case of an ODE, $a_k(t) \equiv a_k$. The basis functions are chosen such that the following requirements are satisfied:

(i) the approximate solution $u_N(s,t)$ must converge to $u(s,t)$ rapidly,

(ii) given coefficients a_k, calculating another set of coefficients b_k such that

$$\frac{d}{ds}\left(\sum_{k=0}^{N} a_k\phi_k(s)\right) = \sum_{k=0}^{N} b_k\phi_k(s),$$

should be easy,

(iii) the conversion between coefficients a_k, $k = 0, 1, \ldots, N$ and the function values $u(s_j,t)$ at grid points $s_j = -L/2 + jL/N$, $j = 0, 1, \ldots, N$, should be fast [32].

In the case of periodic problems, the trigonometric polynomials satisfy all three requirements, while the first two are straightforward, the third was verified with the invention of Fast Fourier Transform (FFT) algorithm in 1965 [20]. On the other hand, for the nonperiodic problems, the trigonometric polynomials do not satisfy the first requirement and imposing the periodicity artificially give rise to irregularity which make the Fourier coefficients a_k decrease as $\mathcal{O}(1/N)$ as $N \to \infty$. Truncated Taylor expansion $u_N(s,t) = \sum_{k=0}^{N} a_k(t)s^k$ also do not help for requirement (i) since the convergence over $[-1,1]$ requires $u(s,t)$ to be very smooth. The most successful function class is orthogonal polynomials of Jacobi type, with Chebyshev and Legendre polynomials as the most important cases.

As a next step, in order to determine the expansion coefficients, consider the residual

$$R_N(s,t) = \mathcal{D}(u_N - u)(s,t).$$

The basic idea is to keep $R_N(s,t)$ as small as possible across the domain while satisfying the boundary conditions. Following are the three ways to achieve this:

1. Tau: The spectral coefficients a_k are chosen so that the boundary conditions are satisfied and $R_N(s,t)$ is orthogonal to as many basis functions $\phi_k(s)$ as possible.

2. Galerkin: The original basis functions are first recombined into new basis functions so that the boundary conditions are satisfied. Then, the coefficients a_k are chosen so that $R_N(s,t)$ is orthogonal to as many new basis functions as possible.

3. Collocation or pseudo-spectral (PS): Similar to tau method, the coefficients a_k are selected so that the boundary conditions satisfied, and it is desired that $R_N(s,t)$ is zero at as many (suitably chosen) spatial gridpoints as possible.

Let us also comment that all these methods work equally well for linear problems. However, in the case of nonlinear problems, the pseudo-spectral (collocation) approach is particularly easy to apply as it involves the product of numbers rather than determining the expansion coefficients for products of expansions. Moreover, the convergence of pseudo-spectral approximations for smooth functions is $\mathcal{O}(N^{-m})$ for every m with N is the number of nodes, and $\mathcal{O}(c^N)$ $(0 < c < 1)$ for functions that are analytic. Such behavior is known as *spectral accuracy.*

A.3.1 Application to the helical M-polygon problem

In Chapter 2, to solve the coupled system of VFE and Schrödinger map equation numerically, we employed the pseudo-spectral discretization in space and due to the periodicity of the tangent vector, the trigonometric polynomials were used. In the following lines, we describe how the periodicity plays an important role in reducing the computation cost [22].

Reduction of computation cost using symmetries

As the tangent vector $\mathbf{T}$ is 2π-periodic in space, we discretise the interval $[0, 2\pi)$ into N nodes, i.e., $s_j = 2\pi j/N$ for $j = 0, 1, \ldots, N-1$. In order to compute $\mathbf{T}_s$ and $\mathbf{T}_{ss}$, we note that for a periodic function $Z(s)$ evaluated at s_j, its derivatives at s_j can be spectrally approximated as

$$Z_s(s_j) = \sum_{k=-N/2}^{N/2-1} ik\hat{Z}(k)e^{2\pi ijk/N}, \quad Z_{ss}(s_j) = -\sum_{k=-N/2}^{N/2-1} k^2\hat{Z}(k)e^{2\pi ijk/N}, \tag{A.16}$$

where

$$\hat{Z}(k) = \sum_{j=0}^{N-1} Z(s_j)e^{-2\pi ijk/N} \quad k = 0, 1, \ldots, N-1. \tag{A.17}$$

Note that both (A.16)–(A.17) are inverse and direct discrete Fourier transforms (DFT) of N elements, can be computed efficiently using the Fast Fourier algorithm (FFT)

[33]. Next, from (2.17) we have that the $\mathbf{T}$ is invariant under the rotation of $2\pi/M$ about z-axis and this fact helps us in reducing the computation cost of (A.16)–(A.17) to N/M elements. In this regard, let us consider the first two component of $\mathbf{T}$ and denote $U(s_j) = T_1(s_j,t) + iT_2(s_j,t)$ so that $U(s_{j+N/M}) = U(s_j)e^{2\pi i/M}$,

$$\begin{aligned}
\hat{U}(k) &= \sum_{j=0}^{N-1} U(s_j)e^{-2\pi ijk/N} \\
&= \sum_{l=0}^{M-1}\sum_{j=0}^{N/M-1} U(s_{j+l\frac{N}{M}})e^{-2\pi i(j+l\frac{N}{M})k/N} = \sum_{l=0}^{M-1}\sum_{j=0}^{N/M-1} U(s_j)e^{2\pi il/M}e^{-2\pi ijk/N-2\pi ilk/M} \\
&= \sum_{l=0}^{M-1}\Big(\sum_{j=0}^{N/M-1} U(s_j)e^{-2\pi ijk/N}\Big)e^{-2\pi i(k-1)l/M} \\
&= \sum_{j=0}^{N/M-1} U(s_j)e^{-2\pi ijk/N}\cdot\sum_{l=0}^{M-1} e^{-2\pi i(k-1)l/M}.
\end{aligned}$$

Using

$$\sum_{l=0}^{M-1} e^{-2\pi i(k-1)l/M} = \begin{cases} M, & \text{if } k-1 \equiv 0 \bmod M, \\ 0, & \text{if } k-1 \not\equiv 0 \bmod M. \end{cases}$$

we obtain

$$\hat{U}(k) = \begin{cases} M\sum_{j=0}^{N/M-1} U(s_j)e^{-2\pi ijk/N}, & \text{if } k \equiv 1 \bmod M, \\ 0, & \text{if } k \not\equiv 1 \bmod M. \end{cases}$$

Thus, the non-zero $\hat{U}(k)$ are computed using the DFT of N/M elements:

$$\hat{U}(Mk+1) = M\sum_{j=0}^{N/M-1} U(s_j)e^{-2\pi ij(Mk+1)/N} = M\sum_{j=0}^{N/M-1}\Big[U(s_j)e^{-2\pi ij/N}\Big]e^{-2\pi ijk/(N/M)}$$

for $k = 0, 1, \cdots, N/M-1$. Following the same steps as above for T_3, the third component of $\mathbf{T}$ and using

$$T_3(s_{j+N/M}) = T_3(s_j),$$

we get

$$\hat{T}_3(k) = \sum_{j=0}^{N-1} T_3(s_j)e^{-2\pi ijk/N}$$

$$
\begin{aligned}
&= \sum_{l=0}^{M-1} \sum_{j=0}^{N/M-1} U(s_{j+l\frac{N}{M}}) e^{-2\pi i(j+l\frac{N}{M})k/N} \\
&= \sum_{l=0}^{M-1} \sum_{j=0}^{N/M-1} U(s_j) e^{-2\pi ijk/N - 2\pi ilk/M} \\
&= \sum_{j=0}^{N/M-1} U(s_j) e^{-2\pi ijk/N} \cdot \sum_{l=0}^{M-1} e^{-2\pi ikl/M} \\
&= \begin{cases} M \sum_{j=0}^{N/M-1} U(s_j) e^{-2\pi ijk/N}, & if k \equiv 0 \bmod M, \\ 0, & if k \not\equiv 0 \bmod M. \end{cases}
\end{aligned}
$$

and the non-zero elements of $\hat{T}_3(k)$ are obtained with a FFT of N/M elements

$$
\hat{U}(Mk) = M \sum_{j=0}^{N/M-1} U(s_j) e^{-2\pi ij(Mk)/N} = M \sum_{j=0}^{N/M-1} U(s_j) e^{-2\pi ijk/(N/M)} \tag{A.18}
$$

for $k = 0, 1, \cdots, N/M - 1$.

Moreover, the computation of the derivatives using N/M elements is done using the inverse FFT. In this direction, using $k = M\tilde{k} + 1$ for $\tilde{k} = 0, 1, \ldots, N/M - 1$

$$
\begin{aligned}
U_s(s_j) &= \sum_{k=-N/2}^{N/2-1} ik\hat{U}(k) e^{2\pi ijk/N} \\
&= \sum_{k\prime=-N/(2M)}^{N/(2M)-1} i(M\tilde{k}+1)\hat{U}(M\tilde{k}+1) e^{2\pi ij(M\tilde{k}+1)/N} \\
&= \left[\sum_{\tilde{k}=-N/(2M)}^{N/(2M)-1} i(M\tilde{k}+1) e^{2\pi ij\tilde{k}/(N/M)} \; \hat{U}(M\tilde{k}+1) \right] e^{2\pi ij/N},
\end{aligned}
$$

and

$$
U_{ss}(s_j) = \left[- \sum_{\tilde{k}=-N/(2M)}^{N/(2M)-1} (M\tilde{k}+1)^2 e^{2\pi ij\tilde{k}/(N/M)} \; \hat{U}(M\tilde{k}+1) \right] e^{2\pi ij/N}
$$

and

$$
\begin{aligned}
T_{3_s}(s_j) &= \sum_{\tilde{k}=-N/(2M)}^{N/(2M)-1} iM\tilde{k} e^{2\pi ij\tilde{k}/(N/M)} \; \hat{U}(M\tilde{k}) \\
T_{3_{ss}}(s_j) &= - \sum_{\tilde{k}=-N/(2M)}^{N/(2M)-1} (M\tilde{k})^2 e^{2\pi ij\tilde{k}/(N/M)} \; \hat{U}(M\tilde{k}),
\end{aligned}
$$

for $j = 0, 1, \ldots, N/M - 1$.

A.4 Generalized Frenet–Serret frame

In the classical theory of continuous curves in $\mathbb{R}^3$, to describe a moving coordinate frame along a sufficiently differentiable space, the Frenet–Serret formulas are employed [56]. However, the main drawback of the Frenet–Serret frame is that it requires the curvature to be nonzero everywhere. Thus, for many curves such as straight lines, it is not possible to work with this frame, as a result, we look for a new generalization. In the following lines, we derive it for both the Euclidean and hyperbolic cases. In this regard, when we use $\pm$, the positive sign corresponds to the Euclidean and the negative one to the hyperbolic case. Similarly, by using $\mp$, we refer to the Euclidean case with negative sign and to the hyperbolic case with positive sign.

Let us consider an arbitrary orthonormal basis $\{\mathbf{T}, \mathbf{e}_1, \mathbf{e}_2\}$ where the tangent vector $\mathbf{T}$, normal $\mathbf{e}_1$ and binormal $\mathbf{e}_2$ satisfy $\mathbf{T} \wedge_\pm \mathbf{e}_1 = \mathbf{e}_2$, $\mathbf{e}_1 \wedge_\pm \mathbf{e}_2 = \pm\mathbf{T}$ and $\mathbf{T} \wedge_\pm \mathbf{e}_2 = -\mathbf{e}_1, \mathbf{T} \circ_\pm \mathbf{T} = \pm 1, \mathbf{e}_1 \circ_\pm \mathbf{e}_1 = 1 = \mathbf{e}_2 \circ_\pm \mathbf{e}_2$.
Since $\mathbf{T} \circ_\pm \mathbf{T}_s = 0$, $\mathbf{T} \perp \mathbf{T}_s$, hence, we can express

$$\mathbf{T}_s = \kappa_1 \, \mathbf{e}_1 + \kappa_2 \, \mathbf{e}_2, \tag{A.19}$$

and similarly, we have

$$\mathbf{e}_{1,s} = \kappa_4 \, \mathbf{T} + \kappa_3 \, \mathbf{e}_2, \tag{A.20}$$

$$\mathbf{e}_{2,s} = \kappa_5 \, \mathbf{T} + \kappa_6 \, \mathbf{e}_1, \tag{A.21}$$

where κ_j, $j = 1, 2, \ldots, 6$ are real constants to be determined later.
Furthermore, differentiating $\mathbf{e}_1 \circ_\pm \mathbf{T} = 0$ gives

$$\mathbf{e}_{1,s} \circ_\pm \mathbf{T} = -\mathbf{e}_1 \circ_\pm \mathbf{T}_s,$$

and computing it using (A.19)–(A.20) yields $\kappa_1 = \mp\kappa_4$. Similarly, using the orthogonality of $\mathbf{T}$, $\mathbf{e}_2$ and $\mathbf{e}_1$, $\mathbf{e}_2$, we get $\kappa_5 = \mp\kappa_2$ and $\kappa_6 = -\kappa_3$, respectively. Consequently, by replacing $\kappa_1 = \alpha$, $\kappa_2 = \beta$, $\kappa_3 = \gamma$, we obtain the new generalized Frenet–Serret frame as

$$\begin{pmatrix} \mathbf{T} \\ \mathbf{e}_1 \\ \mathbf{e}_2 \end{pmatrix}_s = \begin{pmatrix} 0 & \alpha & \beta \\ \mp\alpha & 0 & \gamma \\ \mp\beta & -\gamma & 0 \end{pmatrix} \cdot \begin{pmatrix} \mathbf{T} \\ \mathbf{e}_1 \\ \mathbf{e}_2 \end{pmatrix}. \tag{A.22}$$

Remark that when $\alpha = \kappa$, the curvature of the curve and $\gamma = \tau$, the torsion of the curve, and $\beta = 0$, we recover the original Frenet–Serret frame (1.1), (1.11). On the other hand, $\gamma = 0$ yields the so-called Bishop frame [14]. Next, in order to determine how α, β, γ are related to κ and τ, we look at the relationship between the two orthonormal frames which is given by

$$\begin{pmatrix} \mathbf{T} \\ \mathbf{e}_1 \\ \mathbf{e}_2 \end{pmatrix} = \begin{pmatrix} 1 & 0 & 0 \\ 0 & \cos(\theta(s)) & -\sin(\theta(s)) \\ 0 & \sin(\theta(s)) & \cos(\theta(s)) \end{pmatrix} \cdot \begin{pmatrix} \mathbf{T} \\ \mathbf{n} \\ \mathbf{b} \end{pmatrix}, \tag{A.23}$$

for some angle θ that is a function of s [19]. Thus, by differentiating the expression for $\mathbf{e}_1$ and $\mathbf{e}_2$, with respect to s, we get

$$\begin{aligned} \mathbf{e}_{1,s} &= \mathbf{n}_s \cos(\theta) - \mathbf{n} \sin(\theta)\theta' - \mathbf{b}_s \sin(\theta) - \mathbf{b} \cos(\theta)\theta', \\ &= (-\kappa \mathbf{T} + \tau \mathbf{b}) \cos(\theta) - \mathbf{n} \sin(\theta)\theta' - (-\tau \mathbf{n}) \sin(\theta) - \mathbf{b} \cos(\theta)\theta', \\ \mathbf{e}_{2,s} &= \mathbf{n}_s \sin(\theta) + \mathbf{n} \cos(\theta)\theta' + \mathbf{b}_s \cos(\theta) - \mathbf{b} \sin(\theta)\theta' \\ &= (-\kappa \mathbf{T} + \tau \mathbf{b}) \sin(\theta) + \mathbf{n} \cos(\theta)\theta' + (-\tau \mathbf{n}) \cos(\theta) - \mathbf{b} \sin(\theta)\theta'. \end{aligned} \tag{A.24}$$

On the other hand, from (A.22)–(A.23)

$$\begin{aligned} \mathbf{e}_{1,s} &= \mp\alpha \mathbf{T} + \gamma \mathbf{e}_2 = \mp\alpha \mathbf{T} + \gamma(\mathbf{n} \sin(\theta) + \mathbf{b} \cos(\theta)), \\ \mathbf{e}_{2,s} &= \mp\beta \mathbf{T} - \gamma \mathbf{e}_1 = \mp\beta \mathbf{T} - \gamma(\mathbf{n} \cos(\theta) - \mathbf{b} \sin(\theta)). \end{aligned} \tag{A.25}$$

Finally, by comparing (A.24)–(A.25), we obtain

$$\begin{cases} \alpha = \kappa \cos(\theta), \ \beta = \kappa \sin(\theta), \\ \gamma = \tau - \theta'. \end{cases} \tag{A.26}$$

Recall that in the Bishop frame, i.e., the one we use while dealing with polygonal curves, $\gamma = 0$, as a result,

$$\theta(s) = \int^s \tau(\tilde{s}) d\tilde{s}.$$

A.4.1 $\psi = \alpha + i\beta$ satisfies the NLS equation

In the framework of the generalized Frenet–Serret frame, the filament function as in (1.14) takes the following form

$$\psi = \kappa e^{i \int_0^s \tau} = \alpha + i\beta.$$

We show that both in the Euclidean and hyperbolic setting, ψ satisfies the NLS equation. To begin with, let us define

$$\mathbf{N} = \mathbf{e}_1 + i\mathbf{e}_2, \tag{A.27}$$

then from (1.17), we write

$$\begin{aligned} \mathbf{T}_s &= \alpha\mathbf{e}_1 + \beta\mathbf{e}_2 = \frac{1}{2}\left(\bar{\psi}\mathbf{N} + \psi\bar{\mathbf{N}}\right), \\ \mathbf{N}_s &= \mathbf{e}_{1,s} + i\mathbf{e}_{2,s} = \mp(\alpha + i\beta)\mathbf{T} = \mp\psi\mathbf{T}. \end{aligned} \tag{A.28}$$

By noting that $\mathbf{T} \wedge_\pm \mathbf{N} = -i\mathbf{N}$, we can express

$$\begin{aligned} \mathbf{T}_t = \mathbf{T} \wedge_\pm \mathbf{T}_{ss} &= \mathbf{T} \wedge_\pm \left[\tfrac{1}{2}(\bar{\psi}\mathbf{N} + \psi\bar{\mathbf{N}})\right]_s \\ &= \tfrac{1}{2}\mathbf{T} \wedge_\pm \left[\bar{\psi}\mathbf{N}_s + \bar{\psi}_s\mathbf{N} + \psi_s\bar{\mathbf{N}} + \psi\bar{\mathbf{N}}_s\right] \\ &= \frac{i}{2}\left(\psi_s\bar{\mathbf{N}} - \bar{\psi}_s\mathbf{N}\right). \end{aligned}$$

As a next step, we write

$$\mathbf{N}_t = a_1\mathbf{T} + a_2\mathbf{N} + a_3\bar{\mathbf{N}},$$

where the constants a_1, a_2 and a_3 are calculated using

$$\begin{aligned} \mathbf{N} \circ_\pm \mathbf{T} = 0 &\implies \mathbf{N}_t \circ_\pm \mathbf{T} = -\mathbf{N} \circ_\pm \mathbf{T}_t = -i\psi_s, \\ \mathbf{N} \circ_\pm \mathbf{N} = 0 &\implies \mathbf{N}_t \circ_\pm \mathbf{N} = 0, \\ \mathbf{N} \circ_\pm \bar{\mathbf{N}} = 2 &\implies \mathbf{N}_t \circ_\pm \mathbf{N} + \mathbf{N} \circ_\pm \bar{\mathbf{N}}_t = 0. \end{aligned} \tag{A.29}$$

Note that the last equation implies that the real part of $\mathbf{N}_t \circ_\pm \bar{\mathbf{N}}$ is equal to zero, i.e., $\mathbf{N}_t \circ_\pm \bar{\mathbf{N}} = iR$, $R \in \mathbb{R}$. As a result, we obtain $a_1 = \mp i\psi_s$, $a_2 = \frac{i}{2}R$, $a_3 = 0$, and

$$\mathbf{N}_t = \mp i\psi_s\mathbf{T} + \frac{i}{2}R\mathbf{N}.$$

By differentiating it with respect to s yields

$$\begin{aligned} \mathbf{N}_{ts} &= \mp i\psi_{ss}\mathbf{T} \mp i\psi_s\mathbf{T}_s + \tfrac{i}{2}R_s\mathbf{N} + \tfrac{i}{2}R\mathbf{N}_s \\ &= \mp(i\psi_{ss} + \tfrac{i}{2}\psi R)\mathbf{T} \mp \tfrac{i}{2}\psi_s(\bar{\psi}\mathbf{N} + \psi\bar{\mathbf{N}}) + \tfrac{i}{2}R_s\mathbf{N}. \end{aligned} \tag{A.30}$$

On the other hand,

$$\begin{aligned}\mathbf{N}_{st} &= (\mp\psi\mathbf{T})_t = \mp\psi_t\mathbf{T} \mp \tfrac{i}{2}\psi\left(\psi_s\bar{\mathbf{N}} - \bar{\psi}_s\mathbf{N}\right)\\ &= \mp\psi_t\mathbf{T} \mp \tfrac{i}{2}\psi\psi_s\bar{\mathbf{N}} \pm \tfrac{i}{2}\psi\bar{\psi}_s\mathbf{N}.\end{aligned} \tag{A.31}$$

Equating the coefficients of $\mathbf{T}$ and $\mathbf{N}$ in (A.30)–(A.31) gives

$$\begin{aligned}&\psi_t = i\psi_{ss} + \tfrac{i}{2}R\psi,\\ &\tfrac{i}{2}R_s = \pm\tfrac{i}{2}\psi\bar{\psi}_s \pm \tfrac{i}{2}\bar{\psi}\psi_s \implies R = \pm|\psi|^2 + A(t),\ A(t)\in\mathbb{R},\end{aligned} \tag{A.32}$$

and

$$\psi_t = i\psi_{ss} \pm \tfrac{i}{2}\psi(|\psi|^2 + A(t)).$$

Bibliography

[1] R. J. Arms and F. R. Hama. Localized-Induction Concept on a Curved Vortex and Motion of an Elliptic Vortex Ring. *Physics of Fluids*, 8(4):553–559, 1965. doi: https://doi.org/10.1063/1.1761268.

[2] Uri M. Ascher, Steven J. Ruuth, and Brian T. R. Wetton. Implicit-Explicit Methods for Time-Dependent Partial Differential Equations. *SIAM Journal on Numerical Analysis*, 32(3):797–823, 1995. doi: https://epubs.siam.org/doi/10.1137/0732037.

[3] V. Banica and L. Vega. On the Stability of a Singular Vortex Dynamics. *Communications in Mathematical Physics*, 286(2):593–627, 2009. doi: https://doi.org/10.1007/s00220-008-0682-3.

[4] V. Banica and L. Vega. Scattering for 1D cubic NLS and singular vortex dynamics. *Journal of the European Mathematical Society (JEMS)*, 14(1):209–253, 2012. doi: 10.4171/JEMS/300.

[5] V. Banica and L. Vega. Stability of the Self-similar Dynamics of a Vortex Filament. *Archive for Rational Mechanics and Analysis*, 210(3):673–712, 2013. doi: https://doi.org/10.1007/s00205-013-0660-6.

[6] V. Banica and L. Vega. The initial value problem for the Binormal Flow with rough data. *Annales scientifiques de l'ENS*, 48(6):1421–1453, 2015. doi: 10.24033/asens.2273.

[7] V. Banica and L. Vega. Singularity formation for the 1-D cubic NLS and the Schrödinger map on $\mathbb{S}^2$. *Communications on Pure and Applied Analysis*, 17(4):1317–1329, 2018. doi: 10.3934/cpaa.2018064.

[8] V. Banica and L. Vega. Evolution of polygonal lines by the binormal flow. *arXiv:1807.06948*, 2018. to appear in Annals of PDE.

[9] V. Banica and L. Vega. On the energy of critical solutions of the binormal flow. *arXiv:1907.08789*, 2019. to appear in Communications in Partial Differential Equations.

[10] C. Bardos, P. L. Sulem, and C. Sulem. On the continuous limit for a system of classical spins. *Communications in Mathematical Physics*, 107(3):431–454, 1986. doi: https://projecteuclid.org/euclid.cmp/1104116142.

[11] G. K. Batchelor. *An Introduction to Fluid Dynamics*. Cambridge Mathematical Library. Cambridge University Press, 1967.

[12] M. V. Berry and S. Klein. Integer, fractional and fractal Talbot effects. *Journal of Modern Optics*, 43:2139–2164, 1996. doi: https://doi.org/10.1080/09500349608232876.

[13] M. V. Berry, I. Marzoli, and W. Schleich. Quantum carpets, carpets of light. *Physics World*, 14(6):39–44, 2001. doi: https://doi.org/10.1088/2058-7058/14/6/30.

[14] Richard L. Bishop. There is More than One Way to Frame a Curve. *The American Mathematical Monthly*, 82(3):246–251, 1975. doi: 10.2307/2319846.

[15] T. F. Buttke. A Numerical Study of Superfluid Turbulence in the Self-Induction Approximation. *Journal of Computational Physics*, 76(2):301–326, 1998. doi: https://doi.org/10.1016/0021-9991(88)90145-3.

[16] C. Canuto, M. Y. Hussaini, A. Quarteroni, and T. A. Zang. *Spectral methods in fluid dynamics, Springer Series in Computational Physics*. Springer-Verlag, NewYork, 1988.

[17] F. Catoni, R. Cannata, V. Catoni, and P. Zampetti. Hyperbolic trigonometry in two-dimensional space-time geometry. *Nuovo Cimento B*, 118(5):475–492, 2003.

[18] F. Chamizo and A. Córdoba. Differentiability and Dimension of Some Fractal Fourier Series. *Advances in Mathematics*, 142(2):335–354, 1999. doi: https://doi.org/10.1006/aima.1998.1792.

[19] Jerome J. Connor. *Analysis of Structural Member Systems*. Ronald P, US, 1976.

[20] J. W. Cooley and J. W. Tukey. An Algorithm for the Machine Calculation of Complex Fourier Series. *Mathematics of Computation*, 19(90):297–301, 1965. doi: 10.2307/2003354.

[21] F. de la Hoz. Self-similar solutions for the 1-D Schrödinger map on the hyperbolic plane. *Mathematische Zeitschrift*, 257(1):61–80, 2007. doi: https://doi.org/10.1007/s00209-007-0115-6.

[22] F. de la Hoz and L. Vega. Vortex filament equation for a regular polygon. *Nonlinearity*, 27(12):3031–3057, 2014. doi: 10.1088/0951-7715/27/12/3031.

[23] F. de la Hoz and L. Vega. On the Relationship between the One-Corner Problem and the M-Corner Problem for the Vortex Filament Equation. *Journal of Nonlinear Science*, 28(6):2275–2337, 2018. doi: 10.1007/s00332-018-9477-7.

[24] F. de la Hoz, C. J. García-Cervera, and L. Vega. A Numerical Study of the Self-Similar Solutions of the Schrödinger Map. *SIAM Journal on Applied Mathematics*, 70(4):1047–1077, 2009.

[25] F. de la Hoz, S. Kumar, and L. Vega. On the Evolution of the Vortex Filament Equation for regular M-polygons with nonzero torsion. *SIAM Journal on Applied Mathematics*, 80(2):1034–1056, 2020. doi: 10.1137/19M1272755.

[26] F. de la Hoz, S. Kumar, and L. Vega. Vortex Filament Equation for regular planar l-polygons in the hyperbolic plane,. *In preparation*, 2020.

[27] Q. Ding. A note on the NLS and the Schrödinger flow of maps. *Physics Letters A*, 248:49–56, 1998.

[28] Q. Ding. The gauge equivalence of the NLS and the Schr¨odinger flow of maps in $2 + 1$ dimensions. *J. Phys. A: Math. Gen.*, 32:5087–5096, 1999.

[29] Q. Ding and J. Inoguchi. Schrödinger flows, binormal motion for curves and the second AKNS-hierarchies. *Chaos soltons and Fractals*, 21:669–677, 2004.

[30] J. J. Duistermaat. Selfsimilarity of "Riemann's Nondifferentiable function". *Nieuw Archief voor Wiskunde*, (4) 9(3):303–337, 1991.

[31] François Fillastre. Polygons of the Lorentzian plane and spherical simplexes. *Elemente der Mathematik, European Mathematical Society*, 69(3):144–155, 2014. doi: 10.4171/EM/256.

[32] B. Fornberg. *A practical guide to pseudospectral methods*. Cambridge University Press, Cambridge, 1996.

[33] M. Frigo and S. G. Johnson. The design and implementation of FFTW3. *Proceedings of the IEEE*, 93(2):216–231, 2005. doi: 10.1109/JPROC.2004.840301.

[34] F. F. Grinstein and E. J. Gutmark. Flow control with noncircular jets. *Annual Review of Fluid Mechanics*, 31:239–272, 1999. doi: https://doi.org/10.1146/annurev.fluid.31.1.239.

[35] F. F. Grinstein, E. J. Gutmark, and T. Parr. Nearfield dynamics of subsonic, free square jets. A computational and experimental study. *Physics of Fluids*, 7: 1483–1497, 1995. doi: https://doi.org/10.1063/1.868534.

[36] S. Gutiérrez, J. Rivas, and L. Vega. Formation of singularities and self-similar vortex motion under the localized induction approximation. *Communications in Partial Differential Equations*, 28(5–6):927–968, 2003. doi: https://doi.org/10.1081/PDE-120021181.

[37] J. C. Hardin. The velocity field induced by a helical vortex filament. *The Physics of Fluids*, 25(11):1949–1952, 1982. doi: https://doi.org/10.1063/1.863684.

[38] H. Hasimoto. A soliton on a vortex filament. *Journal of Fluid Mechanics*, 51(3): 477–485, 1972. doi: https://doi.org/10.1017/S0022112072002307.

[39] S. Jaffard. The spectrum of singularities of Riemann's function. *Revista Matematicá Iberoamericana*, 12(2):441–460, 1996.

[40] R. L. Jerrard and D. Smets. On the motion of a curve by its binormal curvature. *Journal of the European Mathematical Society*, 17(6):1487–1515, 2015. doi: http://dx.doi.org/10.4171/JEMS/536.

[41] B. Khesin. The vortex filament in any dimension. *Procedia IUTAM*, 7:135–140, 2013. doi: 10.1016/j.piutam.2013.03.016.

[42] D. Kleckner, M. Scheeler, and T. M. Irvine. The Life of a Vortex Knot. *arXiv:1310.3321*, 2013.

[43] N. Koiso. The vortex filament equation and a semilinear Schrödinger equation in a Hermitian symmetric space. *Osaka Journal of Mathematics*, 34(1):199–214, 1997. doi: 10.18910/9985.

[44] M. Lakshmanan. Continuum spin system as an exactly solvable dynamical system. *Physics Letters A*, 61:53–54, 1977. doi: https://doi.org/10.1016/0375-9601(77)90262-6.

[45] R. López. Differential Geometry of Curves and Surfaces in Lorentz-Minkowski space. *arXiv:0810.3351*, 2008.

[46] A. J. Majda and A. L. Bertozzi. *Vorticity and Incompressible Flows*. Cambridge Texts in Applied Mathematics. Cambridge University Press, 2002.

[47] T. Nishiyama and A. Tani. Solvability of the localized induction equation for vortex motion. *Communications in Mathematical Physics volume*, 162:433–445, 1994. doi: https://doi.org/10.1007/BF02101741.

[48] P. J. Olver. Dispersive quantization. *The American Mathematical Monthly*, 117 (7):599–610, 2010. doi: 10.4169/000298910X496723.

[49] Mustafa Özdemir and Melek Erdoğdu. On the Rotation Matrix in Miknowski Space-Time. *Reports on Mathematical Physics*, 74(1):27–38, 2014. doi: 10.1016/S0034-4877(14)60055-0.

[50] C. S. Peskin and D. M. McQueen. Mechanical equilibrium determines the fractal fiber architecture of the aortic heart valve leaflets. *American Journal of Physiology*, 266(1):H319–H328, 1994. doi: https://doi.org/10.1152/ajpheart.1994.266.1.H319.

[51] John G. Ratcliffe. *Foundations of Hyperbolic manifolds*. Graduate texts in Mathematics, volume 149. Springer, New York, second edition, 2006.

[52] R. L. Ricca. Physical interpretation of certain invariants for vortex filament motion under LIA. *Physics of Fluids A*, 4:938–944, 1992. doi: https://doi.org/10.1063/1.858274.

[53] L. S. Da Rios. Sul moto d'un liquido indefinito con un filetto vorticoso di forma qualunque. *Rendiconti del Circolo Matematico di Palermo (1884-1940)*, 22(1):117–135, 1906. doi: https://doi.org/10.1007/BF03018608. In Italian.

[54] B. Rosenfeld and B. Wiebe. *Geometry of Lie Groups*, volume 393. Springer US, 1997. ISBN: 978-1-4757-5325-7.

[55] P. G. Saffman. *Vortex Dynamics*. Cambridge Monographs on Mechanics. Cambridge University Press, 1995.

[56] M. Spivak. *A Comprehensive Introduction to Differential Geometry*, volume 5. Publish or Perish (Houston), 1979.

[57] J. V. Stern and C. S. Peskin. Fractal dimension of an aortic heart valve leaflet. *Fractals*, 2(3):461–464, 1994. doi: https://doi.org/10.1142/S0218348X9400065X.

[58] H. F. Talbot. Facts relating to optical science. No. IV. *The London, Edinburgh, and Dublin Philosophical Magazine and Journal of Science*, 9(56):401–407, 1836. doi: 10.1080/14786443608649032.

[59] Lloyd N. Trefethen. *Spectral Methods in MATLAB*. SIAM, Philadelphia, 2000.

[60] J. Walrave. Curves and surfaces in Minkowski space, Thesis (Ph.D.). *Katholieke UniversiteitLeuven (Belgium)*, 1995.